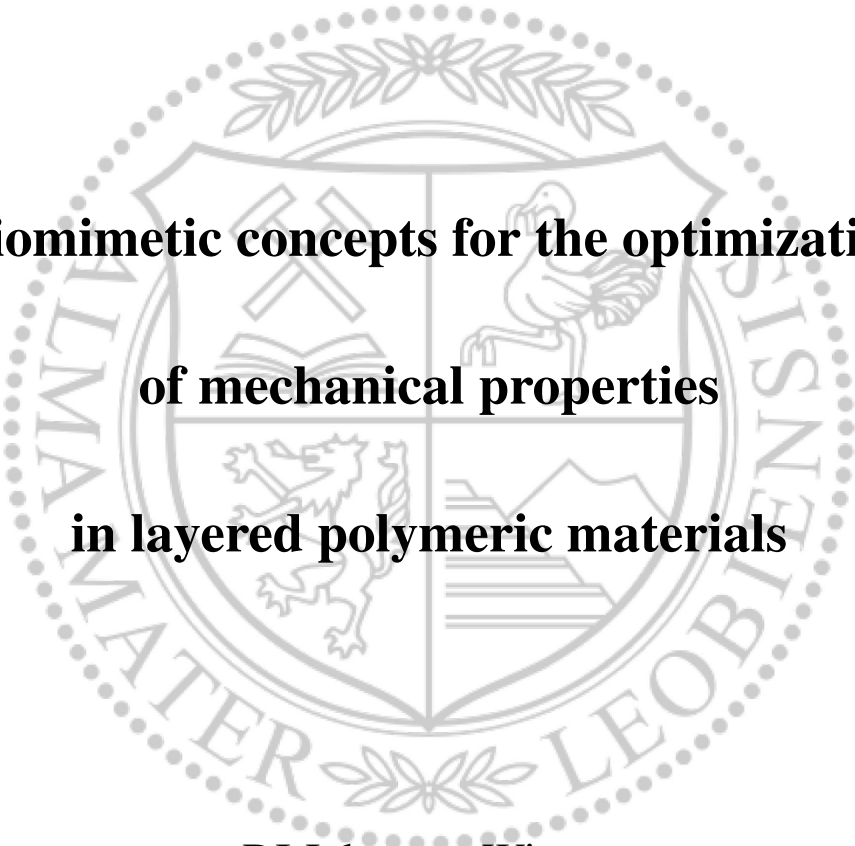Materials Science and Testing of Polymers

Doctoral Thesis

Biomimetic concepts for the optimization of mechanical properties in layered polymeric materials

DI Johannes Wiener

Leoben, February 2023

MONTANUNIVERSITÄT LEOBEN
www.unileoben.ac.at

AFFIDAVIT

I declare on oath that I wrote this thesis independently, did not use other than the specified sources and aids, and did not otherwise use any unauthorized aids.

I declare that I have read, understood, and complied with the guidelines of the senate of the Montanuniversität Leoben for "Good Scientific Practice".

Furthermore, I declare that the electronic and printed version of the submitted thesis are identical, both, formally and with regard to content.

Date 16.02.2023

Signature Author
Johannes Wiener

Dissertation

Biomimetic concepts for the optimization of mechanical properties in layered polymeric materials

February 2023

This cumulative Dissertation was authored by:

DI Johannes Wiener

born 11th March 1993

in Graz (Styria, Austria)

Chair of Materials Science and Testing of Polymers

Department Polymer Engineering and Science, Montanuniversitaet Leoben

Somewhere, something incredible is waiting to be known.

\- Carl Sagan

Preamble

Acknowledgements

I would like to express my gratitude to the many persons who contributed to the success of my academic pursuits. First of all, I want to thank my friends and family, especially my parents Brigitte and Hannes, who have always supported me during my years of study. Returning home has always been a source of replenishment for the mind's capacities after periods of intense work.

Special thanks go to Prof. Gerald Pinter for the opportunity to do this doctoral thesis at the Institute of Materials Science and Testing of Polymers as well as to Dr. Florian Arbeiter for his excellent guidance in the face of practical and theoretical challenges alike. I would also like to thank Prof. Otmar Kolednik for most fruitful discussions and for sharing his immense knowledge in the field of fracture mechanics.

I am also grateful for financial support by the Austrian Research Promotion Agency (FFG), the Montanuniversitaet Leoben and our industry parnters, who enabled and encouraged the elaborate scientific research presented in this thesis.

Last but certainly not least, I deeply appreciate all my colleagues at WPK, who have become dear friends over the course of the years. Working within such an amazing environment always felt more like a privilege than a chore. Thank you for all the support, advice, adventurous business trips and athletic competitions in tabletop soccer!

Abstract

Many biological materials exhibit outstanding mechanical properties that combine stiffness with high toughness and damage tolerance. One example is the skeleton of deep-sea sponges, which shows greatly increased fracture toughness due to soft interlayers (ILs) within a brittle matrix material. These crack arresting properties are explained by the so-called material inhomogeneity effect. Therein, a reduction of crack driving force (CDF) is attributed to the noticeable differences in Young's modulus and yield stress between the constituents.

Although comparable structures have already been mimicked using metals or ceramics, a detailed study has not yet been conducted for polymers. Within the scope of this thesis, the material inhomogeneity effect was replicated in bio-inspired composites made of polypropylene-based materials. Different layer architectures were explored, which can generally be divided into microlayer composites, where layers are only a few microns thick, and multilayer composites, where layer sizes are in the sub-millimeter range.

The objective is to increase fracture toughness and damage tolerance by using soft ILs, while avoiding stiffness reduction due to the soft material. To enable a thorough investigation of stiffness and toughness in such complex structures, targeted modifications were introduced to existing procedures from elastic plastic fracture mechanics, material testing and simulation.

Using these adapted methods, the crucial roles of material selection, defect size, layer thickness and crack re-initiation after arrest were explored in detail. For example, the optimal layer size for microlayer composites was determined as the size of the largest inherent defects. With such an architecture, Charpy impact strength of a brittle matrix

material could be increased by more than 11 times. Fracture energy under tensile loading was also improved 33-fold. Unfortunately, the enormous benefits to toughness and flaw tolerance were also accompanied by decreases in stiffness by up to 90%.

For applications where stiffness is of high priority, multilayer composites are a promising alternative. Specimen stiffness of these composites can be preserved better due to larger matrix layer sizes. More specifically, the largest improvement to fracture toughness[1] could be measured at 3.86 times the matrix toughness, while 75% of stiffness could be maintained. The best solution in terms of stiffness only sacrificed 6% of the matrix values, while fracture toughness could be increased by a factor of 2.81.

Ultimately, guidelines for the design of these optimal structures were deduced, which are intended for later use in engineering applications.

---

[1]Fracture toughness was determined in single edge notch bending tests using an adapted version of the J-integral.

Kurzfassung

Viele biologische Materialien weisen herausragende mechanische Eigenschaften auf, welche Steifigkeit mit hoher Zähigkeit und Schadenstoleranz vereinen. Ein Beispiel ist das Skelett von Tiefseeschwämmen, das dank weicher Zwischenschichten in einem spröden Matrixmaterial eine stark erhöhte Bruchzähigkeit besitzt. Diese rissstoppenden Eigenschaften können mit dem sogenannten Material-Inhomogenitätseffekt erklärt werden. Dabei kann eine Reduktion der risstreibenden Kraft den beachtlichen Unterschieden des Elastizitätsmoduls und der Fließspannung der Konstituenten zugeschrieben werden.

Obwohl vergleichbare Strukturen bereits mit Metallen oder Keramiken nachgestellt wurden, wurde bisher keine detailierte Studie an Kunststoffen durchgeführt. Im Rahmen dieser Arbeit wurde der Material-Inhomogenitätseffekt in biologisch-inspirierten Compositen repliziert, wobei alle verwendeten Materialien auf Polypropylen basierten. Verschiedene Schichtarchitekturen wurden erforscht, welche im Allgemeinen in Mikroschichtverbunde, bei denen Einzelschichten nur wenige Mikrometer dick sind, und Mehrschichtverbunde, bei denen Schichtdicken im Sub-Millimeterbereich liegen, unterteilt werden können.

Das Ziel war es, die Bruchzähigkeit und Schadenstoleranz durch den Einsatz von weichen Zwischenschichten zu erhöhen, während eine Reduktion der Steifigkeit durch das weiche Material vermieden werden sollte. Um eine genaue Untersuchung von Steifigkeit und Zähigkeit in derart komplexen Strukturen zu ermöglichen, wurden gezielte Modifikationen an existierenden Verfahren der elastisch-plastischen Bruchmechanik, Simulation und Materialprüfung vorgenommen.

Durch den Einsatz dieser adaptierten Methoden wurden die entscheidenden Einflüsse von Materialauswahl, Defektgröße, Schichtdicke und Riss-Reinitiierung nach dem Rissstopp

aufgezeigt. Beispielsweise wurde die optimale Schichtdicke in Mikroschichtverbunden als die Abmaße der größten inhärenten Defekte bestimmt. Durch derartige Architekturen konnte die Charpy-Schlagzähigkeit eines spröden Matixmaterials um das 11-fache erhöht werden. Die Bruchenergie unter Zugbelastung wurde ebenfalls um einen Faktor von 33 erhöht. Unglücklicherweise wurden die enormen Vorteile der Zähigkeit und Schadenstoleranz auch von einer Reduktion der Steifigkeit von bis zu 90% begleitet.

Für Anwendungen, in denen Steifigkeit von hoher Priorität ist, stellen Mehrschichtverbunde eine vielversprechende Alternative dar. Die Prüfkörpersteifigkeit in diesen Verbunden kann dank dickerer Matrixschichten besser erhalten werden. Genauer gesagt konnten die größten Verbesserungen der Bruchzähigkeit[2] auf das 3.86-fache der Matrixzähigkeit bestimmt werden, während 75% der Steifigkeit erhalten blieben. Die beste Lösung in Bezug auf Steifigkeit büßte nur 6% der Matrixwerte ein, während die Bruchzähigkeit um einen Faktor von 2.81 erhöht werden konnte.

Abschließend wurden Richtlinien für optimale Strukturen abgeleitet, welche für den späteren Einsatz in technischen Anwendungen gedacht sind.

---

[2]Die Bruchzähigkeit wurde in Versuchen an einseitig gekerbten Biegeproben durch eine adaptierte Version des J-Integrals bestimmt.

Contents

Nomenclature: acronyms

Abbreviation	Description
CDF	crack driving force
CT	computed tomography
CZ	cohesive zone
DMA	dynamic mechanical analysis
FE	finite element
IF	interface
IL(s)	interlayer(s)
$J-R$ curve	crack growth resistance curve
PP	polypropylene
PP-B	polypropylene block co-polymer
PP-H	polypropylene homo-polymer
PP-Soft	very compliant polypropylene
PP-St	standard polypropylene
SENB	single edge notch bending
TSL	traction separation law

Nomenclature: mathematical signs

Symbol	Description	Unit
a	crack length	[mm]
a_c	impact strength (unnotched)	[kJ/m^2]
a_{cN}	impact strength (notched)	[kJ/m^2]
a_0	initial crack length	[mm]
Δa	crack extension	[mm]
a^*	corrected crack length	[mm]
Δa^*	corrected crack extension	[mm]
b	ligament length	[mm]
b_0	distance from initial notch to first IL	[mm]
b_1	ligament length after 1st IL	[mm]
b_2	ligament length after 2nd IL	[mm]
B	specimen thickness	[mm]
β	parameter determining plastic zone size	[-]
C	compliance	[mm/N]
C_{IL}	inhomogeneity term of one IL	[kJ/m^2]
C_{inh}	inhomogeneity term of one IF	[kJ/m^2]
δ	distance between crack flanks	[mm]
δ_f	distance between crack flanks at failure	[mm]
E	Young's modulus	[MPa]
E_b	bending modulus	[MPa]

E^{eq}	specimen stiffness (equivalent modulus)	[MPa]
E'	storage modulus	[MPa]
ε	strain	[%]
ε_{appl}	applied strain	[%]
ε_{res}	residual strain	[%]
Γ	integration path	[-]
Γ_{CZ}	separation energy	[-]
I	area moment of inertia	[m^4]
η	geometry factor	[-]
J	J-integral	[kJ/m^2]
$J_{applied}$	applied J-integral (loading parameter)	[kJ/m^2]
J_c	fracture toughness	[kJ/m^2]
J_c^{ML}	fracture toughness of multilayer composite	[kJ/m^2]
J_{exp}	experimental J-integral	[kJ/m^2]
J_{far}	far field J-integral	[kJ/m^2]
J_{tip}	J-integral at crack tip	[kJ/m^2]
J_0	experimental J-integral without crack length correction	[kJ/m^2]
k	slope of regression line	[-]
l	support length	[mm]
ν	Poisson's Ratio	[-]
ν_{LL}	load line displacement	[mm]
P	potential energy	[J]

r_y^{IL}	plastic zone radius	[mm
s	normal vector to Γ	[-]
σ	stress	[MPa]
σ_{CZ}	cohesive stress	[MPa]
σ_{max}	cohesive strength	[MPa]
σ_y	yield stress	[MPa]
t	layer thickness	[mm]
$tan\delta$	mechanical loss factor	[-]
$\underline{T}$	force vector normal to *Gamma*	[N]
$\underline{u}$	displacement vector	[m]
U	area under force displacement curve	[Nmm]
W	specimen width	[mm]
W_{el}	elastic work	[J]
Ω	relative fracture toughness	[-]

1. Introduction

1.1. Motivation

Material science has always sought to discover and understand novel materials to satisfy the demands of society. Not only good mechanical performance and functionality, but also cost efficiency are required. Especially in recent years, sustainability and prudent use of resources have gained importance as well. In order to satisfy these needs, combining existing materials in innovative ways is a more promising approach than creating an entirely new material class [1–6]. In fact, nature itself abides by this principle and many biological materials are a combination of different base materials. Many of these materials are well known to literature due to their excellent material properties [7, 8]. High stiffness and strength are often paired with damage tolerance and fracture toughness [9, 10], while also serving various other functions (e.g. blood cell production in bone [11–13]). Due to the obvious advantages of these materials, it is desirable to investigate if such structures can be replicated with engineering materials.

In most cases, superior properties are possible in biological materials due to the synergy between several constituents, that are combined in complex, hierarchical microstructures [14–17]. One well-known example is the brick-and-mortar structure of nacre [18, 19], which is depicted in Figure 1a and 1b. Hexagonal platelets made of stiff but brittle aragonite contribute strength and stiffness, while less than 1 wt% of soft protein provides the structure with fracture toughness and damage tolerance [9, 20–24]. Crack deflection and platelet-pullout are the key mechanisms to improve the performance of the brittle matrix material [9, 18, 19, 25, 26]. Unfortunately, comparable microstructures are challenging to reproduce on an industrial scale, since processing techniques such as 3D-printing

1

[27–29] or other advanced procedures [18, 30, 31] are required.
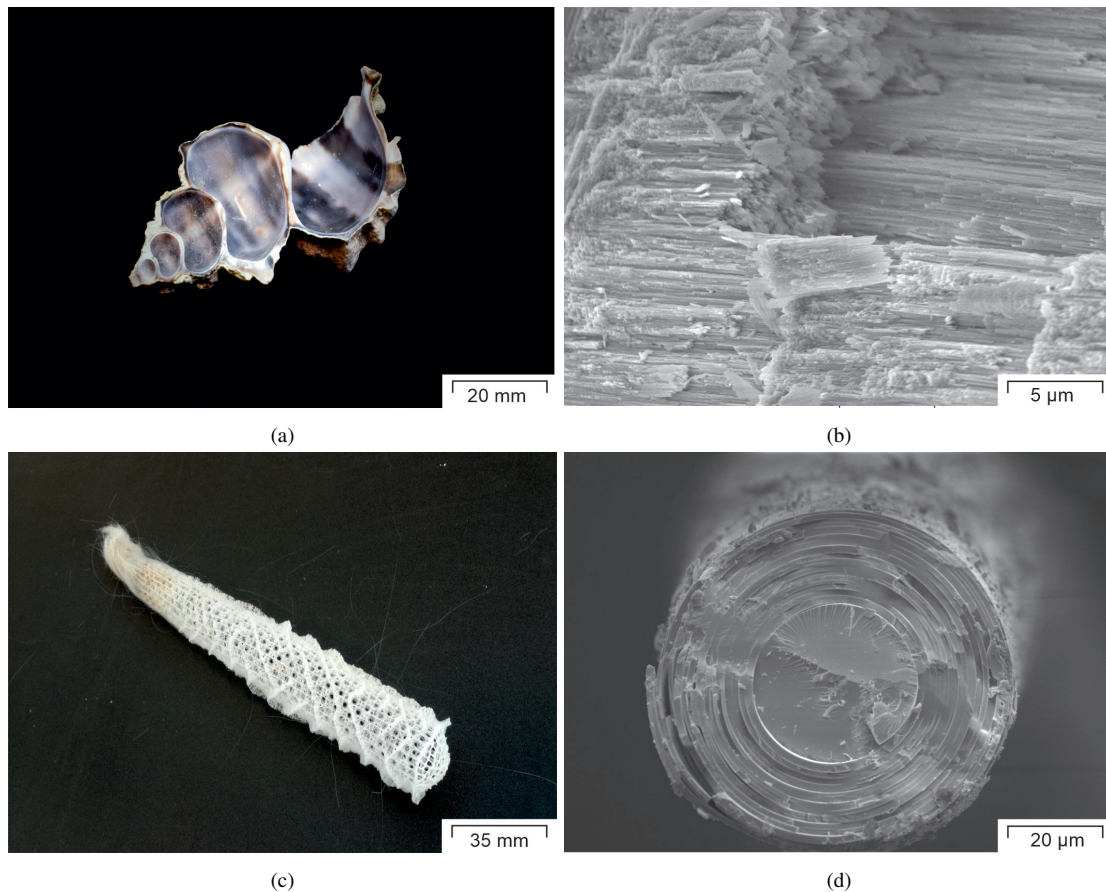

Figure 1: Depiction of (a, b) nacre and (c,d) the skeleton of a deep-sea sponge on a macroscopic and microscopic scale.

However, not all natural materials rely on complicated architectures to yield exceptional mechanical properties. Deep-sea sponges also show high toughness and stiffness in their skeletons [10, 16, 17, 32, 33], although they do not exhibit a microstructure as complex as nacre. In this case, the improved fracture toughness stems from the crack arresting properties of soft protein interlayers (ILs) within a matrix of bio-glass [32, 34–36]. The rod-like components of the sponge's skeleton are made of alternating, concentric rings of

the two base materials [17], which is shown in Figure 1c and 1d. This particular structure could be readily manufactured in a microlayer co-extrusion process [37–39]. Due to the increased applicability to cylindrical construction elements or co-extruded pipes this structure may be an attractive option for the use in industry.

Transferring the concept of soft ILs to engineering materials has already shown great success in various material classes. Sistaninia et al. [40] demonstrated the crack arresting properties of low strength steel within a high strength steel matrix. The same principle applies when using entirely different materials such as soft polymer ILs in high-strength aluminum alloys [41, 42], or thin films of various metals [43]. Fromm et al. even applied this biomimetic strategy to laminates made of metal and diamond layers, which resulted in increased damage tolerance [44].

Using layered structures showed great success in ceramics as well. In addition to soft ILs [45], layers with compressive residual stresses can be used to optimise strength and toughness [46, 47], or manipulate crack paths in beneficial ways [48]. Bermejo et al. were able to illustrate that such compressive layers in Al_2O_3–ZrO_2 laminates can be utilized to increase resistance against crack growth as well as flaw tolerance [49]. By transferring these concepts to thin piezoelectric films, major improvements are possible for microelectromechanical systems [50].

Studies on polymer adhesive layers in a glass matrix by Lee et al. reveal, that the transition of material properties play a significant role in crack propagation near material interfaces (IFs) [51]. Lach et al. came to similar conclusions regarding polymer bi-layer materials, where the resistance against stable crack propagation is influenced near the material IF [52]. Therein, the mismatch in material properties as well their resistance against

3

plastic deformation are stated as the most crucial factors. Nonetheless, such approaches were never intentionally used for polymers to optimize the portfolio of mechanical properties.

For that reason, the potential of soft ILs in polypropylene (PP) based, layered materials was explored in the present work. The thesis focuses on the replication and investigation of soft ILs in reinforced polymers, which were inspired by the layered structure of the deep-sea sponge. While a replication of the natural microstructure can improve mechanical performance, simplified layer architectures with few, well placed ILs may also yield great results for industrial applications. In both cases, finding design criteria for optimized fracture toughness and stiffness was of particular interest within this thesis.

1.2. Objectives

The main objective of this thesis was to replicate the crack arresting properties of biological materials in polymers. There are several functions, which have to be fulfilled by a pair of matrix and IL in order to improve the performance of the composite overall. On the one hand, growing cracks need to be stopped by the ILs in order to increase fracture toughness of the composite material. On the other hand, new cracks should not be able to initiate easily after crack arrest. Despite the introduction of the soft component, the composite should also maintain high stiffness.

Therefore, two different approaches were investigated separately. Namely, microlayer composites with a multitude of ILs, which are more similar to the structure of biological materials, and multilayer composites with a limited number of optimized ILs, which promise higher feasibility as engineering applications.

Especially the viscoelastic-plastic material behavior of polymers was expected to cause

4

complications, because plastic and viscous deformation may decrease the effectiveness of some ILs. Therefore, novel approaches had to be developed and established procedures were refined in order to overcome these challenges. Based on these modified techniques, guidelines for the design of effective layered architectures with high toughness and stiffness were deduced in the end.

1.3. Structure of the thesis

As previously described, this cumulative thesis pursued two separate approaches to layered structures, namely microlayer composites and multilayer composites. Section 2 addresses microlayer composites, which attempt to closely replicate natural materials by using thin layers with thicknesses of few microns. The effects of layer thickness and the material's inherent defect size on the impact strength and damage tolerance of the material are discussed. Despite comparably challenging manufacturing, the complexity of its natural counterpart could not be entirely matched. Although considerable advantages in terms of toughness were shown, microlayer composites also showed a reduction of stiffness as a result.

Therefore, the study was extended to multilayer composites in Section 3, where only a few ILs with thicknesses in the sub-millimeter range were used. This approach is more appealing for engineering applications due to the increased feasibility. However, ILs must be well-designed in these cases, where structural integrity may depend on a single IL. Thus, methods to investigate fracture toughness and specimen stiffness of polymeric multilayer materials are discussed in detail. The necessary adaptations made to existing procedures of elastic plastic fracture mechanics represent a core part of this thesis. This section also includes basic approaches for material selection based on literature and FE-studies in order

5

to determine promising pairs for matrix-IL combinations.

New questions arose during the discussion of unexpected failure behavior, which was ultimately linked to crack re-initiation phenomena after arrest. Since these processes are a crucial part of ultimate specimen failure, they were investigated separately in Section 3.4. Experimental and simulation based methods are presented to characterize the accumulation of damage and determine the initiation of cracks.

The cumulative thesis concludes with a summary of the main findings and an outlook is given, which suggests areas of interest to be explored in future studies. Notable contributions to the state of the art were published in peer-reviewed journals which are included in full at the end of the thesis. A short overview of ***Publications I-V*** can also be found in Table 1.

Table 1: Overview of peer-reviewed publications.

Abbreviation	Title	Related topic
Publication I	Optimization of Mechanical Properties and Damage Tolerance in Polymer-Mineral Multilayer Composites (Wiener et al., 2021)	impact strength and damage tolerance of microlayer composites
Publication II	Bioinspired toughness improvement through soft interlayers in mineral reinforced polypropylene. (Wiener et al., 2020)	experimental proof of concept for multilayer composites
Publication III	Application of the material inhomogeneity effect for the improvement of fracture toughness of a brittle polymer (Tiwari et al., 2020)	FE simulation of multilayer composites
Publication IV	Influence of Layer Architecture on the Material Inhomogeneity Effect in Polymer Multilayer Composites (Wiener et al., 2022 a)	optimization of stiffness and toughness in multilayer composites
Publication V	Characterization methods for strain induced damage in polypropylene (Wiener et al., 2022 b)	determination of microstructural damage

2. Replication of biological materials

2.1. Classical strategies for toughening polymers

For polymers, it is common practice to improve strength, stiffness or creep resistance by introducing particles or fibers [53–56]. Many combinations of matrix and filler are known and catalogued [6, 57]. However, the reinforcement often leads to embrittlement as well. One countermeasure is optimizing particle orientation, which increases reinforcement while also reducing the possible defect size in the intended loading direction [39, 58]. Alternatively, soft components may be added for increased ductility and toughness, which is usually done by blending or compounding [59–61]. Unlike natural materials, these approaches yield random distributions and orientations of reinforcing or toughening agents. To introduce the desired microstructures, more sophisticated processing techniques are required.

2.2. Toughness enhancement via biomimicry

The improved fracture toughness of many biological materials is caused by their intricate microstructures [21–23] of various constituents. In the case of the deep-sea sponge, crack arresting properties are achieved through alternating layers of soft[3] protein and hard matrix material [32, 34–36]. In addition to neutralizing growing cracks, the maximum defect size in the material is also limited to the thickness of one matrix layer, which makes the initiation of new cracks more difficult. Kolednik et al. revealed, that optimized spacing of layers also relies on the loading situation [62]. Therefore, optimized architectures must be designed with the intended application in mind.

---

[3]In this context, "soft" refers to a material with a low Young's modulus, E, and/or yield stress, σ_y, while "hard" refers to a material with high E and σ_y.

In order to replicate the layered structure of deep-sea sponges, an array of specialized techniques could be considered. These include 3D-printing, freeze casting or magnetically assisted additive manufacturing [18, 27, 28, 30, 31]. Physical or chemical vapor deposition processes can also be used, if the technique is feasible for the intended materials [44]. Crystallization kinetics of materials may be exploited as well to produce tailored patterns in thin layers [63–67]. Yuri Estrin and his colleagues [14, 68, 69] suggest severe plastic deformation as an effective means to alter material properties in defined patterns. Unfortunately, many of these techniques have limited applicability for polymers or are not possible at all.

However, recent advances in additive manufacturing enable the mimicry of various biological structures [8], which can be manufactured with great accuracy and increasing options of processable materials [70–72]. Using hybrid techniques, it is possible to combine various base resins in one process and tailor mechanical properties [73]. Successful biomimicry is shown, for example, by Yadav et al., who replicated the brick and mortar structure of nacre using acrylonitrile butadiene styrene and found 20% increased strain at break and 44% increased toughness [29]. Stögerer et al. report similar findings for acrylate based structures with a 22% increase of strain at break, leading to an increase in fracture toughness of 70% [73].

Nonetheless, interfacial strength is often reduced in comparison to bulk materials and structural integrity could suffer, unless the process is highly optimized [74–77]. Although the strategic placement of ILs is appealing, Waly et al. [78] pointed out that crack arrest always competes with crack penetration and crack deflection. Depending on the length of the IL, a different mechanism may be dominant, thus also influencing overall energy

absorption. Additionally, 3D-printing techniques tend to be rather time consuming, which is a criterion of exclusion for many industrial applications.

Fortunately, there is an established production technique, which can be adapted to produce micro-layered structures on large scales. Layered composites can be created using a static mixer in a co-extrusion process [37, 38, 79], which is illustrated in Figure 2. This extrusion based processing technique offers the potential of large throughputs in addition to the fabrication of micron-sized layers. The layer thickness is varied by repeatedly folding the melt strand, so that the number of layers doubles while their thickness is halved. Micro- and nanolayer-coextrusion have been used to reap various benefits, such as improved barrier properties [80–82], flame retardancy [83] and even semi-conductivity by creating metal filled polymers [84, 85]. Although the design options are not as vast as for 3D-printing, they are sufficient for the intended architecture.
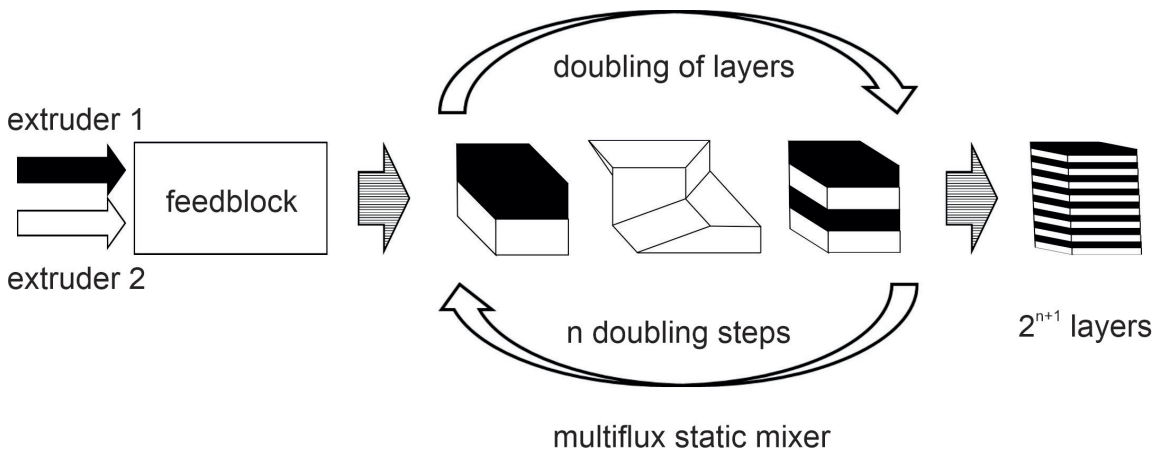

Figure 2: Multistatic mixer used in the co-extrusion of microlayer composites [37, 38].

9

2.3. Opportunities and challenges for microlayer composites

2.3.1. Potential improvements to toughness and ductility

For particle-reinforced microlayer composites, a reduction of layer size promises improved properties as well. The limitation of defect size in combination with increased particle orientation results in enhanced ductility, crack path tortuosity and crack tip blunting [39, 58, 86, 87]. Jia et al. [27] found that microlayered structures can achieve toughness values more than 5 times higher than their constituents. Mueller et al. could link the improved alignment of talcum particles to an increase of fracture strain [39, 58]. They report improvements by up to 400% between 64 and 256 layers, although higher and lower layer counts did not perform as well.

2.3.2. Layer integrity

Although the potential of layered materials is great, certain criteria must be fulfilled to ensure crack arresting properties. On the one hand, some sources point out that interfacial strength between the phases is crucial to success in replicating the properties of biological materials [88, 89]. On the other hand, ILs must be intact, continuous layers in order to function properly. Baer et al [58] claim, that problems during manufacture of very thin layers, such as particle agglomeration, led to a decrease of fracture strain. Mueller et al. [80] even reported quasi-brittle fracture at 1024 or more layers.

The results of *Publication I* show, that smaller layer sizes indeed cause an increase in impact strength in the unnotched state, a_c, by a factor of 4.5. Interestingly, two plateaus are formed as a function of matrix layers size (Figure 3a). The transition region is reached as soon as matrix layer thickness is reduced below the size of the largest reinforcing particles (ca. 25 μm). Presumably, this effect is caused by the forceful orientation of the largest

particles and agglomerates, which can then no longer act as sites for crack initiation (Figure 3b). When the majority of particles is aligned, decreasing layer size brings no more benefits and the upper plateau is reached.

In contrast to Baer and Mueller [39, 58], no lower limit for IL thickness was found, since even ILs in the low micron range were effective at hindering crack growth. Consequently, excellent processing quality can be assumed due to the absence of delaminations, agglomerations and embrittlement at smaller layer sizes.

$$D_C > t$$

$$\frac{D_C}{t} < 1 \rightarrow Mode\ I\ failure\ hindered$$

$$D_C < t$$

$$\frac{D_C}{t} > 1 \rightarrow Mode\ I\ failure\ facilitated$$

(a)

(b)
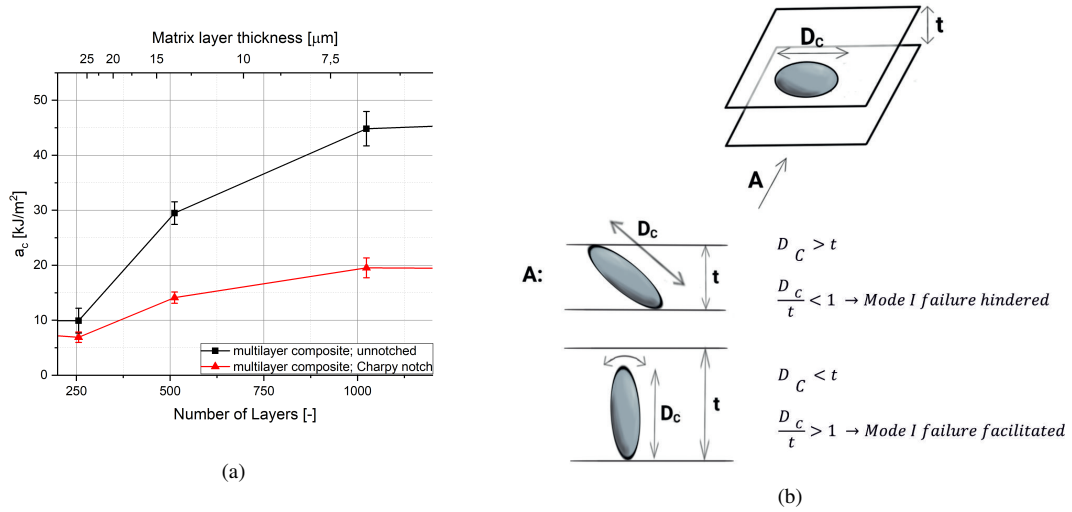
Figure 3: (a) Impact strength depending on the number and thickness of layers and (b) orientation of particles by force during processing.

Preliminary studies to ***Publication I*** also included specimens, where the layer structure was disturbed by turbulences during manufacturing (Figure 4a). In these cases, no benefits could be attained and the overall material behavior closely resembled that of a blend. When continuous layers could be produced (Figure 4b), flaw tolerance was greatly increased, thus improving impact strength. The importance of separate, continuous layers can be confirmed by other sources, for example Stögerer et al., who came to a similar
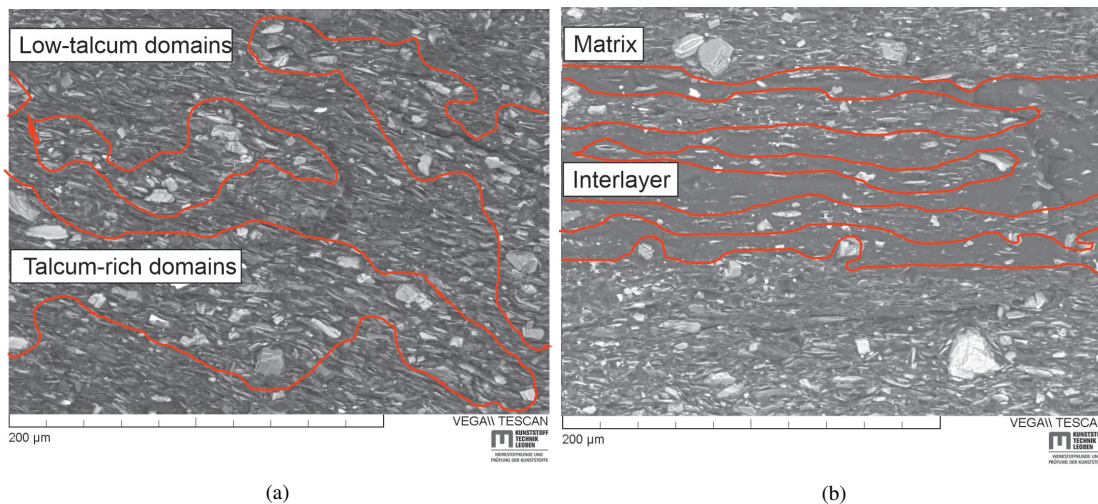
conclusion in resin-based 3-D printing [73].

Figure 4: (a) Layered structure that was disturbed by turbulences during processing and (b) continuous microlayers.

2.3.3. Stress decoupling

Unfortunately, a decrease of stiffness is often observed simultaneously to an increase of toughness when soft ILs are used. Concerning the aforementioned examples, the toughness increase in Stögerer et al. was accompanied by a slight reduction of yield strength. The Young's modulus, E, was also reduced to half of the matrix stiffness [73], while Yadav et al. reported a modulus reduction of 62% [29]. The 400% increased toughness of layered structures in Jia et al. [27] came at the cost of 90% of the matrix material's stiffness. They attribute the harsh reduction to the small resistance of the soft phase towards shear deformations, which is also why interlocking structures retained higher stiffness.

In order to reveal specific effects of the layered structure, the most promising composites in **Publication I** were compared to blends of the same material composition and the

matrix material. In addition to a_c, the impact strength in notched state, a_{cN}[4], and the bending modulus, E_b, are also relevant for mechanical performance. A diagram in the style of an Ashby plot [1] can be generated (Figure 5a and 5b), which compares these mechanical parameters.
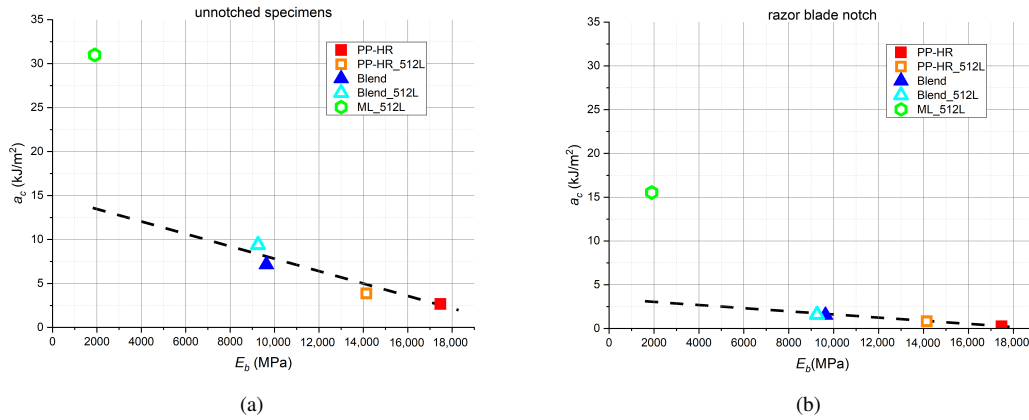

Figure 5: Impact strength versus bending modulus for (a) unnotched and (b) razor blade notched specimens according to ***Publication I***.

A trend line can be recognized between the matrix material (PP-HR, PP-HR_512L[5]) and the blends (Blend, Blend_512L), roughly adhering to the rule of mixture. Along this trend line, increased toughness comes at the cost of stiffness. Although this trade-off is also true for the layered structure (ML_512L), the composite lies above the trend line, meaning that the increase in toughness outweighs the stiffness loss. More precisely, the layered material showed $a_c = 30.99$ kJ/m^2, which is more than 11 times the impact strength of the brittle matrix material, which was only 2.66 kJ/m^2.

---

[4]Razor blade notches were used in this contribution.

[5]In this context, the extension "_512L" indicates a material that was processed in a microlayer extrusion process. The procedure was also performed on the matrix material and the blend to observe the effects of particle orientation during processing.

The increased flaw tolerance of the layered structures that was found in ***Publication I*** is emphasized in Figure 5b, where the values for specimens with razor blade notches are shown. The microlayered material is able to retain approximately half of the impact strength from the unnotched state (15.53 kJ/m^2), while the values plummet for all other materials (e.g. only 0.25 kJ/m^2 for the matrix material). The enhanced damage tolerance stems from a change in fracture behavior: All blends and the matrix exhibit brittle fracture behavior, while the microlayer composite benefits from crack tip blunting and even crack arrest.

Although these improvements surpass many values given in literature, E_b was also reduced to 11% of the matrix material. Similar results were obtained in unnotched tensile tests, where fracture energy could be increased by 33 times while sacrificing 76% of stiffness (Figure 6a and 6b).
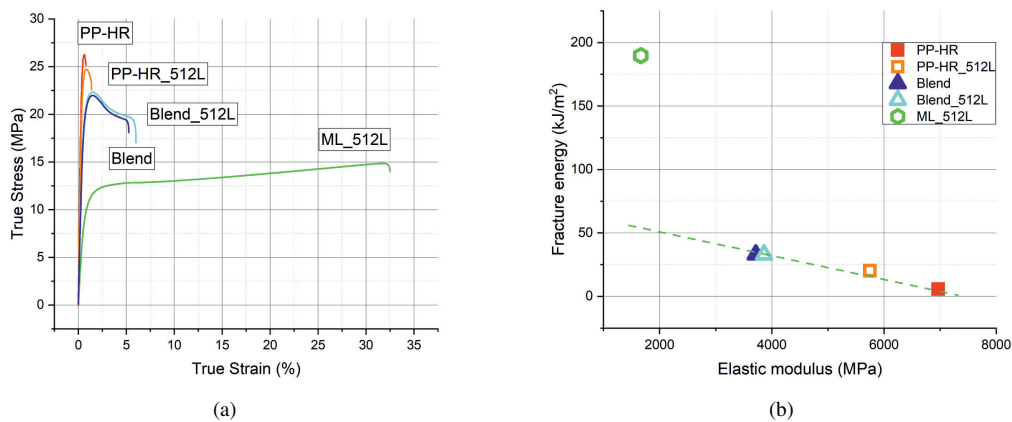

Figure 6: (a) Stress-strain curves of unnotched tensile specimens were evaluated to obtain (b) fracture energy and elastic modulus.

The common denominator for stiffness loss in literature as well as in ***Publication I*** are very compliant ILs under bending loads. A plausible explanation is the decoupling

14

of stresses between matrix ligaments, which is illustrated in Figure 7. The IL material is so compliant, that the loads are not transferred properly between the matrix ligaments. Instead, these sections of matrix material develop stress distributions independently from one another. Under a bending load this leads to separate bending stress distributions for each matrix ligament. As a consequence, bending stress maxima are less pronounced and exhibit lower maximum stresses in smaller layers.
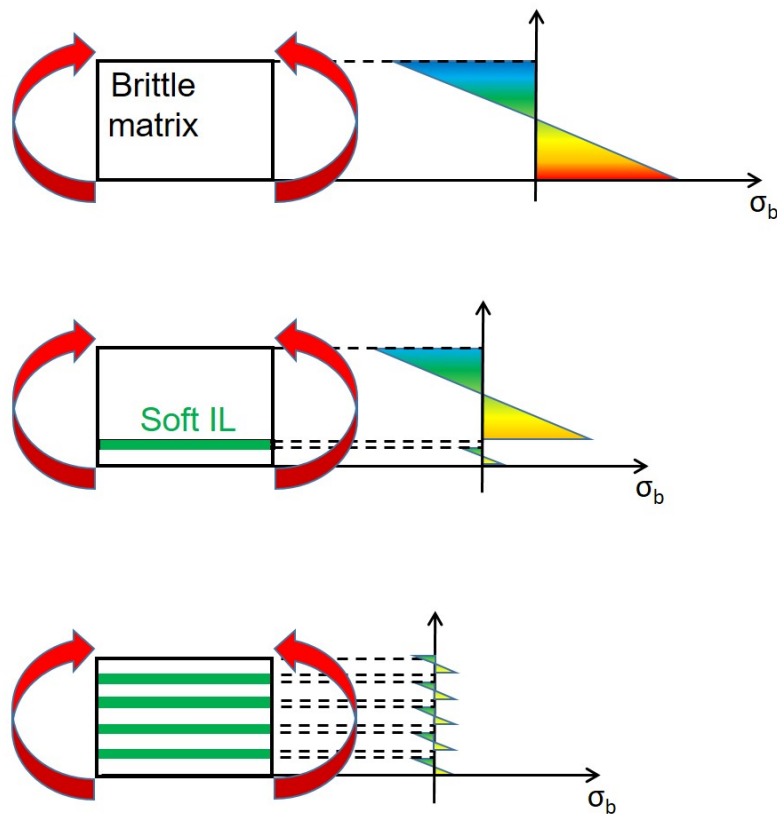
Figure 7: Decoupling of stresses due to very compliant ILs.

When stresses are evenly distributed instead of having one extreme maximum, the development of one fatal crack is less likely. However, there is a significant drawback to the reduction in layers size: Flexural rigidity is determined by the area moments of inertia, I_{layer}, of all matrix layers combined, which can be estimated with Equation 1. Therein, t is the matrix layer thickness and B_{layer} is the width of one layer[6]. The flexural rigidity of the ILs and shear between the layers are neglected, because these contributions are supposedly small due to the low modulus of the IL material. As can be seen, the reduction is especially severe under bending loads, where t contributes with an exponent of three.

$$flexural\ rigidity = \Sigma\left(E_{matrix}I_{layer}\right) = E_{matrix}\Sigma\left(\frac{B_{layer}t^3}{12}\right) \tag{1}$$

Despite significant improvements to toughness, the reduction of stiffness poses a serious limitation for many applications. Additionally, guaranteeing layer integrity may still be difficult when processing very thin layers. Here, millions of years of evolution prove superior and the performance of the deep-sea sponge cannot be reached. On the one hand, the cylindrical shape along with variable matrix layer sizes (large in the center, small near the outer fiber) is optimized to endure bending loads [36]. On the other hand, the sponge can grow its ILs much thinner while still maintaining layer integrity. Thus, the biological material can afford to use ≤1% of soft phase, while the investigated replications required 15% for stable processing conditions. In order to decrease the detrimental effects of stress decoupling and reduce the complexity of layer architectures the use of multilayer composites with a limited number of soft ILs is advisable and was further explored in ***Publication II*** to ***IV***.

---

[6]The cross sections of the layers are assumed to be rectangular.

3. Biomimicry in engineering applications

Using a limited number of ILs in a multilayer approach is an alternative to microlayer composites that promises higher stiffness due to the larger matrix layer sizes. This is an attractive option when the failure behavior is known and the IL(s) can be placed strategically where cracks are expected to grow. Hence, the use in engineering applications is promising, since loading situations are well-defined in most cases. If only a limited number of ILs are responsible for crack arrest, these must be designed in an optimal way to ensure structural integrity. Thus, fracture mechanical methods are presented in this section in order to analyze the failure of layered materials in a more detailed way.

3.1. Characterization of layered materials using fracture mechanics

The material response to the tip of a crack can be described with well-established approaches from linear-elastic fracture mechanics [90–92], such as the stress intensity factor [93], K, or the energy release rate [94], G. Some early contributions already attempted to extend K-based approaches to bi-material interfaces (IF) [95, 96]. Huajian et al. applied modulus perturbation methods to illustrate the effects of fibers and other inclusions on the stress distribution around a crack tip [97]. In similar considerations it was shown that these stress fields can be superposed [98], thus enabling the description of multilayer composites by adding contributions from all individual IFs. The consensus is that a spatial variation of E greatly influences stress distributions and may increase or decrease the value of K at the crack tip.

The elastic-plastic and viscous behavior of polymers is highly non-linear, so that concepts from linear-elastic fracture mechanics are not likely to produce accurate results.

Methods from elastic-plastic fracture mechanics have been used instead for a better understanding of the crack arresting properties in polymer multilayers. A promising parameter is the so-called J-integral, J, which was proposed by Rice in 1968 as a means to describe the fracture toughness of non-linear elastic materials [99]. J is calculated as a line integral from the lower to the upper crack flank (Equation 2 and Figure 8), where W_{el} is the elastic work of deformation, Γ the integration path, $\underline{T}$ the force vector normal to Γ and $\underline{u}$ is the displacement vector. For two bodies of the same thickness B, J describes the difference in potential energy caused by a difference in their crack lengths, a.

$$ J = \int_{\Gamma} W_{el}dy - \underline{T}\frac{\delta\underline{u}}{\delta\underline{x}}ds = -\frac{1}{B}\frac{dP}{da} \tag{2} $$
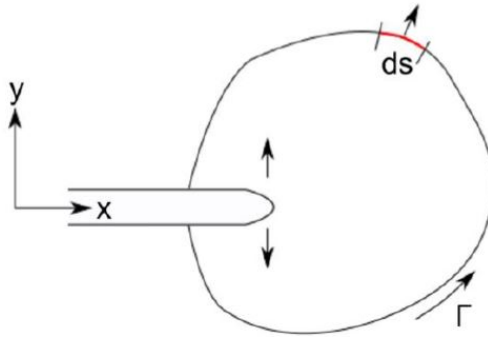

Figure 8: Integration path Γ for J around the crack tip [99].

J can also be used for elastic-plastic materials, as long as no unloading processes occur. If unloading happens as a consequence of crack growth, corrections are usually made (e.g. in [100, 101]) to account for certain amounts of crack extension, Δa. If the crack tip is the only singularity in the stress strain-field, any arbitrary path enclosing the crack tip will yield the same result.

18

As a result of this path independence, J directly at the crack tip, J_{tip}, is equal to the far field value, J_{far}, so that $J_{tip} = J_{far}$ for homogeneous materials. On the one hand, J_{far} is usually determined from a path including the whole specimen, so it can be calculated using the externally applied load and load line displacement. On the other hand, J_{tip} can be seen as a measure for local crack driving force (CDF) [102]. Crack growth is possible when J_{tip} becomes larger than a critical value, which is regarded as fracture toughness of the material, J_c. However, the stress-strain fields are disturbed by the interfaces (IFs) in heterogeneous materials. The chosen path for evaluation matters in these cases, since an IF can either be crossed or avoided. The same principle applies for gradients of Young's modulus, E, and yield stress, σ_y, which also cause a change in J_{tip} depending on the path taken [103–105]. As a result, J looses its path-independence in heterogeneous materials and, in general, $J_{tip} \neq J_{far}$.

Simha et al. [102] solved this problem by introducing an additional inhomogeneity term, C_{inh}, which accounts for the influence of an IF. The calculation of C_{inh} is based on the concept of configurational forces [106, 107], which was spearheaded by Eshelby [108–111] and does not impose as many constraints as Rice's J. In short, configurational forces were originally designed for metals to describe the thermodynamic forces that govern the behavior of inclusions, pores, dislocations etc.. However, the concept may also be applied to describe the configurational force at the crack tip, where it happens to coincide with the definition of J_{tip}. Additional terms for an IF between phases can be obtained, thus enabling the description of the crack tip near soft ILs without any further assumptions.

Most notably, this approach is not restricted to any type of material behavior and can even be used for elastic-plastic and inhomogeneous materials. Since an IL has two IFs,

19

the modified J_{tip} consists of J_{far} and two inhomogeneity terms (Equation 3). The resulting variation of J_{tip} caused by the IFs is called material inhomogeneity effect. The concept can not only be applied for a single IL, but also for multiple ILs, where the inhomogeneity terms of all IFs in the vicinity are superposed instead.

$$J_{tip} = J_{far} + C_{inh1} + C_{inh2} = J_{far} + C_{IL} \tag{3}$$

Describing CDF in this manner can be utilized to describe periodical structures [112] such as the aforementioned nacre or deep-sea sponges. Kolednik et al. used a similar approach to investigate the influence of periodicity on the damage tolerance of these hierarchical materials [35]. The study concluded, that the tolerance to flaws is, among other factors such as applied load, greatly influenced by the spacing of ILs.

Although there is a multitude of other parameters, which influence the material inhomogeneity effect [43, 113], considerations in this thesis shall be limited to differences in E and σ_y, resulting in three possible categories of inhomogeneity:

- E-inhomogeneity, where the IL material has a lower E than the matrix and σ_y is similar

- σ-inhomogeneity, where the IL material has a lower σ_y than the matrix and E is similar [7]

- $(E - \sigma)$-inhomogeneity, where σ_y and E are different

---

[7]Pure σ-inhomogeneities are excluded from further discussion, because material combinations of this sort are rarely seen for polymers which are chemically compatible and could be used to produce multilayer composites.

20

Although E- and σ-inhomogeneities can work on their own, the combined $(E - \sigma)$-inhomogeneity is usually favored in terms of crack arresting properties.

Sistaninia et al. conducted more detailed finite element (FE) studies [114] on J_{tip} in the vicinity of a single, soft IL in a hard matrix and found fascinating results: J_{tip} is increased in comparison to J_{far} at the hard-to-soft IF and equally decreased at the soft-to-hard-IF. As a result, a minimum and a maximum are formed when a growing crack encounters a soft IL, which is shown in Figure 9a and 9b (taken from **Publication II**). An increase of J_{tip} above J_{far} equals an increase in CDF and crack growth is facilitated, which is called anti-shielding effect. A reduction below J_{far} correlates to a reduction in CDF and is called shielding-effect.
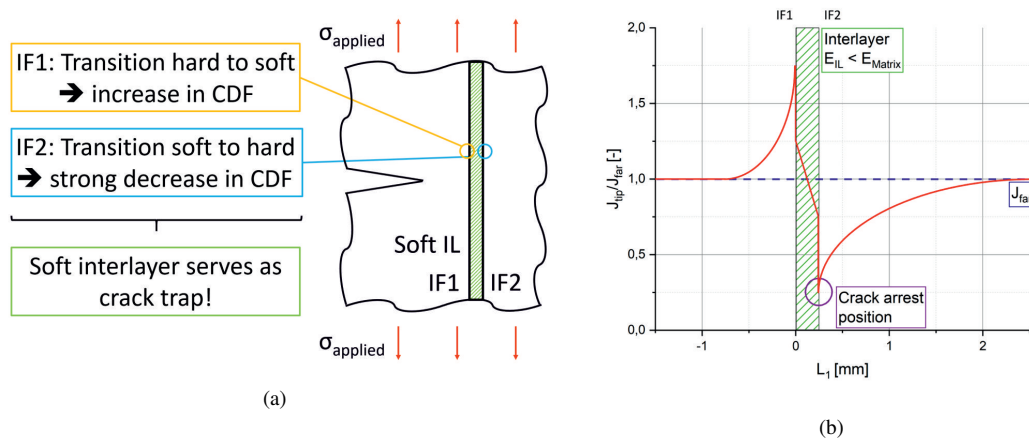
Figure 9: (a) Loading of a material with a soft IL leading to (b) a variation of crack driving force.

The anti-shielding effect only accelerates the failure process, but does not change the failure behavior. The shielding-effect, on the other hand, can alter the fracture process by arresting growing cracks. These findings are in agreement with experimental results presented by Zechner et al. [41], who investigated high strength aluminum alloys with

soft polymeric ILs. In this example, the failure behavior of single edge notch tension specimens was changed from crack growth to tensile failure. Studies by Lach et al. found comparable variations of J caused by the IF in PP-based bi-materials [115], indicating that the approach is valid for polymers too. This assumption is supported by findings in ***Publication II***, where the failure mode in single edge notch bending specimens could also be transformed to a bending fracture due to soft ILs. This was visible as crack arrest in combination with extensive plastic deformation in the post-IL regime (Figure 10a) instead of the quasi-brittle fracture, which is typical for the homogeneous matrix material (Figure 10b).

(a)   (b)
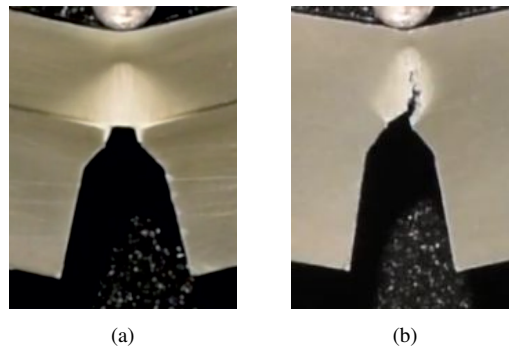
Figure 10: Specimen failure through (a) bending fracture after crack arrest at a soft IL and (b) crack growth in a homogeneous specimen.

An analysis of CDF in multilayered polymers is presented in ***Publication III*** to evaluate pairs of matrix and IL materials. For this approach the ratio of the minimum of J_{tip} and the applied J_{far} was determined as a measure of crack arresting properties. J_{tip} was calculated for different positions of the crack tip in a specimen with a soft IL using material parameters based on ***Publication II***. From the resulting variation of CDF, the magnitude of the inhomogeneity effect could be obtained (Figure 11). By varying the properties of the base materials, a promising pair of IL and matrix may be chosen before manufacturing

the test specimens. The study concluded, that unreinforced types of PP can be suitable IL materials in a matrix of talcum reinforced PP, which are capable of arresting growing cracks, as demonstrated in Figure 10a.
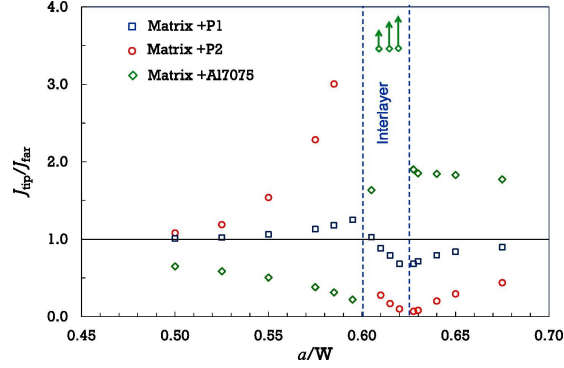

Figure 11: Analysis of CDF due to interlayers in a reinforced polymer matrix conducted in **Publication III**.

3.2. Adaptations for polymeric materials

To validate the promising results of **Publication III** for polymeric materials, further testing on composites with different pairs of materials and layer designs was performed in **Publication II** and **Publication IV**. Since J_{tip} cannot be measured experimentally, the experimental J-integral, J_{exp}, according to Hale and Ramsteiner [100] was used instead. This technique is a multispecimen approach for single edge notch bending (SENB) specimens, which was originally intended for homogeneous materials. When plotting the $J - R$ curve of a composite specimen according to [100], large scattering occurs due to the soft IL, as is shown in the left part of Figure 12a. The scattering is caused by variances in geometry parameters of multilayered specimens, which are shown in Figure 12b. Most notably the distance from the initial notch to the first IL, b_0, exhibits considerable variance due to influences from both the manufacturing and the notching process. A corrected crack extension, $\Delta a^* = \Delta a - b_0$, is introduced to replace Δa in the $J - R$ curves (right part of

23

Figure 12a). The purpose of this parameter shift is to compensate for the variances in b_0 and simultaneously offer a method to evaluate the fracture toughness of specimens with ILs.
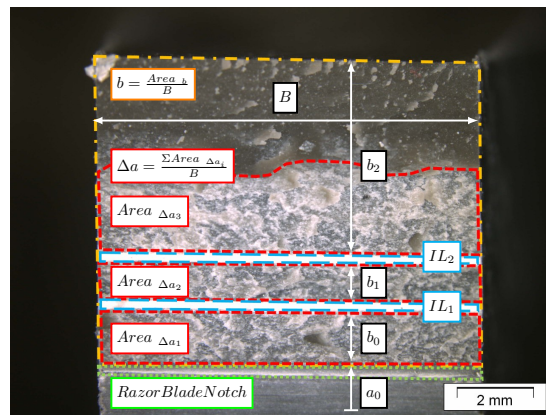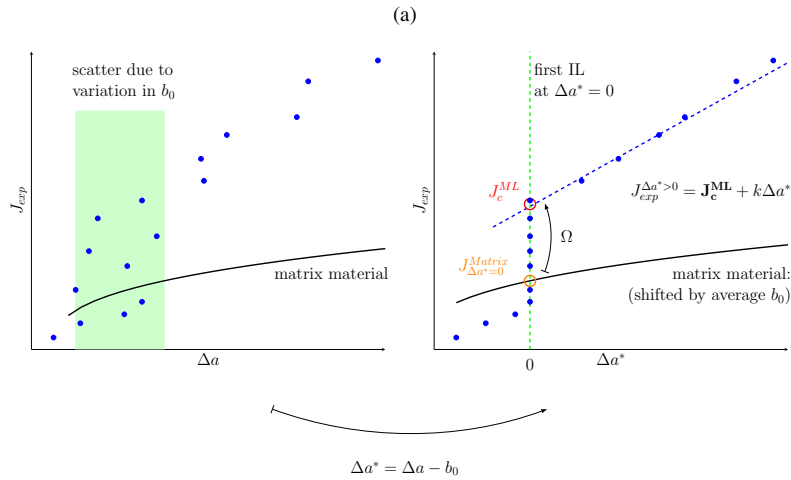
Figure 12: (a) Adaptations to the $J-R$ curve for heterogeneous materials and (b) analysis of fracture surfaces of multilayered SENB specimens.

Additionally, conventional definitions for fracture toughness may not be appropriate for specimens with soft ILs. As shown in the right part of Figure 12a, the post-IL regime can be described by a linear regression line in the form $J_{exp}^{\Delta a^* > 0} = J_c^{ML} + k\Delta a^*$. Therein,

J_c^{ML} is the required energy to overcome the IL, which is regarded as fracture toughness of the composite. A comparison can be made between J_c^{ML} and J_{exp} of the matrix[8] at $\Delta a^* = 0$, which simply describes the relative increase of fracture toughness caused by the IL. This parameter is named Ω and the corresponding formula is shown in Equation 4. As a counterpart to Ω, an equivalent modulus, E^{eq}, was introduced in **Publication IV**. E^{eq} is based on the calculation for the bending modulus in ASTM E1820 [116] and can be used to rank the stiffness of multilayer composites and compare them to the matrix material.

$$\Omega = \frac{J_c^{ML}}{J_{\Delta a^*=0}^{Matrix}} \tag{4}$$

Armed with these tools, it was possible to analyze the experimental data gathered in **Publication II** in greater detail. ILs of standard PP (PP-St) and soft PP (PP-Soft) were introduced into matrices made of talcum reinforced PP and the focus was set on the proof of concept for polymeric multilayer materials. The most important difference between the two IL materials was the type of inhomogeneity towards the matrix: PP-Soft showed an $(E-\sigma)$ - inhomogeneity, while PP-St had a pure E-inhomogeneity. In all cases, PP-Soft ILs led to crack arrest due to the $(E-\sigma)$-inhomogeneity. The phenomenon is clearly visible as vertical increase of J_{exp} at $\Delta a^* = 0$, representing an increasing load without further crack growth until a new crack initiates behind the IL. The most successful configuration in terms of increased fracture toughness is depicted in Figure 13a, where a PP-Soft IL caused a relative increase of fracture toughness of $\Omega = 3.86$. Investigations of the crack growth rate reveal a complete stop of crack advancement at $\Delta a^* = 0$ (Figure 13b). Nonetheless, E^{eq} suffered due to the introduction of the soft IL and was reduced by 25% from 3903 MPa

---

[8]The matrix curves are shifted by an average amount of b_0 in these considerations.
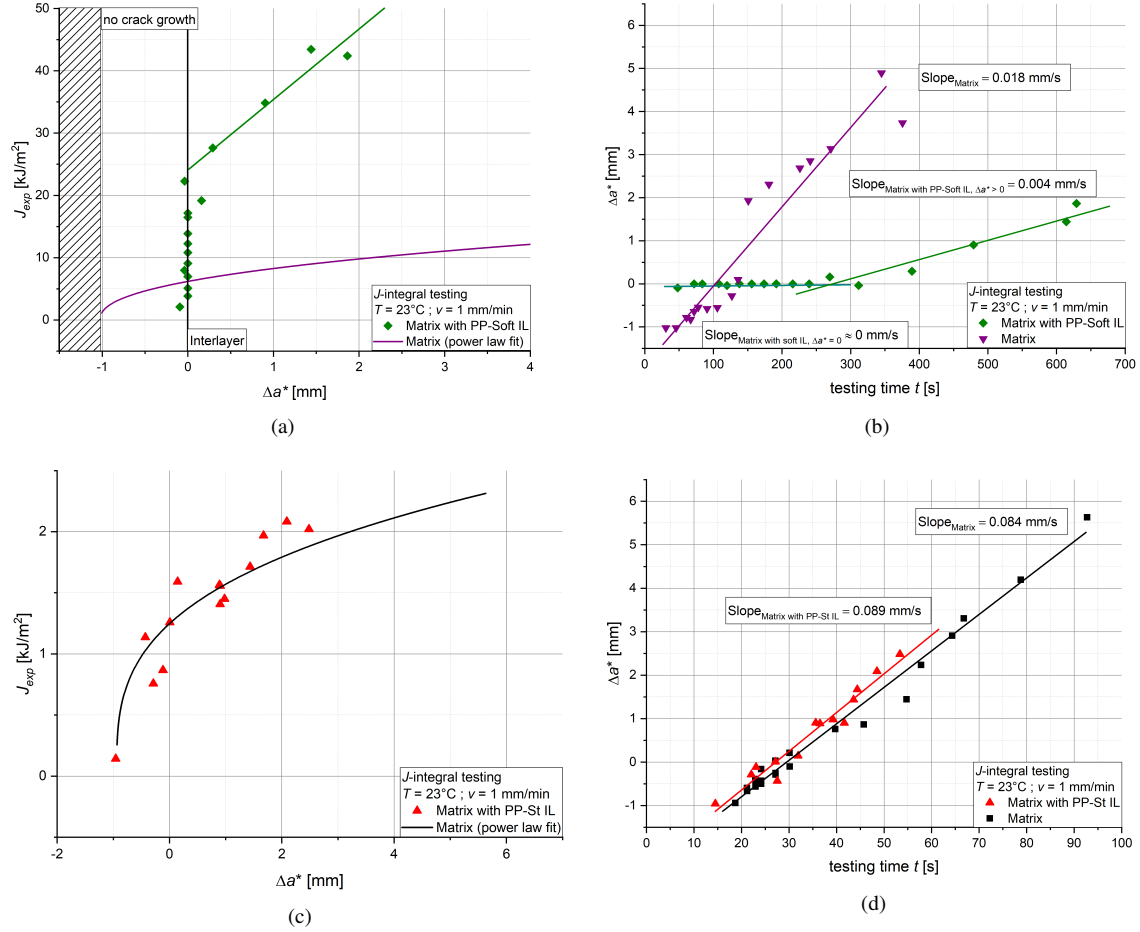
to 2926 MPa compared to the matrix material.

Figure 13: (a) $J-R$ curve of multilayer specimens with PP-Soft IL, (b) the corresponding crack growth rate as well as (c) $J-R$ curve of specimens with PP-St IL and (d) the corresponding crack growth rate.

These improvements to fracture toughness are in the same order of magnitude as stated by other sources. In ceramics, for example, a 60% increase in fracture toughness was found for multilayered thin films made of TiN and SiOx or CrN and Cr as constituents [117, 118]. On the other hand, improvements in high strength steels range from 5 to

26

over 35 times[9] [40, 62], although the differences may also be influenced by the typical testing methods (SENB for polymers and ceramics versus single edge notched tension for metals). Regarding polymers, Arbeiter et al. found increased fracture toughness in 3-D printed specimens made of glycol modified polyethylene terephthalate with thermoplastic copolyester as soft ILs, resultig in Ω-values between 3 and 4 [119].

Additionally it was shown that, contrary to the predictions via CDF in **Publication III**, not all promising combinations of E_{IL}/E_{Matrix} and $\sigma_{IL}/\sigma_{Matrix}$ led to an improvement in fracture toughness. Figure 13c[10] shows such an example of a PP-St IL, where no improvements in terms of fracture toughness could be achieved. Despite a predicted inhomogeneity effect of J_{tip}/J_{far} = 0.68, crack growth proceeded in the same way as in the matrix material (Figure 13d).

3.2.1. Influence of layer architectures

To further clarify, which combinations are effective, a more extensive study was conducted in **Publication IV**. Although the base material remained the same, a wider variety of layer architectures was investigated. The objective was to find an optimum of properties, while also observing the failure behavior of various multilayer architectures. Apart from that, more attention was turned to the balance between stiffness and toughness. The tradeoff between material properties is rarely the focus of discussion, although Mueller et al. found configurations, where fracture toughness could be increased without detrimental effects to other mechanical properties. More precisely, they could achieve improve-

---

[9]Calculated as ratio of J_{exp} between the first increment of crack extension versus J_{exp} when overcoming the IL.

[10]Matrix systems between Figure 13 (a, b) and (c, d) are not the same, resulting in different absolute values for J_{exp} and crack growth rate.

ments up to 130% fracture strain and 60% total fracture energy in rod-like struts made of polymethylmethacrylate with coaxial interfaces, while completely maintaining stiffness, strength and density [120].

The results of all investigated layer architectures from **Publication IV** are presented in Figure 14[11]. Similar to the previous results in Figure 13a, PP-Soft ILs led to increased fracture toughness at the cost of stiffness. Once crack arrest was achieved, increasing layer thickness, t, did not bring any benefits to fracture toughness, but instead reduced specimen stiffness as a result of the increased percentage of soft material. Adding an additional layer slightly increased Ω, but also decreased E^{eq} in the process. While improvements to fracture toughness ranged from 43% to 105%, E^{eq} suffered by up to 53% of matrix stiffness.

The same effects could not be observed with PP-St ILs, owing to the higher σ_y (pure E-inhomogeneity). E^{eq} retained high values between 90-95% of the matrix material in all cases. Unfortunately, the E-inhomogeneity was not sufficient to arrest cracks in the majority of cases. This appeared to be the case in specimens with PP-St IL, where the IL thickness $t \leq 0.9$ mm.

Specimens with a PP-St IL and $t \approx 0.9$ mm fell within a transition region from an ineffective IL towards crack arrest. In these cases, the contour of the curve is step-like, as is seen in specimens with PP-Soft ILs (Figure 13a). Nonetheless, fracture toughness was not improved and $\Omega \approx 1$.

However, the benefits of the E-inhomogeneity were preserved in specimens with larger ILs (2x0.9 mm for the case presented in **Publication IV**) and cracks stopped growing at

---

[11]The example from Figure 13a and 13b is excluded, since the matrix systems are not the same.

the first IL. Ω was increased to 2.81 as a result, even surpassing the composites with PP-Soft ILs in this matrix system. Additionally, specimen stiffness remained high with $E^{eq} \approx 5500$ MPa (94% of matrix material).
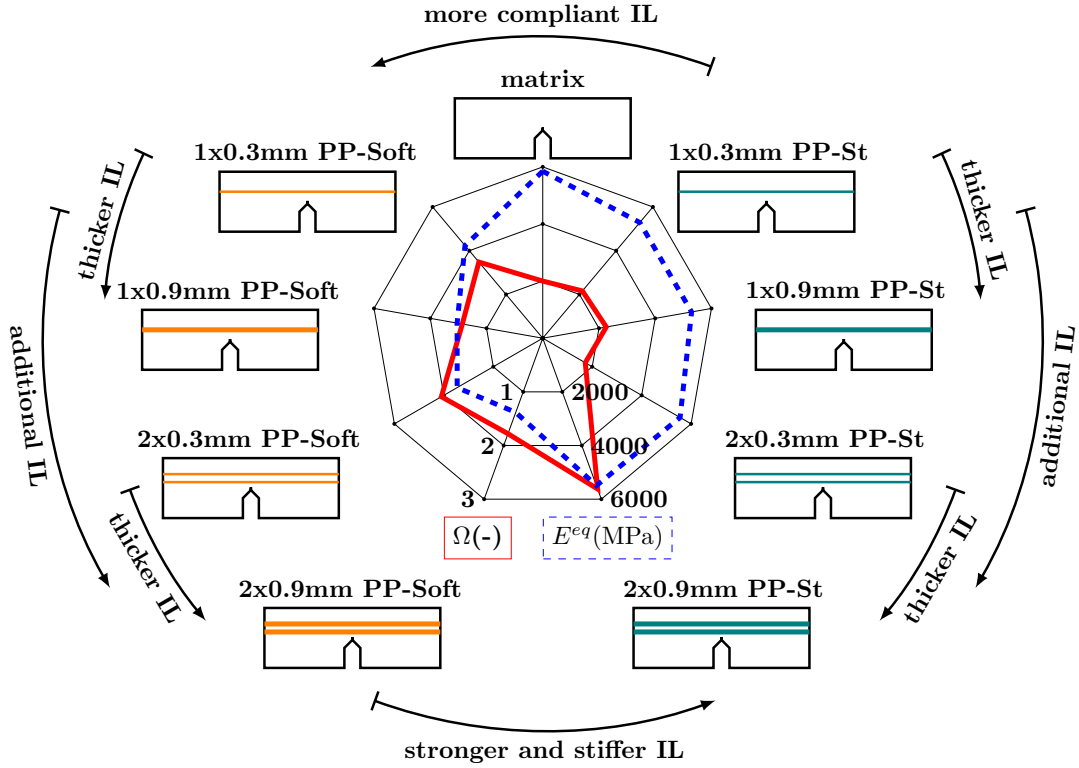

Figure 14: Overview of investigated multilayer architectures with their corresponding specimen stiffness and relative fracture toughness.

To sum up, a configuration was found, which exhibits the most desirable combination of stiffness and toughness despite only showing an E-inhomogeneity. These results are on a par and even surpass the improvements of previous endeavors in other material classes [36, 41, 45, 114, 118, 120].

As a rule of thumb, literature suggests, that the highest reduction of CDF can be

achieved, if $E_{IL} < 0.2E_{Matrix}$ [62] and $\sigma_y^{IL} < 0.3\sigma_y^{Matrix}$ [36, 114]. As shown in Figure 14, not all architectures with these ratios show improvements to fracture toughness. As an additional requirement, layer thickness appears to be important as well in some cases. In addition to that, all composites with $(E-\sigma)$-inhomogeneity showed a significantly reduced stiffness. Thus, two more phenomena need to be addressed, namely stress decoupling in multilayer composites as well as the influence of layer thickness.

3.2.2. Stress decoupling in multilayer composites

The decoupling of stresses mentioned in Section 2.3.3 could also be observed in greater detail in **Publication IV** in specimens with PP-Soft ILs. Although the reduction in area moment of inertia was not as severe as for microlayer composites, the effects on stiffness and the force-displacement curve were still considerable (Figure 15).

In addition to reduced specimen stiffness, the poor stress transfer between ligaments led to abrupt unloading events when individual matrix ligaments failed. These so-called pop-ins are clearly visible in the corresponding force-displacement curves. Comparable behavior is also reported for rod-like struts of polymethylmethacrylate [120] or layered ceramics [47]. However, it should be pointed out that pop-ins do not necessarily correlate to toughening mechanisms. They are merely the result of stick-slip effects that occur during fracture in combination with unloading [121].

However, the decoupling can be minimized in multilayer composites by using stronger IL materials. In **Publication IV**, specimens with PP-St ILs did not exhibit any pop-ins, were able to retain higher specimen stiffness and, in some cases, even achieved increased fracture toughness. These examples prove, that the material inhomogeneity effect can be found independently from stress decoupling effects, meaning that correctly designed ILs

30

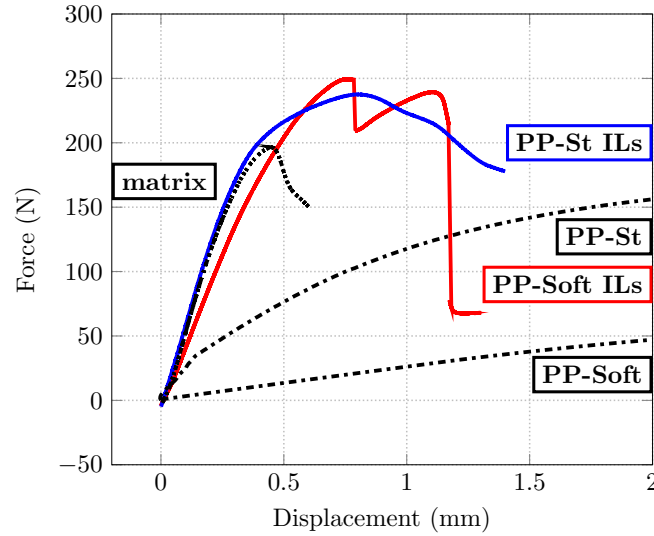can improve fracture toughness without serious drawbacks to stiffness.

Figure 15: Force-displacement curves for multilayer specimens with $(E - \sigma)$-inhomogeneity (PP-Soft ILs) and pure E-inhomogeneity (PP-St ILs).

3.3. Design of IL thickness

In addition to the material pairing, the IL thickness, t, may play a significant role in some cases. The best composites boast high fracture toughness due to the crack arrester effect, but also retain high stiffness. This optimum can be achieved, when the t is large enough for the material inhomogeneity effect to work, but no larger in order to preserve stiffness.

According to Sistaninia et al. [114], the optimum thickness should be approximately as large as the radius of the plastic zone, r_y^{IL}, of the IL, so that $t \approx r_y^{IL}$. However, r_y^{IL} can grow in size as loading increases throughout the experiment. This is reflected in Equation 5 [122], where the load is expressed in the form of J, which becomes larger the more force

is applied to the specimen.

$$t \geq r_y^{IL} = \beta \frac{J E_{IL}}{\sigma_{y,IL}^2 \left(1 - v_{IL}^2\right)} \tag{5}$$

E-inhomogeneities in particular show reduced effectiveness under higher loading, which is presumably caused by r_y^{IL} growing larger than t. For polymers in particular, this has to be taken into account due to their highly plastic behavior in comparison to many metals and ceramics. In contrast, σ-inhomogeneities retain most of their crack arresting properties, even if $r_y^{IL} > t$ [62]. Due to this limitation, strong IL materials should only be used in multilayer composites with optimized dimensions, while they are a poor option for any microlayer composites with very thin t.

In Equation 5, $\beta = \frac{1}{6\pi}$ for plain strain conditions, while for plain stress conditions $\beta = \frac{1}{2\pi}$ and the term $\left(1 - v_{IL}^2\right)$ is omitted. In **Publication III**, both variants were assessed in FE simulations and compared with experimental results from **Publication II**. It could be concluded that plane stress elements yield a better approximation, suggesting that plane stress conditions are dominating for this specific choice of material and specimen geometry.

A reasonable estimate of J is required to calculate r_y^{IL} and design the IL accordingly. Using the fracture toughness of the brittle matrix material, J_c^{Matrix}, will most likely yield values that are too small, since the fracture toughness of the composite is larger than the matrix on its own. On the other hand, using the fracture toughness of the IL material, J_c^{IL}, is also incorrect and would lead to an overestimation of r_y^{IL}. Polymeric IL were found to not fracture during the experiment, meaning that J_c^{IL} is larger than any of the applied J_{exp} during testing. Although an overdimensioned IL is not detrimental to fracture toughness,

32

specimen stiffness would likely be reduced. With efficient and sustainable applications in mind, the unnecessary use of material is undesirable too.

A more precise estimate for J may be deduced from the experimental $J - R$ curve. For that purpose, the development of J_{exp}, Δa^* and the corresponding r_y^{IL} during SENB testing are depicted in Figure 16.
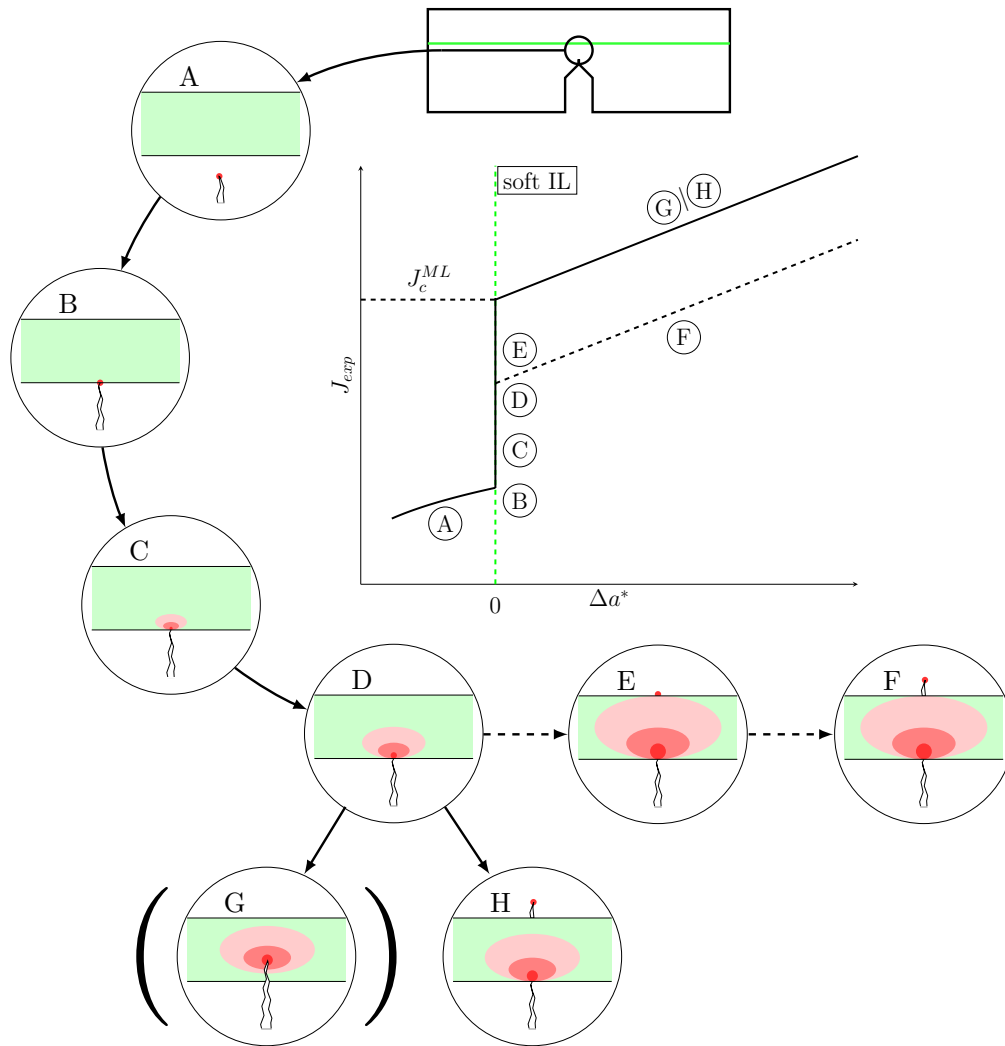

Figure 16: Evolution of plastic zone size throughout the $J - R$ curve.

r_y is small in the initial stages (Figure 16 A, r_y is colored in shades of red), when the crack propagates within the matrix material of the b_0-section. This changes when the first soft IL is reached and the crack is arrested (B). At this point, a r_y^{IL} starts to develop in the IL material (C). During the stage of crack arrest, r_y^{IL} grows proportionally to J_{exp}, while $\Delta a^* = 0$ (D). Under the steady increase of load, three different outcomes are possible in theory:

- In some cases, t falls into a transition region, where the inhomogeneity effect functions initially, but r_y^{IL} grows until the entire IL is plastically deformed (E). Then, the material inhomogeneity effect is lost and a new crack re-initiates in the matrix material behind the IL (F). This may also be the explanation for some experiments in *Publication IV*, where the $J - R$ curves had a characteristic step-like shape of crack arresting specimens without any benefits to fracture toughness.

- The IL itself starts to fracture when locally $J_{tip} > J_c^{IL}$ (G). As mentioned above, this outcome was not observed for the investigated composites in this thesis.

- Ideally, crack re-initiation in the matrix happens without any influence from the arrested crack tip or the deformed IL. In this case, a new crack forms in the matrix material, as if it were an unnotched bending specimen (H). Without an initial notch, the required amount of energy for specimen failure is maximized due to the formation of the new crack tip. In the absence of a stress concentration, the matrix material may even form a sizeable plastic zone of its own and further increase the amount of consumed energy. This type of failure was observed in *Publication II* as well as *Publication IV* and requires $t > r_y^{IL}$. Assuming plane stress conditions, as

suggested in **Publication III**, and the experimentally determined material parameters from **Publication IV** ($J = J_c^{ML} = 3.69$ kJ/m^2, $E = 1444$ MPa, $\sigma_y = 23.9$ MPa), an estimation according to Equation 5 yields $r_y^{IL} = 1.49$ mm. This result is in good agreement with the observed transition region between 0.9 and 2x0.9 mm of IL thickness, where crack arrest started to become effective.

In conclusion, crack stopping layers do not only rely on the ratio of mechanical parameters, but also correct dimensioning of the IL. The benefits of E-inhomogeneities may even be lost entirely, if t is chosen suboptimally. Plastic deformation of the entire IL could lead to crack re-initiation (Figure 17a) in thin IL, while architectures with sufficiently large t can contain the plastic zone and arrest cracks (Figure 17b).
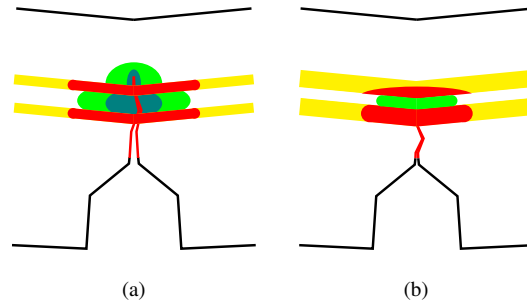

(a)   (b)

Figure 17: (a) Plastic deformation leading to crack re-initiation and (b) a plastic zone contained within two large ILs.

All of the discussed criteria are summed up in Table 2, where two out of three requirements must be fulfilled in order to increase fracture toughness.

Table 2: Requirements for crack arresting ILs.

inhomogeneity	$\frac{E_{IL}}{E_{Matrix}}$	$\frac{\sigma_y^{IL}}{\sigma_y^{Matrix}}$	$\frac{r_y^{IL}}{t}$
E	< 0.2	≈ 1	< 1
$E - \sigma$	< 0.2	< 0.3	arbitrary

Although sizeable improvements to fracture toughness could be achieved by following these guidelines, there are limits to how much loading a material can endure. Findings in *Publication II* suggest, that the upper limit load in terms of J_{exp} after crack arrest is determined by the matrix system. Multilayers showed vastly different fracture toughness depending on the talcum content in their matrices, despite having the same IL material, layer architecture and failure progression (Figure 16 A-H). To be more specific, a matrix of medium talcum reinforced PP could achieve values of $J_c^{ML} = 24.07$ kJ/m^2 and $\Omega = 3.86$, while a matrix of highly talcum reinforced PP could only reach $J_c^{ML} = 1.94$ kJ/m^2 and $\Omega = 1.74$.

A closer inspection of failing specimens revealed, why the matrix systems were so influential. As depicted in Figure 18a and 18b, the matrix with lower talcum content could endure higher plastic deformations and absorb more energy before a new crack initiated behind the IL and the specimen finally broke. Thus, ultimate failure is actually determined by the deterioration of the matrix material to an extent, that a new crack is able to form. It is therefore necessary to understand the connection of loading parameters and microstructural damage in polymers, which will be investigated in the following section.
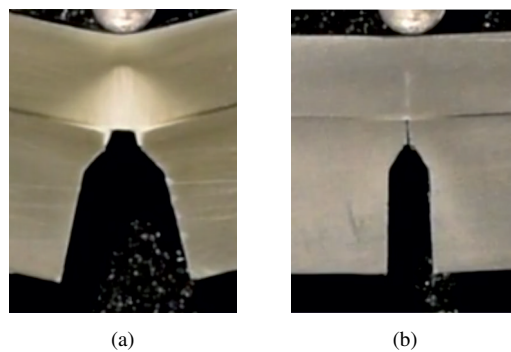

(a)　　　　　　　(b)

Figure 18: Crack re-initiation in specimens with matrices of PP with (a) medium and (b) high talcum reinforcement.

3.4. Methods to determine crack re-initiation

The re-initiation of cracks determines the final fracture toughness of multilayer composites after crack arrest and should be treated with the same care as the design of the IL. The re-initiation process is comparable to the formation of cracks in unnotched materials, which is governed by the initiation, growth and coalescence of microscopic damage phenomena.

For polymers, there are several well known types of damage to the microstructure, where the most prominent ones are shown and described in Figure 19a to 19d. These include voids [123], microcracks [124], polar fans [125–129] and crazes [130–132].

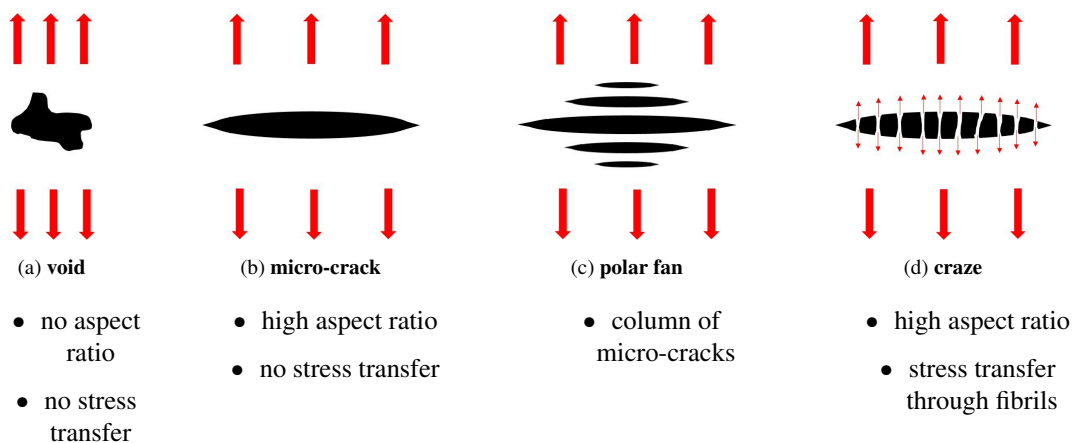|			
(a) **void**	(b) **micro-crack**	(c) **polar fan**	(d) **craze**
• no aspect ratio • no stress transfer	• high aspect ratio • no stress transfer	• column of micro-cracks	• high aspect ratio • stress transfer through fibrils

Figure 19: Common forms of microdamage in polymers including (a) voids, (b) microcracks, (c) polar fans and (d) crazes.

In polymer blends and composites, such defects commonly initiate from pre-existing irregularities such as rubber particles [133] or reinforcing particles [134, 135]. The amorphous boundary layer between spherulites in semicrystalline polymers acts in a similar way, while large and well defined crystals hinder the formations of voids [136, 137]. Even

in amorphous polymers, which appear homogeneous at first glance, local irregularities in molecular packing can act as initiation sites [123].

Under dilational stresses, these defects can grow and coalesce [138], especially when stresses are near or above the yield stress [139]. Larger defects as well as new cracks are formed throughout the process [138, 140]. As a result of increasing damage, E often decreases on a macroscopic scale due to the loss of load bearing surface on a microscopic level [141].

Usually, time-consuming and expensive methods, such as computed tomography (CT) or scatter electron microscopy need to be used to characterize damage to the microstructure [139, 142]. Both techniques are typically carried out post mortem, since temporal resolution is not sufficient for monitoring experiments at common load rates. Olufsen et al. [143] could achieve X-ray tomography measurements at decent loading rates by using post-processing tools on cracked round bar specimens. While effective, this approach also requires axisymmetric specimens. Another option is to rely on synchrotron radiation to achieve high-energy X-rays. Unfortunately, these strategies are difficult to implement on small lab scales or in an industrial environment. For that reason, two alternative approaches to determine crack re-initiation after arrest are explored in the following sections.

3.4.1. Simulation of crack re-initiation

In **Publication III**, cohesive zone (CZ) modeling [144] was used to describe the entire fracture process of multilayered specimens, including crack re-initiation. A particular type of element, which is able to fracture under certain conditions, was used to simulate crack growth. More specifically, a so-called traction separation law (TSL) determines the cohesive stress, σ_{CZ}, depending on the distance between the crack flanks, δ. Although

more complex laws are available [145–147], a simple bi-linear relation (Figure 20) is often sufficient to describe the separation energy, Γ_{CZ}, according to Equation 6.

$$\Gamma_{CZ} = \frac{1}{2}(\sigma_{max}\delta_f) \tag{6}$$

Therein, σ_{max} is the cohesive strength and δ_f is the separation of the crack faces at failure. Following procedures from literature [148–150], a set of CZ parameters (σ_{max} and Γ_{CZ}) can be calibrated. This is done by modeling Δa and the corresponding load line displacement, v_{LL}, with various pairs of σ_{max} and Γ_{CZ}. After a subsequent comparison with experimental data (Figure 21a), the best fit values are chosen as parameters for the investigated materials.
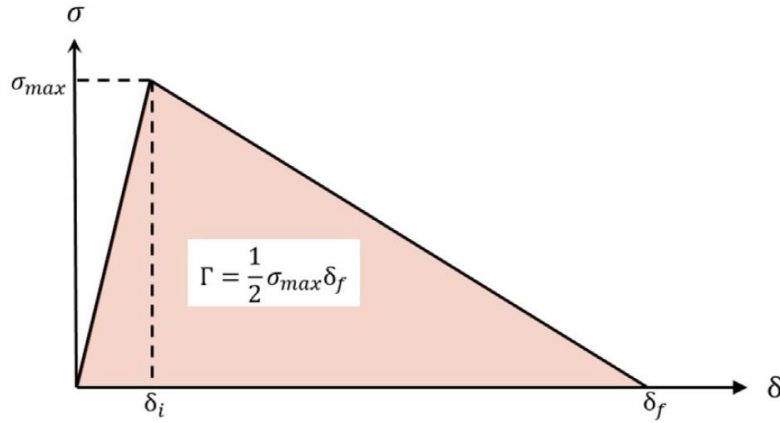

Figure 20: Bi-linear traction separation law describing the separation energy of cohesive elements.

Pandya et al. [151, 152] conducted detailed studies on TSLs of polytheylene and point out, that loading rate and constraint effects have significant influence on the simulated crack growth. The constraint also depends on specimen thickness as well as the current position of the crack tip (a/W) [90]. Consequently, the constraint and stress triaxiality

before and after crack arrest are vastly different and separate sets of parameters need to be obtained for the two regimes. Thus, the calibration procedure must be repeated for post-IL crack extension, Δa_{PostIL}. It is illustrated in Figure 21b, that this set of parameters starts to produce crack growth at much higher values of v_{LL}. As a result, Γ_{CZ} is greatly increased compared to the pre-IL regime, reflecting the energy required for the re-initiation process.

Phenomenologically speaking, the large increase in post-IL toughness stems from extensive plastic deformation in combination with micro-damage happening in the post-IL regime (Figure 10). Creating additional voids and/or crazes is a cavitational process [142], which dissipates energy. As a result, crack re-initiation is energy-expensive due to the need to generate a new crack tip through coalescence of microstructural damage. This reasoning is supported by several sources in literature, where decent results are reported after utilizing damage-induced plasticity as toughening mechanism [153–155].
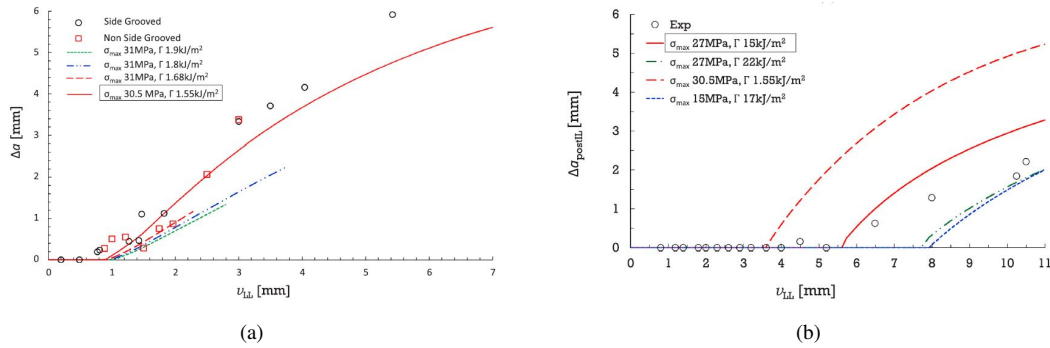

Figure 21: Calibration of cohesive zone parameters for (a) the pre-IL and (b) the post-IL regime.

Using this approach in *Publication III*, it was possible to reconstruct the $J_{exp} - \Delta a^*$ curve from *Publication II* (Figure 22). Crack growth, crack arrest and crack re-initiation are combined into one model. It should be noted that these parameters are only valid for the calibrated configuration. If material composition or layer architecture vary, the

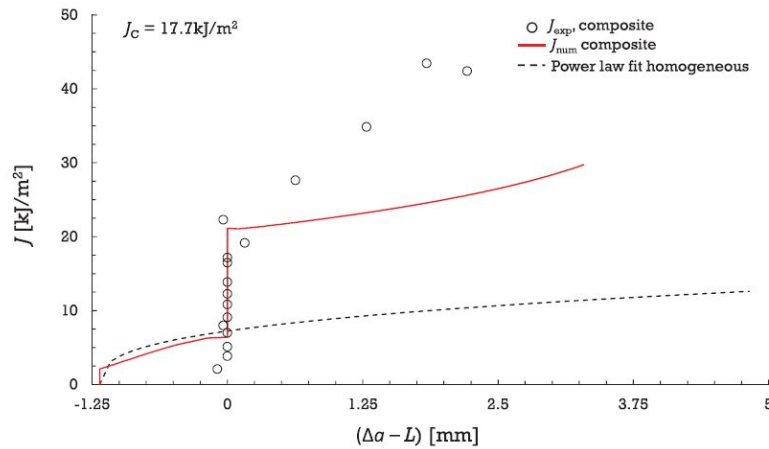constraints of the crack tip will be different and errors may arise.

Figure 22: Reconstruction of the experimental $J - R$ curve using cohesive zone modeling.

3.4.2. Experimental assessment of accumulated damage

Several mechanical techniques were investigated in ***Publication V*** in order to find a simple approach for assessing structural health. The objective was to develop a straight forward and easy-to-use method, that can determine the onset of permanent damage, which will eventually lead to the formation of a new crack. Therein, E was used as measure of structural integrity. The procedure should yield an estimate for critical strain, which can easily be implemented in the design process, e.g. as threshold value in preliminary FE studies.

Load-unload experiments turned out to be ill-suited to characterize microstructural damage. The influence of creep was significant, since these tests were performed under tension for a prolonged period of time. Therefore, a decrease of E with increasing applied strain, ε_{appl}, was mainly caused by viscoelastic effects and not by permanent damage. Figure 23 shows the considerable decline of stiffness with increasing number of cycles,

41

even at comparably low strains. This indicates, that time-dependence should also play a major role in the effectiveness of crack-stopping layers. Similar to the value of E or σ_y, the size of plastic zones is also time dependent and should be investigated in the future in more details as well.
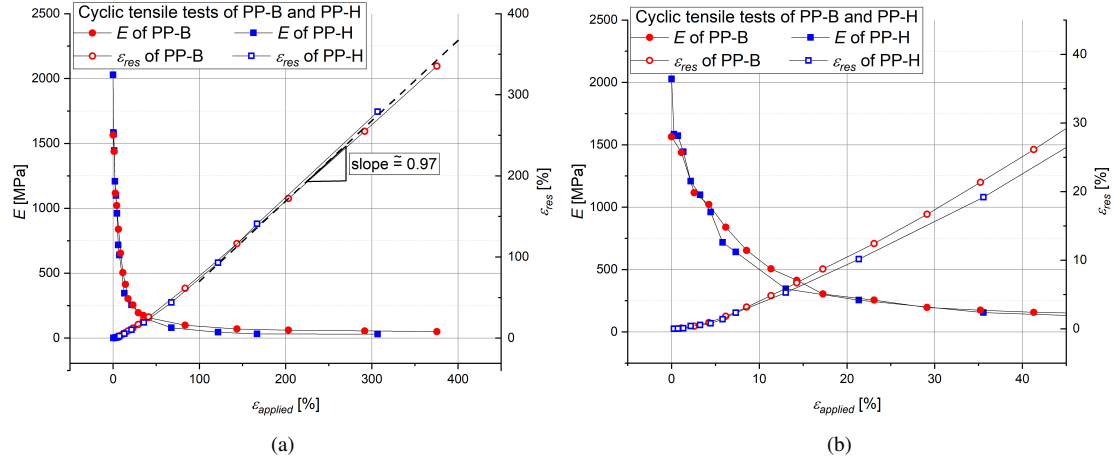

Figure 23: (a) Decrease of E in load-unload experiments over a wide range of applied strain and (b) the initial 50% of strain in greater detail.

Such influences of time-dependence could be avoided by using a combination of pre-straining and subsequent dynamic mechanical analysis (DMA). In a thorough relaxation period between introducing strain and measuring E, the majority of relaxation processes were completed and any remaining changes to E could be linked to actual damage. Applying this method revealed E to be stable for much larger strains before damage phenomena started to affect stiffness. As discussed in **Publication V**, E of a PP block co-polymer (PP-B) remained constant for 10% of strain. E started to decline slowly for larger strains due to the formation of microcracks (Figure 24a and 24b). A PP homopolymer (PP-H) remained intact for 15% of pre-strain, before showing a slight increase of E in combination with emerging polar fans (Figure 24c). The increase of E may have been caused by orientation
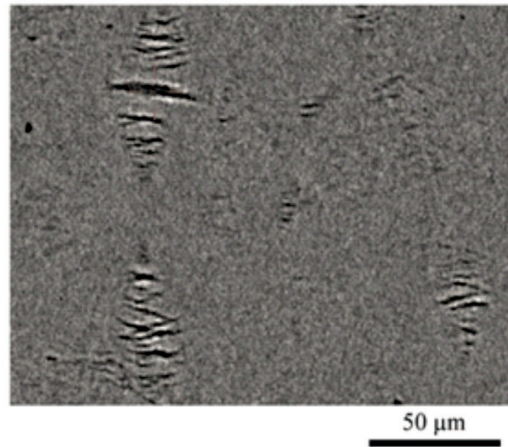
effects, that optimized the stress transfer of macromolecules. Nonetheless, the loss of load bearing surface is expected to outweigh this cold drawing effect at higher ε_{appl}. By assessing the regions of stable E, a critical strain could be obtained, at which no deterioration of the microstructure happened yet.
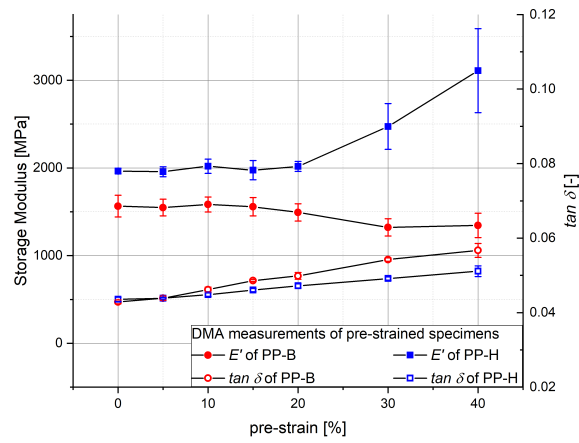
(a)
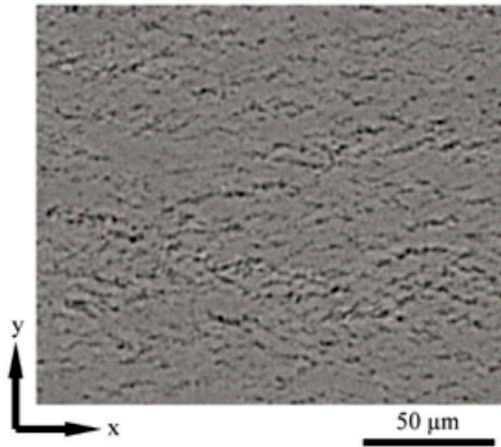
(b)

(c)

Figure 24: (a) Evolution of E in dynamic mechanical analysis of pre-strained specimens and the microstructures of (b) a PP block co-polymer, PP-B, and (c) a PP homopolymer, PP-H, with 40% pre-strain, recorded in μ-CT.

43

4. Summary and conclusions

Within the scope of this thesis, mechanical behavior and failure of polypropylene based microlayer [12] and multilayer [13] composites were explored using adapted methods for heterogeneous materials.

4.1. Results found in this thesis

Microlayer composites with $(E - \sigma)$-inhomogeneity showed greatly increased impact strength and high damage tolerance. Impact strength in regard to the matrix material showed an increase by a factor of 11.7 in combination with increased flaw tolerance. The improvement of fracture energy in tensile tests even amounted to 33 times. Nonetheless, these microlayer composites also exhibited reduced stiffness by 89% and 76%, respectively. This undesired side effect was a consequence of the soft IL material and small layer sizes, which ultimately led to a loss of flexural rigidity.

In multilayer composites, larger matrix sections were used for increased flexural stiffness, while cracks were arrested by a low number ILs. Multilayer composites with an $(E - \sigma)$-inhomogeneity exhibited increased fracture toughness regardless of IL thickness, t, but suffered from reduced specimen stiffness as well. The best configuration attained an increase of relative fracture toughness of 3.86, while specimen stiffness was reduced by 25%. Stiffness could be kept high when using a pure E-inhomogeneity. However, IL with smaller t were unable to produce crack arresting properties in such a material pairing. This ineffectiveness is a limitation specific to E-inhomogeneities and is caused by visco-plastic

---

[12]Composites with many layers, where the thickness is in the range of microns.
[13]Composites with few layers, where the thickness is in the sub-millimeter range.

deformation of the IL. Nonetheless, an optimum between stiffness and toughness could be achieved in specimens where IL(s) are large enough to contain the fully developed plastic zone. The best case scenario in **Publication IV** showed an increase in fracture toughness by 181% while retaining 94% of matrix stiffness.

Crack re-initiation is also a crucial part of overall fracture toughness and is determined by the fracture of the remaining matrix ligament after crack arrest. Crack growth and re-initiation could be modeled using a cohesive zone law. However, two sets of parameters had to be obtained from experimental data to describe the pre-IL as well as the post-IL failure behavior. Alternatively, an experimental procedure is presented in **Publication V**, where dynamic mechanical analysis was performed on pre-strained specimens. This method is capable of estimating a critical strain for permanent damage, which represents an onset for crack formation.

4.2. Deduction of design guidelines

Two comparably simple design criteria can be deduced for microlayer composites with maximum toughness:

- The IL should be made of a very soft material and as thin as processing allows for, provided the ILs can be produced as continuous layers.

- The matrix ligament thickness should be smaller than the size of the critical defects. These can be particle sizes, inclusions, agglomerates etc..

For a more balanced combination of stiffness and toughness, multilayer composites should be considered. Corresponding design criteria are summarized in Table 3. As a simplified rule of thumb, two out of these three conditions have to be fulfilled in order to

45

achieve crack arresting properties. It should be noted, that for $(E-\sigma)$-inhomogeneities, increased fracture toughness comes at the cost of stiffness, while t is arbitrary. E-inhomogeneities, on the other hand, feature high toughness and stiffness, but require more care when designing layer thickness.

Table 3: Simplified conditions for the design of crack arresting ILs.

inhomogeneity	$\frac{E_{IL}}{E_{Matrix}}$	$\frac{\sigma_y^{IL}}{\sigma_y^{Matrix}}$	$\frac{r_y^{IL}}{t}$
E	< 0.2	≈ 1	< 1
$E - \sigma$	< 0.2	< 0.3	arbitrary

The outcome of all presented endeavors is a spectrum of configurations for micro- and multilayer composites. Therein, properties can range from maximum toughness to compromises between stiffness and toughness and even include optimal solutions, where both parameters are high. A final summary of all approaches is given in Figure 25.
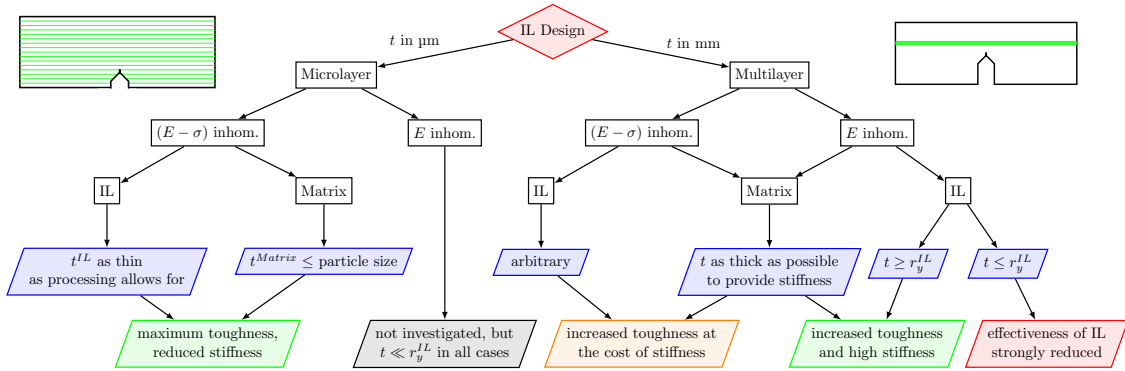

Figure 25: Overarching summary of investigated microlayer and multilayer architectures.

46

5. Outlook

In the presented thesis, investigations on layer thicknesses, plastic zone sizes and fracture mechanical parameters have been made separately in order to formulate the underlying guidelines more clearly. For future works, these findings may be combined in a comprehensive study, e.g. using FE methods, where critical strains, local values of J and specimen stiffness can be investigated simultaneously.

So far, all investigations have been made at room temperature and at standardized loading rates (Charpy or ESIS TC4 recommendation [100]). These conditions do not represent all requirements for real-life applications. Due to the viscoelastic and temperature-dependent nature of polymeric materials, the ratios of σ and E as well as plastic zone development are subject to change under different conditions. Thus, similar studies should also be conducted throughout a range of temperatures and loading rates (e.g. impact or long term loading) to investigate effectiveness for a variety of applications. Despite the variable material properties, the applied methodology remains the same.

Regarding crack re-initiation, there exist numerous alternative approaches to describe crack initiation (e.g. plastic flow criteria [156] or probablistic models for crack formation in damaged layers [157–159]), which are not discussed in this thesis. Dedicated future works may shed light on these phenomena.

The investigated mechanical principles also apply to materials produced by other processing techniques. Therefore, additively manufactured structures are an excellent candidate for future applications. With optimized IL being exclusively placed at critical locations, novel components can utilize crack arresting properties while keeping the stiffness loss to an absolute minimum.

Nonetheless, all presented concepts can readily be applied to extruded or injection-molded parts as well. Therefore, future works should aim to further improve methodology or even employ the discovered knowledge in novel industrial applications.

6. Additional contributions within the framework of this thesis

6.1. Publications in peer-reviewed journals

1. F. Arbeiter, M. Spoerk, J. Wiener, A. Gosch, G. Pinter, Fracture mechanical characterization and lifetime estimation of near-homogeneous components produced by fused filament fabrication, Polymer Testing 66 (2018) 105–113. doi:10.1016/j.polymertesting.2018.01.002.

2. S. Petersmann, M. Spoerk, W. van de Steene, M. Üçal, J. Wiener, G. Pinter, F. Arbeiter, Mechanical properties of polymeric implant materials produced by extrusion-based additive manufacturing, Journal of the mechanical behavior of biomedical materials 104 (2020) 103611. doi:10.1016/j.jmbbm.2019.103611.

3. D. Hennen, D. Hartmann, P. H. Rieger, A. Oesterreicher, J. Wiener, F. Arbeiter, M. Feuchter, E. Fröhlich, M. Pichelmayer, S. Schlögl, T. Griesser, Exploiting the carbon and oxa michael addition reaction for the synthesis of yne monomers: Towards the conversion of acrylates to biocompatible building blocks, ChemPhotoChem 4 (7) (2020) 476–480. doi:10.1002/cptc.201900199.

4. M. Drvoderic, M. Gfrerrer, J. Wiener, G. Pinter, M. Pletz, C. Schuecker, Comparing crack density and dissipated energy as measures for off-axis damage in composite laminates, International Journal of Fatigue (under review)

6.2. Conference contributions

1. J. Wiener, F. Arbeiter, M. Spörk, A. Gosch, G. Pinter, Influence of strand orientation on mechanical properties in near homogeneous FFF-produced PLA parts, poster presentation, 17th International Conference on Deformation Yield and Fracture of Polymers (DYFP 2018), Kerkrade, Netherlands

2. J. Wiener, F. Arbeiter, M. Spörk, A. Gosch, G. Pinter, Material selection, testing and validation of additively manufactured components, oral presentation and conference proceedings, Annual Technical Conference of the Society of Plastics Engineers (ANTEC 2018), Orlando, United States of America

3. J. Wiener, F. Arbeiter, O. Kolednik, G. Pinter, Replicating the material inhomogeneity effect of biological materials to increase the fracture toughness in polymers, poster presentation, 18th International Conference on Deformation Yield and Fracture of Polymers (DYFP 2022), Kerkrade, Netherlands

4. J. Wiener, F. Arbeiter, A. Tiwari, O. Kolednik, G. Pinter, Crack arrester effect in mineral-reinforced PP through soft Interlayers, oral presentation, 17th Conference on Deformation and Fracture of Polymers (PolymerTec 2020), Merseburg, Germany (attended online)

5. C. Schneider, J. Wiener, C. Sperling, G. Pinter, A. Brunner, Non-Destructive Detection of Damage Processes in Glass Fiber Reinforced Polymers under Fatigue Loading, oral presentation, Eighth International Conference on Fatigue of Composites (ICFC 2021), online conference

6. J. Wiener, C. Schneider, C. Sperling, M. Gfrerrer, G. Pinter, Non-destructive detection of damage processes during fatigue loading in glass-fibre reinforced polymers, oral presentation and conference proceedings, 2nd European Non-Destructive Testing and Condition Monitoring Days (ENDTCM 2021), Prague, Czech Republic (attended online)

7. J. Wiener, B. Plank, F. Arbeiter, O. Kolednik, G. Pinter, Distinguishing between irreversible damage and time-dependent effects in polymers, oral presentation, 18th European Mechanics of Materials Conference (EMMC 2022), Oxford, United Kingdom

8. J. Wiener, M. Gfrerrer, C. Schneider, G. Pinter, Density Based Clustering as a Tool to Analyze Acoustic Emission Signals, oral presentation and conference proceedings, 20th European Conference on Composite Materials (ECCM 2022), Lausanne, Switzerland

9. J. Wiener, F. Preissegger, B. Plank, F. Arbeiter, O. Kolednik, G. Pinter, Methods to Differentiate Between Viscoelastic Effects and Microstructural Damage in Polypropylene, oral presentation, 15th International Conference on Advanced Computational Engineering and Experimenting (ACEX 2022), Florence, Italy

6.3. Supervised theses

1. F. Preissegger, "Charakterisierung des realen Spannungs-Dehnungs-Verhaltens und Schädigungsbeginns von Polypropylen". Bachelor thesis, Montanuniversitaet, Leoben, 2019.

2. C. Sperling, "Zerstörungsfreie in-situ-Detektion von Schädigungsprozessen bei Ermüdungsbelastung zur Charakterisierung von Faserverbundwerkstoffen". Master thesis, Montanuniversitaet, Leoben, 2021.

References

[1] M. Ashby, D. Cebon, Materials selection in mechanical design, Le Journal de Physique IV 03 (C7) (1993) C7–1–C7–9. doi:10.1051/jp4:1993701.

[2] R. O. Ritchie, The conflicts between strength and toughness, Nature materials 10 (11) (2011) 817–822. doi:10.1038/nmat3115.

[3] J. G. Park, D. H. Keum, Y. H. Lee, Strengthening mechanisms in carbon nanotube-reinforced aluminum composites, Carbon 95 (2015) 690–698. doi:10.1016/j.carbon.2015.08.112.

[4] A. Rohatgi, D. J. Harach, K. S. Vecchio, K. P. Harvey, Resistance-curve and fracture behavior of ti–al3ti metallic–intermetallic laminate (mil) composites, Acta Materialia 51 (10) (2003) 2933–2957. doi:10.1016/S1359-6454(03)00108-3.

[5] A. Hosseini Monazzah, H. Pouraliakbar, R. Bagheri, S. M. Seyed Reihani, Al-mg-si/sic laminated composites: Fabrication, architectural characteristics, toughness, damage tolerance, fracture mechanisms, Composites Part B: Engineering 125 (2017) 49–70. doi:10.1016/j.compositesb.2017.05.055.

[6] G. W. Ehrenstein, Polymer-Werkstoffe: Struktur - Eigenschaften - Anwendung, 3rd Edition, Hanser, München, 2011.

[7] Z. Jia, Y. Yu, L. Wang, Learning from nature: Use material architecture to break the performance tradeoffs, Materials & Design 168 (2019) 107650. doi:10.1016/j.matdes.2019.107650.

[8] M. K. Islam, P. J. Hazell, J. P. Escobedo, H. Wang, Biomimetic armour design strategies for additive manufacturing: A review, Materials & Design 205 (2021) 109730. doi:10.1016/j.matdes.2021.109730.

[9] F. Barthelat, H. D. Espinosa, An experimental investigation of deformation and fracture of nacre–mother of pearl, Experimental Mechanics 47 (3) (2007) 311–324. doi:10.1007/s11340-007-9040-1.

[10] C. Levi, J. L. Barton, C. Guillemet, E. Le Bras, P. Lehuede, A remarkably strong natural glassy rod: The anchoring spicule of the monorhaphis sponge, Journal of Materials Science Letters 8 (3) (1989) 337–339. doi:10.1007/BF00725516.

[11] E. F. Morgan, G. L. Barnes, T. A. Einhorn, The bone organ system, in: Osteoporosis, Elsevier, 2013, pp. 3–20. doi:10.1016/B978-0-12-415853-5.00001-7.

[12] F. Libonati, G. X. Gu, Z. Qin, L. Vergani, M. J. Buehler, Bone-inspired materials by design: Toughness amplification observed using 3d printing and testing, Advanced Engineering Materials 18 (8) (2016) 1354–1363. doi:10.1002/adem.201600143.

[13] F. Libonati, M. J. Buehler, Advanced structural materials by bioinspiration, Advanced Engineering Materials 19 (5) (2017) 1600787. doi:10.1002/adem.201600787.

[14] Y. Estrin, Y. Bréchet, J. Dunlop, P. Fratzl, Architectured Materials in Nature and Engineering, Vol. 282, Springer International Publishing, Cham, 2019. doi:10.1007/978-3-030-11942-3.

[15] Y. Estrin, Y. Beygelzimer, R. Kulagin, P. Gumbsch, P. Fratzl, Y. Zhu, H. Hahn, Architecturing materials at mesoscale: some current trends, Materials Research Letters 9 (10) (2021) 399–421. doi:10.1080/21663831.2021.1961908.

[16] A. Miserez, J. C. Weaver, P. J. Thurner, J. Aizenberg, Y. Dauphin, P. Fratzl, D. E. Morse, F. W. Zok, Effects of laminate architecture on fracture resistance of sponge biosilica: Lessons from nature, Advanced Functional Materials 18 (8) (2008) 1241–1248. doi:10.1002/adfm.200701135.

[17] J. Aizenberg, J. C. Weaver, M. S. Thanawala, V. C. Sundar, D. E. Morse, P. Fratzl, Skeleton of euplectella sp. structural hierarchy from the nanoscale to the macroscale, Science (New York, N.Y.) 309 (5732) (2005) 275–278. doi:10.1126/science.1112255.

[18] H. Zhao, Z. Yang, L. Guo, Nacre-inspired composites with different macroscopic dimensions: strategies for improved mechanical performance and applications, NPG Asia Materials 10 (4) (2018) 1–22. doi:10.1038/s41427-018-0009-6.

[19] A. Dutta, S. A. Tekalur, M. Miklavcic, Optimal overlap length in staggered architecture composites under dynamic loading conditions, Journal of the Mechanics and Physics of Solids 61 (1) (2013) 145–160. doi:10.1016/j.jmps.2012.08.005.

[20] J. Song, C. Fan, H. Ma, L. Liang, Y. Wei, Crack deflection occurs by constrained microcracking in nacre, Acta Mechanica Sinica 34 (1) (2018) 143–150. doi:10.1007/s10409-017-0724-1.

[21] H. Gao, Application of fracture mechanics concepts to hierarchical biomechanics

of bone and bone-like materials, International Journal of Fracture 138 (1-4) (2006) 101–137. doi:10.1007/s10704-006-7156-4.

[22] M. A. Meyers, P.-Y. Chen, A. Y.-M. Lin, Y. Seki, Biological materials: Structure and mechanical properties, Progress in Materials Science 53 (1) (2008) 1–206. doi:10.1016/j.pmatsci.2007.05.002.

[23] B. Ji, H. Gao, Mechanical principles of biological nanocomposites, Annual Review of Materials Research 40 (1) (2010) 77–100. doi:10.1146/annurev-matsci-070909-104424.

[24] G. Tan, Q. Yu, Z. Liu, X. Wang, M. Zhang, Y. Liu, Z. Zhang, R. O. Ritchie, Compression fatigue properties and damage mechanisms of a bioinspired nacre-like ceramic-polymer composite, Scripta Materialia 203 (2021) 114089. doi:10.1016/j.scriptamat.2021.114089.

[25] A. Dutta, S. A. Tekalur, Crack tortuousity in the nacreous layer – topological dependence and biomimetic design guideline, Int. J. Solids Struct. (International Journal of Solids and Structures) 51 (2) (2014) 325–335. doi:10.1016/j.ijsolstr.2013.10.006.

[26] R. O. Ritchie, Mechanisms of fatigue crack propagation in metals, ceramics and composites: Role of crack tip shielding, Materials Science and Engineering: A 103 (1) (1988) 15–28. doi:10.1016/0025-5416(88)90547-2.

[27] Z. Jia, L. Wang, 3d printing of biomimetic composites with improved fracture toughness, Acta Materialia 173 (2019) 61–73. doi:10.1016/j.actamat.2019.04.052.

[28] Z. Jia, Y. Yu, S. Hou, L. Wang, Biomimetic architected materials with improved dynamic performance, Journal of the Mechanics and Physics of Solids 125 (2019) 178–197. doi:10.1016/j.jmps.2018.12.015.

[29] R. Yadav, R. Goud, A. Dutta, X. Wang, M. Naebe, B. Kandasubramanian, Biomimicking of hierarchal molluscan shell structure via layer by layer 3d printing, Industrial & Engineering Chemistry Research 57 (32) (2018) 10832–10840. doi:10.1021/acs.iecr.8b01738.

[30] L.-B. Mao, H.-L. Gao, H.-B. Yao, L. Liu, H. Cölfen, G. Liu, S.-M. Chen, S.-K. Li, Y.-X. Yan, Y.-Y. Liu, S.-H. Yu, Synthetic nacre by predesigned matrix-directed mineralization, Science (New York, N.Y.) 354 (6308) (2016) 107–110. doi:10.1126/science.aaf8991.

[31] Y. Yang, X. Song, X. Li, Z. Chen, C. Zhou, Q. Zhou, Y. Chen, Recent progress in biomimetic additive manufacturing technology: From materials to functional structures, Advanced Materials (2018) e1706539doi:10.1002/adma.201706539.

[32] A. Woesz, J. C. Weaver, M. Kazanci, Y. Dauphin, J. Aizenberg, D. E. Morse, P. Fratzl, Micromechanical properties of biological silica in skeletons of deep-sea sponges, Journal of Materials Research 21 (08) (2006) 2068–2078. doi:10.1557/jmr.2006.0251.

[33] W. E. G. Müller, X. Wang, K. Kropf, H. Ushijima, W. Geurtsen, C. Eckert, M. N. Tahir, W. Tremel, A. Boreiko, U. Schlossmacher, J. Li, H. C. Schröder, Bioorganic/inorganic hybrid composition of sponge spicules: Matrix of the giant spicules

and of the comitalia of the deep sea hexactinellid monorhaphis, Journal of structural biology 161 (2) (2008) 188–203. doi:10.1016/j.jsb.2007.10.009.

[34] P. Fratzl, H. S. Gupta, F. D. Fischer, O. Kolednik, Hindered crack propagation in materials with periodically varying young's modulus—lessons from biological materials, Advanced Materials 19 (18) (2007) 2657–2661. doi:10.1002/adma.200602394.

[35] O. Kolednik, J. Predan, F. D. Fischer, P. Fratzl, Bioinspired design criteria for damage-resistant materials with periodically varying microstructure, Advanced Functional Materials 21 (19) (2011) 3634–3641. doi:10.1002/adfm.201100443.

[36] M. Sistaninia, O. Kolednik, Improving strength and toughness of materials by utilizing spatial variations of the yield stress, Acta Materialia 122 (2017) 207–219. doi:10.1016/j.actamat.2016.09.044.

[37] T. Köpplmayr, E. Mayrhofer, C. Unterweger, Thermo-mechanical properties of β-nucleated polypropylene multilayers, Polymer Testing 39 (2014) 79–85. doi:10.1016/j.polymertesting.2014.08.001.

[38] T. Köpplmayr, J. Miethlinger, Modeling viscoelastic flow in a multiflux static mixer, AIP Conference Proceedings, American Institute of Physics, 2014, pp. 556–559. doi:10.1063/1.4873842.

[39] C. D. Mueller, S. Nazarenko, T. Ebeling, T. L. Schuman, A. Hiltner, E. Baer, Novel structures by microlayer coextrusion?talc-filled pp, pc/san, and hdpe/lldpe, Polymer Engineering & Science 37 (2) (1997) 355–362. doi:10.1002/pen.11678.

[40] M. Sistaninia, R. Kasberger, O. Kolednik, To the design of highly fracture-resistant composites by the application of the yield stress inhomogeneity effect, Composite Structures 185 (2018) 113–122. doi:10.1016/j.compstruct.2017.10.081.

[41] J. Zechner, O. Kolednik, Fracture resistance of aluminum multilayer composites, Engineering Fracture Mechanics 110 (2013) 489–500. doi:10.1016/j.engfracmech.2012.11.007.

[42] E. Munch, M. E. Launey, D. H. Alsem, E. Saiz, A. P. Tomsia, R. O. Ritchie, Tough, bio-inspired hybrid materials, Science (New York, N.Y.) 322 (5907) (2008) 1516–1520. doi:10.1126/science.1164865.

[43] D. Kozic, H.-P. Gänser, R. Brunner, D. Kiener, T. Antretter, O. Kolednik, Crack arrest in thin metallic film stacks due to material- and residual stress inhomogeneities, Thin Solid Films 668 (2018) 14–22. doi:10.1016/j.tsf.2018.10.014.

[44] T. Fromm, S. Bruns, M.-C. Müller, A. Fink, R. Borchardt, S. M. Rosiwal, K. Durst, Bioinspired damage tolerant diamond-metal laminates by alternating cvd and pvd processes, Materials & Design 213 (2022) 110315. doi:10.1016/j.matdes.2021.110315.

[45] C. Chen, J. Pascual, F. Fischer, O. Kolednik, R. Danzer, Prediction of the fracture toughness of a ceramic multilayer composite – modeling and experiments, Acta Materialia 55 (2) (2007) 409–421. doi:10.1016/j.actamat.2006.07.046.

[46] L. Sestakova, R. Bermejo, Z. Chlup, R. Danzer, Strategies for fracture toughness,

strength and reliability optimisation of ceramic-ceramic laminates, International journal of materials research 102 (6) (2011) 613–626.

[47] A.-K. Hofer, R. Walton, O. Ševeček, G. L. Messing, R. Bermejo, Design of damage tolerant and crack-free layered ceramics with textured microstructure, Journal of the European Ceramic Society 40 (2) (2020) 427–435.

[48] R. Bermejo, "toward seashells under stress": Bioinspired concepts to design tough layered ceramic composites, Journal of the European Ceramic Society 37 (13) (2017) 3823–3839.

[49] R. Bermejo, J. Pascual, T. Lube, R. Danzer, Optimal strength and toughness of al2o3–zro2 laminates designed with external or internal compressive layers, Journal of the European Ceramic Society 28 (8) (2008) 1575–1583.

[50] K. Coleman, R. Bermejo, D. Leguillon, S. Trolier-McKinstry, Thickness dependence of crack initiation and propagation in stacks for piezoelectric microelectromechanical systems, Acta Materialia 191 (2020) 245–252.

[51] C. S. Lee, S. G. Kim, H. J. Kim, S. H. Ahn, Measurement of anisotropic compressive strength of rapid prototyping parts, J. Mater. Process. Technol. (Journal of Materials Processing Technology) 187-188 (2007) 627–630. doi:10.1016/j.jmatprotec.2006.11.095.

[52] R. Lach, T. Krolopp, P. Hutar, W. Grellmann, Influence of the interface and the additional layer on the stable crack propagation through polyolefin bilayered structures, Procedia Materials Science 3 (2014) 867–872. doi:10.1016/j.mspro.2014.06.141.

[53] Z. Zhang, J.-L. Yang, K. Friedrich, Creep resistant polymeric nanocomposites, Polymer 45 (10) (2004) 3481–3485. doi:10.1016/j.polymer.2004.03.004.

[54] J. Raghavan, M. Meshii, Creep of polymer composites, Composites Science and Technology 57 (12) (1998) 1673–1688. doi:10.1016/S0266-3538(97)00104-8.

[55] H. H. Kausch, P. Beguelin, M. Fischer, Failure of particulate reinforced polymers, Mechanics of Composite Materials 36 (3) (2000) 177–184. doi:10.1007/BF02681868.

[56] J. X. Chan, J. F. Wong, A. Hassan, Z. Mohamad, N. Othman, Mechanical properties of wollastonite reinforced thermoplastic composites: A review, Polymer Composites 41 (2) (2020) 395–429. doi:10.1002/pc.25403.

[57] H. Domininghaus, P. Elsner, P. Eyerer, T. Hirth, Kunststoffe: Eigenschaften und Anwendungen, 8th Edition, VDI-Buch, Springer, Heidelberg u.a, 2012.

[58] E. Baer, A. Hiltner, D. Jarus, Relationship of hierarchical structure to mechanical properties, Macromolecular Symposia 147 (1) (1999) 37–61. doi:10.1002/masy.19991470106.

[59] D. R. Paul, J. W. Barlow, Polymer blends, Journal of Macromolecular Science, Part C 18 (1) (1980) 109–168. doi:10.1080/00222358008080917.

[60] M. Hara, J. A. Sauer, Synergism in mechanical properties of polymer/polymer blends, Journal of Macromolecular Science, Part C 38 (2) (1998) 327–362. doi:10.1080/15583729808544529.

[61] J. W. Barlow, D. R. Paul, Polymer blends and alloys?a review of selected considerations, Polymer Engineering & Science 21 (15) (1981) 985–996. doi:10.1002/pen.760211502.

[62] O. Kolednik, R. Kasberger, M. Sistaninia, J. Predan, M. Kegl, Development of damage-tolerant and fracture-resistant materials by utilizing the material inhomogeneity effect, Journal of Applied Mechanics (86) (2019) 1–12. doi:10.1115/1.4043829.

[63] S. J. Pan, J. Im, M. J. Hill, A. Keller, A. Hiltner, E. Baer, Structure of ultrathin polyethylene layers in multilayer films, Journal of Polymer Science Part B: Polymer Physics 28 (7) (1990) 1105–1119. doi:10.1002/polb.1990.090280709.

[64] Y. Jin, M. Rogunova, A. Hiltner, E. Baer, R. Nowacki, A. Galeski, E. Piorkowska, Structure of polypropylene crystallized in confined nanolayers, Journal of Polymer Science Part B: Polymer Physics 42 (18) (2004) 3380–3396. doi:10.1002/polb.20211.

[65] F. Qiu, M. Wang, Y. Hao, S. Guo, The effect of talc orientation and transcrystallization on mechanical properties and thermal stability of the polypropylene/talc composites, Composites Part A: Applied Science and Manufacturing 58 (2014) 7–15. doi:10.1016/j.compositesa.2013.11.011.

[66] D. S. Langhe, A. Hiltner, E. Baer, Melt crystallization of syndiotactic polypropylene in nanolayer confinement impacting structure, Polymer 52 (25) (2011) 5879–5889. doi:10.1016/j.polymer.2011.10.018.

[67] Z.-Z. Li, M. Li, Y.-x. Feng, Z. Zhang, Y.-E. Wen, Q.-Q. Huang, Z. Lu, H. Bai, H.-L. Wang, B.-B. Xu, H. Cölfen, P. Fratzl, S. Amini, Y. Jiang, Bioinspired compartmentalization strategy for coating polymers with self-organized prismatic films, Chemistry of Materials 33 (23) (2021) 9240–9251. doi:10.1021/acs.chemmater.1c02868.

[68] V. Beloshenko, I. Vozniak, Y. Beygelzimer, Y. Estrin, R. Kulagin, Severe plastic deformation of polymers, MATERIALS TRANSACTIONS 60 (7) (2019) 1192–1202. doi:10.2320/matertrans.MF201912.

[69] R. Kulagin, Y. Beygelzimer, A. Bachmaier, R. Pippan, Y. Estrin, Benefits of pattern formation by severe plastic deformation, Applied Materials Today 15 (2019) 236–241. doi:10.1016/j.apmt.2019.02.007.

[70] L. Wang, J. Lau, E. L. Thomas, M. C. Boyce, Co-continuous composite materials for stiffness, strength, and energy dissipation, Advanced Materials 23 (13) (2011) 1524–1529. doi:10.1002/adma.201003956.

[71] L. S. Dimas, G. H. Bratzel, I. Eylon, M. J. Buehler, Tough composites inspired by mineralized natural materials: Computation, 3d printing, and testing, Advanced Functional Materials 23 (36) (2013) 4629–4638. doi:10.1002/adfm.201300215.

[72] J. R. Raney, B. G. Compton, J. Mueller, T. J. Ober, K. Shea, J. A. Lewis, Rotational 3d printing of damage-tolerant composites with programmable mechanics, Proceedings of the National Academy of Sciences of the United States of America 115 (6) (2018) 1198–1203. doi:10.1073/pnas.1715157115.

[73] J. Stögerer, S. Baumgartner, A. Hochwallner, J. Stampfl, Bio-inspired toughening of composites in 3d-printing, Materials 13 (21) (2020) 4714.

[74] M. Spoerk, F. Arbeiter, H. Cajner, J. Sapkota, C. Holzer, Parametric optimization of intra- and inter-layer strengths in parts produced by extrusion-based additive manufacturing of poly(lactic acid), Journal of Applied Polymer Science 134 (41) (2017) 45401. doi:10.1002/app.45401.

[75] Ö. Bayraktar, G. Uzun, R. Çakiroğlu, A. Guldas, Experimental study on the 3d-printed plastic parts and predicting the mechanical properties using artificial neural networks, Polymers for Advanced Technologies 28 (8) (2017) 1044–1051.

[76] B. Reddy, N. Reddy, A. Ghosh, Fused deposition modelling using direct extrusion, Virtual and Physical Prototyping 2 (1) (2007) 51–60.

[77] J. Torres, M. Cole, A. Owji, Z. DeMastry, A. P. Gordon, An approach for mechanical property optimization of fused deposition modeling with polylactic acid via design of experiments, Rapid Prototyping Journal (2016).

[78] C. Waly, S. Petersmann, F. Arbeiter, Multimaterial extrusion–based additive manufacturing of compliant crack arrester: Influence of interlayer length, thickness, and applied strain rate, Advanced Engineering Materials (2022) 2101703doi:10.1002/adem.202101703.

[79] Kaineder, Hannes, Untersuchungen zur coextrusion von polyolefinen, Bachelor thesis, Johannes Kepler University, Linz (2018).

[80] C. Mueller, V. Topolkaraev, D. Soerens, A. Hiltner, E. Baer, Breathable polymer films produced by the microlayer coextrusion process, Journal of Applied Polymer Science 78 (4) (2000) 816–828. doi:10.1002/1097-4628(20001024)78:4<816::AID-APP150>3.0.CO;2-D.

[81] D. Jarus, A. Hiltner, E. Baer, Barrier properties of polypropylene/polyamide blends produced by microlayer coextrusion, Polymer 43 (8) (2002) 2401–2408. doi:10.1016/S0032-3861(01)00790-X.

[82] E. P. Giannelis, Polymer layered silicate nanocomposites, Advanced Materials 8 (1) (1996) 29–35. doi:10.1002/adma.19960080104.

[83] J. W. Gilman, C. L. Jackson, A. B. Morgan, R. Harris, E. Manias, E. P. Giannelis, M. Wuthenow, D. Hilton, S. H. Phillips, Flammability properties of polymer−layered-silicate nanocomposites. polypropylene and polystyrene nanocomposites †, Chemistry of Materials 12 (7) (2000) 1866–1873. doi:10.1021/cm0001760.

[84] S. Nazarenko, A. Hiltner, E. Baer, Polymer microlayer structures with anisotropic conductivity, Journal of Materials Science 34 (7) (1999) 1461–1470. doi:10.1023/A:1004527205239.

[85] S. Nazarenko, M. Dennison, T. Schuman, E. V. Stepanov, A. Hiltner, E. Baer, Creating layers of concentrated inorganic particles by interdiffusion of polyethylenes in microlayers, Journal of Applied Polymer Science 73 (14) (1999) 2877–2885. doi:10.1002/(SICI)1097-4628(19990929)73:14<2877::AID-APP11>3.0.CO;2-O.

[86] H. Gao, B. Ji, I. L. Jager, E. Arzt, P. Fratzl, Materials become insensitive to flaws at nanoscale: lessons from nature, Proceedings of the National Academy of Sciences of the United States of America 100 (10) (2003) 5597–5600. doi:10.1073/pnas.0631609100.

[87] R. Qu, R. Maaß, Z. Liu, D. Tönnies, L. Tian, R. O. Ritchie, Z. Zhang, C. A. Volkert, Flaw-insensitive fracture of a micrometer-sized brittle metallic glass, Acta Materialia 218 (2021) 117219. doi:10.1016/j.actamat.2021.117219.

[88] K. Wu, Z. Zheng, S. Zhang, L. He, H. Yao, X. Gong, Y. Ni, Interfacial strength-controlled energy dissipation mechanism and optimization in impact-resistant nacreous structure, Materials & Design 163 (2019) 107532. doi:10.1016/j.matdes.2018.12.004.

[89] G. X. Gu, M. Takaffoli, M. J. Buehler, Hierarchically enhanced impact resistance of bioinspired composites, Advanced Materials 29 (28) (2017). doi:10.1002/adma.201700060.

[90] T. L. Anderson, T. L. Anderson, Fracture Mechanics: Fundamentals and Applications, Third Edition, 3rd Edition, CRC Press, Hoboken, 2005.
URL http://gbv.eblib.com/patron/FullRecord.aspx?p=1449389

[91] D. Broek, Elementary engineering fracture mechanics, Springer Netherlands, Dordrecht, 1986. doi:10.1007/978-94-009-4333-9.

[92] D. Broek, The practical use of fracture mechanics, repr Edition, Kluwer, Dordrecht, 1997.

[93] G. R. Irwin, Analysis of stresses and strains near the end of a crack traversing a plate, Journal of Applied Mechanics 24 (3) (1957) 361–364. doi:10.1115/1.4011547.

[94] A. A. Griffith, Vi. the phenomena of rupture and flow in solids, Philosophical Transactions of the Royal Society of London. Series A, Containing Papers of a Mathematical or Physical Character 221 (582-593) (1921) 163–198. doi:10.1098/rsta.1921.0006.

[95] A. R. Zak, M. L. Williams, Crack point stress singularities at a bi-material interface, Journal of Applied Mechanics 30 (1) (1963) 142. doi:10.1115/1.3630064.

[96] T. S. Cook, F. Erdogan, Stresses in bonded materials with a crack perpendicular to the interface, International Journal of Engineering Science 10 (8) (1972) 677–697. doi:10.1016/0020-7225(72)90063-8.

[97] G. Huajian, Fracture analysis of nonhomogeneous materials via a moduli-perturbation approach, Int. J. Solids Struct. (International Journal of Solids and Structures) 27 (13) (1991) 1663–1682. doi:10.1016/0020-7683(91)90068-Q.

[98] S. Muju, Crack propogation in bimaterial multilayered periodically microcracking composite media, Composites Science and Technology 60 (12-13) (2000) 2213–2221. doi:10.1016/S0266-3538(00)00016-6.

[99] J. R. Rice, A path independent integral and the approximate analysis of strain concentration by notches and cracks, Journal of Applied Mechanics 35 (2) (1968) 379. doi:10.1115/1.3601206.

[100] G. E. Hale, F. Ramsteiner, J-fracture toughness of polymers at slow speed, in: Fracture Mechanics Testing Methods for Polymers, Adhesives and Composites, Vol. 28 of European Structural Integrity Society, Elsevier, 2001, pp. 123–157. doi:10.1016/S1566-1369(01)80031-5.

[101] K.-H. Schwalbe, B. Neale, A procedure for determining the fracture behaviour of materials-the unified fracture mechanics test method efam gtp 94, Fat. Fract. Eng. Mater. Struct. (Fatigue & Fracture of Engineering Materials and Structures) 18 (4) (1995) 413–424. doi:10.1111/j.1460-2695.1995.tb01185.x.

[102] N. Simha, F. Fischer, O. Kolednik, C. Chen, Inhomogeneity effects on the crack driving force in elastic and elastic–plastic materials, Journal of the Mechanics and Physics of Solids 51 (1) (2003) 209–240. doi:10.1016/S0022-5096(02)00025-X.

[103] O. Kolednik, The yield stress gradient effect in inhomogeneous materials, Int. J. Solids Struct. (International Journal of Solids and Structures) 37 (5) (2000) 781–808. doi:10.1016/S0020-7683(99)00060-8.

[104] N. K. Simha, F. D. Fischer, O. Kolednik, J. Predan, G. X. Shan, Crack tip shielding or anti-shielding due to smooth and discontinuous material inhomogeneities, International Journal of Fracture 135 (1-4) (2005) 73–93. doi:10.1007/s10704-005-3944-5.

[105] R. Cao, Q. Yu, Y. Li, R. O. Ritchie, Dual-gradient structure leads to optimized combination of high fracture resistance and strength-ductility synergy with minimized final catastrophic failure, Journal of Materials Research and Technology 15 (2021) 901–910. doi:10.1016/j.jmrt.2021.08.102.

[106] G. A. Maugin, Material forces: Concepts and applications, Applied Mechanics Reviews 48 (5) (1995) 213. doi:10.1115/1.3005101.

[107] M. E. Gurtin, Configurational Forces as Basic Concepts of Continuum Physics, Vol. 137, Springer New York, New York, NY, 2000. doi:10.1007/b97847.

[108] J. D. Eshelby, The force on an elastic singularity, Philosophical Transactions of the Royal Society of London. Series A, Containing Papers of a Mathematical or Physical Character 244 (877) (1951) 87–112. doi:10.1098/rsta.1951.0016.

[109] J. D. Eshelby, The elastic energy-momentum tensor, Journal of Elasticity 5 (3-4) (1975) 321–335. doi:10.1007/BF00126994.

[110] J. D. Eshelby, The force on a disclination in a liquid crystal, Philosophical Magazine A 42 (3) (1980) 359–367. doi:10.1080/01418618008239363.

[111] J. D. Eshelby, Energy relations and the energy-momentum tensor in continuum mechanics, in: J. M. Ball, D. Kinderlehrer, P. Podio-Guidugli, M. Slemrod (Eds.), Fundamental Contributions to the Continuum Theory of Evolving Phase Interfaces in Solids, Springer Berlin Heidelberg, Berlin, Heidelberg, 1999, pp. 82–119. doi:10.1007/978-3-642-59938-5_5.

[112] F. D. Fischer, J. Predan, P. Fratzl, O. Kolednik, Semi-analytical approaches to assess the crack driving force in periodically heterogeneous elastic materials, International Journal of Fracture 173 (1) (2012) 57–70. doi:10.1007/s10704-011-9657-z.

[113] O. Kolednik, J. Predan, F. D. Fischer, Cracks in inhomogeneous materials: Compre-

hensive assessment using the configurational forces concept, Engineering Fracture Mechanics 77 (14) (2010) 2698–2711. doi:10.1016/j.engfracmech.2010.07.002.

[114] M. Sistaninia, O. Kolednik, Effect of a single soft interlayer on the crack driving force, Engineering Fracture Mechanics 130 (2014) 21–41. doi:10.1016/j.engfracmech.2014.02.026.

[115] R. Lach, T. Krolopp, P. Hutař, E. Nezbedová, W. Grellmann, Influence of welding and composition on the short-term stable crack propagation through polyolefin single- and bilayered structures, in: W. Grellmann, B. Langer (Eds.), Deformation and Fracture Behaviour of Polymer Materials, Vol. 247 of Springer Series in Materials Science, Springer International Publishing, Cham and s.l., 2017, pp. 211–227. doi:10.1007/978-3-319-41879-7_15.

[116] ASTM International E08 Committee, ASTM E1820, Test method for measurement of fracture toughness (2019). doi:10.1520/E1820-01.

[117] R. Daniel, M. Meindlhumer, J. Zalesak, B. Sartory, A. Zeilinger, C. Mitterer, J. Keckes, Fracture toughness enhancement of brittle nanostructured materials by spatial heterogeneity: a micromechanical proof for crn/cr and tin/siox multilayers, Materials & design 104 (2016) 227–234.

[118] R. Bermejo, R. Daniel, C. Schuecker, O. Paris, R. Danzer, C. Mitterer, Hierarchical architectures to enhance structural and functional properties of brittle materials, Advanced Engineering Materials 19 (4) (2017) 1600683.

[119] F. J. Arbeiter, S. Petersmann, J. Wiener, F. Oesterreicher, M. Spoerk, G. Pin-

ter, Using compliant interlayers as crack arresters in 3-d-printed polymeric structures, Materials Performance and Characterization 9 (5) (2020) 20190201. doi:10.1520/MPC20190201.

[120] J. Mueller, J. R. Raney, D. M. Kochmann, K. Shea, Stiffness-independent toughening of beams through coaxial interfaces, Advanced Science 10 (2018) 1800728. doi:10.1002/advs.201800728.

[121] S. Kochiyama, W. Fang, M. A. Monn, H. Kesari, Sawtooth patterns in flexural force curves of structural biological materials are not signatures of toughness enhancement: Part i, Journal of the mechanical behavior of biomedical materials 119 (2021) 104362. doi:10.1016/j.jmbbm.2021.104362.

[122] G. R. Irwin, Plastic zone near a crack and fracture toughness, Proceeding in Sagamore Ordnance Material Conference (1960) IV63–1V78.

[123] A. Galeski, Strength and toughness of crystalline polymer systems, Progress in Polymer Science 28 (12) (2003) 1643–1699. doi:10.1016/j.progpolymsci.2003.09.003.

[124] W. Retting, Mechanik der Kunststoffe: Die mechanischen Eigenschaften von Polymer-Werkstoffen ; mit 6 Tabellen, Studientexte Kunststofftechnik, Hanser, München, 1992.

[125] G. Boisot, L. Laiarinandrasana, J. Besson, C. Fond, G. Hochstetter, Experimental investigations and modeling of volume change induced by void growth in

polyamide 11, International Journal of Solids and Structures 48 (19) (2011) 2642–2654. doi:10.1016/j.ijsolstr.2011.05.016.

[126] A. Pawlak, A. Galeski, Cavitation during tensile deformation of polypropylene, Macromolecules 41 (8) (2008) 2839–2851. doi:10.1021/ma0715122.

[127] H.-A. Cayzac, K. Saï, L. Laiarinandrasana, Damage based constitutive relationships in semi-crystalline polymer by using multi-mechanisms model, International Journal of Plasticity 51 (2013) 47–64. doi:10.1016/j.ijplas.2013.06.008.

[128] L. Laiarinandrasana, T. F. Morgeneyer, H. Proudhon, F. N'guyen, E. Maire, Effect of multiaxial stress state on morphology and spatial distribution of voids in deformed semicrystalline polymer assessed by x-ray tomography, Macromolecules 45 (11) (2012) 4658–4668. doi:10.1021/ma3005247.

[129] L. Laiarinandrasana, N. Selles, O. Klinkova, T. F. Morgeneyer, H. Proudhon, L. Helfen, Structural versus microstructural evolution of semi-crystalline polymers during necking under tension: Influence of the skin-core effects, the relative humidity and the strain rate, Polymer Testing 55 (2016) 297–309. doi:10.1016/j.polymertesting.2016.09.012.

[130] J. Karger-Kocsis, T. Bárány, Polypropylene Handbook, Springer International Publishing, Cham, 2019. doi:10.1007/978-3-030-12903-3.

[131] W. Grellmann, B. Langer (Eds.), Deformation and Fracture Behaviour of Polymer Materials, Vol. 247 of Springer Series in Materials Science, Springer International

Publishing, Cham and s.l., 2017. doi:10.1007/978-3-319-41879-7.

URL http://dx.doi.org/10.1007/978-3-319-41879-7

[132] T. McLeish, C. Plummer, A. M. Donald, Crazing by disentanglement: non-diffusive reptation, Polymer 30 (9) (1989) 1651–1655. doi:10.1016/0032-3861(89)90325-X.

[133] V. Delhaye, A. H. Clausen, F. Moussy, R. Othman, O. S. Hopperstad, Influence of stress state and strain rate on the behaviour of a rubber-particle reinforced polypropylene, International Journal of Impact Engineering 38 (4) (2011) 208–218. doi:10.1016/j.ijimpeng.2010.11.004.

[134] V. Delhaye, A. H. Clausen, F. Moussy, O. S. Hopperstad, R. Othman, Mechanical response and microstructure investigation of a mineral and rubber modified polypropylene, Polymer Testing 29 (7) (2010) 793–802. doi:10.1016/j.polymertesting.2010.07.001.

[135] H. S. Katz, J. V. Milewski (Eds.), Handbook of fillers for plastics, 2nd Edition, Van Nostrand Reinhold, New York, 1987.

[136] G.-M. Kim, G. H. Michler, M. Gahleitner, J. Fiebig, Relationship between morphology and micromechanical toughening mechanisms in modified polypropylenes, Journal of Applied Polymer Science 60 (9) (1996) 1391–1403. doi:10.1002/(SICI)1097-4628(19960531)60:9<1391::AID-APP15>3.0.CO;2-5.

[137] T. Kawai, S. Soeno, S.-i. Kuroda, S. Koido, T. Nemoto, M. Tamada, Deformation induced void formation and growth in β nucleated isotactic polypropylene, Polymer 178 (2019) 121523. doi:10.1016/j.polymer.2019.05.065.

[138] T. F. Guo, J. Faleskog, C. F. Shih, Continuum modeling of a porous solid with pressure-sensitive dilatant matrix, Journal of the Mechanics and Physics of Solids 56 (6) (2008) 2188–2212. doi:10.1016/j.jmps.2008.01.006.

[139] A. S. Ognedal, A. H. Clausen, T. Berstad, T. Seelig, O. S. Hopperstad, Void nucleation and growth in mineral-filled pvc – an experimental and numerical study, International Journal of Solids and Structures 51 (7-8) (2014) 1494–1506. doi:10.1016/j.ijsolstr.2013.12.042.

[140] A. S. Ognedal, A. H. Clausen, A. Dahlen, O. S. Hopperstad, Behavior of pvc and hdpe under highly triaxial stress states: An experimental and numerical study, Mechanics of Materials 72 (2014) 94–108. doi:10.1016/j.mechmat.2014.02.002.

[141] J. Mohanraj, D. C. Barton, I. M. Ward, A. Dahoun, J. M. Hiver, C. G'Sell, Plastic deformation and damage of polyoxymethylene in the large strain range at elevated temperatures, Polymer 47 (16) (2006) 5852–5861. doi:10.1016/j.polymer.2006.06.008.

[142] S. N. Olufsen, K. R. Tekseth, D. W. Breiby, A. H. Clausen, O. S. Hopperstad, A technique for in situ x-ray computed tomography of deformation-induced cavitation in thermoplastics, Polymer Testing 91 (2020) 106834. doi:10.1016/j.polymertesting.2020.106834.

[143] S. N. Olufsen, A. H. Clausen, D. W. Breiby, O. S. Hopperstad, X-ray computed tomography investigation of dilation of mineral-filled pvc under monotonic loading, Mechanics of Materials 142 (2020) 103296. doi:10.1016/j.mechmat.2019.103296.

[144] W. Brocks, Cohesive strength and separation energy as characteristic parameters of fracture toughness and their relation to micromechanics, Structural Durability & Health Monitoring (Vol.1, No.4) (2005) pp. 233–244. doi:10.3970/sdhm.2005.001.233.

[145] A. Needleman, A continuum model for void nucleation by inclusion debonding, Journal of Applied Mechanics 54 (3) (1987) 525–531. doi:10.1115/1.3173064.

[146] V. Tvergaard, J. W. Hutchinson, The relation between crack growth resistance and fracture process parameters in elastic-plastic solids, Journal of the Mechanics and Physics of Solids 40 (6) (1992) 1377–1397. doi:10.1016/0022-5096(92)90020-3.

[147] A. Needleman, An analysis of tensile decohesion along an interface, Journal of the Mechanics and Physics of Solids 38 (3) (1990) 289–324.

[148] C. R. Chen, O. Kolednik, I. Scheider, T. Siegmund, A. Tatschl, F. D. Fischer, On the determination of the cohesive zone parameters for the modeling of micro-ductile crack growth in thick specimens, International Journal of Fracture 120 (3) (2003) 517–536. doi:10.1023/A:1025426121928.

[149] C. R. Chen, O. Kolednik, Comparison of cohesive zone parameters and crack tip stress states between two different specimen types, International Journal of Fracture 132 (2) (2005) 135–152. doi:10.1007/s10704-005-0626-2.

[150] C. R. Chen, O. Kolednik, J. Heerens, F. D. Fischer, Three-dimensional modeling of ductile crack growth: Cohesive zone parameters and crack

tip triaxiality, Engineering Fracture Mechanics 72 (13) (2005) 2072–2094. doi:10.1016/j.engfracmech.2005.01.008.

[151] K. C. Pandya, A. Ivankovic, J. G. Williams, Cohesive zone modelling of crack growth in polymers part 2 –numerical simulation of crack growth, Plastics, Rubber and Composites 29 (9) (2000) 447–452. doi:10.1179/146580100101541283.

[152] K. C. Pandya, J. G. Williams, Cohesive zone modelling of crack growth in polymers part 1 –experimental measurement of cohesive law, Plastics, Rubber and Composites 29 (9) (2000) 439–446. doi:10.1179/146580100101541274.

[153] Z. Bartczak, A. Argon, R. Cohen, M. Weinberg, Toughness mechanism in semi-crystalline polymer blends: Ii. high-density polyethylene toughened with calcium carbonate filler particles, Polymer 40 (9) (1999) 2347–2365. doi:10.1016/S0032-3861(98)00444-3.

[154] I. Kemal, A. Whittle, R. Burford, T. Vodenitcharova, M. Hoffman, Toughening of unmodified polyvinylchloride through the addition of nanoparticulate calcium carbonate, Polymer 50 (16) (2009) 4066–4079. doi:10.1016/j.polymer.2009.06.028.

[155] A. S. Argon, R. E. Cohen, Toughenability of polymers, Polymer 44 (19) (2003) 6013–6032. doi:10.1016/S0032-3861(03)00546-9.

[156] M. J. Kanters, T. Kurokawa, L. E. Govaert, Competition between plasticity-controlled and crack-growth controlled failure in static and cyclic fatigue of thermoplastic polymer systems, Polymer Testing 50 (2016) 101–110. doi:10.1016/j.polymertesting.2016.01.008.

[157] A. Chudnovsky, M. Kachanov, Interaction of a crack with a field of microcracks, International Journal of Engineering Science 21 (8) (1983) 1009–1018. doi:10.1016/0020-7225(83)90078-2.

[158] A. Chudnovsky, A. Moet, Thermodynamics of translational crack layer propagation, Journal of Materials Science 20 (2) (1985) 630–635. doi:10.1007/BF01026535.

[159] A. Chudnovsky, B. Kunin, A probabilistic model of brittle crack formation, Journal of Applied Physics 62 (10) (1987) 4124–4129. doi:10.1063/1.339128.

7. Bibliography

7.1. *Publication I*

Title:	Optimization of Mechanical Properties and Damage Tolerance in Polymer-Mineral Multilayer Composites
Authors:	Johannes Wiener[a], Hannes Kaineder[b], Otmar Kolednik[c], Florian Arbeiter[a]
Affiliation:	[a] Materials Science and Testing of Polymers, Montanuniversitaet Leoben, 8700 Leoben, Austria [b] Institute of Polymer Extrusion and Compounding, Johannes Kepler University Linz, 4040 Linz, Austria; [c] Erich-Schmid-Institute of Materials Science, Austrian Academy of Science, 8700 Leoben, Austria
DOI:	https://doi.org/10.3390/ma14040725
Conceptualization:	Johannes Wiener (70%), Florian Arbeiter (30%)
Methodology:	Johannes Wiener (60%), Hannes Kaineder (20%), Florian Arbeiter (20%)
Validation:	equal contribution by all authors
Investigation:	Johannes Wiener (70%), Hannes Kaineder (30%)
Writing-Original Draft:	Johannes Wiener (80%), Florian Arbeiter (20%)
Writing-Review & Editing	equal contribution by all authors
Supervision	Florian Arbeiter (80%), Otmar Kolednik (20%)

Article

Optimization of Mechanical Properties and Damage Tolerance in Polymer-Mineral Multilayer Composites

Johannes Wiener [1], Hannes Kaineder [2], Otmar Kolednik [3] and Florian Arbeiter [1],*

[1] Materials Science and Testing of Polymers, Montanuniversitaet Leoben, 8700 Leoben, Austria;
johannes.wiener@unileoben.ac.at

[2] Institute of Polymer Extrusion and Compounding, Johannes Kepler University Linz, 4040 Linz, Austria;
hannes.kaineder@jku.at

[3] Erich-Schmid-Institute of Materials Science, Austrian Academy of Science, 8700 Leoben, Austria;
Otmar.Kolednik@oeaw.ac.at

* Correspondence: florian.arbeiter@unileoben.ac.at; Tel.: +43-(0)3842-402-2122

Abstract: Talcum reinforced polypropylene was enhanced with a soft type of polypropylene in order to increase the impact strength and damage tolerance of the material. The soft phase was incorporated in the form of continuous interlayers, where the numbers of layers ranged from 64 to 2048. A blend with the same material composition (based on wt% of the used materials) and the pure matrix material were investigated for comparison. A plateau in impact strength was reached by layered architectures, where the matrix layer thickness was as small or smaller than the largest talcum particles. The most promising layered architecture, namely, 512 layers, was subsequently investigated more thoroughly using instrumented Charpy experiments and tensile testing. In these tests, normalised parameters for stiffness and strength were obtained in addition to the impact strength. The multilayered material showed remarkable impact strength, fracture energy and damage tolerance. However, stiffness and strength were reduced due to the addition of the soft phase. It could be shown that specimens under bending loads are very compliant due to a stress-decoupling effect between layers that specifically reduces bending stiffness. This drawback could be avoided under tensile loading, while the increase in toughness remained high.

Keywords: multilayer; biomimetic design; damage tolerance; polypropylene; microlayer

1. Introduction

To use polymers in engineering applications successfully, a certain level of mechanical properties, such as stiffness, strength and impact strength, are required. Due to inherent limitations of the material properties, this is not always possible. Therefore, polymers are often reinforced with glass fibres, carbon fibres or mineral particles. Kausch et al., for example, found a strong increase in stiffness when adding alumina to polystyrene [1]. If surface treatment is performed correctly, mineral fillers can also increase the strength of a polymer matrix [2]. As a result of the reduced chain mobility, improvements were also found in the long-term creep behaviour [3,4]. Comparisons of the many useful combinations of matrices and reinforcements are available in extensive volumes for polymeric materials [5,6]. Unfortunately, high filler contents also lead to embrittlement, making these materials unusable for certain applications (e.g., when impact loading or high deformations are expected). Solutions must be found to counteract the embrittlement while preserving the benefits of the reinforcement. One approach is to maximize particle orientation parallel to the expected loading direction. While optimizing the load bearing capacity of the particles, this practice may also reduce defect size [7,8]. Another approach is to add a soft component as a toughening agent to increase the impact strength [9–11]. The conventional method for this is blending, e.g., by compounding, which leads to a random distribution

of the soft phase. The change in properties roughly adheres to the rule of mixture, so that improvements in impact strength may come at the cost of stiffness and strength [9–11].

Alternatively, the soft phase can be incorporated as distinct domains, for example, as continuous layers in a co-extrusion process [12,13]. Studies on natural materials suggest great potential for alternating layers of stiff and compliant material [14–17]. Publications on nacre show its remarkable toughness, although its main component is brittle aragonite [18,19]. The skeleton of deep sea sponges also reveals astounding toughness and flexibility, especially considering that it is mostly made out of glass [20–24]. Bone is known to have outstanding strength-to-weight and stiffness-to-weight ratios [25] while also serving an organ-like function for the production of blood cells [26]. In most cases, a combination of high stiffness and high toughness in these materials can be traced back to intricate microstructures [27–31]. Small domains of protein-based soft phases within a stiff and brittle matrix phase ($CaCO_3$, SiO_2 etc.) act as toughness enhancers in these materials. Kolednik et al. showed that the soft domains are crucial for the increase in fracture toughness, as they encourage crack arresting mechanisms [32]. In nacre-like materials, crack deflection and platelet pull-out are able to further increase fracture toughness [33–35]. Replicating such microcomposites with commercial materials holds great potential for science and industry and is, therefore, worth investigating. One possibility would be the so-called material inhomogeneity effect, which can help to stop cracks at soft interlayers (IL). Various sources point out that a large difference in yield stress is required in order to diminish the crack driving force [32,36,37]. Such crack arresting properties of a soft IL have already been found in polymeric materials with one or two soft ILs [38–40].
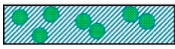
To further deepen the understanding of this effect, and exhaust the possibilities of this mechanism, the properties of polypropylene/talcum composites with an increased number of layers (up to 2048) are investigated in this work. Several studies on micro- and nanolayer coextrusion already show the high potential of this method in multiple fields of research. Literature ranges from improved barrier properties [41–43] and flame retardancy [44] to altered crystallisation behaviour [45–48] and even semi-conductivity in metal filled polymers [49,50]. Publications on mechanical behaviour [7,8] report an increase in fracture strain, when average layer thickness is decreased below a certain critical threshold. To date, these studies have mainly focused on microstructural aspects of the multilayer materials, without further analysis of the trade-off between stiffness and toughness, which often has to be made [51,52]. In this contribution, we aim to offer a thorough investigation of the mechanical properties of a brittle matrix material, which are enhanced with different toughening techniques. A comparison between conventional blending, high particle orientation and a defined microstructure in the form of alternating layers is made regarding bending stiffness, impact strength and damage tolerance.

2. Materials and Methods

2.1. Specimen Preparation

An overview of all investigated materials is summarized in Table 1. Therein, the material composition, a brief description as well as a schematic drawing of the microstructure are given. To accomplish the various layer architectures, a microlayer co-extrusion technique was used [12,13,53]. All materials were supplied in the form of extruded sheets with a thickness of 4 mm. From these, Charpy specimens according to DIN EN ISO 179-1 [54] were manufactured with different notch types (unnotched, Charpy-notched and razor blade notched according to [55–57]). As shown in Figure 1, all notches were introduced flatwise, so the effect of a layered plate could be observed. Additionally, tensile test specimens (Type 1A) were prepared in order to be tested according to DIN EN ISO 527 [58]. Detailed descriptions of the investigated materials as well as the processing technique are given in Appendix A.

Table 1. Overview of investigated materials including their abbreviation, material composition, description and schematic of microstructure.

Abbreviation	Depiction	Material Composition	Description	Toughening Mechanism
PP-HR		Highly reinforced PP	Homogeneous bulk material	-
PP-HR_512L		Highly reinforced PP	Bulk material processed in 512 identical layers	High orientation
Blend		Highly reinforced PP and soft PP (87:13)	Blended material	Soft component
Blend_512L		Highly reinforced PP and soft PP (87:13)	Blended material processed in 512 identical layers	Soft component + high orientation
ML_512L		Highly reinforced PP:soft PP (87:13)	Two different materials processed in 512 alternating layers	Soft component + high orientation + defined microstructure
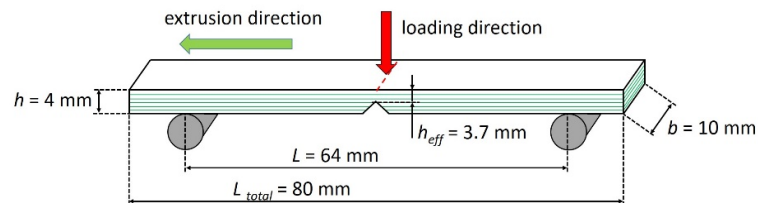
Figure 1. Charpy specimen dimensions with the notch introduced flatwise.

2.2. Testing Methods

Uninstrumented as well as instrumented Charpy experiments were performed according to DIN EN ISO 179-1fA for notched and DIN EN ISO 179-1fU for unnotched specimens. An effective cross-sectional area, A_{eff}, and the impact strength, a_c, were calculated according to Equations (1) and (2). Therein, b is the specimen width, h_{eff} the effective thickness and U the area under the force–displacement curve. Due to high oscillation during the instrumented impact tests, the maximum force, F_{max}, and initial slope could not be reliably determined from the raw data. Therefore, a fit of cubic splines was created for each curve, which was then used to determine the maximum force and initial slope. The slope was calculated from the differences in force, ΔF, and displacement, Δv, in the initial, linear part of the curve. From the initial slope in the unnotched state, the bending modulus, E_b, was calculated according to Equation (3) to compare the stiffness of the materials. The calculation is in agreement with DIN EN ISO 178 [59], although the testing speed in this case is much higher than in conventional three-point-bending tests. E_b should, therefore, be seen as a ranking parameter in these specific considerations and cannot be quantitatively compared to values obtained from quasi-static experiments. In order to remove the influence of specimen geometry, F_{max} was divided by A_{eff} of each individual specimen. The formula for the normalised maximum Force, F_{max}^{norm}, is shown in Equation (4).

$$A_{eff} = bh_{eff} \tag{1}$$

$$a_c = \frac{U}{A_{eff}} \tag{2}$$

$$E_b = \frac{\Delta F}{\Delta v} \frac{L^3}{4bh_{eff}^3} \tag{3}$$

$$F_{max}^{norm} = \frac{F_{max}}{A_{eff}} \tag{4}$$

All tensile tests were performed according to DIN EN ISO 527, where the Young's modulus, E, the ultimate tensile strength, σ_{UTS}, and the elongation at break, ε_{br}, were measured. In these tensile tests, the area under the force–displacement curve was corrected for elastic unloading and taken as fracture energy, which acted as a measure for toughness. To investigate the microstructure of the samples, scanning electron microscopy was applied, whereas the fractographs were generated from the backscatter electron to give an improved contrast between talcum particles and the polymer matrix. A more detailed description of all testing procedures is presented in Appendix A.

3. Results and Discussion

3.1. Impact Strength of Multilayer Composites

In Figure 2a, the impact strength values of the layered composites are shown for Charpy notched and unnotched specimens. The numbers of layers range from 64 to 2048. Up to 256 layers, it appears that increasing the number of layers has no significant influence on the impact strength. However, increasing the number of layers beyond this point leads to a drastic increase in impact strength for both unnotched and Charpy notched specimens. At 1024 layers, the impact strength reaches a plateau of 45 kJ/m^2 for unnotched and 20 kJ/m^2 in the notched state. A further increase in the number of layers yields no improvements of impact strength. In comparison to the lower numbers of layers, this plateau value represents an increase in impact strength of approximately 4.5 times in the unnotched and three times in the notched state.
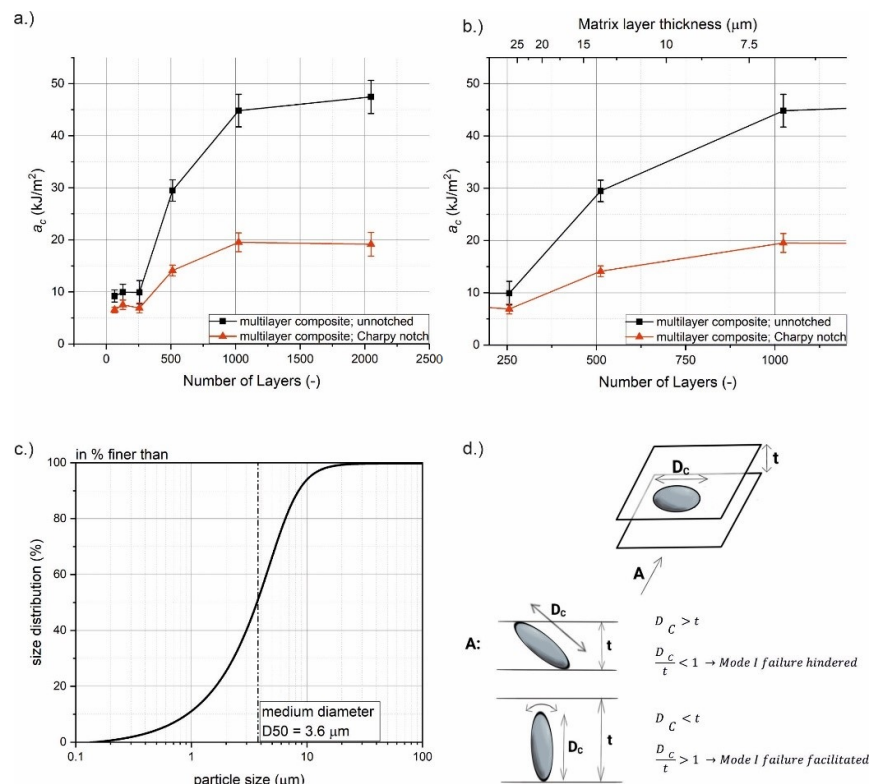

Figure 2. (**a**) Impact strength versus number of layers for a multilayer composite, (**b**) a magnification of the plateau region, (**c**) the size distribution of the talcum particles in the matrix and (**d**) a representation of large talcum particle orientation in a thin matrix layer.

In Figure 2b, the transition region from the lower to the upper plateau is shown with greater magnification. The added scale at the top of Figure 2b shows the matrix layer thickness t. An explanation of this effect could be that the increased orientation of large talcum particles during the microlayering process improves the impact strength. No

further improvement appears after all particles are oriented in extrusion direction. This improvement in impact strength might be also affected by the ratio of particle size to matrix layer thickness. The size distribution of talcum particles in the matrix is shown in Figure 2c. It is seen that the impact strength only increases when the matrix layer thickness falls below a critical dimension, $t < D_C$. This critical dimension is the size of the largest talcum particles in the distribution, which are critical for failure when left unoriented. Thus, improvements of impact strength can be seen for matrix layer thicknesses of $t < 13.6$ μm. At this point, the matrix layers become smaller than the largest talcum particles which, therefore, have to be forcefully oriented during processing. As a result, these large particles are oriented along the layer plane, and their ability to act as critical defect for layer failure is diminished (Figure 2d). Note that the critical normal stress components for Mode I fracture lie in a plane perpendicular to the layer plane (Figure 1). If the matrix layer thickness is greater than D_C, some of the large particles can be aligned perpendicular to the layer plane. If such a particle debonds from the matrix during impact loading, a large void oriented along the nominal fracture plane is formed. In that case, Mode I failure is facilitated, representing the worst-case scenario. Reducing the layer thickness below a certain threshold (approximately 7.8 μm in this specific case) brings no further improvement, since all large particles are already oriented. As a result, lower and upper plateaus in impact strength are formed.

Baer et al. [7] and Mueller et al. [8] found similar trends for talcum-filled PP composites, where the fracture strain started to increase drastically with an increasing number of layers. In these contributions, the altered material behaviour could also be linked to an increased degree of particle orientation. However, no lower plateau region was reported in these publications. Additionally, the fracture strain started to decrease again after a peak region instead of forming an upper plateau. The decrease in fracture strain at higher numbers of layers was attributed to particle agglomeration during processing. Mueller et al. even report quasi brittle fracture at 1024 layers or more. Up to 2048 layers, no such limitations could be found in the present investigation, indicating a high quality of processing. However, these sources agree that the limitation of defect size is responsible for the increased ductility along with a tortuous crack path, crack tip blunting and enhanced particle alignment [7]. Building on the results of this preliminary study, the most promising multilayer composite was selected for a more detailed investigation. More specifically, the composition with 512 layers (start of plateau region) was chosen for closer examination in further experiments.

3.2. Comparison of Single and 512-Layer Coextruded Materials

The transition region between the lower and upper plateau of impact strength is of special interest for understanding the changes in microstructure and failure mechanism. Hence, the multilayer material with 512 layers, ML_512L, was chosen for closer investigation instead of the composite with 1024 layers. Although ML_512L showed great results in the uninstrumented Charpy experiments, not much more is known of its material properties. It is not entirely clear yet whether the improvements in impact strength stem from particle orientation, the addition of soft phase or from the layered microstructure. Thus, ML_512L as well as comparable blends and the matrix material (see Table 1 for more details) were investigated more thoroughly in instrumented Charpy experiments. The experiments aim to provide a more detailed impression of material behaviour, including stiffness and damage tolerance. Representative force–displacement curves from the instrumented Charpy experiments are shown in Figure 3. The figure shows the fitted data from the unnotched specimens. E_b, F_{max}^{norm} and a_c were obtained from the instrumented Charpy tests for all investigated materials and notch types. The results are given in full detail in Table A1 in Appendix B. A graphic representation of all obtained material parameters for unnotched, Charpy-notched and razor blade notched specimens is given in Figure 4a.
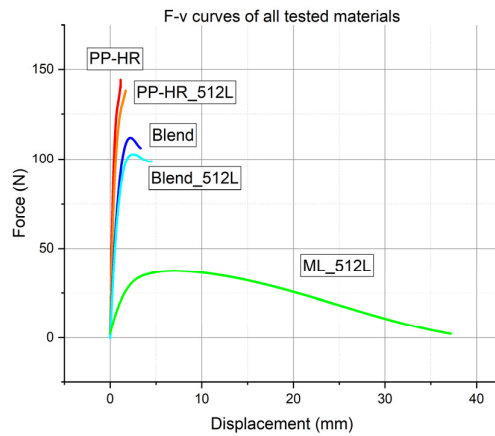
Figure 3. Representative force–displacement curves in instrumented Charpy experiments for unnotched materials.
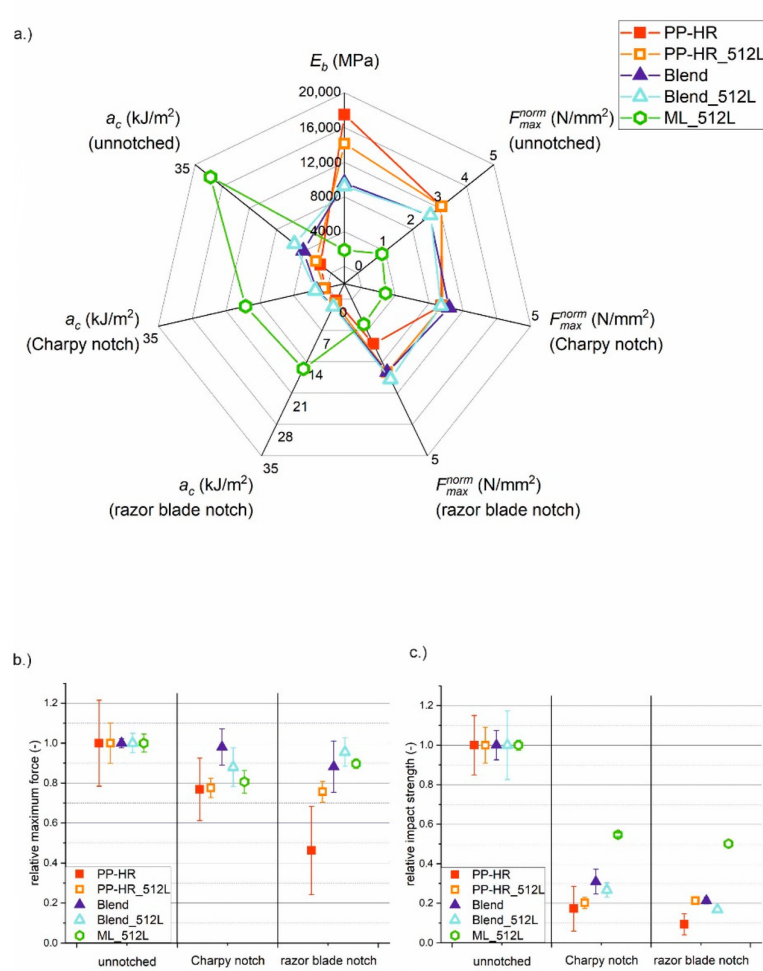

Figure 4. (**a**) Overview of E_b, F_{max}^{norm} and a_c for unnotched, Charpy-notched and razor blade notched specimens of all tested materials. The notch sensitivity and data scattering of (**b**) F_{max}^{norm} and (**c**) a_c is depicted by referencing each value to the unnotched state of that material.

The force–displacement curves for PP-HR and PP-HR_512L (see Figure 3) resulted in high values of F_{max}^{norm} and E_b due to the high mineral content. However, high displacements

could not be reached before the materials failed. For both homogeneous materials, the failure behaviour was a complete and brittle fracture without visible plastic deformation. PP-HR exhibited very low impact strength, especially in comparison to materials with a soft phase. The microlayering process of PP-HR_512L led to a minor improvement in a_c over PP-HR, owing to a slight increase in elongation at break. However, the impact strength was still low compared to the blends and multilayer materials. These minor effects may be attributed to an increased degree of orientation, accompanied by a reduction in defect size. Additionally, E_b of PP-HR_512L was reduced to 81% of PP-HR as a result of the microlayering process.

In order to give an impression of data scattering and notch sensitivity, the relative values for F_{max}^{norm} and a_c are plotted against the notch type in Figure 4b,c. The values for Charpy and razor blade notches are viewed in relation to the unnotched state of the same material, so the unnotched reference state was always given a value of 1. PP-HR was especially susceptible to any type of notching. The maximum force and impact strength were greatly decreased with increasing notch sharpness. The impact strength was even reduced by up to 90% in the presence of a razor blade notch. It is clear that such a material cannot be used for structural applications, since even small defects or scratches could lead to catastrophic failure under impact loading. PP-HR also showed the highest data scattering, which was probably caused by the size distribution of talcum particles. In the absence of a microlayering process, larger agglomerates of particles were not broken up during processing, leading to larger initial defects in the material. This may also have led to the low values of F_{max}^{norm} and a_c in the notched states. In the unnotched and Charpy notched state, PP-HR_512L showed roughly the same relative values of F_{max}^{norm} and a_c, but offered an improvement in the razor blade notched state. While PP-HR dropped to relative values of 50%, PP-HR_512L retained approximately 75% of F_{max}^{norm}. Regarding impact strength, PP-HR_512L retained 20% of a_c in the presence of a sharp notch. The layering process also reduced the data scattering for PP-HR_512L, suggesting that very large agglomerates were broken up during the microlayering process. Thus, the variance in initial defect size was reduced, which led to more uniform values and less notch sensitivity.

The two blends had an overall reduced content of mineral filler by 13% compared to the matrix material. Therefore, F_{max}^{norm} and E_b were smaller than for PP-HR, but the impact strength of the matrix material could be drastically improved. While E_b was reduced by approximately one third, the impact strength could be increased by 170% (Blend) and 250% (Blend_512L), respectively. As could already be assumed from the force–displacement curves, the microlayering process was beneficial to the ductility of the blend. One possible explanation for the increased ductility of Blend_512L is a more finely dispersed microstructure due to the microlayering process accompanied by an overall reduction in defect size. While the distribution of the matrix and soft phase was still random, large bulks of matrix-rich material were less likely. In the Blend, these areas were able to form a percolating network, which acted as a stiff but brittle skeleton within the material. As a result, the Blend_512L had increased impact strength for all three notch types, owing to its increased elongation at break. Although F_{max}^{norm} appeared to be lower for Blend_512L at first glance (see Figure 3), this difference lies within the standard deviation of the measurement. However, both blends suffered from reduced impact strength when introducing a notch. As a result, impact strength was reduced by 75% for Charpy notches and 80% for razor blade notches. For both blends, the failure behaviour was a complete fracture with small plastic zones around the fracture plain. Although the soft phase increased the absolute level of impact strength, the material was almost as damage intolerant as the matrix material. Despite the domains of soft phase, the random microstructure was ill-suited to stop cracks from advancing.

For ML_512L, the failure behaviour was a partial fracture with large plastic zones around the crack tip. Due to the high compliance of ML_512L, the specimens were pulled through the Charpy fixture after a large amount of displacement, instead of breaking. Figure 3 shows the lowest forces, the highest displacements and a gradual reduction in

force to 0 N as the specimens were pulled through the fixture. Despite the low values for F_{max}^{norm} and E_b, specimens with continuous interlayers had outstanding impact strength owing to the high displacements that could be endured. Although E_b was reduced by a factor of 9.2 compared to PP-HR, the multilayer material had an impact strength over 60 times higher than the matrix material in the presence of a sharp notch (15.53 compared to 0.25 kJ/m^2). Additionally, this multilayer composite showed the highest damage tolerance out of all investigated materials, retaining relative values of 80–90% for F_{max}^{norm} for all notch types and 50% of a_c in the razor blade notched state. These properties were not only caused by the addition of the soft phase, but also by the layered microstructure. Despite having the same material composition, ML_512L with a razor blade notch showed an impact strength twice as high as the unnotched Blend. Blends, on the other hand, exhibited comparably high stiffness, but could not offer the crack arresting properties associated with a multilayer microstructure. It is crucial that the soft phase is arranged in a defined structure stretching the whole cross section, e.g., as layers, so crack growth cannot avoid the soft domains. Thus, the multitude of soft layers could enhance damage tolerance through crack tip blunting and by limiting defect size.

3.3. Synergistic Effect of Layered Architecture

For a reasonable evaluation of a material, both toughness and stiffness need to be considered simultaneously. For that reason, the measured values for a_c are plotted against E_b in Figure 5. All unnotched materials are depicted in Figure 5a, while the razor blade notched materials are shown in Figure 5b. All observed trends remain qualitatively the same for notched and unnotched specimens. However, the absolute values of a_c in the razor blade notched state are smaller. The values for Charpy notched specimens are not shown separately, since the difference in trends to the razor blade notched specimens is negligible. Similar to an Ashby plot, this depiction allows for a more comprehensive assessment of materials. PP-HR and PP-HR_512L are the stiffest, but also the most brittle materials. Apparently, the microlayering process increased the ductility of PP-HR_512L, thus increasing the impact strength while simultaneously decreasing E_b. The two blends are not as stiff, but tougher than the homogeneous materials. The microlayered Blend_512L shows higher a_c but is also more compliant than the Blend. Similar to PP-HR, the microlayering process caused changes in the material behaviour of the Blend in the form of increased ductility. Generally, all blends and homogeneous materials lie on a connection line, and a change in material composition (soft phase content) would result in a shift along this line. When comparing ML_512L to this reference line, the low stiffness is clearly outweighed by the increased impact strength, so that the data point lies significantly above the line.
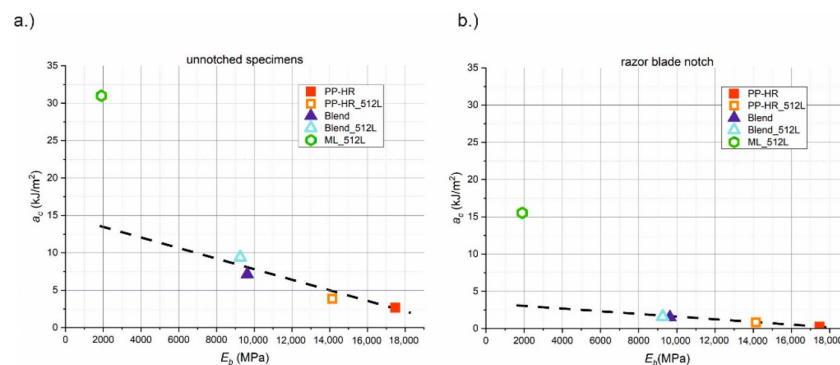

Figure 5. Comparison of stiffness and toughness showing impact strength versus the bending modulus E_b for (**a**) unnotched and (**b**) razor blade notched specimens.

The combination of stiffness and toughness of ML_512L is very different to Blend_512L, highlighting once again the significance of the microstructure in two materials of the same composition. Therefore, the microstructure of the blends and ML materials was analysed

using SEM-micrographs. As can be seen in Figure 6a, the Blend shows a microstructure of a randomly distributed matrix phase and soft phase. The domains of matrix material tend to be richer in talcum particles, while domains that are rich in soft phase have little to no reinforcing particles in them (indicated by red lines in Figure 6a). A percolating network of matrix material can form in this material, thus facilitating catastrophic failure. Matrix and IL material in Blend_512L (Figure 6b) are more finely dispersed due to the microlayering process, so that no clear domains can be assigned. This is the reason for the increased strain at break and impact strength, but also the reduced stiffness. While the randomly distributed soft phase has a beneficial effect on toughness, continuous ILs are most effective at stopping cracks. As shown in Figure 6c, bands of IL material act as crack arresters in the multilayer composite ML_512L. The boundaries of matrix material and IL are also indicated by red lines in Figure 6c. For the IL to be effective, the bands of soft material must be continuous throughout the specimen. Otherwise, the maximum possible defect size is not limited to the layer thickness and the benefits to toughness may be lost. This assumption is confirmed by Baer et al. [7], where processing-induced talcum agglomerations interfered with the layer structure, and the benefits to fracture strain were lost.
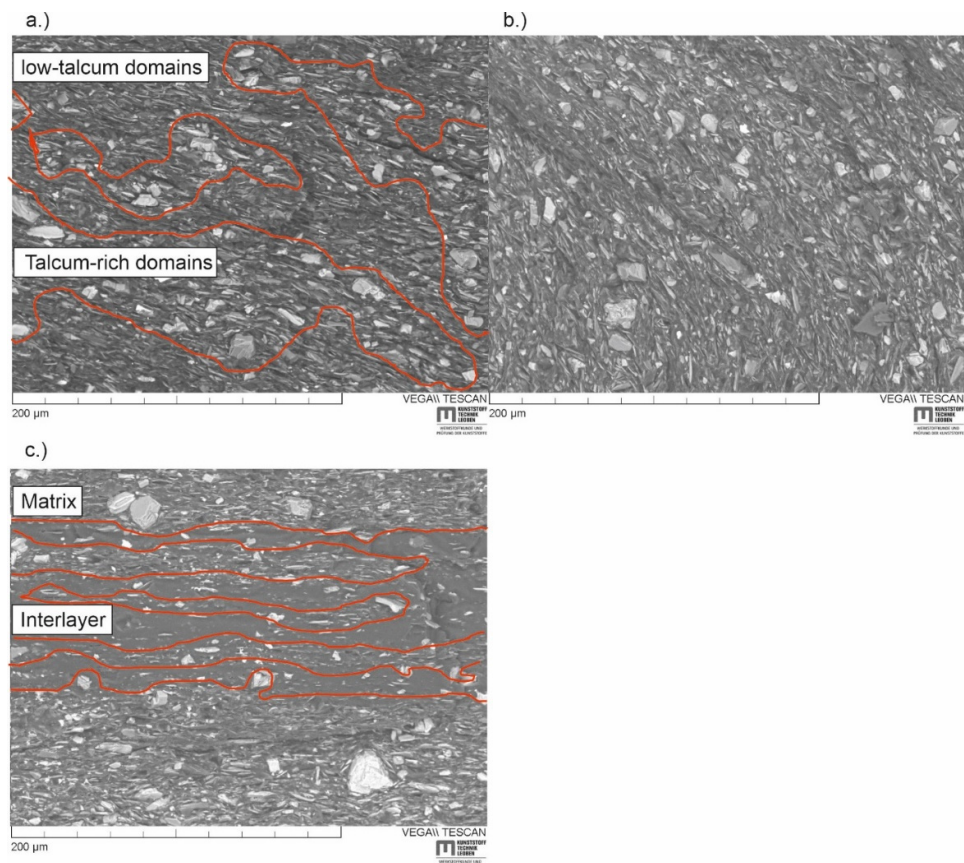

Figure 6. (**a**) SEM-micrographs of a cryofractured Blend and (**b**) Blend_512_L without defined layer structure and (**c**) a cryofractured ML_512L with distinct layers. Talcum-rich domains are separated from low-talcum domains by red lines.

While continuous bands of soft material lead to damage tolerance, they can also alter the stress distribution and failure mechanism of a material. To illustrate this, the matrix ligaments in a multilayer composite are simplified as bending specimens, which is an accurate description, e.g., during a Charpy experiment. If the Young's Modulus of the IL material is very low compared to that of the matrix, the load bearing matrix ligaments

cannot transfer stresses to one another. The stresses of individual ligaments are decoupled, while the deflection remains the same for all layers [38]. Figure 7 depicts such a case, where all individual ligaments behave like separate bending specimens and possess a neutral axis of their own. When adding an increasing number of ILs, the load is distributed more evenly between the various matrix layers and stress maxima are less pronounced. It is more difficult to reach the necessary stresses to break the matrix ligaments. However, a side effect is a strongly reduced bending stiffness. Although a ligament might seem far away from the neutral axis of the entire specimen, no contribution according to the parallel axes theorem (also known as Steiner theorem) is made towards the area moment of inertia. Since the area moment of inertia is strongly dependent on the thickness of the individual layers, h_{eff}/n, a multilayer composite will have less bending stiffness than a comparable bulk material the higher the number of layers, n, is. Thus, a material with a microstructure of alternating soft and stiff layers will be tougher but more compliant compared to a blend of similar material composition.
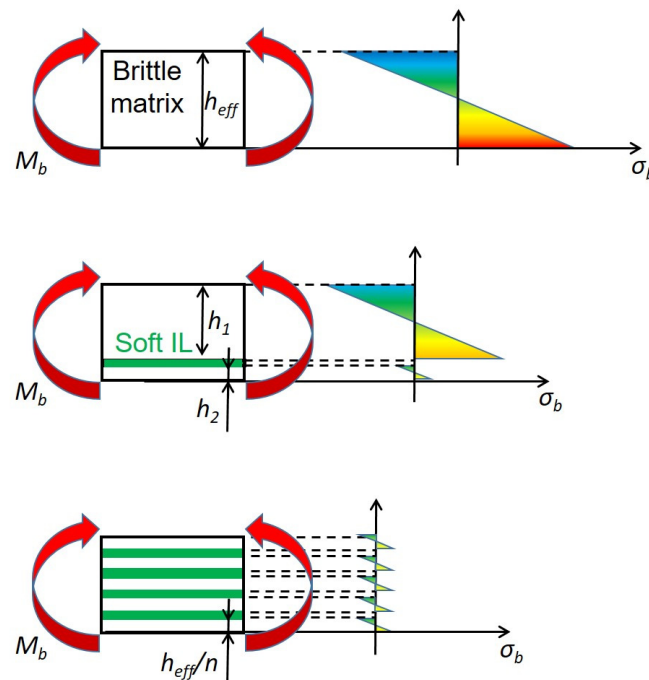

Figure 7. Decoupling of bending stresses due to soft and compliant interlayers in a stiff and brittle matrix. Stress maxima and area moment of inertia decrease as an increasing number of layers are added.

This effect is scarcely described in the literature. To the authors' knowledge, only increased stiffness has been reported for multilayered materials [7,8], owing to increased particle orientation. In this special case, the benefits of orientation are unfortunately outweighed by the described decoupling effect. Nevertheless, the high mismatch in material properties that causes the stress decoupling is necessary for optimizing fracture toughness. Numerous fracture mechanical publications clearly state that the optimal crack arresting properties of soft layers can only be realized when the IL component is considerably more compliant or has a significantly lower yield stress than the matrix [32,37].

3.4. Influence of Loading Direction

The previous sections show that the increase in impact strength of ML composites comes at a high cost in stiffness. This, however, is only true for a bending load, since the main reason behind it is the reduction in the area moment of inertia. Additionally, the pulling through led to a drop-off in force in a Charpy setup (see Figure 3).

In a tensile loading situation, we expect similar benefits for fracture toughness and less of a drawback in stiffness. Due to the lack of well-established single edge notch tension standards for polymers, tensile tests were only performed in the unnotched state according to DIN EN ISO 527. True stress–strain curves of all investigated materials as well as a comparison of stiffness and toughness and an overview of material parameters are shown in Figure 8. The exact values as well as the relative values with PP-HR as reference material are presented in Table A2 in Appendix C.
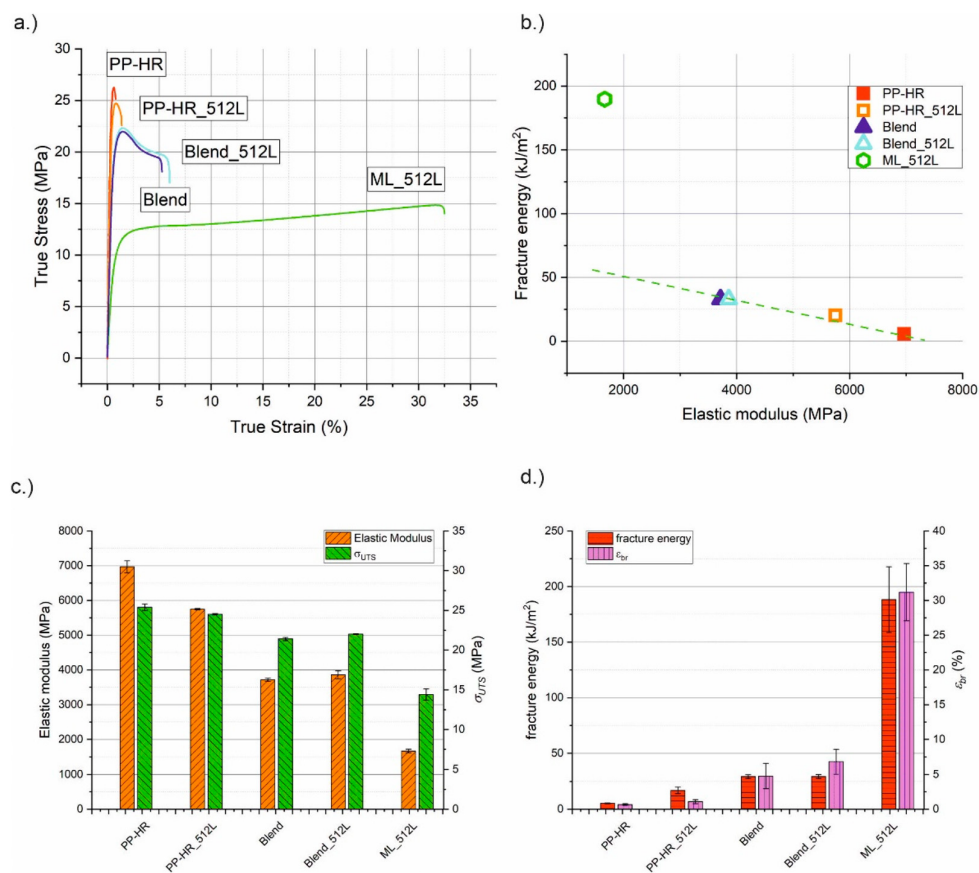

Figure 8. (**a**) Representative true stress–strain curves of all investigated materials in tensile tests and (**b**) an overview of the observed material parameters, where (**c**) the elastic modulus and ultimate tensile strength and (**d**) the fracture energy and strain at break are depicted in more detail.

The absolute values of the modulus in the tensile tests were much lower than those evaluated from the Charpy experiments. This is most likely caused by the considerably lower testing speed of the tensile tests. As mentioned earlier, the parameter E_b was primarily used as a ranking parameter and is not recommended for quantitative comparisons to measurements with different experimental conditions. PP-HR shows the highest values for E and σ_{UTS} but also the lowest ε_{br} and the lowest fracture energy. These material parameters serve as reference points to compare the other materials. The microlayering process had a beneficial influence on the ductility of PP-HR_512L. Due to an increase in ε_{br} of 60%, the fracture energy increased by 3.5 times compared to PP-HR. This, however, came at the

cost of stiffness, leading to an almost 20% decrease in *E*. For the blends, the introduction of the soft phase reduced *E* to approximately 55% of the reference material, and σ_{UTS} was also reduced by up to 15%. Owing to a considerable increase in ε_{br}, the fracture energy increased to almost six times the value of PP-HR. Blend_512L appears to be slightly stiffer, stronger and more ductile than the Blend. However, the differences between the two lies within standards deviations. All in all, the micro layering process showed a negligible influence on the tensile properties of the blends. Incorporating the soft phase in the form of continuous IL brought further benefits to material ductility, namely, ε_{br} could be increased from less than 1% (PP-HR) to over 30% (ML_512L). The fracture energy surpassed the matrix material by more than 30 times. Despite an identical material composition, the blends were outperformed by a factor of 5, thus reinforcing that the microstructure of the incorporated soft phase is essential.

The reduction in stiffness was not as severe as in the bending setup, so that approximately one quarter of *E* could be retained. In a tension setup, specimen stiffness is only influenced by the total cross-sectional area of the matrix ligaments, which is undiminished by the layered microstructure. Since the more ductile plane stress state is favoured in the thin matrix layers due to the aforementioned stress decoupling, stiffness is still lower than for the blends. The tensile specimens also cannot slide out of the clamping fixture during the experiment. As a result, an actual fracture of the entire specimen is guaranteed, and the full extent of necessary fracture energy can be measured. In addition, a strain hardening could be observed after the yield point in the tensile experiments. Thus, almost 60% of σ_{UTS} of PP-HR could be preserved. A comparison of fracture energy versus *E* in Figure 8b reveals that ML_512L lies above the trendline of homogeneous materials and blends again. Figure 8c shows, that *E* and σ_{UTS} could be kept relatively high for ML_512L, while ε_{br} and the fracture energy excel in comparison to the other materials (see Figure 8d). In conclusion, the toughening effects of the soft IL can be utilized most effectively in a tensile loading situation. While the fracture energy is maximized, the drawbacks for σ_{UTS} and especially *E* can be kept to a minimum.

4. Conclusions

Talcum particle-reinforced polypropylene was investigated through Charpy impact tests and tensile tests. A soft phase of very compliant polypropylene was incorporated in the form of blending as well as continuous soft interlayers (IL).

The materials were assessed regarding stiffness, maximum force and area under the force–displacement curves that were obtained in instrumented Charpy experiments. The influence of notch type (unnotched, Charpy-notch and razor blade notch) and number of layers on impact strength were investigated.

A plateau in impact strength could be reached when the matrix layer thickness was as small or smaller than the size of the largest reinforcing particles, which was 13.6 µm in the investigated talcum particles. The impact strength in the plateau region increased up to 4.5 times compared to specimens with larger matrix layer thicknesses.

Continuous layers led to a high damage tolerance. While multilayered specimens retained over 50% of their original impact strength, blends and homogeneous materials suffered reductions of 80% or more. Thus, introducing the soft phase in the form of continuous layers proved to be a considerably more effective toughening mechanism than the blending of matrix and IL material in a comparable ratio.

The increase in toughness comes at the cost of bending stiffness and maximum force due to a loss in moment of inertia, which is proportional to the number of layers. This is a side effect of stress decoupling between individual matrix layers, since the IL material is too compliant to transfer stresses.

Similar benefits to fracture energy could be found in tensile tests of the multilayer material, but the decrease in strength and stiffness could be partially avoided due to the tensile loading. More specifically, 24% of matrix stiffness could be preserved under tensile loading compared to only 11% in a bending setup.

Author Contributions: Conceptualization, J.W. and F.A.; methodology, J.W., H.K., O.K. and F.A.; validation, J.W., H.K., O.K. and F.A.; formal analysis, J.W., F.A.; investigation, J.W., H.K., O.K. and F.A.; resources, F.A. and O.K.; data curation, J.W. and H.K.; writing—original draft preparation, J.W. and F.A.; writing—review and editing, J.W., H.K., O.K. and F.A.; visualization, J.W. and F.A.; supervision, F.A. and O.K.; project administration, F.A. and O.K.; funding acquisition, F.A. All authors have read and agreed to the published version of the manuscript.

Institutional Review Board Statement: Not applicable.

Informed Consent Statement: Not applicable.

Data Availability Statement: The data presented in this study are available on request from the corresponding author. The data are not publicly available due to ongoing research.

Conflicts of Interest: The authors declare no conflict of interest. The funders had no role in the design of the study; in the collection, analyses, or interpretation of data; in the writing of the manuscript, or in the decision to publish the results.

Appendix A

The following is a detailed description of the tested materials and the methods used for investigation.

Appendix A.1. Materials

An overview of all investigated materials is summarized in Table 1. Therein, the material composition, a brief description as well as a schematic drawing of the microstructure are given. All material combinations consist of only two material bases. The matrix material in all investigated combinations consists of a stiff extrusion grade polypropylene, which is highly reinforced with talcum particles (PP-HR, 60 wt% talcum particles). The second material in this study is a compliant type of PP with a very low yield stress, which was used as a toughness enhancing component (termed IL for interlayer) to offer an extreme contrast between the hard and the soft phase. From these two base materials, four more material composites were generated by varying the material composition and processing technique. In a first step, layered composites with different numbers of layers, ranging from 64 to 2048, were prepared. These composites are oriented due to the multilayer extrusion process and exhibit a defined microstructure of alternating layers. All layered materials had the same amount of matrix material and soft interlayer (87% PP-HR to 13% IL). These co-extruded materials were used for a first analysis of the influence of different numbers of layers. Subsequently, a more thorough analysis of the composite with 512 layers was performed. Therefore, this configuration is specifically titled ML_512L. A blend with the same material composition was manufactured to differentiate between the effect of the soft component alone and the effects of orientation and microstructure. This material was simply labelled as Blend. It does not show the high degree of orientation found in a multilayer material, and the microstructure is a random distribution of soft phase within the matrix. The Blend and the homogeneous matrix material were produced also in 512 identical layers (PP-HR_512L, Blend_512L) to observe possible effects of particle orientation due to the microlayering process. All materials were supplied in the form of extruded sheets with a thickness of 4 mm.

Appendix A.2. Preparation of Materials via Multilayer Co-Extrusion

Multilayer materials were manufactured using two Extrunet ECE-30 extruders and a multiflux static mixer with a modular design. Melt strands of the matrix and IL material are joined in a feedblock after passing the extruders. After passing the feedblock, one module of the static mixer divides the two layers of melt vertically, before placing the halves on top of each other horizontally (see Figure A1). Thus, each additional module doubles the number of layers, so the final number of layers is 2^{n+1}, with n being the number of modules. This processing routine has proven to provide neatly stacked polypropylene multilayer materials with uninterrupted continuous layers [12,13].
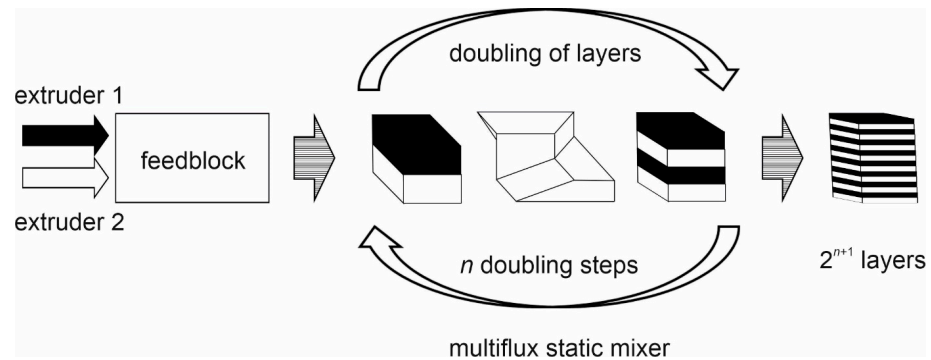

Figure A1. Multilayer extrusion using a multiflux static mixer, adapted from [53].

Appendix A.3. Specimen Preparation

As mentioned above, materials were supplied as 4 mm thick plates. From these, Charpy specimens according to DIN EN ISO 179-1 were manufactured with dimensions of $80 \times 10 \times 4$ mm^3. For every material, unnotched, Charpy-notched and razor blade notched specimens were prepared. As shown in Figure 1, all notches were introduced flatwise, so the effect of a layered plate could be observed. A saw blade with a crack tip radius of 0.25 mm was used to introduce the Charpy-notches. A broaching tool was used to introduce the razor blade notches [55–57]. All notches were prepared to have an overall depth of 0.3 mm, and all specimens were manufactured parallel to extrusion direction. Additionally, tensile test specimens (Type 1A) were prepared in order to be tested according to DIN EN ISO 527.

Appendix A.4. Charpy Measurements

All experiments were performed using a Zwick/Roell HIT25P pendulum. Tests were performed according to DIN EN ISO 179-1fA for notched and DIN EN ISO 179-1fU for unnotched specimens. For each material, 5 individual specimens were tested using a 2J pendulum. In all cases, a flatwise specimen orientation was used, so failure had to progress through all individual layers.

Appendix A.5. Instrumented Charpy Experiments

All experiments were performed using a Zwick/Roell HIT25P with an instrumented 2J pendulum. The pendulum was equipped with a piezo-electric load cell within the fin, and measurements were taken with a sampling rate of 2 MHz. For each measurement series, a total of six specimens were measured with the exception of the multilayered composites. In these cases, only two specimens could be measured due to limited material supply. The specimen orientation was also flatwise in all cases.

Appendix A.6. Data Treatment

Due to high oscillation during the instrumented impact tests, the maximum force, F_{max}, and initial slope could not be reliably determined from the raw data (see Figure A2). Therefore, a total of 10 support points was set manually for each curve. The support points were then used to create a fit of cubic splines, which was later used to determine the maximum force and initial slope.
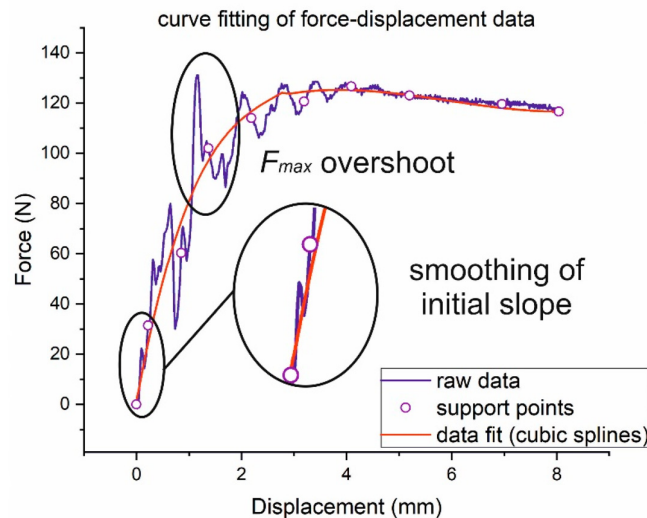

Figure A2. Curve fitting of force–displacement data from instrumented Charpy experiments. Cubic splines were fitted through 10 support points.

Appendix A.7. Normalization of Parameters

From the specimen width, b, and the effective thickness, h_{eff}, an effective cross-sectional area A_{eff} was calculated for all specimens (see Equation (A1)). For unnotched specimens, h_{eff} is equal to the total plate thickness h. For notched specimens, the remaining ligament length at the root of the notch was taken as h_{eff}. The area U was obtained through integration of the force–displacement curve. For this integration, the raw data and not the fits were used. Corrections for elastic unloading were forgone, since the initial slope could not be reliably determined for all specimens. This was mostly the case for the more brittle matrix materials under the influence of a notch, where standard deviations were large even after the curve fitting. The impact strength, a_c, was evaluated for unnotched, Charpy-notched and razor blade notched specimens (Equation (A2)). The maximum force and initial slope were determined from the fitted curves. The slope was calculated from the differences in force, ΔF, and displacement, Δv, in the initial, linear part of the curve. To be exact, the slope was calculated between 0.085 and 0.427 mm deflection, which translates to 0.05% and 0.25% maximum strain. From the initial slope in the unnotched state the bending modulus, E_b was calculated according to Equation (A3) to compare the stiffness of the materials. The calculation is in agreement with DIN EN ISO 178, although the testing speed in this case is much higher than in conventional three-point-bending tests. E_b should, therefore, be seen as a ranking parameter in these specific considerations and cannot be quantitatively compared to values obtained from quasi-static experiments. In order to remove the influence of specimen geometry, the maximum force, F_{max}, was divided by A_{eff} of each individual specimen. The formula for the normalised maximum Force, F_{max}^{norm}, is shown in Equation (A4).

$$A_{eff} = bh_{eff} \tag{A1}$$

$$a_c = \frac{U}{A_{eff}} \tag{A2}$$

$$E_b = \frac{\Delta F}{\Delta v} \frac{L^3}{4bh_{eff}^3} \tag{A3}$$

$$F_{max}^{norm} = \frac{F_{max}}{A_{eff}} \tag{A4}$$

Appendix A.8. Tensile Tests

All tensile tests were performed according to DIN EN ISO 527 using a Zwick Z250 electrodynamic tensile testing machine, equipped with a 10 kN loadcell. In addition to the Young's modulus, E, the ultimate tensile strength, σ_{UTS}, and the elongation at break, ε_{br}, were measured. In the considerations regarding tensile properties, the area under the force–displacement curve was corrected for elastic unloading (see Figure A3) and taken as fracture energy, which acted as measure for toughness.
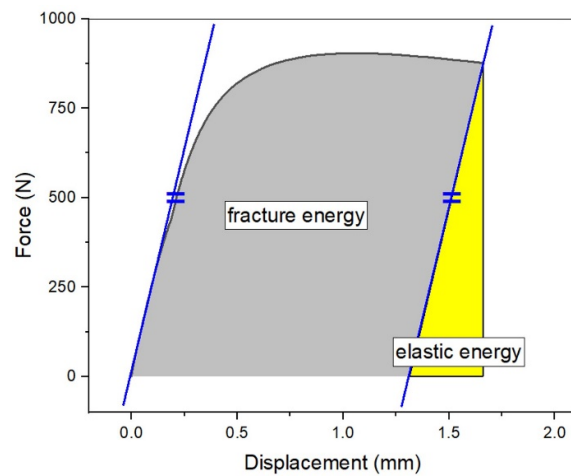

Figure A3. Correction for elastic unloading of the area under the force–displacement curve of tensile tests.

Appendix A.9. SEM-Micrographs

To investigate the microstructure of the samples, scanning electron microscopy was applied. All samples were sputtered with a thin layer of gold to achieve surface conductivity. SEM-graphs were then created using a TESCAN Vega II, whereas the fractographs were generated from the backscatter electron to give an improved contrast between talcum particles and polymer matrix.

Appendix B

Table A1. Results obtained from instrumented Charpy experiments including E_b, F_{max}^{norm} and a_c.

Material	E_b (MPa)	Notch Type	F_{max}^{norm} (N/mm^2)	a_c (kJ/m^2)
PP-HR	17,475 $\pm$ 4056	NoNotch	3.07 $\pm$ 0.66	2.66 $\pm$ 0.40
		Charpy	2.36 $\pm$ 0.48	0.46 $\pm$ 0.30
		Razor	1.42 $\pm$ 0.68	0.25 $\pm$ 0.14
PP-HR_512L	14,141 $\pm$ 794	NoNotch	3.08 $\pm$ 0.31	3.86 $\pm$ 0.35
		Charpy	2.39 $\pm$ 0.15	0.78 $\pm$ 0.11
		Razor	2.33 $\pm$ 0.16	0.82 $\pm$ 0.06

Table A1. *Cont.*

Material	E_b (MPa)	Notch Type	F_{max}^{norm} (N/mm^2)	a_c (kJ/m^2)
Blend	9635 ± 894	NoNotch	2.64 ± 0.06	7.14 ± 0.53
		Charpy	2.59 ± 0.24	2.21 ± 0.45
		Razor	2.33 ± 0.34	1.52 ± 0.12
Blend_512L	9258 ± 1268	NoNotch	2.67 ± 0.13	9.39 ± 1.63
		Charpy	2.35 ± 0.26	2.51 ± 0.34
		Razor	2.55 ± 0.19	1.58 ± 0.13
ML_512L	1903 ± 457	NoNotch	0.88 ± 0.04	30.99 ± 0.80
		Charpy	0.71 ± 0.05	16.95 ± 0.26
		Razor	0.79 ± 0.02	15.53 ± 0.62

Appendix C

Table A2. Material parameters obtained from tensile tests.

|	E (MPa)	ε_{br} (MPa)	σ_{UTS} (MPa)	Fracture Energy Per Area (kJ/m^2)
	Absolute Values:			
PP-HR	6967 ± 173	0.67 ± 0.11	25.4 ± 0.4	5.3 ± 0.3
PP-HR_512L	5748 ± 23	1.08 ± 0.30	24.5 ± 0.1	16.9 ± 2.9
Blend	3714 ± 45	4.75 ± 1.79	21.4 ± 0.2	29.4 ± 1.6
Blend_512L	3862 ± 111	6.81 ± 1.76	22.0 ± 0.04	29.4 ± 1.7
ML_512L	1666 ± 50	31.19 ± 4.13	14.4 ± 0.7	188.2 ± 29.6
	Relative values (PP-HR as reference):			
PP-HR	1	1	1	1
PP-HR_512L	0.83	1.61	0.96	3.54
Blend	0.53	7.09	0.84	5.79
Blend_512L	0.55	10.16	0.87	5.79
ML_512L	0.24	46.55	0.57	33.28

References

1. Kausch, H.H.; Béguelin, P.; Fischer, M. Failure of particulate reinforced polymers. *Mech. Compos. Mater.* **2000**, *36*, 177–184. [CrossRef]
2. Chan, J.X.; Wong, J.F.; Hassan, A.; Mohamad, Z.; Othman, N. Mechanical properties of wollastonite reinforced thermoplastic composites: A review. *Polym. Compos.* **2020**, *41*, 395–429. [CrossRef]
3. Zhang, Z.; Yang, J.-L.; Friedrich, K. Creep resistant polymeric nanocomposites. *Polymer* **2004**, *45*, 3481–3485. [CrossRef]
4. Raghavan, J.; Meshii, M. Creep of polymer composites. *Compos. Sci. Technol.* **1998**, *57*, 1673–1688. [CrossRef]
5. Ehrenstein, G.W. *Polymer-Werkstoffe: Struktur-Eigenschaften-Anwendung*, 3rd ed.; Carl Hanser Verlag: München, Germany, 2011.
6. Domininghaus, H.; Elsner, P.; Eyerer, P.; Hirth, T. (Eds.) *Kunststoffe: Eigenschaften und Anwendungen*; Springer: Heidelberg, Germany, 2012.
7. Baer, E.; Hiltner, A.; Jarus, D. Relationship of hierarchical structure to mechanical properties. *Macromol. Symp.* **1999**, *147*, 37–61. [CrossRef]
8. Mueller, C.D.; Nazarenko, S.; Ebeling, T.; Schuman, T.L.; Hiltner, A.; Baer, E. Novel structures by microlayer coextrusion–talc-filled PP, PC/SAN, and HDPE/LLDPE. *Polym. Eng. Sci.* **1997**, *37*, 355–362. [CrossRef]
9. Paul, D.R.; Barlow, J.W. Polymer Blends. *J. Macromol. Sci. Part C* **1980**, *18*, 109–168. [CrossRef]
10. Hara, M.; Sauer, J.A. Synergism in Mechanical Properties of Polymer/Polymer Blends. *J. Macromol. Sci. Part C* **1998**, *38*, 327–362. [CrossRef]
11. Barlow, J.W.; Paul, D.R. Polymer blends and alloys—A review of selected considerations. *Polym. Eng. Sci.* **1981**, *21*, 985–996. [CrossRef]
12. Köpplmayr, T.; Miethlinger, J. Modeling viscoelastic flow in a multiflux static mixer. In *AIP Conference Proceedings*; American Institute of Physics: College Park, MD, USA, 2014; pp. 556–559.
13. Köpplmayr, T.; Mayrhofer, E.; Unterweger, C. Thermo-mechanical properties of β-nucleated polypropylene multilayers. *Polym. Test.* **2014**, *39*, 79–85. [CrossRef]
14. Libonati, F.; Buehler, M.J. Advanced Structural Materials by Bioinspiration. *Adv. Eng. Mater.* **2017**, *19*, 1600787. [CrossRef]

15. Müller, W.E.G.; Wang, X.; Kropf, K.; Ushijima, H.; Geurtsen, W.; Eckert, C.; Tahir, M.N.; Tremel, W.; Boreiko, A.; Schlossmacher, U.; et al. Bioorganic/inorganic hybrid composition of sponge spicules: Matrix of the giant spicules and of the comitalia of the deep sea hexactinellid Monorhaphis. *J. Struct. Biol.* **2008**, *161*, 188–203. [CrossRef] [PubMed]
16. Fratzl, P.; Gupta, H.S.; Fischer, F.D.; Kolednik, O. Hindered Crack Propagation in Materials with Periodically Varying Young's Modulus—Lessons from Biological Materials. *Adv. Mater.* **2007**, *19*, 2657–2661. [CrossRef]
17. Kolednik, O.; Predan, J.; Fischer, F.D.; Fratzl, P. Bioinspired Design Criteria for Damage-Resistant Materials with Periodically Varying Microstructure. *Adv. Funct. Mater.* **2011**, *21*, 3634–3641. [CrossRef]
18. Barthelat, F.; Espinosa, H.D. An Experimental Investigation of Deformation and Fracture of Nacre—Mother of Pearl. *Exp. Mech.* **2007**, *47*, 311–324. [CrossRef]
19. Yadav, R.; Goud, R.; Dutta, A.; Wang, X.; Naebe, M.; Kandasubramanian, B. Biomimicking of Hierarchal Molluscan Shell Structure Via Layer by Layer 3D Printing. *Ind. Eng. Chem. Res.* **2018**, *57*, 10832–10840. [CrossRef]
20. Aizenberg, J.; Weaver, J.C.; Thanawala, M.S.; Sundar, V.C.; Morse, D.E.; Fratzl, P. Skeleton of Euplectella sp.: Structural Hierarchy from the Nanoscale to the Macroscale. *Science* **2005**, *309*, 275–278. [CrossRef]
21. Levi, C.; Barton, J.L.; Guillemet, C.; Le Bras, E.; Lehuede, P. A remarkably strong natural glassy rod: The anchoring spicule of the Monorhaphis sponge. *J. Mater. Sci. Lett.* **1989**, *8*, 337–339. [CrossRef]
22. Miserez, A.; Weaver, J.C.; Thurner, P.J.; Aizenberg, J.; Dauphin, Y.; Fratzl, P.; Morse, D.E.; Zok, F.W. Effects of Laminate Architecture on Fracture Resistance of Sponge Biosilica: Lessons from Nature. *Adv. Funct. Mater.* **2008**, *18*, 1241–1248. [CrossRef]
23. Müller, W.E.G.; Wang, X.; Cui, F.-Z.; Jochum, K.P.; Tremel, W.; Bill, J.; Schröder, H.C.; Natalio, F.; Schlossmacher, U.; Wiens, M. Sponge spicules as blueprints for the biofabrication of inorganic—organic composites and biomaterials. *Appl. Microbiol. Biotechnol.* **2009**, *83*, 397–413. [CrossRef] [PubMed]
24. Woesz, A.; Weaver, J.C.; Kazanci, M.; Dauphin, Y.; Aizenberg, J.; Morse, D.E.; Fratzl, P. Micromechanical properties of biological silica in skeletons of deep-sea sponges. *J. Mater. Res.* **2006**, *21*, 2068–2078. [CrossRef]
25. Libonati, F.; Gu, G.X.; Qin, Z.; Vergani, L.; Buehler, M.J. Bone-Inspired Materials by Design: Toughness Amplification Observed Using 3D Printing and Testing. *Adv. Eng. Mater.* **2016**, *18*, 1354–1363. [CrossRef]
26. Morgan, E.F.; Barnes, G.L.; Einhorn, T. The Bone Organ System. In *Osteoporosis*, 4th ed.; Elsevier: Amsterdam, The Netherlands, 2013; pp. 3–20. [CrossRef]
27. Gu, G.X.; Takaffoli, M.; Buehler, M.J. Hierarchically Enhanced Impact Resistance of Bioinspired Composites. *Adv. Mater.* **2017**, *29*, 1700060. [CrossRef] [PubMed]
28. Jia, Z.; Wang, L. 3D printing of biomimetic composites with improved fracture toughness. *Acta Mater.* **2019**, *173*, 61–73. [CrossRef]
29. Jia, Z.; Yu, Y.; Hou, S.; Wang, L. Biomimetic architected materials with improved dynamic performance. *J. Mech. Phys. Solids* **2019**, *125*, 178–197. [CrossRef]
30. Jia, Z.; Yu, Y.; Wang, L. Learning from nature: Use material architecture to break the performance tradeoffs. *Mater. Des.* **2019**, *168*, 107650. [CrossRef]
31. Zhao, H.; Yang, Z.; Guo, L. Nacre-inspired composites with different macroscopic dimensions: Strategies for improved mechanical performance and applications. *NPG Asia Mater.* **2018**, *10*, 1–22. [CrossRef]
32. Kolednik, O.; Kasberger, R.; Sistaninia, M.; Predan, J.; Kegl, M. Development of Damage-Tolerant and Fracture-Resistant Materials by Utilizing the Material Inhomogeneity Effect. *J. Appl. Mech.* **2019**, *86*, 1–32. [CrossRef]
33. Song, J.; Fan, C.; Ma, H.; Liang, L.; Wei, Y. Crack deflection occurs by constrained microcracking in nacre. *Acta Mech. Sin.* **2018**, *34*, 143–150. [CrossRef]
34. Dutta, A.; Tekalur, S.A. Crack tortuosity in the nacreous layer-Topological dependence and biomimetic design guideline. *Int. J. Solids Struct.* **2014**, *51*, 325–335. [CrossRef]
35. Dutta, A.; Tekalur, S.A.; Miklavcic, M. Optimal overlap length in staggered architecture composites under dynamic loading conditions. *J. Mech. Phys. Solids* **2013**, *61*, 145–160. [CrossRef]
36. Kolednik, O. The yield stress gradient effect in inhomogeneous materials. *Int. J. Solids Struct.* **2000**, *37*, 781–808. [CrossRef]
37. Sistaninia, M.; Kolednik, O. Effect of a single soft interlayer on the crack driving force. *Eng. Fract. Mech.* **2014**, *130*, 21–41. [CrossRef]
38. Wiener, J.; Arbeiter, F.J.; Tiwari, A.; Kolednik, O.; Pinter, G. Bioinspired toughness improvement through soft interlayers in mineral reinforced polypropylene. *Mech. Mater.* **2020**, *140*, 103243. [CrossRef]
39. Tiwari, A.; Wiener, J.; Arbeiter, F.; Pinter, G.; Kolednik, O. Application of the material inhomogeneity effect for the improvement of fracture toughness of a brittle polymer. *Eng. Fract. Mech.* **2020**, *224*, 106776. [CrossRef]
40. Arbeiter, F.J.; Petersmann, S.; Wiener, J.; Oesterreicher, F.; Spoerk, M.; Pinter, G. Using Compliant Interlayers as Crack Arresters in 3-D-Printed Polymeric Structures. *Mater. Perform. Charact.* **2020**, *9*, 20190201. [CrossRef]
41. Mueller, C.; Topolkaraev, V.; Soerens, D.; Hiltner, A.; Baer, E. Breathable polymer films produced by the microlayer coextrusion process. *J. Appl. Polym. Sci.* **2000**, *78*, 816–828. [CrossRef]
42. Jarus, D.; Hiltner, A.; Baer, E. Barrier properties of polypropylene/polyamide blends produced by microlayer coextrusion. *Polymer* **2002**, *43*, 2401–2408. [CrossRef]
43. Giannelis, E.P. Polymer Layered Silicate Nanocomposites. *Adv. Mater.* **1996**, *8*, 29–35. [CrossRef]

44. Gilman, J.W.; Jackson, C.L.; Morgan, A.B.; Harris, R.; Manias, E.; Giannelis, E.P.; Wuthenow, M.; Hilton, D.; Phillips, S.H. Flammability Properties of Polymer−Layered-Silicate Nanocomposites. Polypropylene and Polystyrene Nanocomposites†. *Chem. Mater.* **2000**, *12*, 1866–1873. [CrossRef]

45. Pan, S.J.; Im, J.; Hill, M.J.; Keller, A.; Hiltner, A.; Baer, E. Structure of ultrathin polyethylene layers in multilayer films. *J. Polym. Sci. Part B Polym. Phys.* **1990**, *28*, 1105–1119. [CrossRef]

46. Jin, Y.; Rogunova, M.; Hiltner, A.; Baer, E.; Nowacki, R.; Galeski, A.; Piorkowska, E. Structure of polypropylene crystallized in confined nanolayers. *J. Polym. Sci. Part B Polym. Phys.* **2004**, *42*, 3380–3396. [CrossRef]

47. Qiu, F.; Wang, M.; Hao, Y.; Guo, S. The effect of talc orientation and transcrystallization on mechanical properties and thermal stability of the polypropylene/talc composites. *Compos. Part A Appl. Sci. Manuf.* **2014**, *58*, 7–15. [CrossRef]

48. Langhe, D.S.; Hiltner, A.; Baer, E. Melt crystallization of syndiotactic polypropylene in nanolayer confinement impacting structure. *Polymer* **2011**, *52*, 5879–5889. [CrossRef]

49. Nazarenko, S.; Hiltner, A.; Baer, E. Polymer microlayer structures with anisotropic conductivity. *J. Mater. Sci.* **1999**, *34*, 1461–1470. [CrossRef]

50. Nazarenko, S.; Dennison, M.T.; Schuman, E.V.; Stepanov, A.; Hiltner, E. Baer, Creating layers of concentrated inorganic particles by interdiffusion of polyethylenes in microlayers. *J. Appl. Polym. Sci.* **1999**, *73*, 2877–2885. [CrossRef]

51. Ashby, M.; Cebon, D. Materials selection in mechanical design. *J. Phys. IV France* **1993**, *03*, C7-1–C7-9. [CrossRef]

52. Ritchie, R. The conflicts between strength and toughness. *Nat. Mater.* **2011**, *10*, 817–822. [CrossRef]

53. Koepplmayr, T. Computational and Experimental Modelling of Microlayer Forming Processes. Ph.D. Thesis, Johannes Kepler University, Linz, Austria, 2014.

54. German Institute for Standardization. *Plastics-Determination of Charpy Impact Properties-Part 1: Non-Instrumented Impact Test (German Version ISO 179-1:2010)*; DIN EN ISO 179-1; DIN: Dublin, Germany, 2010.

55. Martínez, A.; León, N.; Arencón, D.; Salazar, A.; Rodríguez, J. On the effect of the different notching techniques on the fracture toughness of PETG. *Polym. Test.* **2013**, *32*, 1244–1252. [CrossRef]

56. Martinez, A.B.; Salazar, A.; León, N.; Illescas, S.; Rodríguez, J. Influence of the notch-sharpening technique on styrene-acrylonitrile fracture behavior. *J. Appl. Polym. Sci.* **2016**, *133*, 11. [CrossRef]

57. Salazar, A.; Rodríguez, J.; Arbeiter, F.; Pinter, G.; Martínez, A. Fracture toughness of high density polyethylene: Fatigue pre-cracking versus femtolaser, razor sharpening and broaching. *Eng. Fract. Mech.* **2015**, *149*, 199–213. [CrossRef]

58. German Institute for Standardization. *Plastics-Determination of Tensile Properties-Part 1: General Principles (German Version ISO 527-1:2012)*; DIN EN ISO 527; DIN: Dublin, Germany, 2012.

59. German Institute for Standardization. *Plastics-Determination of Flexural Properties (German Version ISO 178:2019)*; DIN EN ISO 178; DIN: Dublin, Germany, 2019.

7.2. *Publication II*

Title:	Bioinspired toughness improvement through soft interlayers in mineral reinforced polypropylene
Authors:	Johannes Wiener[a], Florian Arbeiter[a], Abhishek Tiwari[b,c], Otmar Kolednik[b], Gerald Pinter[a]
Affiliation:	[a] Materials Science and Testing of Polymers, Montanuniversitaet Leoben, 8700 Leoben, Austria [b] Erich-Schmid-Institute of Materials Science, Austrian Academy of Science, 8700 Leoben, Austria [c] Materials Center Leoben GmbH, 8700 Leoben, Austria
DOI:	https://doi.org/10.1016/j.mechmat.2019.103243
Conceptualization:	Johannes Wiener (60%), Florian Arbeiter (40%)
Methodology:	Johannes Wiener (60%), Florian Arbeiter (20%), Otmar Kolednik (20%)
Validation:	equal contribution by all authors
Investigation:	Johannes Wiener (80%), Florian Arbeiter (20%)
Writing- Original Draft:	Johannes Wiener (80%), Florian Arbeiter (20%)
Writing- Review & Editing	equal contribution by all authors
Supervision	Florian Arbeiter (50%) , Gerald Pinter (20%), Otmar Kolednik (30%)
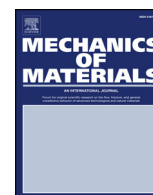
Bioinspired toughness improvement through soft interlayers in mineral reinforced polypropylene

Johannes Wiener[a], Florian Arbeiter[a,*], Abhishek Tiwari[b,c], Otmar Kolednik[b], Gerald Pinter[a]

[a] *Materials Science and Testing of Polymers, Montanuniversitaet Leoben, 8700 Leoben, Austria*
[b] *Erich-Schmid-Institute of Materials Science, Austrian Academy of Science, 8700 Leoben, Austria*
[c] *Materials Center Leoben GmbH, 8700 Leoben, Austria*

A B S T R A C T

The effects of soft, polymeric interlayers on a brittle, mineral reinforced polymer matrix are investigated. Interlayers made of a standard polypropylene (PP) and a soft type of PP are introduced into matrix materials of either highly or moderately mineral particle reinforced PP. Single edge notch bending experiments are performed to characterize the fracture toughness of these composites. The experimental *J*-integral J_{exp} is used to describe the fracture toughness of the investigated materials. The multi-layered materials are compared to the homogeneous matrix material. A modified plotting technique is applied to more distinctly demonstrate the effects of soft layers on J_{exp} as a function of the crack extension Δa. The fracture toughness is evaluated and the slope of the J-Δa curves is used as a qualitative measure of crack growth resistance. In addition, the crack growth rate is recorded. The results show improvements in fracture toughness of almost twenty times of the matrix material, provided the material combination is chosen properly. This increase in fracture toughness is achieved due to a crack-arresting effect in the soft layers, which is followed by an energy-expensive crack re-initiation step.

1. Introduction

A multitude of technical applications strive for a high stiffness and/or high strength to support large loads. Furthermore, a high toughness can be equally important in order to prevent catastrophic failure of vital structures. Unfortunately, these characteristics are often mutually exclusive in engineering materials (Ashby and Cebon 1993; Ritchie 2011). Usually the most reasonable compromise between stiffness and toughness has to be selected as the material of choice. However, for biological materials, the same restrictions do not seem to apply (Jia et al., 2019). The majority of biological materials with load bearing functionality exhibit an astonishingly high fracture toughness, especially when considering their seemingly brittle composition. Close examination of biomaterials reveals that they do not show a homogeneous microstructure but rather complex and elegant hierarchical structures. Additionally, many of these structures also feature secondary functionalities besides the load bearing component. For example, bone tissue is not only designed to support weight and movement related forces of the body. It serves as reservoir for nutrients and minerals while also producing vital components of blood (Morgan et al., 2013).

Two examples of structured bio-materials with a high content of

brittle matrix are nacre, which mainly consists of aragonite ($CaCO_3$) with a negligible amount of protein (Barthelat and Espinosa 2007; Song et al., 2018), as well as the skeleton of the deep sea sponge *Euplectella aspergillum* which also consists of over 99% SiO_2 (bio-glass) and only a small amount of organic material (Aizenberg et al., 2005; Miserez et al., 2008; Woesz et al., 2006; Levi et al., 1989; Müller et al., 2008).

Much research has been conducted on the subject of nacre. On a microscopic scale, the material consists of many interlocking hexagonal platelets (Figs. 1a and b). While the platelets themselves are made of aragonite, the small layers in between them consist of soft and elastic protein. The increase in toughness compared to pure aragonite can be attributed to several different mechanisms. These include platelet pullout, platelet interlocking and the obvious increase in fracture surface (Barthelat and Espinosa 2007; Zhao et al., 2018; Dutta et al., 2013). Recent studies also showed great results for parts produced by 3D-inkjet printing of polymeric resins (Jia et al., 2019; Jia and Wang 2019; Yadav et al., 2018). In all of these applications, the intricate microstructure and their complex deformation and fracture behaviors (Barthelat and Espinosa 2007; Song et al., 2018; Miserez et al., 2008; Dutta et al., 2013; Dutta and Tekalur 2014) lead to improved fracture
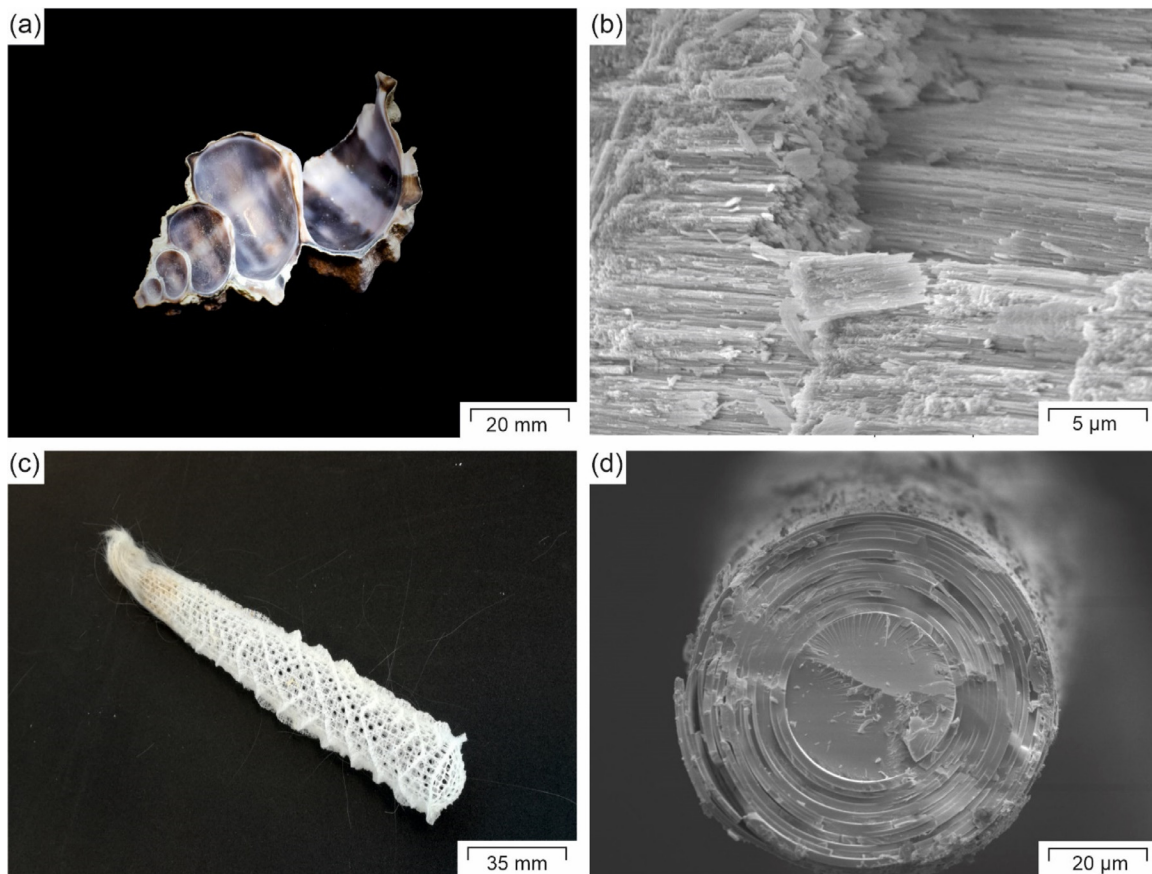

Fig. 1. Structure of biological materials: Conch Shell (a) and its platelet-like microstructure (b) and the deep-sea sponge (c) with its concentric microstructure (d).
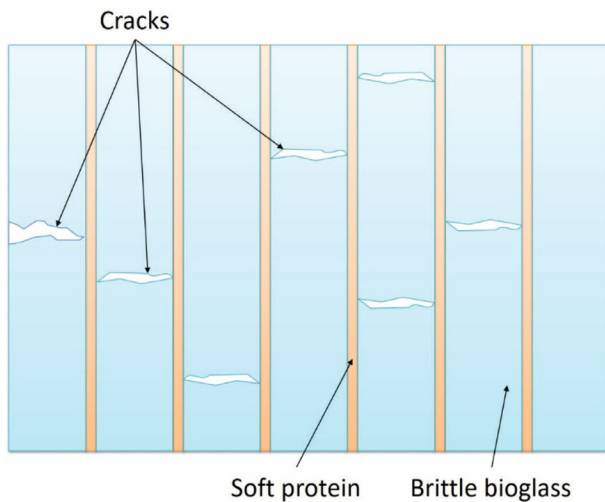

Fig. 2. Crack arrester effect in the skeleton of a deep-sea sponge due to the material inhomogeneity effect.

toughness. Literature such as Wu et al. (Wu et al., 2019) or Gu et al. (Gu et al., 2017) show, that interfacial strength and different layers of hierarchical structure also play an important role in replicating the excellent properties of natural materials. Unfortunately, the structure of nacre has limited potential for industrial applications at the moment. The complex, three-dimensional structure can thus far only be produced by 3D-inkjet printing (Jia et al., 2019; Jia and Wang 2019) or even more advanced manufacturing techniques, such as freeze casting or magnetically assisted additive manufacturing (Zhao et al., 2018; Mao et al., 2016; Yang et al., 2018). It should be noted, that the

majority of commercially available monomer formulations for 3D-inkjet printing are acrylate- or methacrylate based photoreactive resins. The resulting polymers are commonly known to be inherently brittle and potentially harmful for human contact (Gorsche et al., 2016; Ligon-Auer et al., 2016; Friedman et al., 1965; Karalekas and Aggelopoulos 2003; Nylander-French and French 1998), with only a few exceptions (Oesterreicher et al., 2017; Oesterreicher et al., 2016b; Oesterreicher et al., 2016a; Mostegel et al., 2016; Oesterreicher et al., 2016c). Conventional processing techniques for thermoplastic polymers such as injection molding and extrusion are not known to produce nacre-like structures on a large scale yet. Therefore, the industrial use of these structures seems to be limited thus far for polymers.

The skeleton of the deep sea sponge *Euplectella aspergillum* features a microstructure, composed of alternating, concentric rings of bio-glass and soft protein (Figs. 1c and d) (Aizenberg et al., 2005). In comparison to nacre (Figs. 1a and b), neither the concept of platelet pullout and interlocking nor the mechanism of crack deflection can be used to explain its high fracture toughness. The increase in toughness is achieved by the well-designed sequence of soft and hard phases (Woesz et al., 2006; Kolednik et al., 2011). Therein, the layers of soft protein serve as crack-arresters and hinder growing cracks from causing catastrophic failure (Fig. 2).

Several studies have shown that this crack arrest occurs due to the so-called material-inhomogeneity effect (Kolednik et al., 2011; Kolednik 2000; Fratzl et al., 2007). The material inhomogeneity effect describes the influence of a material inhomogeneity on the magnitude of the crack driving force. All that is needed is an interface (IF), interlayer (IL) or even gradient between two materials with different mechanical properties such as elastic modulus E, yield stress σ_y or hardening exponent n. The effect of a material inhomogeneity on the crack driving force was already well known for linear elastic fracture

mechanics (Zak and Williams 1963; Cook and Erdogan 1972; Huajian 1991; Muju 2000; Fischer et al., 2012; Murali et al., 2011; Náhlík et al., 2010). Recent studies by Kolednik et al. (Kolednik et al., 2011; Simha et al., 2005; Simha et al., 2003) present a more general approach based on the configurational force concept (Maugin 1995; Gurtin 2000) and the *J*-integral *J* (Rice 1968) as driving force parameter. Therein, the far field *J*-integral J_{far} is a measure of the driving force induced in the entire specimen by the applied load (Kolednik et al., 2019). The *J*-integral close to the crack tip gives the crack driving force J_{tip}, whose magnitude determines whether a crack is able to propagate or not. For homogeneous hyperelastic materials, the *J*-integral is path-independent, which also means $J_{tip} = J_{far}$. When considering inhomogeneous materials, such as a bimaterial specimen with a single interface, the *J*-integral becomes path-dependent and J_{tip} differs from J_{far} in the form, $J_{tip} = J_{far} + C_{inh}$ (Kolednik et al., 2011; Simha et al., 2005; Simha et al., 2003). The parameter C_{inh} is denominated as material inhomogeneity term.

The main factor influencing C_{inh} is the mismatch in mechanical material parameters, such as σ_y, E or the introduced work until the yield point (Lach et al., 2017; Lach et al., 2014; Lach et al., 2016; Grellmann and Langer 2017). If a crack propagates from a hard to a soft phase, the material inhomogeneity term C_{inh} is positive and increases J_{tip}, which is referred to as anti-shielding effect. Compared to a crack propagating only in one phase, this will lead to a higher crack growth rate. Vice versa, for crack propagation from soft to hard phase, C_{inh} becomes negative and decreases J_{tip} in the process, also known as shielding-effect. In this case, a crack will grow slower or even arrest, since it requires a higher applied load in order to propagate than in a homogeneous phase.

An interlayer can be regarded as two consecutive interfaces, and the inhomogeneity terms for the first and second interface C_{inh1} and C_{inh2} can be summed up in the interlayer inhomogeneity term C_{IL}, as shown in Eqn 1 (Sistaninia and Kolednik 2014),

$$J_{tip} = J_{far} + C_{inh1} + C_{inh2} = J_{far} + C_{IL}. \tag{1}$$

By the introduction of a soft interlayer in a brittle matrix material, the anti-shielding and shielding effects at two interfaces are combined (Sistaninia and Kolednik 2014), see Fig. 3. An exemplary evolution of J_{tip} as a function of the distance between the interlayer and the crack tip L_1 is depicted in Fig. 3b. Therein, a soft interlayer with an elastic modulus of E_{IL} was introduced to a stiff and brittle matrix with an elastic modulus of E_{Matrix}. The curve shows a local minimum at the second interface. By utilizing this effect, a crack trap can be tailored. To overcome such a soft interlayer, the macroscopic loading parameter J_{far}

has to be increased substantially, leading to an improvement in fracture toughness. For the deep sea sponge itself (Kolednik et al., 2011), as well as for several metallic and ceramic materials (Fratzl et al., 2007; Kolednik et al., 2019; Sistaninia and Kolednik 2014; Chen et al., 2007; Müller et al., 2009; Kolednik et al., 2010; Zechner and Kolednik 2013), this shielding and anti-shielding effects could be experimentally proven. Lach et al. (Lach et al., 2014) observed the influence of a material inhomogeneity on cracks growing towards the interface of polymeric bimaterials. While Lach et al. mainly focused on cracks growing towards an interface, the current work focuses on cracks growing to and beyond interlayers of soft material. Therefore, the approach of fracture toughness increase via multi-layer build ups seems promising. However, studies on its effectivity on polymers are still missing.

Polymeric layered structures can be produced by extrusion, or in this case co-extrusion in an efficient manner. Therefore, layered structures appear to be a potent candidate for biomimetic toughness enhanced composites, which could also be used at an industrial scale. Within the scope of this paper co-extruded, thermoplastic multi-layer composites are examined with regard to their fracture toughness increase by introducing soft interlayers and different ratios of mechanical properties.

2. Experimental

2.1. Materials

Since the material inhomogeneity effect relies on a significant mismatch in mechanical properties, a portfolio of materials with vastly different mechanical behavior should be examined. However, good adhesion between individual layers should also be ensured to avoid delamination at the interfaces.

For industrial applications, the use of highly mineral reinforced polymers is appealing. Mineral fillers cause a high stiffness and promote enhanced creep resistance. Furthermore, mineral based fillers are commercially available at a fraction of the price of the polymer matrix. Therefore, four different variations of polypropylene were used in this study. Two polypropylene compounds with different amounts of mineral filler were used as stiff and brittle matrix materials (moderately talcum particle reinforced (PP-MR) and highly reinforced (PP-HR)). For the soft interlayer a standard grade of polypropylene (PP) and a very compliant type of modified PP (PP-S) were used. The exact formulations of used materials are confidential and cannot be disclosed at this time.
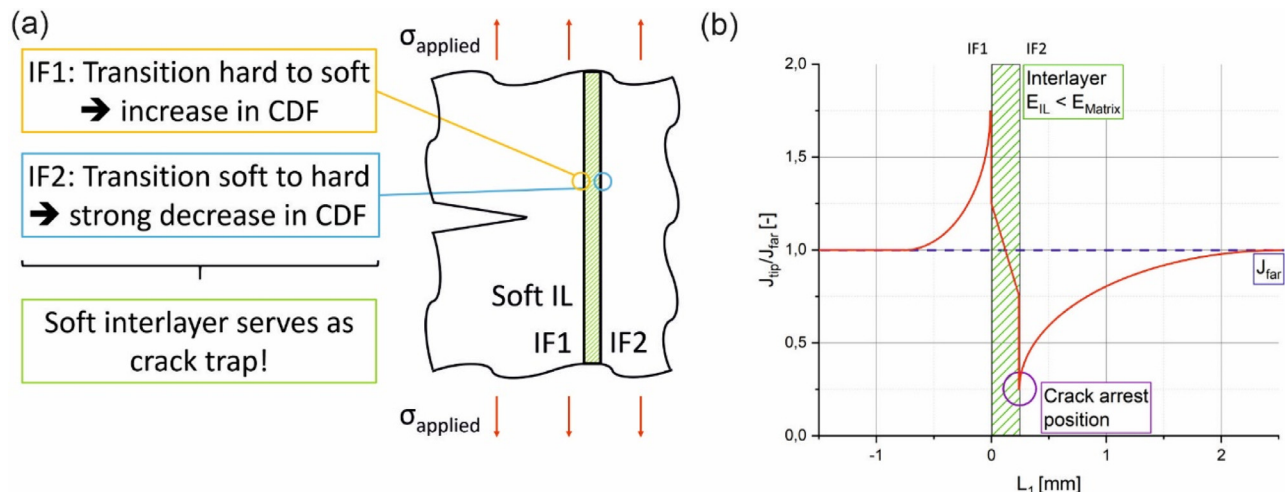

Fig. 3. Basic concept of creating a crack trap utilizing the material inhomogeneity effect (a) and the resulting change of J_{tip} in the vicinity of a soft interlayer (b) (Sistaninia and Kolednik 2014).

Table 1
Nomenclature and material composition for various multilayer configurations.

| Abbreviation | Materials | | number of interlayers | Ratio of mechanical properties | | |
	Matrix	Interlayer		E_{Matrix} / E_{IL}	$\sigma_Y^M / \sigma_Y^{IL}$	$\varepsilon_f^M / \varepsilon_f^{IL}$
ML1	PP-HR	PP	1	4.8	1.1	2.6×10^{-3}
ML2	PP-HR	PP-S	1	28.8	3.4	1.8×10^{-3}
ML3	PP-MR	PP-S	1	18.4	3.3	69.8×10^{-3}
ML4	PP-HR	PP-S	2	28.8	3.4	1.8×10^{-3}

2.1.1. Manufacturing of multi-layer composites

Using aforementioned materials, four different multi-layer composites (ML) were manufactured. The specific material combinations for matrix and interlayer, as well as the ratios of mechanical properties (respective values of matrix and interlayer for elastic modulus, E_{Matrix} and E_{IL}, yield stress,σ_Y^M and σ_Y^{IL}, and failure strains,ε_f^M and ε_f^{IL}) between them are shown in Table 1. Therein, ML1 has a PP-HR matrix with a single PP interlayer. In this combination, the ratios of mechanical properties are comparably low. In ML2, PP-S was used as single interlayer in a PP-HR matrix, leading to higher ratios of mechanical properties. ML3 has a single PP-S interlayer incorporated in a PP-MR matrix to observe the effects of a comparably tough matrix with a high mismatch in mechanical properties. ML4 has the same combination of materials as ML2, but features two interlayers. Using a co-extrusion process, homogeneous and multi-layered sheets with 20 mm thickness were produced. The average thickness of the soft interlayers was approximately 0.3 mm.

2.2. Fracture toughness testing using J-integral

Due to their ductile nature, three of the four investigated PP types do not comply with the assumptions made in linear elastic fracture mechanics. Therefore, methods of elastic plastic fracture mechanics are used to more accurately describe the material behavior of the multi-layer specimens. More precisely, an adaptation of Rice's *J*-integral (Rice 1968; Hale and Ramsteiner 2001) method for polymers was utilized to characterize the fracture toughness. In accordance with the recommendation of the Technical Committee 4 of the European Structural Integrity Society (ESIS TC4 recommendation (Hale and Ramsteiner 2001)), the multi-specimen method using monotonic three point bending tests were performed on single edge notched bending (SENB) specimens.

From the (co)extruded sheets, SENB specimens with the dimensions $80 \times 10 \times 20$ mm^3 were produced (see Fig. 4). The longitudinal axis always coincided with the extrusion direction and the thickness of the sheet was taken as width of specimens (*W*). Machined notches were introduced and sharpened utilizing a broaching tool with a razor blade in order to produce an initial sharp crack with the length a_0 (Martínez et al., 2013; Martínez et al., 2016; Salazar et al., 2015). The initial notch lengths were manufactured to satisfy the relation $0.55 < a_0/W < 0.65$, as stated in (Hale and Ramsteiner 2001).

SENB tests (see Fig. 4b) were performed on the servo-hydraulic testing machine MTS 831 (MTS Systems GmbH, USA) at a crosshead speed of 1 mm/min. After performing the SENB experiments, the specimens were cryo-fractured and examined under a light microscope. An Olympus SZX12 (Olympus Life Science Europe GmbH, Germany) was used to obtain the crack extension, Δa, alongside the geometry data of the specimen under reflected light. To obtain the specimen thickness B and the ligament length W-a_0, three separate measurements were taken across the fracture area and averaged. A polygon was positioned to match the fractured surface and to calculate the fracture surface area. The average crack extension was calculated from the fracture surface area and B. For these measurements, a magnification of 12.5 was used in all cases. A preliminary J-integral, J_0 (which does not consider crack extension), was evaluated using Eq. (2).

$$J_0 = \frac{\eta U}{B(W - a_0)} \tag{2}$$

Therein, U is the area under the load-displacement curve, which was corrected for indentation and machine stiffness as stated in (Hale and Ramsteiner 2001). A value of 2 was used as geometry factor η for SENB specimens. Strictly speaking, the J-integral is only valid for very small crack extensions. To clearly observe fracture behavior before and after the interlayer, specimens had to be tested up to crack lengths of several mm. A crack growth correction according to (Schwalbe and Neale 1995) was performed to compensate for large Δa values. The experimental J-integral J_{exp} was then calculated using Eq. (3).

$$J_{exp} = J_0 * \left[1 - \frac{(0.75\eta - 1)\Delta a}{W - a_0} \right] \tag{3}$$

As is recommended by ESIS TC4 (Hale and Ramsteiner 2001), a power law fit was applied to the data of the four homogeneous materials. The power law formula is displayed in Eq. (4), wherein J_{exp} can be calculated from Δa and the two parameters A and N. All the gathered data can then be presented in a plot of J_{exp} against Δa, also known as *J-R* curve.

$$J_{exp} = A \ \Delta a^N \tag{4}$$

Following the procedure described in (Hale and Ramsteiner 2001) a so-called blunting line was constructed. This line follows the equation
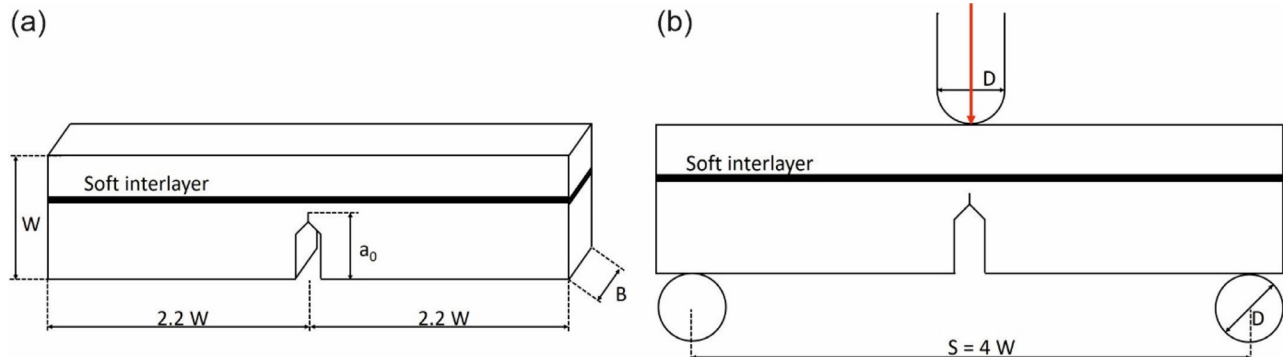

Fig. 4. Dimensions of a SENB specimen (a) and schematic of a bending fixture (b) (Hale and Ramsteiner 2001).
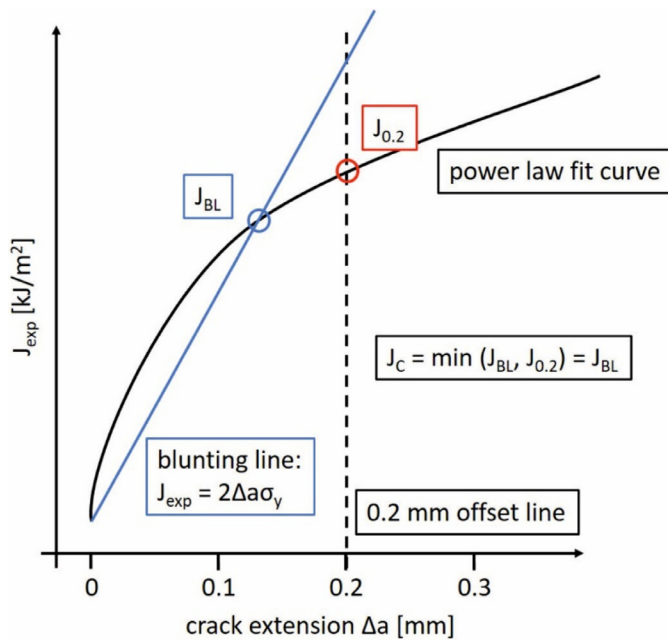
Fig. 5. Determination of J_C from J_{BL} and $J_{0.2}$.

$J_{exp} = 2\Delta a\sigma_y$ and describes the crack tip blunting due to plastic deformation. The intersection of the blunting line with the power law fit curve yields the parameter J_{BL}. The power law fit formula was used to evaluate the J_{exp} value at $\Delta a = 0.2$ mm in order to obtain the value $J_{0.2}$. The initiation toughness parameter J_C was then determined as the smaller value out of J_{BL} and $J_{0.2}$, see Fig. 5.

As shown in several works before, PP shows a rather complex deformation mechanism in fracture mechanical tests whether it is under monotonic (Salazar et al., 2014; Seidler et al., 2001), impact (Martínez et al., 2016; Salazar et al., 2012; Karger-Kocsis et al., 1997), or fatigue (Arbeiter et al., 2016) loading. Thus, a certain amount of data scattering is also expected for the materials at hand. A simple criterion was applied to discard specimens with unstable crack growth to ensure adequate quality of data points in the J-R curve (Lach et al., 2014; Gosch et al., 2018). A linear regression line was fitted to the crack growth Δa versus testing time t. Very far outliers from the trend line were excluded from the evaluation. When introducing interlayers a change of the crack growth rate in the vicinity of the soft layer is expected. Hence, this data exclusion criterion was only applied for homogeneous materials and not for multi-layer configurations.

2.3. Adaptations of Δa-measurement and J-Rplotting technique for materials with interlayers

Due to the complex fracture process of inhomogeneous materials, the conventional methods for crack length measurement and construction of the J-R curve have to be adapted. Presumably, owing to the interlayer material's high failure strain, the interlayer itself stays intact during the experiment and does not break until the specimens are cryo-fractured. Therefore the interlayer thickness, t, was never included in the crack extension Δa. Instead, the individual crack extensions Δa_i in the matrix material were added up to a total Δa. In the case of a single interlayer this leads to $\Delta a = \Delta a_1 + \Delta a_2$ (see Fig. 6a).

Another aspect in multi-layered specimens is that many geometrical parameters are subject to variance related to processing and sample preparation. While the differences may seem small compared to the dimensions of the specimen, even small changes can have a significant influence on the J-R curve. Processing induced variances, such as the distance between the interlayer and the razor blade notch L_0, the interlayer thickness t or the remaining ligament behind the interlayer can

lead to large scatter in the J_{exp} values at the first interface of the interlayer.

To compensate for these variances in geometry, an alternative technique of plotting is used. Instead of applying J_{exp} versus the crack extension Δa, a parameter L was introduced as replacement for Δa (Fig. 6a).The parameter L describes the distance between the first interface of the soft layer and the crack tip. A negative value of L indicates that the crack has not reached the interlayer yet. In this case $L = \Delta a - L_0 < 0$ (see Fig. 6a). In contrast, positive values indicate crack growth beyond the interlayer. In the case of a single interlayer, this means $L = \Delta a - L_0 = \Delta a_2 > 0$. As a result, effects caused by the material inhomogeneity should be clearly visible at or closely around a value of $L = 0$ (Figs. 6b and c).

For the multi-layer composites, a linear regression line for all data points with $L > 0$ was fitted and extrapolated to $L = 0$ (see Fig. 6c). This intersection represents the required energy to overcome the interlayer and initiate crack growth behind it. The obtained value was named J_C^{ML} and served as a measure for the fracture toughness of the composite. The slope of the regression line is proportional to the tearing modulus T ($T = E/\sigma_y^2 * dJ_{exp}/d(\Delta a)$). Although T is known to be geometry dependent, the slope $dJ_{exp}/d(\Delta a)$ shall be used to qualitatively compare the crack growth resistance.

For better comparison, a shifting procedure was also applied for the J-R curves and Δa-t plots (crack extension versus testing time) of the matrix materials. The arithmetic mean of L_0 was calculated from all specimens of the individual multi-layer configurations (e.g. L_0^{ML1}, L_0^{ML3}). The data points and power law fit curves of the respective matrix materials PP-HR and PP-MR were shifted by these values, so that $L_{matrix} = a_{matrix} - L_0^{ML}$. By formulating the parameter L as mentioned, the J-L plot can describe the J_{exp} behavior for both homogeneous as well as multi-layered specimens. This does not influence the representation of the J-R curve as well as the L-t curve of the homogeneous specimens.

3. Results & discussion

3.1. Fracture toughness of homogeneous materials

For all specimens made from PP and PP-S, side grooves with a depth equal to 10% of the thickness B were introduced on each side. This was done to avoid strong curvatures of the crack fronts during the experiments. For PP-HR and PP-MR specimens side grooves were applied only to a part of the specimens that were tested. Fracture mechanical SENB tests could successfully be performed for three out of the four homogeneous materials (PP, PP-MR and PP-HR). The resulting J-R curves are depicted in Fig. 7. The obtained values for the constants A and N of the power law fit (Eq. (4)) as well as the values for $J_{0.2}$, J_{BL} and J_C are shown in Table 2. One material, namely PP-S, was too ductile to be characterized via J-integral at room temperature. During testing the specimens just plastically deformed instead of fracturing. Even at very large deflections, no actual crack extension from the initial razor blade notch could be detected. Additionally, PP showed a great discrepancy between J_{BL} and $J_{0.2}$ (19.32 kJ/m² and 44.59 kJ/m²), making a reliable determination of fracture toughness somewhat difficult. Alternative techniques for determining the initiation toughness parameter include assessment of stretched zone width and height, crack tip opening displacement (CTOD, often used for metals e.g. (Kolednik et al., 2019)) or even the kinetics of the CTOD. (Lach and Grellmann 2017; Lach et al., 2005) However, due to the unreliable measurement of CTOD in polymers at low speeds these methods were forgone in the current contribution. Owing to the higher degree of mineral reinforcement, a reduction in J_C could be observed for PP-HR in comparison to PP-MR (0.23 kJ/m² compared to 1.30 kJ/m²). Interestingly, for PP-MR and PP-HR no difference between side grooved and non-side grooved specimens could be observed. Contrary to ESIS TC4 recommendation, J-R curves were measured up to rather large values of crack extension, to
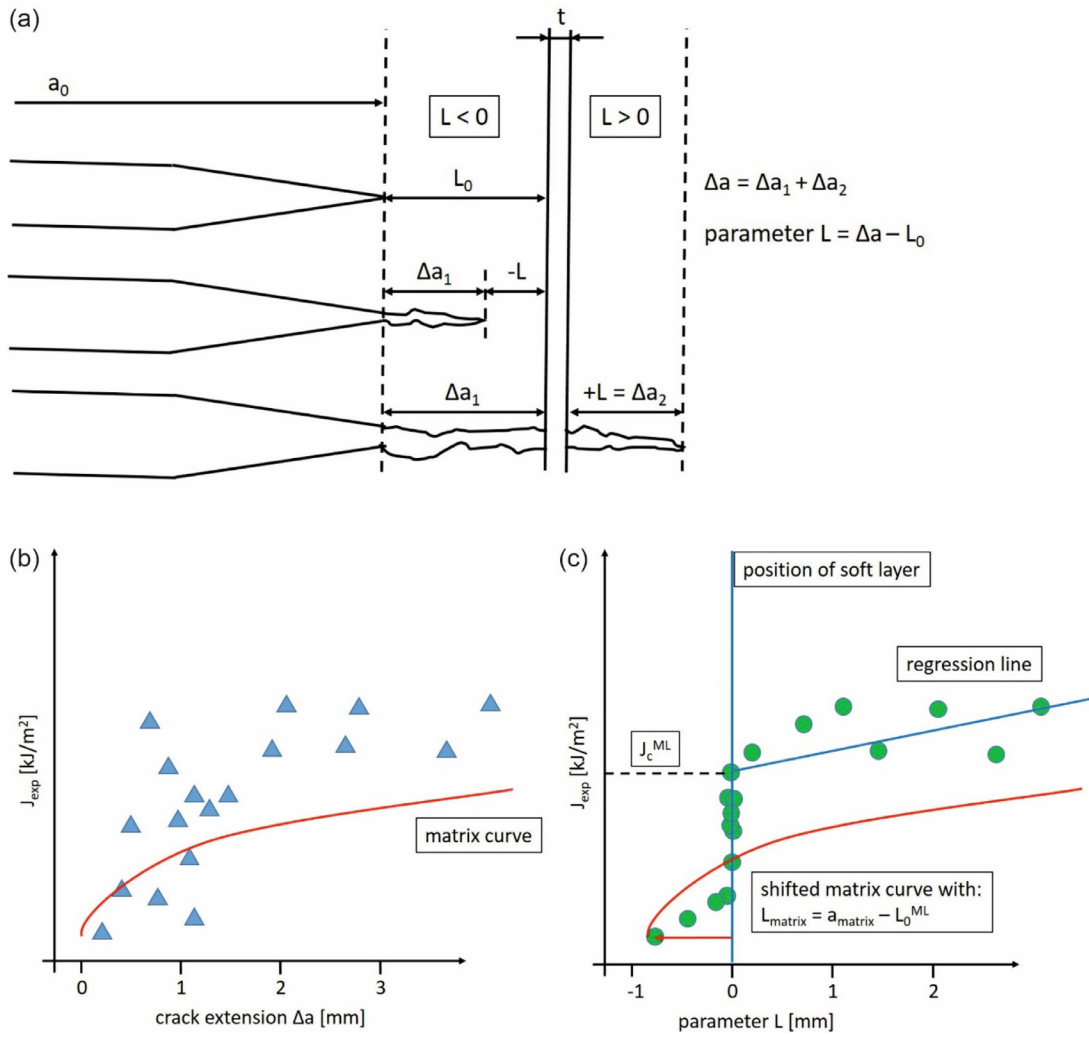
Fig. 6. Calculation of the parameter L (a), conventional plotting of J_{exp} versus Δa (b) and modified plotting technique (c) of J_{exp} versus the distance between crack tip and interlayer (parameter L).
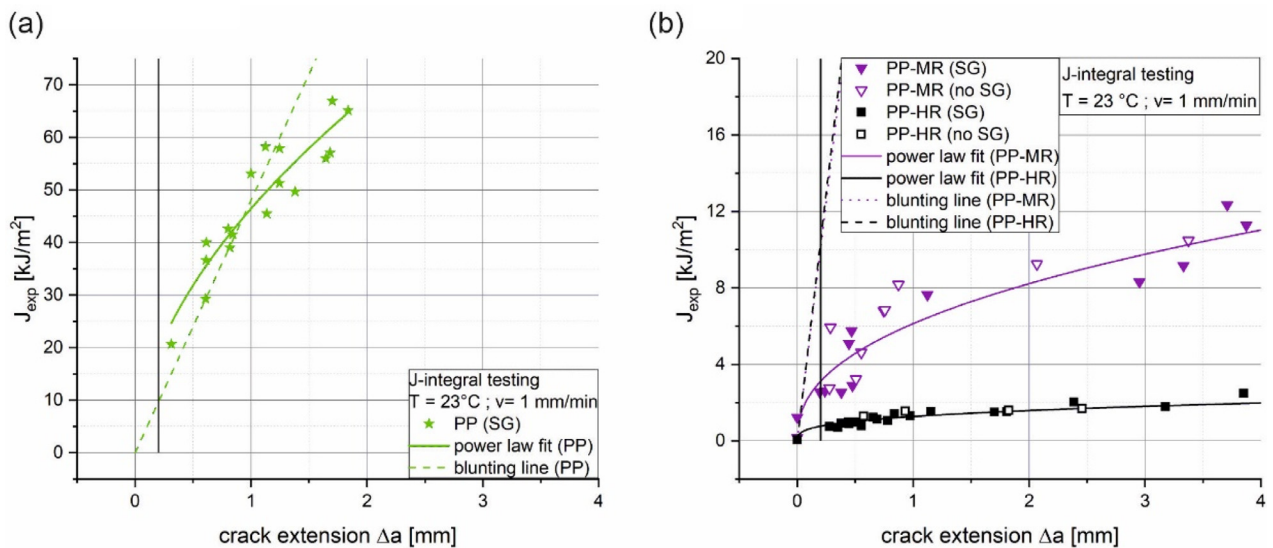

Fig. 7. J-R curve for PP (a), PP-MR (b) and PP-HR (b), tested at a crosshead speed of 1 mm/min. Measurement points, power law fits as well as blunting lines are shown.

Table 2
Overview of and power law fit parameters for Eq. (4), A and N, and fracture toughness parameters $J_{0.2}$, J_{BL}, J_C and J_C^{ML} for the tested materials.

homogeneous materials						multi-layer composites (non-side grooved)	
	A	N	$J_{0.2}$ [kJ/m^2]	J_{BL} [kJ/m^2]	J_C [kJ/m^2]		J_C^{ML} [kJ/m^2]
PP	46.43	0.55	19.32	44.59	19.32	ML1	–
PP-S	–	–	–	–	–	ML2	1.94
PP-MR	6.26	0.41	2.60	1.30	1.30	ML3	24.07
PP-HR	1.27	0.32	0.76	0.23	0.23	ML4	2.42

compare with multi-layer specimens later on.

3.2. Fracture toughness of composites

3.2.1. Multi-layer composite 1 (ML1; matrix: PP-HR; interlayer: PP)

For ML1 specimens side grooves with a depth equal to 10% of B were applied only to a part of the specimens that were tested. The results for ML1 are shown in Fig. 8. Although ML1 contains a comparably tough PP interlayer, no improvements in fracture initiation toughness or crack growth resistance could be achieved compared to pure PP-HR. For non-side grooved specimens the J_{exp}-values are slightly below the matrix material, while the crack growth rate is higher (0.168 mm/s compared to 0.084 mm/s, see Figs. 8a and b). Due to the high constraint caused by the surrounding matrix and the resulting stress triaxiality, the plasticity of the PP interlayer is limited. Although some plastic deformation takes place, no energy consuming large scale yielding is observed. The significant attribute for the toughening of the composite is the inhomogeneity effect, which also affects the crack driving force and stress distribution in matrix regions adjacent to the interlayer. While the ratio of E between the two materials is significant, the same cannot be said for the ratio of σ_y. The yield stress of the matrix is only 10% higher than that of the interlayer. This E-inhomogeneity will be diminished by plastic deformation near the interfaces. As described in (Kolednik et al., 2019), this results in a strongly reduced effectiveness of the interlayer as crack arrester. Hence, the combined inhomogeneity effect ($E + \sigma_y$) is not strong enough to cause a measurable increase in fracture toughness. This would not be so in the case of σ_y-inhomogeneity, whereas the ideal scenario is an inhomogeneity in both E and σ_y. The side grooved specimens coincide with the matrix material PP-HR in both the J-R curve and the crack growth rate. For that reason, no initiation parameter J_C^{ML} was evaluated.

3.2.2. Multi-layer composite 2 (ML2; matrix: PP-HR; interlayer: PP-S)

For ML2 specimens side grooves with a depth equal to 10% of B were applied only to a part of the specimens that were tested. In ML2, the differences of σ_y and E between matrix and interlayer materials are much higher than in ML1. As a result, the ML2 composite shows an E-inhomogeneity as well as a σ_y-inhomogeneity. Hence, the combined inhomogeneity effect should show a greater influence on the fracture toughness. For all the non-side grooved specimens the soft interlayer noticeably influenced the crack growth behavior (see Figs. 9a and b). For ML2, an increase from 0.23 kJ/m^2 (J_C of the PP-HR matrix) to 1.94 kJ/m^2 (J_C^{ML2} of the composite, see Table 2) could be achieved.

The slope of J-R curve, $dJ/d(\Delta a)$, is different in the region $L < 0$, for PP-HR and its composites. The predicted anti-shielding effect becomes visible, since the slope of 0.31 kJ/m^3 for $L < 0$ is visibly lower than for pure PP-HR. When the crack reaches the interlayer, this slope almost becomes a vertical line. The energy for plastic deformation and crack re-initiation behind the interlayer must be overcome first, before another increment of crack extension can be produced. Thereafter, the $dJ_{exp}/d(\Delta a)$ of ML2 is lower than for the matrix PP-HR, 0.18 kJ/m^3 compared to 0.28 kJ/m^3. This might be due to a change in constraint (a/W) and possibly the release of elastically stored energy as additional source of crack driving force.

For $L < 0$, the crack growth rate at 0.055 mm/s was found to be slighltly below the matrix value of 0.084 mm/s. The crack growth rate (evaluated as the slope in the L-t plot, Fig. 9b) almost drops to zero in the proximity of the interlayer. After passing the interlayer the crack growth rate increases to 0.137 mm/s compared to the 0.084 mm/s of PP-HR. As can be seen in Fig. 10a, PP-HR shows no signs of significant plastic deformation or yielding. The only trace of dissipative effects is a slim zone of stress whitening (possibly caused by crazing) that precedes the crack. While the crack is arrested in the interlayer but the loading continues, the majority of introduced energy has no other possibility than to be stored as elastic energy. Once a crack re-initiates in the matrix however, this energy is released again, resulting in an accelerated crack growth. This assumption is confirmed by the decreased slope in the J-R curve for $L > 0$.

For the side-grooved specimens no improvement in fracture toughness could be achieved. The J_{exp}-values are even lower that for PP-HR, while the crack growth rate is higher than for the matrix (0.233 mm/s compared to 0.084 mm/s).

3.2.3. Multi-layer composite 3 (ML3; matrix: PP-MR; interlayer: PP-S)

None of the previously performed experiments showed improvements in fracture toughness when introducing side grooves. Therefore,
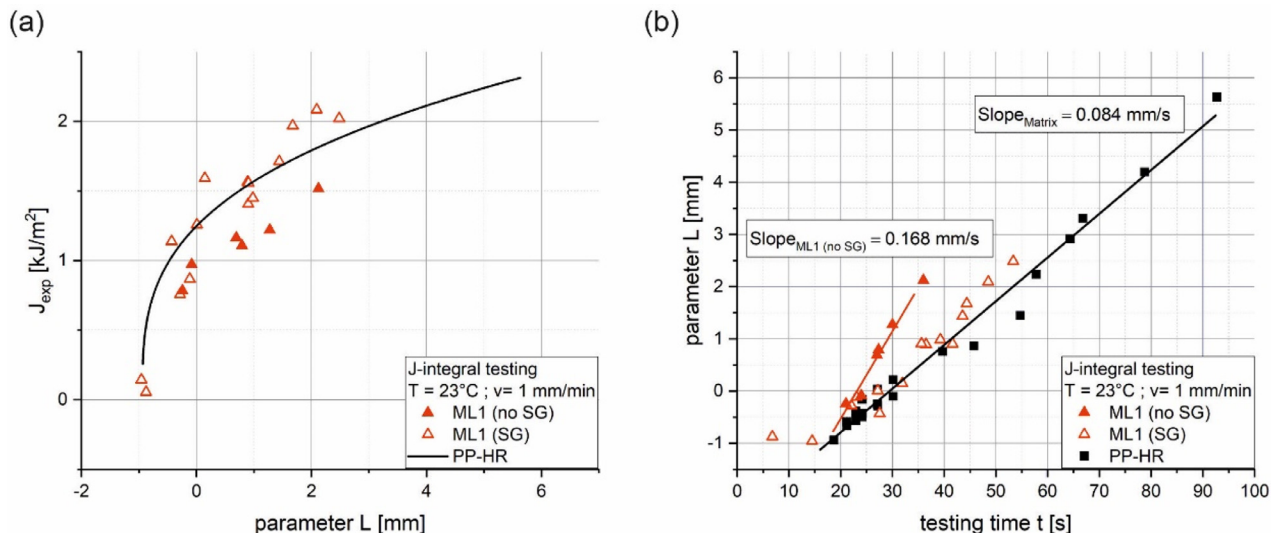

Fig. 8. Modified J-R curve for ML1 displaying J_{exp} versus the parameter L (a) and L versus testing time (b).
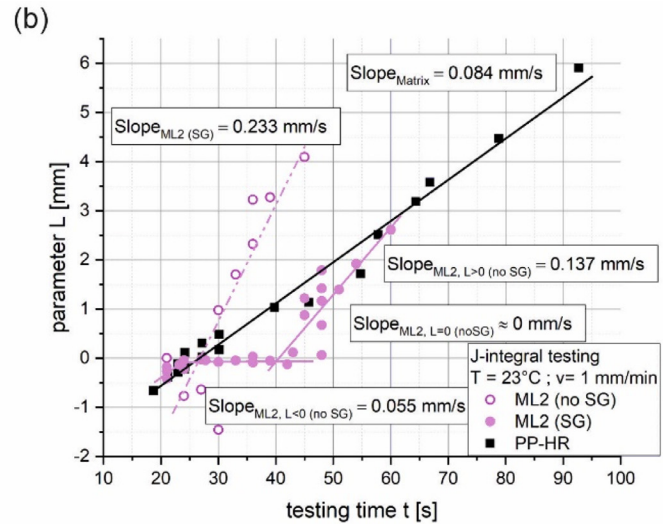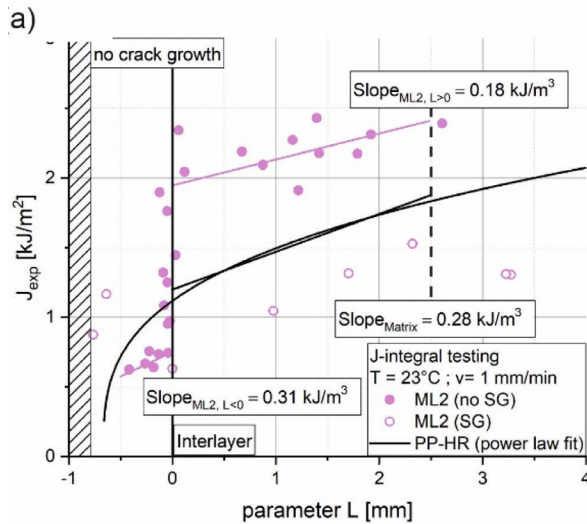
Fig. 9. Modified *J-R* curve for ML2 displaying J_{exp} versus the parameter L (a) and L versus testing time (b).
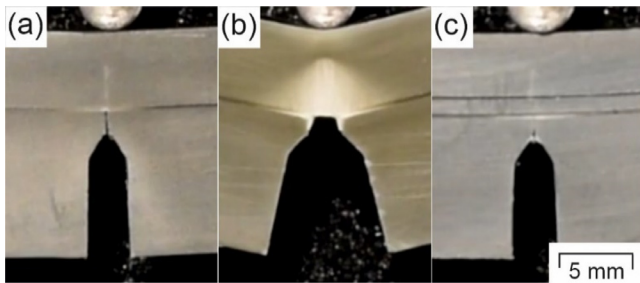

Fig. 10. Plastic zone development shortly before crack re-initiation for ML2 (a), ML3 (b) and ML4 (c).

side grooves were omitted entirely for ML3 specimens. A pronounced increase of J_{exp} can be seen at $L = 0$ for ML3 specimens (Fig. 11a). The increase for ML3 is considerably higher than for ML2. More precisely, the fracture toughness at $L = 0$ increased almost twenty times from 1.30 kJ/m^2 (J_C of PP-MR) to 24.07 kJ/m^2 (J_C^{ML3} of ML3, see Table 2). This is caused by the tougher matrix material, which hinders crack re-

initiation after the first crack hits the interface. What is also worth mentioning is the increased slope of 11.37 kJ/m^3 for $L > 0$ as compared to 1.66 kJ/m^3 of PP-MR. Apparently, the crack growth resistance after passing the interlayer is higher than for the pure matrix. This is possibly caused by the extensive plastic deformation the remaining ligament undergoes before crack re-initiation. Therefore, higher amounts of dissipated energy are required for further crack extension. The possibility to express this in the form of J_{exp} should be taken with care due to invalidation of *J*-integral preconditions. Furthermore, PP-MR is able to undergo a strain softening process without fracture when being loaded past σ_y. This process is comparable to the mechanical rejuvenation effect described by Meijer and Govaert (Meijer and Govaert 2005). Therefore, the applied strains can be delocalized better, while crazing becomes less likely. As a result, the plastically deformed material shows an increase in fracture toughness compared to its undamaged state.

For $L < 0$ cracks propagate a lot faster than in pure matrix material. This behavior can be explained by the variation of crack driving force around the interlayer, which is depicted in Fig. 2b. While the crack driving force behind the soft layer is diminished by the shielding effect, in front of the interlayer the anti-shielding effect leads to an increased
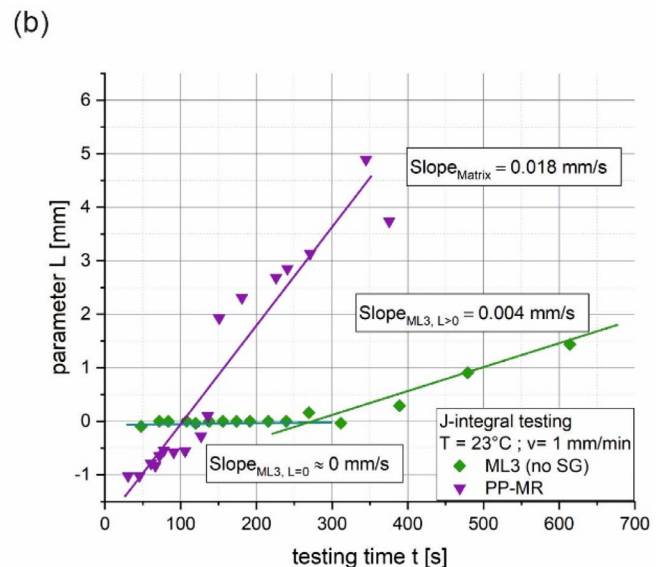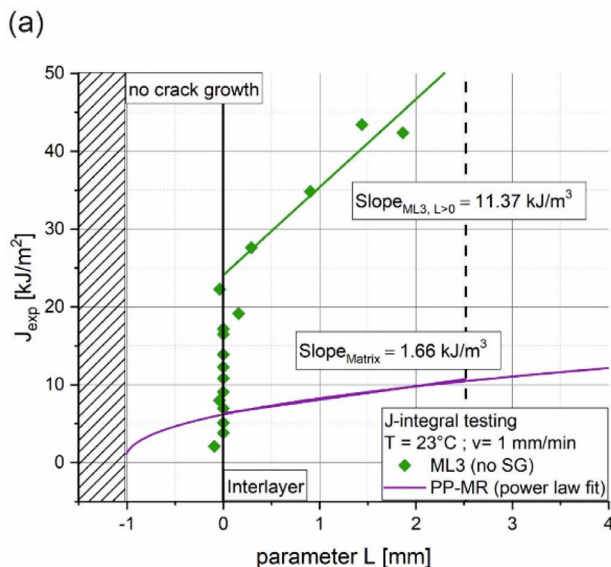

Fig. 11. Modified *J-R* curve for ML3 displaying J_{exp} versus L (a) and L versus testing time (b).
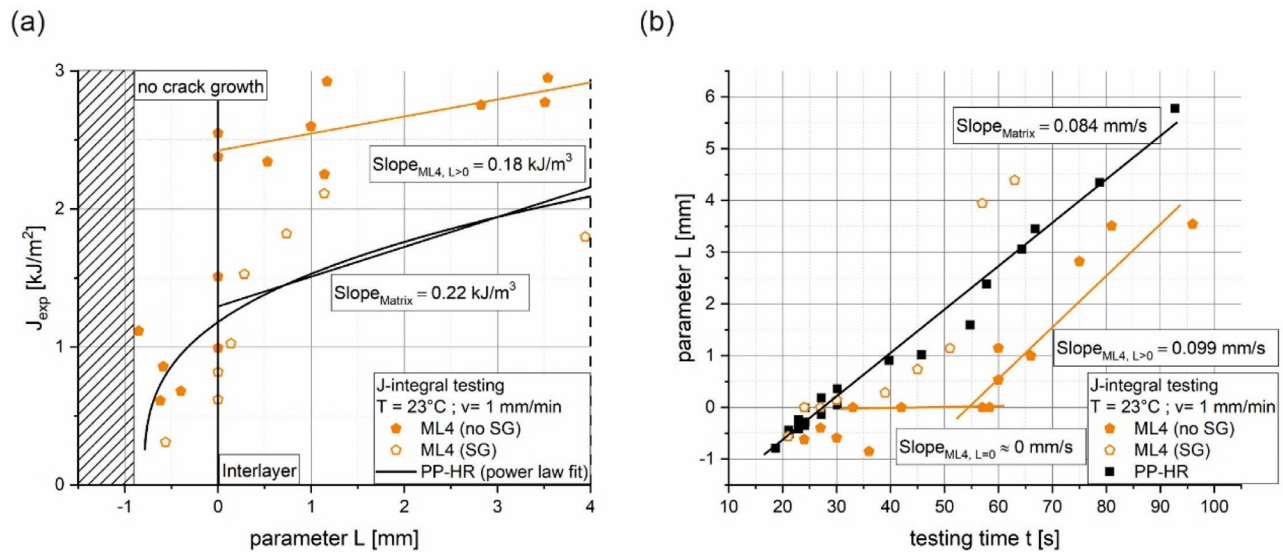
Fig. 12. Modified *J-R* curve for ML4 displaying J_{exp} versus the parameter *L* (a) and *L* versus testing time (b).

crack driving force and crack growth rate. This can also be seen in Fig. 11b, where almost 1 mm of crack extension is reached very rapidly. Smaller crack extensions could not be measured within the scope of the experiments. However, after this fast crack propagation towards the interlayer the crack growth rate rapidly drops to zero upon reaching it. In accordance with the *J-R* curve, the crack growth rate for $L > 0$ is much smaller than for undamaged PP-MR (0.004 mm/s compared to 0.018 mm/s). Once again this indicates tougher material behavior of the plastically deformed matrix material.

3.2.4. Multi-layer composite 4 (ML4; matrix: PP-HR; interlayer: PP-S)

For ML4 specimens side grooves with a depth equal to 10% of *B* were applied only to a part of the specimens that were tested. For non-side grooved specimens a tenfold increase from 0.23 kJ/m^2 to 2.42 kJ/m^2 in fracture toughness could be measured (see Table 2), although the data exhibited big scattering in the ML4 experiments.

The plot of *L* versus testing time in ML4 is similar to ML2. As is depicted in Fig. 12a, the slope in the *J-R* curve for $L > 0$ is slightly smaller than for the matrix (0.18 kJ/m^3 compared to 0.22 kJ/m^3). The crack growth rate (Fig. 12b) almost drops to zero at $L = 0$. With 0.099 mm/s, the crack growth rate behind the interlayer is again larger than for PP-HR (0.084 mm/s), so that for large values of *L* the two curves join again. Due to the higher data scattering, no reliable statement can be made for the slope of the *J-R* curve and the slope in the *L-t* plot for $L < 0$. Just as for ML2, the plastic zone of ML4 was found to be very small (Fig. 10c). The data points for side grooved specimens coincide with the matrix material. Despite what one would expect from a specimen with two interlayers, no second increase in J_{exp} was observed. This is explained by the unexpected failure mechanism, which will be discussed in the next section.

3.2.5. Specimen failure mechanism

Surprisingly, even after a crack has re-initiated beyond an interlayer, the interlayer still remains intact and endures large deformations until rupture (Fig. 6a). This observations was made for all four multilayer configurations. For ML2, ML3 and ML4, the crack is stopped at $L = 0$ and has to re-initiate in the remaining matrix ligament, while for ML1 no such benefits were found. This raises the question which mechanism actually causes the final specimen failure. Fig. 13 depicts different scenarios for the fracture behavior of a SENB specimen with two soft interlayers. The consideration was made for two interlayers (corresponds to ML4) but the discussed failure mechanisms would look the same for a single interlayer composite. In both scenarios, the specimen

is assumed to be already fractured from the initial notch until to the first soft interlayer. Fracture surface is depicted as grey area with black dots, the initial razor blade notch is depicted as white area with black stripes. While the interlayer itself (black area) stays intact, it is not sure where the specimen failure will proceed in the matrix material (white area with black spots). There are two plausible causes for crack re-initiation in the matrix behind the soft layer:

3.2.5.1. Scenario A: the interlayer transfers stresses in a meaningful way.
The interlayer and matrix transfer the bending stress σ_b in the same way and the stress distribution is almost unaffected by the material inhomogeneity. Just as one would expect from a homogeneous sample, the highest stresses occur at the crack tip (Fig. 13a). However, the interlayer material is too tough to fail at this location. It is more likely that the interlayer stays intact and a new crack re-initiates in a part of the matrix closest to the arrested crack. In the depicted case, this would be the middle ligament of the SENB specimen.

3.2.5.2. Scenario B: the interlayer transfers no stresses.
In this case, stress transfer from one ligament to the next is not possible. However, all ligaments have the same deflection. Thus, the ligaments behave like separate, decoupled bending specimens. Each individual ligament posseses its own bending stress distribution (Fig. 13b). Just like before, the interlayers are too tough to break and stop any growing cracks. Now the most critical stress can be found on the tension side of the broadest matrix ligament. For the depicted geometry, the maximum stress and therefore the location for crack re-initiation can be found on the bottom edge of the outermost matrix ligament. If the loading parameters are known, the fracture toughness of a structure can also be optimized. By using equally spaced, small ligaments, the maximum stress can be kept below the matrix material's bending strength (see Fig. 13b).

It should be noted that in both cases specimen failure does not progress through classical crack growth, but rather due to a surpassing of the matrix material strength at a global stress maximum. Any increment of crack extension behind the first soft layer can only happen after a crack re-initiation step.

In order to distinguish which one of the aforementioned failure mechanisms really happens, the fracture surfaces of cryo-fractured SENB specimens were investigated closer. Of course, in ML2 specimens (Fig. 14a and c) crack re-initiation happens behind the first and only interlayer. No differentiation between Scenario A and B can be made in
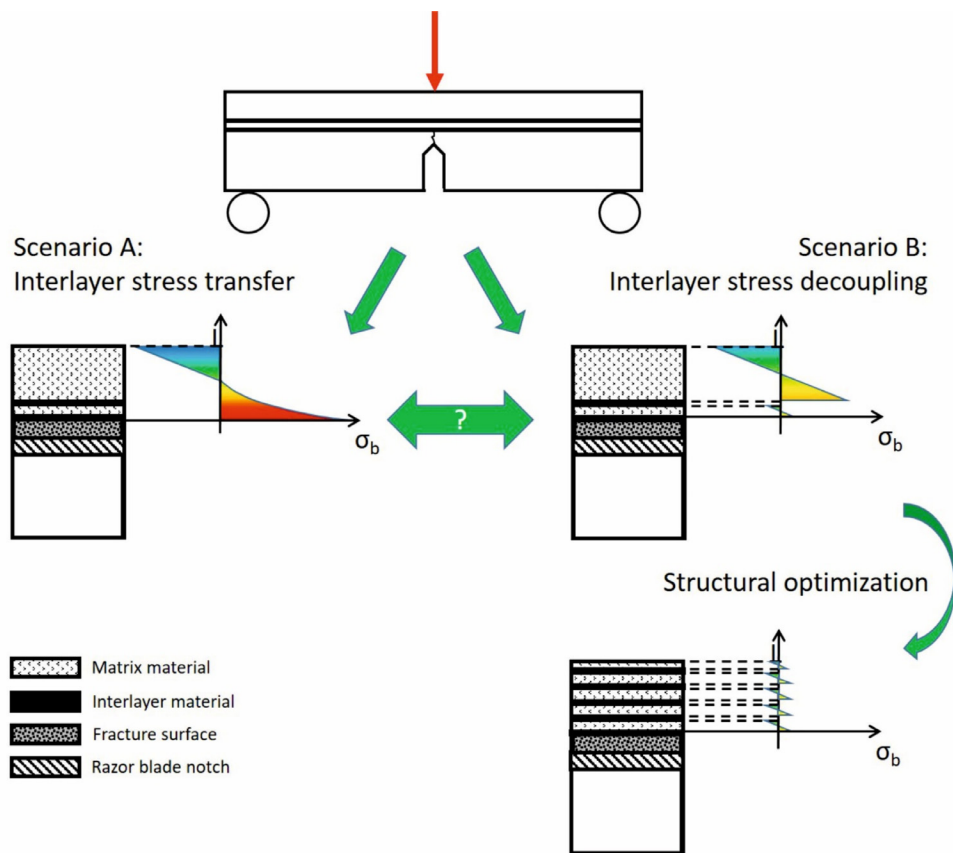
Fig. 13. Possible stress distributions in multi-layered specimens: interlayer is able to transfer stresses well (Scenario A) and interlayer transfers no stresses (Scenario B).

this case. However, fracture surfaces from ML4 specimens (Fig. 14b and d) are more revealing: While the middle ligament is still intact, crack re-initiation takes place in the outermost matrix ligament. The failure of the broadest ligament confirms the assumptions of decoupled bending stresses made in 3.2.5 b. Specimen failure in this case does not proceed consecutively from the first interlayer to the second, but rather due to a simultaneous loading of all deflected ligaments. This gives the explanation why there is no second increase in $J_{\exp}$ for ML4 in Fig. 12a.

In specimens with side grooves the crack re-initiation always started from the bottoms of the side grooves (Fig. 14a and b). For PP-HR the stress concentration introduced by the side grooves is significant enough to greatly facilitate crack re-initiation. In these cases, the side grooves render the introduction of soft layers obsolete. For this reason, no improvements in fracture toughness and crack growth rate could be found.

On the other hand, in the specimens without side grooves, the exact location of re-initiation behind the interlayers varried randomly (Fig. 14c and d). The starting points of failure are most likely local stress concentrations caused by agglomerates of mineral particles. All specimens failing in this way exhibited the increase in fracture toughness and crack growth rate predicted by the material inhomogeneity effect. In these cases, the soft layers worked as intended.

4. Summary & conclusions

Inspired by bio-materials, the effects of soft polymer interlayers on mineral reinforced polymer matrix materials were characterized. The improvements of fracture toughness caused by the soft layers were shown using *J*-integral-based methods from elastic plastic fracture mechanics. The following statements were found to be true in single edge notch bending tests:

- The material inhomogeneity effect was observed in mineral reinforced polypropylene (PP) with PP interlayers. Through the introduction of soft interlayers in brittle matrix materials, improvements in fracture toughness could be achieved due to a crack-arrester effect in the soft layers.
- In order to function as intended, the interlayer material must exhibit large differences in the elastic modulus E and the yield stress σ_y compared to the matrix material. The pure σ_y-inhomogeneity is more influential, while a pure E-inhomogeneity yielded no benefits due to plastic deformation at the interlayer. However, a combined inhomogeneity (E and σ_y) is ideal.
- Once a crack is arrested by a soft layer, specimen failure is determined by crack re-initiation in the matrix material. *Re*-initiation is influenced by matrix and interlayer material and will happen at the location of the highest stress.
  ○ For a moderately mineral reinforced PP matrix, the re-initiation step is difficult, leading to a big increase in fracture toughness .
  ○ Crack re-initiation is easier in a highly mineral reinforced PP matrix. This leads to a smaller improvement in fracture toughness by soft interlayers.
  ○ *Re*-initiation is difficult for an interlayer made of soft PP. No stress transfer was possible between the matrix ligaments, which then behaved like decoupled bending specimens.
  ○ An interlayer made of standard PP yielded no benefits in fracture toughness because the difference in σ_y compared to the matrix was too small.
  ○ The introduction of side grooves to the specimens also greatly facilitated crack re-initiation.
- In order to more clearly depict the influence of soft interlayers, a new plotting technique was developed. Therein, the experimental *J*-integral $J_{\exp}$ is plotted against the newly defined parameter L. From
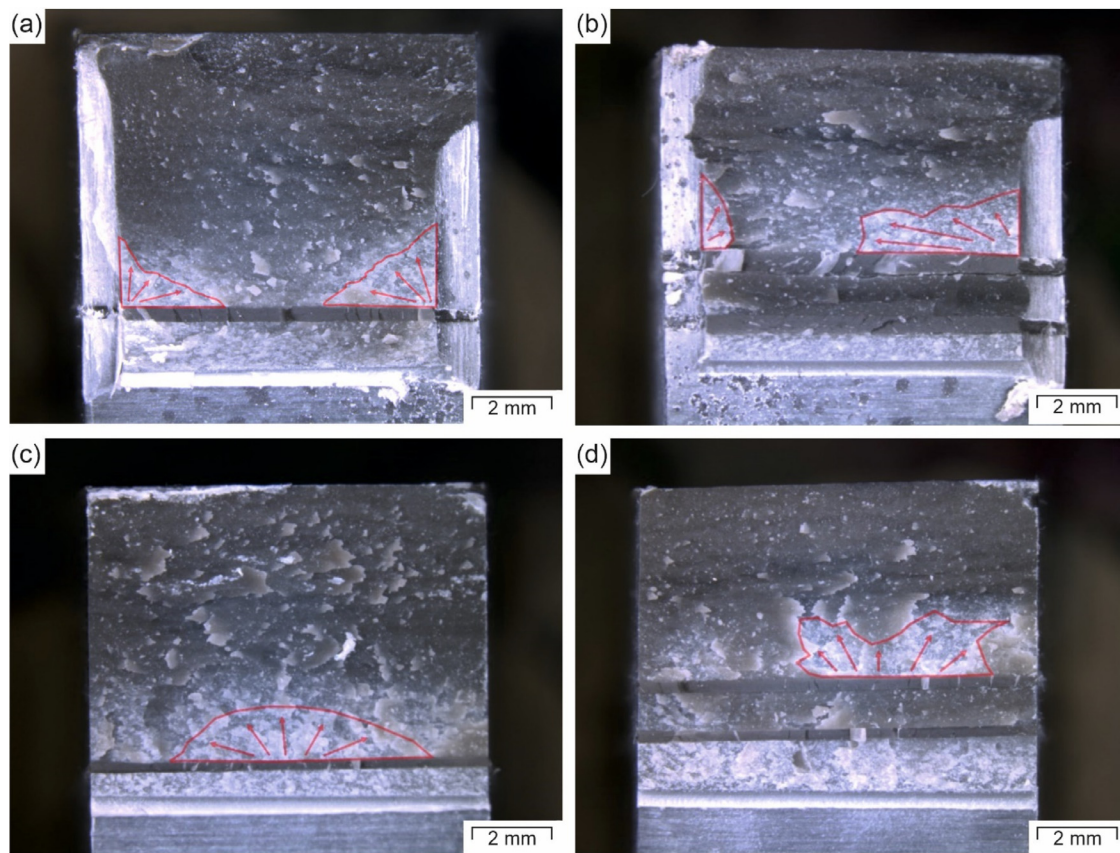
Fig. 14. Fracture surfaces of side grooved ML2 (a), side grooved ML4 (b), non-side grooved ML2 (c) and non-side grooved ML4 specimens (d). Crack re-initiation is indicated with red arrows.

these *J-L* plots, a fracture toughness for multi-layer composites, J_C^{ML}, could be determined.

In future work the influences of interlayer thickness, interlayer position and number of interlayers should be investigated. A full understanding of all influencing factors and their interactions has not been reached yet. The next task would be properly defining material laws, which quantitatively describe not only the crack growth, but also the re-initiation step. With these issues solved, analyzing structures with the help of FE methods could be attempted, yielding a most useful tool for structural optimization in multi-phase composites.

Declaration of Competing Interest

The authors declare that they have no known competing financial interests or personal relationships that could have appeared to influence the work reported in this paper.

Acknowledgements

Supplementary materials

Supplementary material associated with this article can be found, in the online version, at doi:10.1016/j.mechmat.2019.103243.

References

Aizenberg, J., Weaver, J.C., Thanawala, M.S., Sundar, V.C., Morse, D.E., Fratzl, P., 2005. Skeleton of euplectella sp.: structural hierarchy from the nanoscale to the macroscale. Science 309 (5732), 275–278. https://doi.org/10.1126/science.1112255.

Arbeiter, F.J., Frank, A., Pinter, G., 2016. Influence of molecular structure and reinforcement on fatigue behavior of tough polypropylene materials. J. Appl. Polym. Sci. 133 (38), 1237. https://doi.org/10.1002/app.43948.

Ashby, M., Cebon, D., 1993. Materials selection in mechanical design. J. Phys. IV France 03 (C7) C7-1-C7-9. https://doi.org/10.1051/jp4:1993701.

Barthelat, F., Espinosa, H.D., 2007. An experimental investigation of deformation and fracture of nacre–mother of pearl. Exp. Mech. 47 (3), 311–324. https://doi.org/10.1007/s11340-007-9040-1.

Chen, C., Pascual, J., Fischer, F., Kolednik, O., Danzer, R., 2007. Prediction of the fracture toughness of a ceramic multilayer composite – Modeling and experiments. Acta. Mat. 55 (2), 409–421. https://doi.org/10.1016/j.actamat.2006.07.046.

Cook, T.S., Erdogan, F., 1972. Stresses in bonded materials with a crack perpendicular to the interface. Int. J. Eng. Sci. 10 (8), 677–697. https://doi.org/10.1016/0020-7225(72)90063-8.

Dutta, A., Tekalur, S.A., 2014. Crack tortuosity in the nacreous layer – Topological dependence and biomimetic design guideline. Int. J. Solids Struct. (International Journal of Solids and Structures) 51 (2), 325–335. https://doi.org/10.1016/j.ijsolstr.2013.10.006.

Dutta, A., Tekalur, S.A., Miklavcic, M., 2013. Optimal overlap length in staggered architecture composites under dynamic loading conditions. J. Mech. Phys. Solids 61 (1), 145–160. https://doi.org/10.1016/j.jmps.2012.08.005.

Fischer, F.D., Predan, J., Fratzl, P., Kolednik, O., 2012. Semi-analytical approaches to assess the crack driving force in periodically heterogeneous elastic materials. Int. J. Fract. 173 (1), 57–70. https://doi.org/10.1007/s10704-011-9657-z.

Fratzl, P., Gupta, H.S., Fischer, F.D., Kolednik, O., 2007. Hindered crack propagation in materials with periodically varying young's modulus—lessons from biological materials. Adv. Mater. 19 (18), 2657–2661. https://doi.org/10.1002/adma.200602394.

Friedman, M., Cavins, J.F., Wall, J.S., 1965. Relative nucleophilic reactivities of amino groups and mercaptide ions in addition reactions with α,β-Unsaturated compounds 1,2. J. Am. Chem. Soc. 87 (16), 3672–3682. https://doi.org/10.1021/ja01094a025.

Gorsche, C., Seidler, K., Knaack, P., Dorfinger, P., Koch, T., Stampfl, J., Moszner, N., Liska, R., 2016. Rapid formation of regulated methacrylate networks yielding tough materials for lithography-based 3D printing. Polym. Chem. 7 (11), 2009–2014. https://doi.org/10.1039/C5PY02009C.

Gosch, A., Arbeiter, F.J., Berer, M., Pinter, G., 2018. Comparison of J-integral methods for the characterization of tough polypropylene grades close to the glass transition temperature. Eng. Fract. Mech. 203, 2–17. https://doi.org/10.1016/j.engfracmech.2018.06.002.

Grellmann, W., Langer, B., 2017. Deformation and fracture behaviour of polymer materials. Springer Series in Materials Science 247. Springer International Publishing, Cham, pp. s.l.

Gu, G.X., Takaffoli, M., Buehler, M.J., 2017. Hierarchically enhanced impact resistance of bioinspired composites. Adv. Mater. 29 (28). https://doi.org/10.1002/adma.201700060.

Gurtin, M.E., 2000. Configurational Forces as Basic Concepts of Continuum Physics 137 Springer New York, New York, NY.

Hale, G.E., Ramsteiner, F., 2001. J-Fracture toughness of polymers at slow speed. Pages 123–157 in: Fracture Mechanics Testing Methods For Polymers, Adhesives and Composites. Elsevier.

Huajian, G., 1991. Fracture analysis of nonhomogeneous materials via a moduli-perturbation approach. Int. J. Solids Struct. (International Journal of Solids and Structures) 27 (13), 1663–1682. https://doi.org/10.1016/0020-7683(91)90068-Q.

Jia, Z., Wang, L., 2019. 3D printing of biomimetic composites with improved fracture toughness. Acta. Mat. 173, 61–73. https://doi.org/10.1016/j.actamat.2019.04.052.

Jia, Z., Yu, Y., Hou, S., Wang, L., 2019. Biomimetic architected materials with improved dynamic performance. J. Mech. Phys. Solids 125, 178–197. https://doi.org/10.1016/j.jmps.2018.12.015.

Karalekas, D., Aggelopoulos, A., 2003. Study of shrinkage strains in a stereolithography cured acrylic photopolymer resin. J. Mater. Process. Technol. (Journal of Materials Processing Technology) 136 (1–3), 146–150. https://doi.org/10.1016/S0924-0136(03)00028-1.

Karger-Kocsis, J., Varga, J., Ehrenstein, G.W., 1997. Comparison of the fracture and failure behavior of injection-molded α- and β-polypropylene in high-speed three-point bending tests. J. Appl. Polym. Sci. 64 (11), 2057–2066. https://doi.org/10.1002/(SICI)1097-4628(19970613)64:11<2057:AID-APP1>3.0.CO;2-I.

Kolednik, O., 2000. The yield stress gradient effect in inhomogeneous materials. Int. J. Solids Struct. (International Journal of Solids and Structures) 37 (5), 781–808. https://doi.org/10.1016/S0020-7683(99)00060-8.

Kolednik, O., Kasberger, R., Sistaninia, M., Predan, J., Kegl, M., 2019. Development of damage-tolerant and fracture-resistant materials by utilizing the material inhomogeneity effect. J. Appl. Mech. 86, 1–12.

Kolednik, O., Predan, J., Fischer, F.D., 2010. Cracks in inhomogeneous materials: comprehensive assessment using the configurational forces concept. Eng. Fract. Mech. 77 (14), 2698–2711. https://doi.org/10.1016/j.engfracmech.2010.07.002.

Kolednik, O., Predan, J., Fischer, F.D., Fratzl, P., 2011. Bioinspired design criteria for damage-resistant materials with periodically varying microstructure. Adv. Funct. Mater. 21 (19), 3634–3641. https://doi.org/10.1002/adfm.201100443.

Lach, R., Grellmann, W., 2017. Time-Dependent fracture behaviour of polymers at impact and quasi-static loading conditions. In: Grellmann, W., Langer, B. (Eds.), Pages 3–21 in: Deformation and Fracture Behaviour of Polymer Materials. Springer International Publishing, Cham, pp. s.l.

Lach, R., Krolopp, T., Hutar, P., Grellmann, W., 2014. Influence of the interface and the additional layer on the stable crack propagation through polyolefin bilayered structures. Procedia Mater. Sci. 3, 867–872. https://doi.org/10.1016/j.mspro.2014.06.141.

Lach, R., Krolopp, T., Hutar, P., Nezbedova, E., Grellmann, W., 2016. Short-Term stable crack propagation through polyolefin Single- and Bilayered structures - Influence of welding. Composition and Direction of Crack Propagation. SSP 258, 538–541. https://doi.org/10.4028/www.scientific.net/SSP.258.538.

Lach, R., Krolopp, T., Hutař, P., Nezbedová, E., Grellmann, W., 2017. Influence of welding and composition on the short-term stable crack propagation through polyolefin Single- and Bilayered structures. In: Grellmann, W., Langer, B. (Eds.), Pages 211–227 in: Deformation and Fracture Behaviour of Polymer Materials. Springer International Publishing, Cham, pp. s.l.

Lach, R., Seidler, S., Grellmann, W., 2005. Resistance against the intrinsic rate of fracture mechanics parameters for polymeric materials under moderate impact loading. Mech. Time-Depend. Mater. 9 (2–3), 103–119. https://doi.org/10.1007/s11043-005-1084-y.

Levi, C., Barton, J.L., Guillemet, C., Le Bras, E., Lehuede, P., 1989. A remarkably strong natural glassy rod: the anchoring spicule of the monorhaphis sponge. J. Mater. Sci. Lett. 8 (3), 337–339. https://doi.org/10.1007/BF00725516.

Ligon-Auer, S.C., Schwentenwein, M., Gorsche, C., Stampfl, J., Liska, R., 2016. Toughening of photo-curable polymer networks: a review. Polym. Chem. 7 (2), 257–286. https://doi.org/10.1039/C5PY01631B.

Mao, L.-.B., Gao, H.-.L., Yao, H.-.B., Liu, L., Cölfen, H., Liu, G., Chen, S.-.M., Li, S.-.K., Yan, Y.-.X., Liu, Y.-.Y., Yu, S.-.H., 2016. Synthetic nacre by predesigned matrix-directed mineralization. Science 354 (6308), 107–110. https://doi.org/10.1126/science.aaf8991.

Martínez, A.B., León, N., Arencón, D., Rodríguez, J., Salazar, A., 2013. On the effect of the different notching techniques on the fracture toughness of petg. Polym. Test. 32 (7), 1244–1252. https://doi.org/10.1016/j.polymertesting.2013.07.016.

Martínez, A.B., Salazar, A., León, N., Illescas, S., Rodríguez, J., 2016. Influence of the notch-sharpening technique on styrene-acrylonitrile fracture behavior. J. Appl.

Polym. Sci. 133 (32), 11. https://doi.org/10.1002/app.43775.

Maugin, G.A., 1995. Material forces: concepts and applications. Appl. Mech. Rev. 48 (5), 213. https://doi.org/10.1115/1.3005101.

Meijer, H.E.H., Govaert, L.E., 2005. Mechanical performance of polymer systems: the relation between structure and properties. Prog. Polym. Sci. 30 (8–9), 915–938. https://doi.org/10.1016/j.progpolymsci.2005.06.009.

Miserez, A., Weaver, J.C., Thurner, P.J., Aizenberg, J., Dauphin, Y., Fratzl, P., Morse, D.E., Zok, F.W., 2008. Effects of laminate architecture on fracture resistance of sponge biosilica: lessons from nature. Adv. Funct. Mater. 18 (8), 1241–1248. https://doi.org/10.1002/adfm.200701135.

Morgan, E.F., Barnes, G.L., Einhorn, T.A., 2013. The bone organ system. Pages 3–20 in: Osteoporosis. Elsevier.

Mostegel, F.H., Roth, M., Gassner, M., Oesterreicher, A., Piock, R., Edler, M., Griesser, T., 2016. Vinylcarbonates as low-toxic monomers for digital ink-jet inks: promising alternatives to acrylate based systems. Prog. Org. Coat. 94, 116–123. https://doi.org/10.1016/j.porgcoat.2016.01.003.

Muju, S., 2000. Crack propogation in bimaterial multilayered periodically microcracking composite media. Compos. Sci. Technol. 60 (12–13), 2213–2221. https://doi.org/10.1016/S0266-3538(00)00016-6.

Müller, W.E.G., Wang, X., Cui, F.-.Z., Jochum, K.P., Tremel, W., Bill, J., Schröder, H.C., Natalio, F., Schlossmacher, U., Wiens, M., 2009. Sponge spicules as blueprints for the biofabrication of inorganic-organic composites and biomaterials. Appl. microbiol. biot. 83 (3), 397–413. https://doi.org/10.1007/s00253-009-2014-8.

Müller, W.E.G., Wang, X., Kropf, K., Ushijima, H., Geurtsen, W., Eckert, C., Tahir, M.N., Tremel, W., Boreiko, A., Schlossmacher, U., Li, J., Schröder, H.C., 2008. Bioorganic/inorganic hybrid composition of sponge spicules: matrix of the giant spicules and of the comitalia of the deep sea hexactinellid monorhaphis. J. Struct. Biol. 161 (2), 188–203. https://doi.org/10.1016/j.jsb.2007.10.009.

Murali, P., Bhandakkar, T.K., Cheah, W.L., Jhon, M.H., Gao, H., Ahluwalia, R., 2011. Role of modulus mismatch on crack propagation and toughness enhancement in bioinspired composites. Phys. Rev. E 84 (1), 739. https://doi.org/10.1103/PhysRevE.84.015102.

Náhlík, L., Šestáková, L., Hutař, P., Knésl, Z., 2010. Generalized linear elastic fracture mechanics: an application to a crack touching the bimaterial interface. KEM 452–453, 445–448. https://doi.org/10.4028/www.scientific.net/KEM.452-453.445.

Nylander-French, L.A., French, J.E., 1998. Tripropylene glycol diacrylate but not ethyl acrylate induces skin tumors in a twenty-week short-term tumorigenesis study in tg.ac (v-Ha-ras) mice. Toxicol. Pathol. (Toxicologic pathology) 26 (4), 476–483. https://doi.org/10.1177/019262339802600403.

Oesterreicher, A., Ayalur-Karunakaran, S., Moser, A., Mostegel, F.H., Edler, M., Kaschnitz, P., Pinter, G., Trimmel, G., Schlögl, S., Griesser, T., 2016a. Exploring thiol-yne based monomers as low cytotoxic building blocks for radical photopolymerization. J. Polym. Sci. Part A: Polym. Chem. 54 (21), 3484–3494. https://doi.org/10.1002/pola.28239.

Oesterreicher, A., Gorsche, C., Ayalur-Karunakaran, S., Moser, A., Edler, M., Pinter, G., Schlögl, S., Liska, R., Griesser, T., 2016b. Exploring network formation of tough and biocompatible thiol-yne based photopolymers. Macromol. rapid comm. 37 (20), 1701–1706. https://doi.org/10.1002/marc.201600369.

Oesterreicher, A., Moser, A., Edler, M., Griesser, H., Schlögl, S., Pichelmayer, M., Griesser, T., 2017. Investigating photocurable thiol-yne resins for biomedical materials. Macromol. Mater. Eng. 302 (5), 1600450. https://doi.org/10.1002/mame.201600450.

Oesterreicher, A., Wiener, J., Roth, M., Moser, A., Gmeiner, R., Edler, M., Pinter, G., Griesser, T., 2016c. Tough and degradable photopolymers derived from alkyne monomers for 3D printing of biomedical materials. Polym. Chem. 7 (32), 5169–5180. https://doi.org/10.1039/c6py01132b.

Rice, J.R., 1968. A path independent integral and the approximate analysis of strain concentration by notches and cracks. J. Appl. Mech. 35 (2), 379. https://doi.org/10.1115/1.3601206.

Ritchie, R.O., 2011. The conflicts between strength and toughness. Nat. Mater. 10 (11), 817–822. https://doi.org/10.1038/nmat3115.

Salazar, A., Frontini, P.M., Rodríguez, J., 2014. Determination of fracture toughness of propylene polymers at different operating temperatures. Eng. Fract. Mech. 126, 87–107. https://doi.org/10.1016/j.engfracmech.2014.04.023.

Salazar, A., Rico, A., Rodríguez, S., Navarro, J.M., Rodríguez, J., 2012. Relating fracture behavior to spherulite size in conrolled-rheology polypropylenes. Polym. Eng. Sci. 52 (4), 805–813. https://doi.org/10.1002/pen.22145.

Salazar, A., Rodríguez, J., Arbeiter, F., Pinter, G., Martínez, A.B., 2015. Fracture toughness of high density polyethylene: fatigue pre-cracking versus femtolaser, razor sharpening and broaching. Eng. Fract. Mech. 149, 199–213. https://doi.org/10.1016/j.engfracmech.2015.07.016.

Schwalbe, K.-.H., Neale, B., 1995. A procedure for determining the fracture behaviour of materials-The unified fracture mechanics test method efam gtp 94. Fat. Fract. Eng. Mater. Struct. (Fatigue & Fracture of Engineering Materials and Structures) 18 (4), 413–424. https://doi.org/10.1111/j.1460-2695.1995.tb01185.x.

Seidler, S., Koch, T., Grellmann, W., 2001. Crack tip deformation and toughness in polypropylenes. In: 10th International Conference on Fracture (ICF 10), pp. 120–125.

Simha, N.K., Fischer, F.D., Kolednik, O., Predan, J., Shan, G.X., 2005. Crack tip shielding or anti-shielding due to smooth and discontinuous material inhomogeneities. Int. J. Fract. 135 (1–4), 73–93. https://doi.org/10.1007/s10704-005-3944-5.

Simha, N.K., Fischer, F.D., Kolednik, O., Chen, C.R., 2003. Inhomogeneity effects on the crack driving force in elastic and elastic–plastic materials. J. Mech. Phys. Solids 51 (1), 209–240. https://doi.org/10.1016/S0022-5096(02)00025-X.

Sistaninia, M., Kolednik, O., 2014. Effect of a single soft interlayer on the crack driving force. Eng. Fract. Mech. 130, 21–41. https://doi.org/10.1016/j.engfracmech.2014.02.026.

Song, J., Fan, C., Ma, H., Liang, L., Wei, Y., 2018. Crack deflection occurs by constrained microcracking in nacre. Acta. Mech. Sin. 34 (1), 143–150. https://doi.org/10.1007/s10409-017-0724-1.

Woesz, A., Weaver, J.C., Kazanci, M., Dauphin, Y., Aizenberg, J., Morse, D.E., Fratzl, P., 2006. Micromechanical properties of biological silica in skeletons of deep-sea sponges. J. Mater. Res. 21 (08), 2068–2078. https://doi.org/10.1557/jmr.2006.0251.

Wu, K., Zheng, Z., Zhang, S., He, L., Yao, H., Gong, X., Ni, Y., 2019. Interfacial strength-controlled energy dissipation mechanism and optimization in impact-resistant nacreous structure. Mater Des 163, 107532. https://doi.org/10.1016/j.matdes.2018.12.004.

Yadav, R., Goud, R., Dutta, A., Wang, X., Naebe, M., Kandasubramanian, B., 2018. Biomimicking of hierarchal molluscan shell structure via layer by layer 3D printing. Ind. Eng. Chem. Res. 57 (32), 10832–10840. https://doi.org/10.1021/acs.iecr.8b01738.

Yang, Y., Song, X., Li, X., Chen, Z., Zhou, C., Zhou, Q., Chen, Y., 2018. Recent progress in biomimetic additive manufacturing technology: from materials to functional structures. Adv. Mater., e1706539. https://doi.org/10.1002/adma.201706539.

Zak, A.R., Williams, M.L., 1963. Crack point stress singularities at a bi-material interface. J. Appl. Mech. 30 (1), 142. https://doi.org/10.1115/1.3630064.

Zechner, J., Kolednik, O., 2013. Fracture resistance of aluminum multilayer composites. Eng. Fract. Mech. 110, 489–500. https://doi.org/10.1016/j.engfracmech.2012.11.007.

Zhao, H., Yang, Z., Guo, L., 2018. Nacre-inspired composites with different macroscopic dimensions: strategies for improved mechanical performance and applications. NPG Asia Mater 10 (4), 1–22. https://doi.org/10.1038/s41427-018-0009-6.
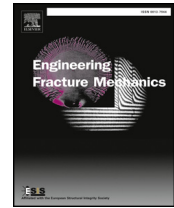
*7.3. **Publication III***

Title:	Application of the material inhomogeneity effect for the improvement of fracture toughness of a brittle polymer
Authors:	Abhishek Tiwari[a,b], Johannes Wiener[c], Florian Arbeiter[c], Gerald Pinter[c], Otmar Kolednik[a]
Affiliation:	[a] Erich-Schmid-Institute of Materials Science, Austrian Academy of Science, 8700 Leoben, Austria [b] Materials Center Leoben GmbH, 8700 Leoben, Austria [c] Materials Science and Testing of Polymers, Montanuniversitaet Leoben, 8700 Leoben, Austria
DOI:	https://doi.org/10.1016/j.engfracmech.2019.106776
Conceptualization:	Abhishek Tiwari (70%), Otmar Kolednik (30%)
Methodology:	Abhishek Tiwari (60%), Johannes Wiener (20%), Otmar Kolednik (20%)
Validation:	equal contribution by all authors
Investigation:	Abhishek Tiwari (70%), Johannes Wiener (30%)
Writing-Original Draft:	Abhishek Tiwari (80%), Otmar Kolednik (20%)
Writing-Review & Editing	equal contribution by all authors
Supervision	Florian Arbeiter (20%) , Gerald Pinter (20%), Otmar Kolednik (60%)

Application of the material inhomogeneity effect for the improvement of fracture toughness of a brittle polymer

Abhishek Tiwari[a,b,*], Johannes Wiener[c], Florian Arbeiter[c], Gerald Pinter[c], Otmar Kolednik[a]

[a] Erich Schmid Institute of Materials Science, Austrian Academy of Sciences, Leoben, Austria
[b] Material Center Leoben Forschung GmbH, Leoben, Austria
[c] Materials Science and Testing of Polymers, Montanuniversitaet Leoben, Austria

A B S T R A C T

In a multilayered structure with a crack, a spatial change in the mechanical properties of the material strongly influences the crack driving force. This material inhomogeneity effect can be utilized to improve the fracture toughness of a given structure by inserting thin, soft interlayers into the material. The effectiveness of this procedure has been demonstrated on high-strength materials, such as metallic alloys and ceramics. It is shown in this article that the material inhomogeneity effect can be also successfully applied to polymers and that it is possible to predict the improvement in fracture toughness by a numerical analysis. First, a numerical case study based on the configurational force concept is performed on a brittle polymer matrix with interlayers made of materials with different strength and Young's modulus. After selecting the most appropriate interlayer material, a composite is fabricated, which contains a single interlayer. Fracture toughness experiments show approximately 7 times higher fracture toughness for the composite in comparison to the homogeneous matrix material. Numerical fracture mechanics tests are performed on homogeneous and composite material using the cohesive zone model for crack growth simulation. A procedure to calibrate the cohesive zone parameters is worked out, which is relatively easy for the homogeneous material, but more sophisticated for the composite material. The numerical analysis provides a tool for predicting the fracture toughness of multi-layered polymer composites.

1. Introduction

It is a common practice to improve the fracture toughness and strength of a component by combining two different materials in various fashions [1–3]. Many of the naturally occurring materials, such as nacre and bone, are found to have enhanced fracture toughness and strength owing to the complex arrays of different materials [4–7]. Munch et al. [8] showed in his study that Al_2O_3, which has a fracture toughness of approximately 2.5 MPa$\sqrt{m}$, when combined with lameller Polymethylmethacrylate (PMMA), results in a fracture toughness of 15 MPa$\sqrt{m}$. The fracture toughness of multilayered components can improve by different extrinsic mechanisms, such as crack deflection and meandering, zone shielding, contact shielding, etc. [9]. However, the fracture toughness of a multi-layer system can be influenced just by the presence of material inhomogeneity. The material inhomogeneity effect arises due to a spatial variation of the mechanical property of the material. In presence of a material inhomogeneity, the crack driving force

---

Nomenclature

List of symbols and abbreviations

a_o	initial crack length
b_o	initial ligament length
dl	a line element of an interface
e	unit vector in the direction of crack extension
f	configurational force vector
r_{pl}	plastic zone radius
t	thickness of interlayer
B	thickness of fracture mechanics specimen
B_N	net thickness of fracture mechanics specimen
C_{IF1}, C_{IF2}	material inhomogeneity due to first interface, and second interface
C_{inh}	material inhomogeneity term
E	Young's modulus
H	full length of the fracture mechanics specimen
J	J-integral
J_o	experimental J-integral
J_{exp}	experimental J-integral with crack growth correction
J_{num}	numerically evaluated J-integral
J_{tip}	near-tip J-integral or crack driving force
J_{far}	far-field J-integral
J_C	fracture initiation toughness measured in terms of J-integral
L	distance of first interface from current crack tip
P	force applied to the fracture mechanics specimen
S	span length of a single edge notched bend specimen
η	dimensionless parameter with a value of 2 for single edge notched bend specimen
δ	separation distance in cohesive elements

|	
δ_i	separation distance at damage initiation in cohesive elements
δ_f	separation distance at failure in cohesive elements
ε_{eng}	engineering strain
$\varepsilon_{eng,pl}$	engineering plastic strain
ε_{true}	true strain
$\varepsilon_{true,pl}$	true plastic strain
v_{LL}	load line displacement
ψ	J reduction coefficient
σ_o	yield strength
σ_{eng}	engineering stress
σ_{true}	true stress
Γ	separation energy
Σ	contour along the interface between two materials
Δa	amount of crack extension
Δa_{preIL}	amount of crack extension before an interlayer
Δa_{postIL}	amount of crack extension after an interlayer
CDF	crack driving force
CPE4	bilinear plane strain quadrilateral element
CPS4	bilinear plane stress quadrilateral element
CZ	cohesive zone
ESIS	European Structural Integrity Society
FE	finite element
min	minutes
mm	millimeters
NSG	non side grooved
P1, P2	interlayer materials
Roller-1	loading roller in a single edge notched bend specimen
Roller-2	support roller in a single edge notched bend specimen
SENB	single edge notched bend specimen
SG	side grooved
TSL	traction separation law
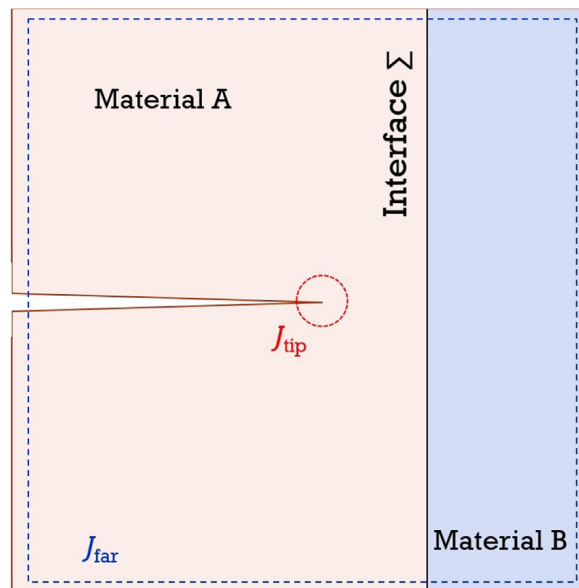
Fig. 1. Schematic representation of the material inhomogeneity, C_{inh}, in presence of an interface between Material A and Material B in front of a crack.

(CDF), expressed as near-tip J-integral, J_{tip}, is different from the far-field J-integral, J_{far}, which can be seen as the driving force generated by the applied load. The difference between J_{tip} and J_{far}, is the so called "material inhomogeneity term", C_{inh}. This material inhomogeneity term can be calculated by applying the concept of configurational forces [10–12].

Configurational forces are thermodynamic driving forces on defects in materials. Examples are voids, cracks, interfaces, dislocations, etc [13,14]. The material inhomogeneity term, C_{inh}, equals the sum of the configurational forces emanating from all the material inhomogeneities in a body. For example, in a bimaterial system of materials A and B with a crack, as shown in Fig. 1, the interface, Σ, between the two material acts as a material inhomogeneity, which influences the crack driving force. The material inhomogeneity term, C_{inh}, in this case is given by the sum of the configurational forces, $\mathbf{f}$, along the interface

$$C_{inh} = \mathbf{e} \cdot \int_\Sigma \mathbf{f} dl, \qquad (1)$$

where $\mathbf{e}$ denotes the unit vector in the direction of crack extension and dl is a line element of Σ [10,11]. Note that the configurational force at an interface has a dimension of N/m^2, whereas a configurational force in the bulk of a material has a dimension of N/m^3. The material inhomogeneity term has the same dimension as the J-integral, kJ/m^2. The crack driving force, J_{tip}, therefore, is described as

$$J_{tip} = J_{far} + C_{inh}. \qquad (2)$$

In cases where a transition from comparatively stiff to compliant material occurs, the scalar material inhomogeneity term, C_{inh}, is positive. This results in a greater J_{tip} in comparison to J_{far}, causing an anti-shielding effect on the crack tip. In an opposite scenario where a compliant to stiff transition occurs, J_{tip} will be smaller than J_{far}, resulting in a shielding effect.

When an interlayer of a secondary material is placed in a matrix, there exist two interfaces at the left and right boundaries of the interlayer. In this case the material inhomogeneity term, C_{inh} is given by a cumulative effect of the first and second interfaces [15,16], IF1 and IF2,

$$C_{inh} = C_{IF1} + C_{IF2}, \qquad (3)$$

where C_{IF1} and C_{IF2} are calculated by Eq. (1) along the respective interfaces.

The material inhomogeneity effect may arise due to the differences in Young's modulus (E), or due to differences in yield strength (σ_o) for ideal plastic material behaviour[1]. These two categories are called E-inhomogeneity and σ_o- inhomogeneity. The material inhomogeneity can also be a combination of both, which is referred to as $(E + \sigma_o)$-inhomogeneity. The effect of material inhomogeneity in a multi-layer system in general perspective and the differences due to E-, σ_o- and $(E + \sigma_o)$-inhomogeneity is described in detail by Kolednik et al. [17].

The skeleton of a deep sea sponge is a classical example of fracture toughness improvement due to material inhomogeneity effect, which has been analysed in detail by Kolednik et al. [7]. The structure of the sponge consists of cylindrical layers of brittle bio-glass with thin interlayers of soft protein, which improves the fracture toughness of the structure. Experimental evidence for the improvement of fracture toughness by utilizing the material inhomogeneity effect has been presented by Zechner and Kolednik [18] on a aluminium multilayer with polymer interlayers, and by Sistaninia et al. [19] and Kolednik et al. [17] on steel multilayers. The fracture toughness of ceramic multilayers can be improved by combining the effects of E-inhomogeneity and spatial residual stress variation [20]. Similar effects can be observed in thin film systems Kozic et al. [21]. Lee et al. [22] demonstrated, using analytical calculations and experiments, that a transition in material's mechanical response plays a significant role in crack propagation across adhesive polymer interlayer in a glass matrix.

In the class of polymer materials, the influence of material inhomogeneity on fracture toughness is not yet investigated. In comparison to conventional metallic or ceramic materials, polymers show a very soft mechanical response. The Young's modulus and yield strength of polymers are significantly smaller than for metallic or ceramic materials. Therefore, the significance of the material inhomogeneity effect in a composite made of polymer matrix is questionable, as the material inhomogeneity effect depends on the differences in the mechanical behaviour of the materials.

Therefore, a preliminary numerical analysis will be performed to examine material inhomogeneity effects for different types of interlayers in a brittle polymer matrix. Based on the results of this examination, which is described in the next section, a composite with the best interlayer material will be manufactured and tested in order to determine the improvement in fracture toughness due to the interlayer (Section 3). The fracture behaviour of the homogeneous brittle polymer as well as the composite will be studied numerically in Section 4.

2. Numerical evaluation of the material inhomogeneity effects for a brittle polymer matrix

2.1. Evaluation of crack driving force

The brittle polymer matrix material, whose fracture toughness shall be improved, is a polypropylene compound with moderate reinforcement of talcum particles. The material inhomogeneity effect is evaluated for three different types of interlayer materials. Two interlayer materials, P1 and P2, are polymers that behave softer than the matrix material. Interlayer material P1 is a standard grade of polypropylene, whereas the material P2 is a very compliant grade of modified polypropylene. These polymer materials are a part of ongoing research. Therefore, the exact compositional and microstructural details cannot be disclosed at this point. Similar

---

[1] The material inhomogeneity may also arise due to differences in hardening exponents for materials with same σ_o.

materials have been investigated by [23,24]. The third interlayer material is the aluminium alloy Al7075-T6, which has a higher Young's modulus and yield strength than the matrix material. The material inhomogeneity effect is evaluated by assuming stationary cracks in single edge notched tension (SENT) specimens, but with crack tips at different locations with respect to the interlayer. The
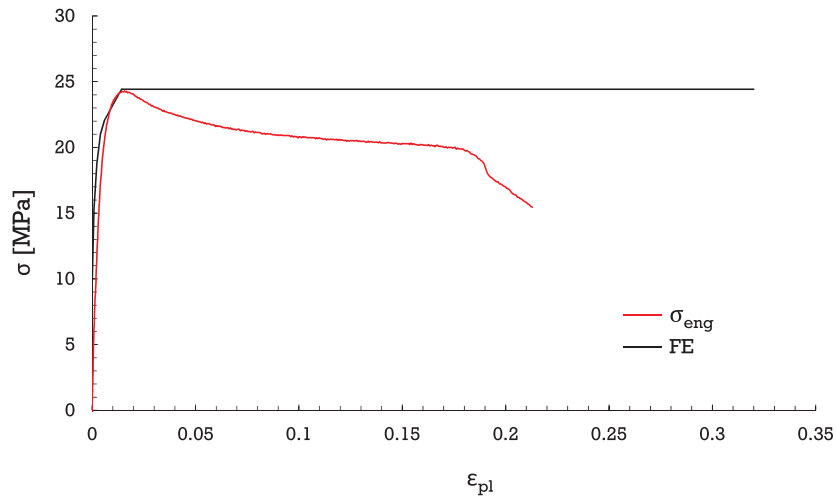
(a) Matrix material
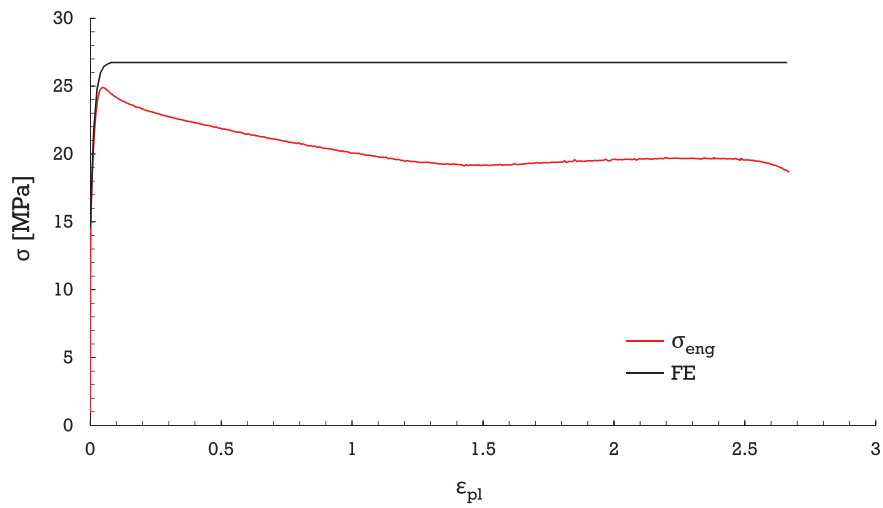
(b) Interlayer material (P1)
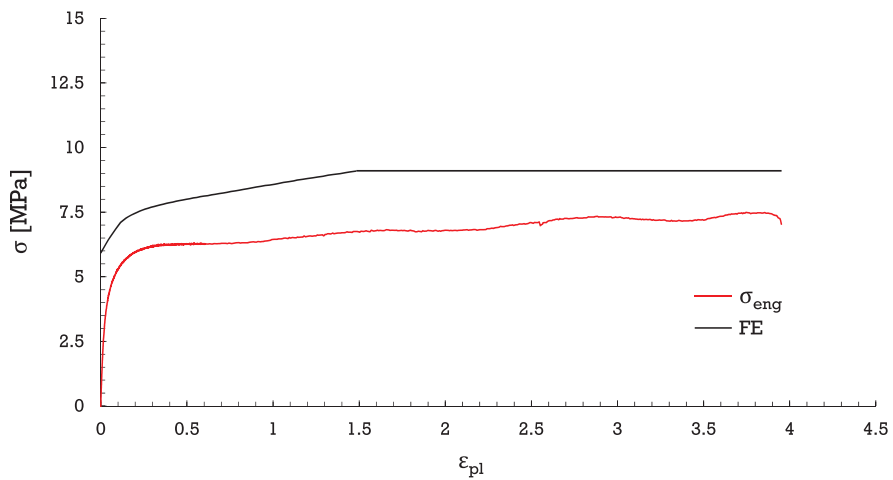
(c) Interlayer material (P2)

Fig. 2. Uniaxial stress-plastic strain behaviour of (a) matrix, (b) interlayer P1 and (c) interlayer P2 materials.

numerical modelling is performed using the commercial FE package ABAQUS [25]. The specimen has a width, $W = 20$ mm, and a height, $H = 45$ mm; the initial crack length is $a_o = 10$ mm. The interlayer has a thickness of $t = 0.5$ mm. The first interface of the interlayer (IF1) lies at a distance of $L = 2$ mm from the initial crack tip. Only half of the specimen is modelled with two-dimensional plane strain elements using small strain formulation. The element size near the crack tip is 0.1×0.1 mm^2. The crack driving force, J_{tip}, is evaluated using Eq. (2) and Eq. (3). Hereby, for each crack tip position, the load is adjusted so that a constant value of the far-field J-integral appears, $J_{far} = 2.4$kJ/m^2. The value of J_{far} is calculated by an integration of the configurational forces inside the far-field contour and multiplication with the unit vector in crack extension direction, **e**. Alternatively, J_{far} could also be evaluated by applying the virtual crack extension method of ABAQUS [26]. The far-field contour is a contour, which lies near the outer boundary of the specimen. The shape of this contour is indicated in Fig. 1 (also in Fig. 10). The configurational forces are calculated after the FE stress-strain analysis, using a post-processing program. Details about the post-processing code are provided in Kolednik et al. [17]. The maximum influence of the material inhomogeneity effect is expected at the interfaces, IF1 and IF2 [16]. Therefore, an accurate calculation of the crack driving force near these locations of the crack tip is important. However, modelling for crack tip positions *exactly* at the interface is impossible, arising from the fact that the nodes at the interfaces are shared by two different materials. In order to get accurate J_{tip}-values, a certain number of elements should lie between crack tip and interface. The closest crack tip positions are 0.1 mm (10 elements) away from the interface IF1 and 0.05 mm at (5 elements) away from IF2. There are mainly two reasons for performing the J_{tip} calculation at a distance and not exactly at the interfaces. First reason is the discretization in FE analysis. Secondly, the accurate estimates of C_{inh} and J_{tip} require that the interfaces should not be in contact with the process zone of the crack tip. The process zone lies in front of the crack tip. Therefore, the distance between crack tip and interface should be larger when a crack is approaching an interface than in the case where the crack has already crossed the IF, compare Fig. 4 (b).

2.2. Material properties and numerical implementation

In general, polymers especially Polypropylene shows mechanical behaviour, which is strongly dependent on loading rate. However, the rate dependence is not so strong for a polypropylene filled moderately with mineral particles [23]. As the polymer investigated here is moderately reinforced with talcum particles, the rate dependence of mechanical response is not taken into consideration. The Young's moduli of the polymer matrix and interlayer materials are obtained by fitting the engineering stress versus strain response in the range of 0.05 to 0.25% strain, which is in accordance with ISO 527 [27]. The tensile tests to obtain the uniaxial response of the polymer materials are performed at a cross-head speed of 1 mm per minute (mm/min). The tensile specimens are of rectangular shape with an initial minimum cross-section of 10×4 mmtextsuperscript2 and a gauge length of 20 mm. Five tensile specimens were tested for every material, and the data from a representative specimen, which followed the average behaviour, was selected as input for the finite element analysis. The representative engineering stress (σ_{eng}) versus engineering plastic strain ($\varepsilon_{eng,pl}$) curves are shown in Fig. 2.

The mechanical properties assigned to the matrix and polymer interlayer materials in the FE simulations are obtained from these experiments. For values up to the maximum engineering stress, the σ_{eng} versus $\varepsilon_{eng,pl}$ data are converted into true stress (σ_{true}) versus true plastic strain ($\varepsilon_{true,pl}$) values. Ideally plastic material behaviour is assumed for higher plastic strain values, as shown in Fig. 2. The true stress values for the material P2 become very high due to very large strains in the material. To avoid such high stresses, which can appear under uniaxial loading but are unrealistic for the triaxial stress state in front of a crack tip, the true stress is truncated at a plastic strain of 150% and is assumed to remain constant beyond this point. Young's modulus, E, and yield stress, σ_o, for the Al7075 interlayer are taken from the work of Zechner and Kolednik [18]. Since the hardening is small, the material is modelled as linear elastic-ideally plastic material. The mechanical properties of all matrix and interlayer materials are listed in Table 1.

2.3. Preliminary analysis results

Fig. 3 shows, for the three different interlayer materials, the variation of the ratio, J_{tip}/J_{far}, for different crack tip locations. If the crack tip location is far from the interlayer, the value of J_{tip}, is equal to J_{far}, showing no influence of the material inhomogeneity. For softer interlayer materials, P1 and P2, the ratio, J_{tip}/J_{far}, increases with increasing a/W, until the crack reaches the first interface ($a/W = 0.6$). The reason is the anti-shielding effect of IF1. Inside the interlayer, the shielding effect of IF2 becomes more and more significant, and the ratio, J_{tip}/J_{far}, decreases. For crack tip locations, beyond the interlayer, J_{tip}/J_{far} increases again and reaches J_{far} for higher values of a/W.

The minimum value of the ratio, J_{tip}/J_{far}, resembles the maximum degree of J reduction under the influence of material inhomogeneity. Hence, a J reduction coefficient, ψ, can be described as

Table 1
Material properties of the matrix and interlayer materials for the preliminary FE analysis.

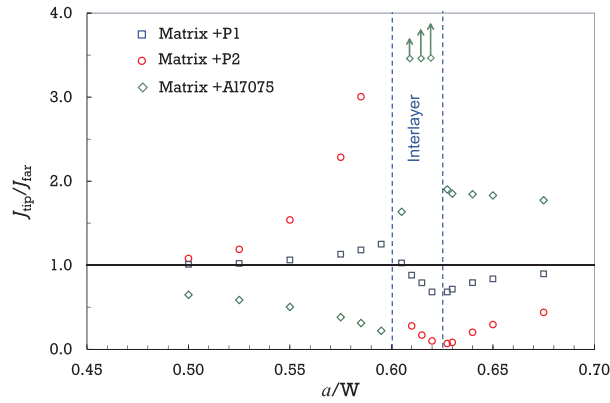| Materials		Young's Modulus (E) [MPa]	Poisson's ratio (ν)	Yield strength (σ_o) [MPa]	J reduction coefficient (ψ)
Matrix		4400	0.3	20	
490ptInterlayer]	IL1	1297	0.44	24	0.68
	IL2	251	0.28	6	0.067
	Al7075	70,000	0.3	500	0.22

Fig. 3. Ratio of near tip to far field *J*-integral for different crack tip locations with respect to the interlayer.

$$\psi = \frac{\min(J_{\text{tip}})}{J_{\text{far}}}, \tag{4}$$

where $\min(J_{\text{tip}})$ is the minimum value of J_{tip} out of the values obtained for different crack tip locations [16,19]. A small value of ψ suggests a large fracture toughness improvement, since a high load is required for crack growth.

The stiffer interlayer made of Al7075 results in a similar behaviour of $J_{\text{tip}}/J_{\text{far}}$, but opposite in nature. The ratio $J_{\text{tip}}/J_{\text{far}}$ first decreases for $a/W < 0.6$, due to the strong shielding effect arising at IF1 owing to a stiff to compliant transition. Therefore, the minimum J_{tip}-value occurs at IF1. A strong anti-shielding effect is found near IF2 inside the interlayer.

The *J*-reduction coefficients of the three interlayer materials are listed in Table 1. In response to the question raised previously in Section 1, Fig. 3 shows that in the class of polymer materials, the material inhomogeneity effect is significant when a large difference in mechanical properties between matrix and interlayer exists. This is so for P2 material where the Young's modulus is 0.057 times of the Young's modulus of the matrix material and the yield strength is 0.3 times that of the matrix material. This results in a very low *J* reduction coefficient, $\psi = 0.067$.

The interlayer material P1 shows a low propensity for crack arrest, since J_{tip} shows only little decrease near IF2 and the *J*-reduction coefficient is high, $\psi = 0.67$. The main reason is that only an *E*-inhomogeneity (with a ratio of 0.3) appears; the yield strengths are similar. For elastic material behaviour, this ratio is high enough for a significant material inhomogeneity effect. However, the *E*-inhomogeneity effect is strongly reduced in case of high plastic deformation [12,17].

Fig. 3 shows that, for low-strength materials such as polymers, the insertion of stiffer interlayers might be an interesting option for providing crack arrest and an increase in fracture toughness. The Al7075 interlayer produces a *J*-reduction coefficient of $\psi = 0.22$, i.e., it is three times higher than that for the interlayer material P2. Note that the (inverse) *E*- and σ_0-ratios of Al7075 with respect to the matrix material are 0.063 and 0.04, respectively, i.e., the ratios are comparable or even better than that of the material P2. The reason for the lower ψ-value in the material P2 lies, presumably, in the low yield strength of this material. The reason is that the elastic strain energy stored in the material, which is low for low σ_0, is essential for delivering the crack driving force.

From the numerical evaluations presented in this section, it is evident that P2 is the best interlayer material, showing the smallest *J*-reduction coefficient [2]. Therefore, it can be expected that the insertion of a P2-interlayer will result in a considerable fracture toughness improvement of the brittle polymer matrix material. To check the reality of this assumption, a composite was fabricated, which contains a single interlayer of P2-material. Fracture mechanics experiments were performed on the homogeneous matrix material, as well as on the composite material. The details of the fracture mechanics experiments are discussed in the next section.

3. Fracture mechanics experiments

3.1. Experimental details

The fracture mechanics tests are performed on single edge notched bend (SENB) specimens under three point bending. The dimensions of the composite specimen are shown in Fig. 4. The specimens have a width, *W* of 20 mm, a thickness of $B = 10$ mm, and a height of $H = 90$ mm. The span length, *S*, is 80 mm. The initial crack length, a_0, is approximately 12 mm for homogeneous specimens and 11 mm for composite specimens. The initial crack is implemented by razor blade cutting. The distance between initial crack tip and first interface of the interlayer is approximately $L \approx 1.2$ mm. The thickness of the interlayer (*t*) is approximately 0.35 mm. Both interlayer location (*L*) and interlayer thickness exhibit scatter due to manufacturing limitations. The scatter for *L* is in the range of 0.79 to 1.32 mm, and for *t* in the range of 0.21 to 0.45 mm. Both side grooved (SG) and non-side grooved (NSG) specimens are tested for the homogeneous material. The side grooves were made by power saw with a root radius of 0.25 mm, see Fig. 4 (a). The side grooved specimens have 25 % reduction in the net thickness, B_{N}. Only NSG specimens are tested for composite

---

[2] This is so for applications where the strength of the interlayer material does not play a role. For other applications, a material with higher strength might be the best option, leading to a somewhat enhanced *J*-reduction coefficient.
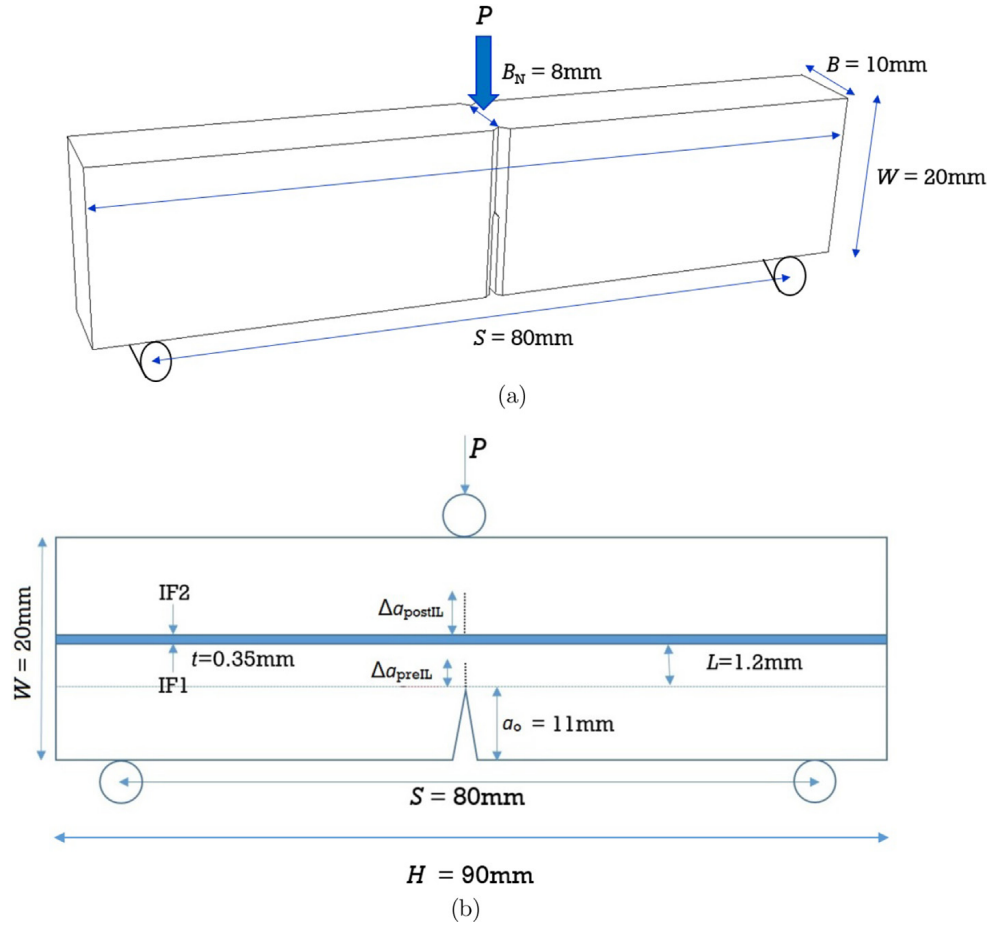
Fig. 4. Schematic of SENB for (a) homogeneous and (b) composite specimens.

material.

The fracture mechanics tests are carried out in accordance with the procedure recommended by the European Structural Integrity Society (ESIS) [28,29]. The tests are performed at room temperature in displacement control mode with a cross-head speed of 1 mm/min.

The experimental J-integral is calculated from the load, P, versus load-line displacement, v_{LL}, response. The experimental J integral, J_0, is calculated as [28],

$$J_0 = \frac{\eta U}{B_N (W - a_0)},$$

(5)

where η is a dimensionless parameter, which has a value of 2 for SENB specimens, and U is the area under the P versus v_{LL} curve. The crack extension, Δa, for the fracture mechanics tests on homogeneous specimens is measured after cryo-fracturing the remaining ligament of the specimens and measuring the average distance between initial (a_o) and final crack lengths (a).

A special procedure is applied for the composite material, as it is observed in the experiments that the interlayer remains intact, and a new crack is initiated in the matrix material beyond the interlayer. Therefore, Δa is calculated by adding the crack extensions pre and post interlayer as,

$$\Delta a = \Delta a_{preIL} + \Delta a_{postIL},$$

(6)

Since the crack extension, Δa, is large in comparison to the initial ligament length, $b_0 = W - a_o$, a crack growth correction [29] is applied to obtain the experimental J-integral, J_{exp}, as

$$J_{exp} = J_0 \cdot [1 - \frac{(0.75\eta - 1)\Delta a}{(W - a_0)}].$$

(7)

Multi-specimen testing is performed in order to obtain the J-Δa behaviour for the homogeneous as well as composite materials. Fracture initiation toughness, J_C is obtained by the intersection of J-Δa curve with 0.2 mm verticle offset line [29]. More details on the experiments and testing procedures used in this work is provided in Wiener et al. [30].

3.2. Experimental results

The J-Δa curve for the homogeneous matrix material is shown in Fig. 5. The fracture initiation toughness of the homogeneous matrix material, J_C, is found to be 2.4 kJ/m^2. The J-Δa curve obtained from SG specimens does not show significant difference to that of NSG specimens. The J-Δa curve for the composite material is shown in Fig. 6. For better representation and in order to allow for the scatter due to different interlayer locations, J_{exp} is plotted against $\Delta a - L$. For comparison, the power-law fit curve of the homogeneous specimens is also drawn. The material inhomogeneity effect is clearly seen in Fig. 6, as the fracture toughness of the composite is much higher (approximately 7 times) than that of homogeneous matrix material. Fig. 7 (a) and (b) show the homogeneous and composite specimens at the moment before crack growth is initiated. The improvement in fracture toughness can be deduced from the different bending angles and crack tip opening displacements. Fig. 7 (c) and (d) show specimens, which were broken in liquid nitrogen after a crack extension of approximately 2 mm. The initial crack is marked as blue line, the crack extension as red line. In case of the composite specimen, the crack does not cross the interlayer, but a new post-IL crack is initiated. The deformation zones in front of the crack are also visible, marked as green lines. It is seen that, for the same amount of crack extension, the composite specimen requires a much larger deformation zone, resulting in an improved fracture toughness. In order to examine the effect of material inhomogeneity on a growing crack and in order to check whether it is possible to predict the improvement in fracture toughness, the crack growth behaviour of the homogeneous as well as composite material shall be numerically modelled. This will be shown in the next section.

4. Numerical simulations of fracture mechanics experiments

4.1. Crack growth modelling

Crack growth in the numerical fracture mechanics tests are simulated using the cohesive zone (CZ) model.

In cohesive zone modelling, a layer of special type of elements is placed along the prospective crack path. The constitutive behaviour of such special elements, also known as cohesive elements, is implemented by a traction separation law (TSL), which determines the cohesive stress, σ as function of the separation of the crack faces, δ. There are various types of possible TSLs, such as a cubic form [31], a trapezoidal form [32], and an exponential form [33]. A sophisticated measurement of the TSL was performed by Pandya and Williams [34] on polyethylene. The TSL was obtained by measuring the load and the separation at the minimum cross-sectional area of a circumferentially notched tensile specimen. The experimentally obtained TSL was applied numerically to simulate the fracture behaviour in three point bending [35]. Pandya et al. [35] concluded that the rate effect and the constraint effect on the TSL are very important and can result in significant differences between the experimental and numerical crack growth behaviour. As stated earlier in Section 2.2, rate dependent crack growth modelling would be important for pure polypropylene due to its strong rate dependent mechanical behaviour. However, for a polypropylene moderately filled with talcum, this effect can be safely avoided. Further investigation on the effect of rate dependent mechanical behaviour is a subject of our future investigation. Convergence of the numerical solutions is also an issue for cohesive elements, and a viscous regularization [36] has been found to solve this problem. Modelling crack growth using CZ method has been studied extensively by many researchers and a large amount of literature exists on this subject. A comprehensive summary of the method is provided by Brocks [37]. It should be mentioned that alternative approaches
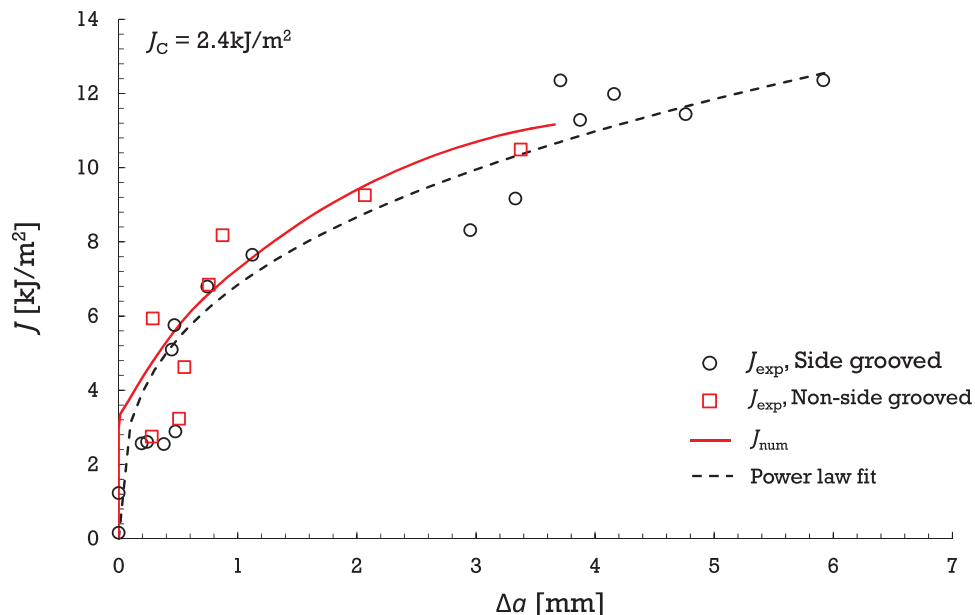

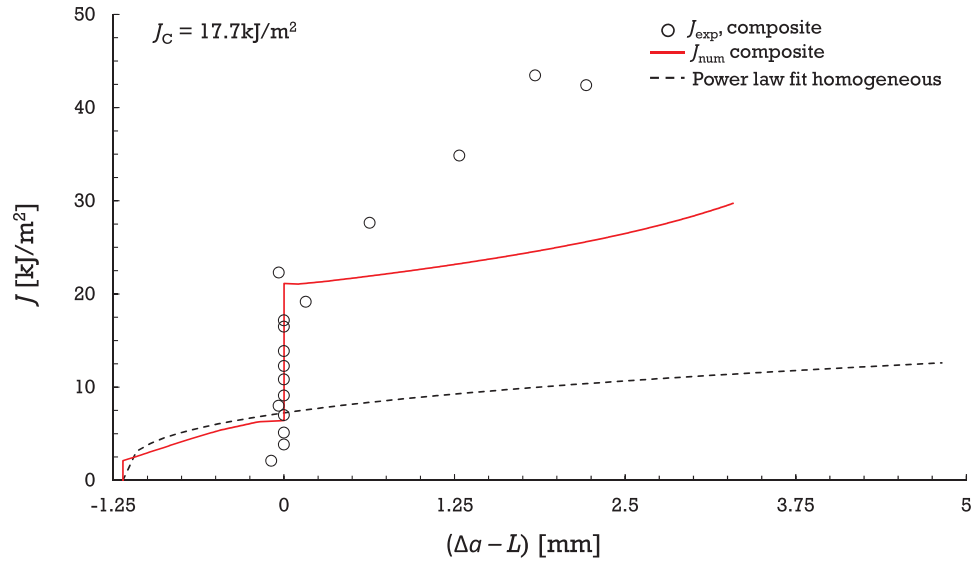**Fig. 5.** Experimental and numerical J-integral versus crack extension curves of homogeneous matrix material.

Fig. 6. Experimental and numerical *J*-integral versus (Δ*a*-*L*) curves of composite specimens in comparison with the power-law fit curve for the homogeneous specimens.

are also applicable for modelling the crack extension, such as the phase field model, see e.g. Hossain et al. [38].

In this work, a simple bi-linear TSL is used, which is shown schematically in Fig. 9. The separation energy Γ is the area under the traction versus normal separation curve described as

$$\Gamma = \frac{1}{2}(\sigma_{max} \cdot \delta_f),$$ (8)

where σ_{max} is the cohesive strength and δ_f is the normal separation distance at failure. There are mainly these two CZ parameters, σ_{max} and separation energy Γ, needed for CZ implementation. Since the cohesive elements have a constitutive thickness of 1, the initial slope of the traction separation law in Fig. 9 equals the Youngs modulus *E* and the separation distance at maximum stress σ_{max}, δ_i, equals σ_{max}/E. Note that, this is the separation distance where the cohesive elements start to damage. Chen et al. [39], Chen and Kolednik [40], Chen et al. [41] have systematically studied the effect of constraint on the CZ modelling in two and three dimensions. Important findings from their work in context with the cohesive zone modelling in two dimensions are:

- A unique set of values for CZ parameters, σ_{max} and Γ, should be determined by calibrating the crack extension, Δ*a*, against one of the loading parameters (either *J*, v_{LL}, or crack opening displacement), along with load-displacement behaviour.
- The initiation of crack extension is solely dependent on the value of Γ, which is usually smaller than the experimentally obtained fracture initiation toughness, J_C, as there is always some amount of energy dissipated in plastic work before initiation of crack extension.
- The slope of Δ*a* versus loading parameter curve depends on both σ_{max} and Γ. The slope decreases with increasing σ_{max} and Γ values.

Similar behaviour of *J*-Δ*a* behaviour from both side-grooved and non-side grooved specimens suggests that a two dimensional finite element analysis would be accurate and computationally efficient method. Therefore, the finite element computations are performed in two dimensions.

From the experimental results of the multi-specimen test presented in Section 3.2, a single fracture mechanics specimen is identified, which represents the average experimental *P*-v_{LL} behaviour. The FE model follows the dimension of this representative specimen, which has an initial ligament length, b_o = 7.5 mm. The dimensions and the mesh of the homogeneous fracture mechanics model are shown in Fig. 10.

The loading roller (Roller 1), and the support roller (Roller 2) in the three point bend model have a radius of 2 mm, which is also the root radius of the rollers in the experiments. Roller 1 is allowed to move in negative x direction and Roller 2 is fixed. The element size in the vicinity of initial ligament are of dimension 0.1×0.1 mmtextsuperscript2. Linear shape functions with small strain formulation are used. The FE solutions are obtained using full integration method. The elements near Roller 2 are refined to a size of 0.01 mm to have better sliding contact and, hence, trigonal elements were used in this region to avoid mesh refinement in the whole model. The contact between pins and adjacent specimen edges follows finite sliding with surface based tracking of the contact zone.

4.2. Calibration of modelling parameters

4.2.1. Stiffness calibration

The load versus load-line displacement response obtained from plane strain and plane stress elements are compared with the experimental response in Fig. 11. It shows that calculations based on plane strain elements (CPE4) result in a stiffer *P* versus v_{LL}

(a) homogeneous material (P2)

(b) composite material

(c) homogeneous material $\Delta a = 2.06\text{mm}$

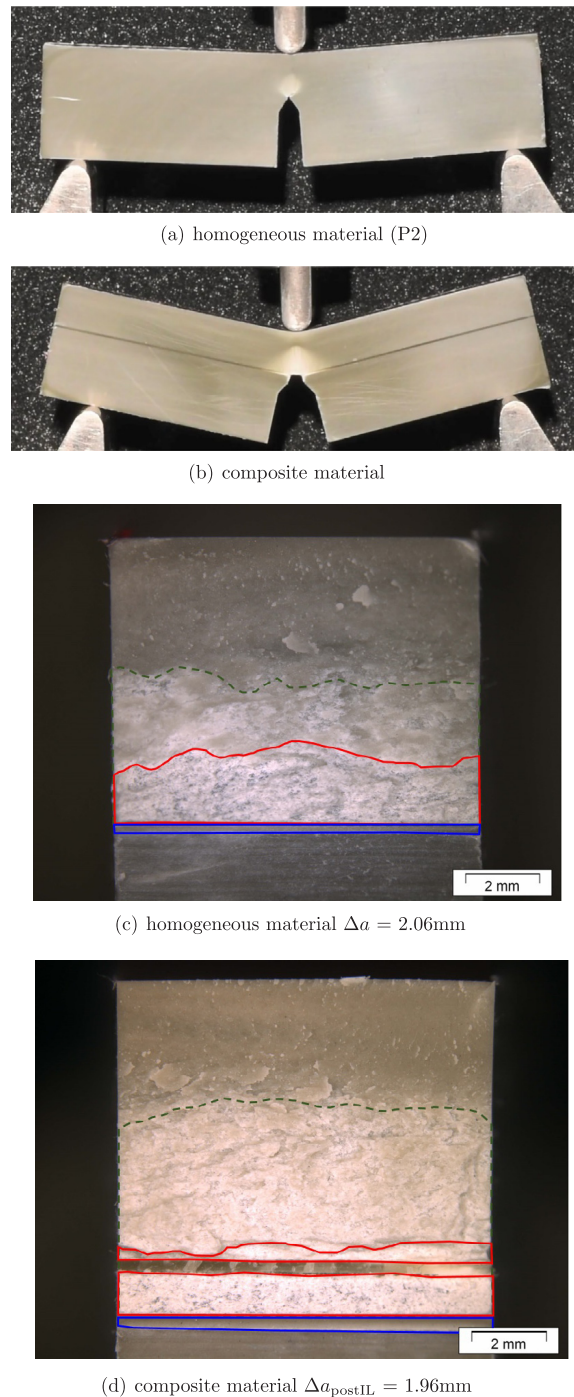(d) composite material $\Delta a_{\text{postIL}} = 1.96\text{mm}$

Fig. 7. Extent of crack tip opening just before crack initiation in (a) homogeneous and (b) composite specimens, along with the fractograph of (c) homogeneous and of (d) composite specimen corresponding to a crack extension, Δa of 2 mm, showing the deformation zone (green line), crack extension (red line) and initial crack length (blue line). (For interpretation of the references to colour in this figure legend, the reader is referred to the web version of this article.)

response in comparison to the one measured experimentally. Plane stress elements (CPS4) reflect the initial experimental P-v_{LL} curve more precisely.

It is usually expected that the presence of a crack creates a triaxial stress state in front of the crack tip and, therefore, most fracture tests are modelled under plane strain assumptions. This assumption is, however, not completely true even for metallic materials, as it is well known that due to the change of the constraint levels in out-of-plane direction from the mid-section to the side surface, a gradient from plane strain to plane stress exists. This gradient of constraint level depends on the thickness of the specimen, as well as on the strength of the material.

In order to check this, the plastic zone radius, r_{pl}, for plane stress is calculated as
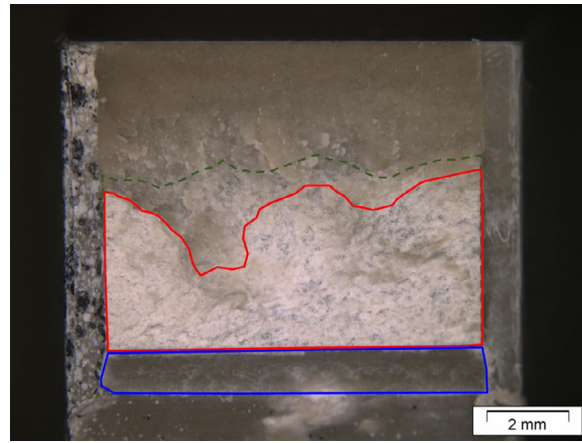
(a) SG $\Delta a = 0.745$mm
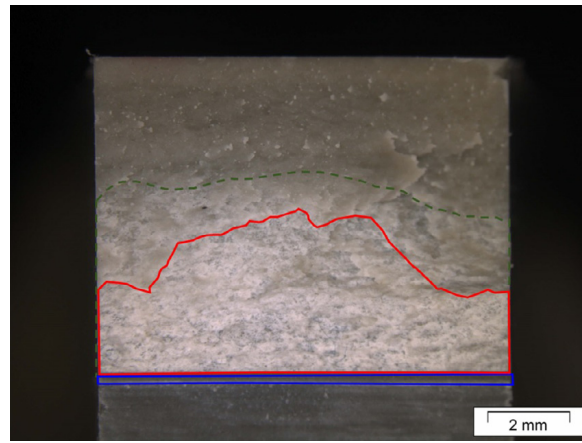
(b) NSG $\Delta a = 0.756$mm

Fig. 8. Fractographs of (a) homogeneous side grooved and (b) non side grooved specimens showing the deformation zone (green line), crack extension (red line) and initial crack length (blue line) corresponding to an approximate crack extension of 3.3 mm. (For interpretation of the references to colour in this figure legend, the reader is referred to the web version of this article.)
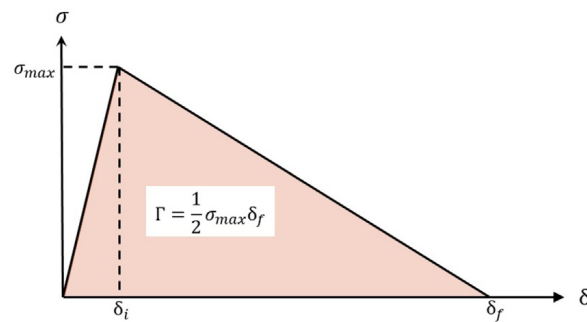

Fig. 9. Bi-linear traction separation law in a cohesive element.

$$r_{pl} = \frac{1}{2\pi}\left(\frac{JE}{\sigma_0^2}\right). \tag{9}$$

For $J = 2$kJ/m^2 and $\sigma_0 = 15$ MPa Eq. (9) yields a value of $r_{pl} = 6.2$ mm, which is more than half of the thickness of the SENB specimen, leaving no room for a plane strain zone to exist. Therefore, it is plausible that the specimens behave close to plane stress condition. For this reason, the SG and NSG specimens yield similar J-Δa curves in the experiments, see Section 3. The deformation zones for a crack extension of approximately 3.3 mm are shown in Fig. 8 for homogeneous, SG and NSG specimens, marked with green lines. The initial crack length is marked in blue, the crack extension in red. The deformation zones are not significantly different in both cases. This supports the argument that the level of constraint is not very different in SG and NSG cases.
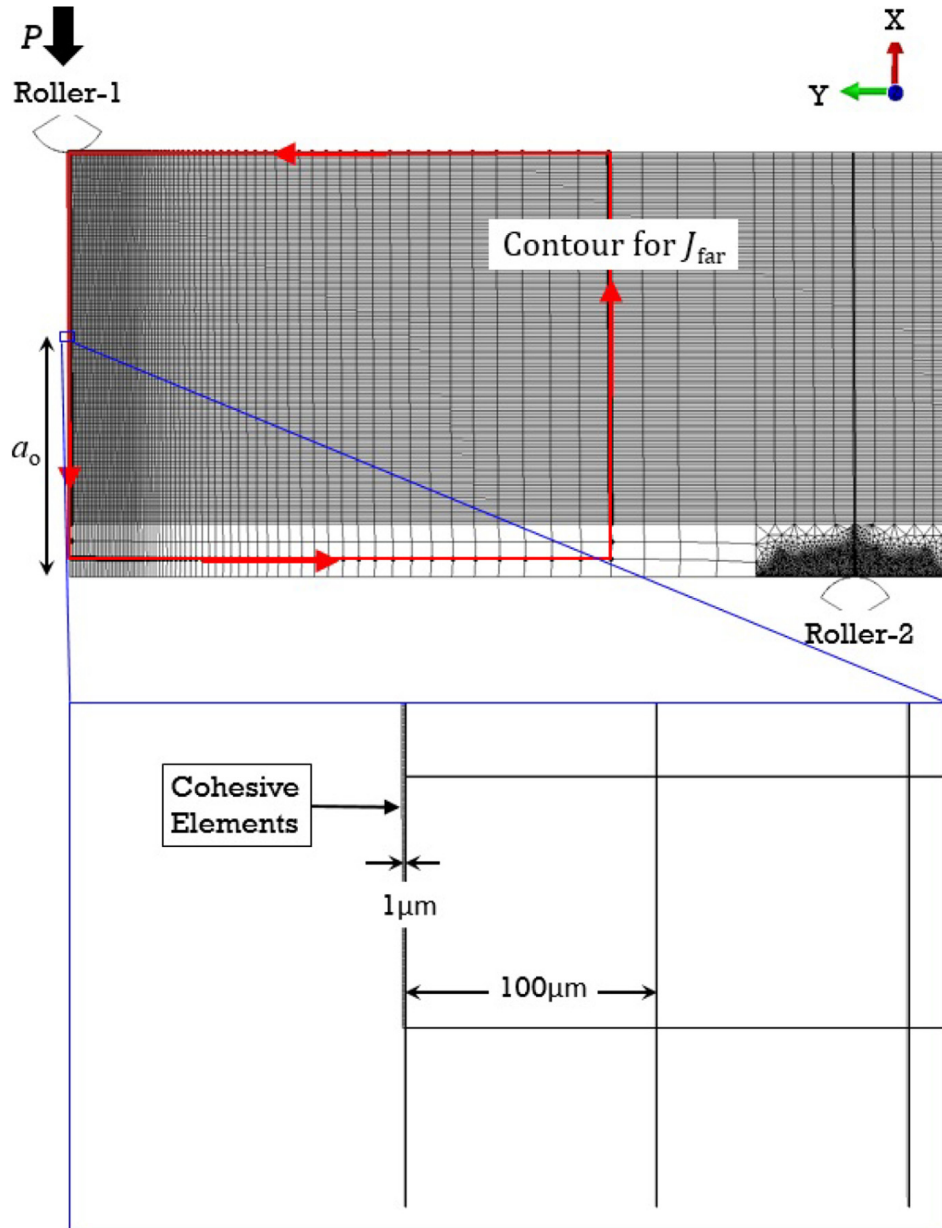
Fig. 10. Mesh and dimensions of three point bend model of homogeneous matrix material showing half-symmetric view along with the far-field contour, and details of crack tip and CZ elements.

4.2.2. Calibration of cohesive zone parameters for homogeneous specimens

The findings of Chen et al. [39] are used to find appropriate values of the CZ parameters, σ_{max} and Γ, see Section 4.1. For several possible σ_{max}-Γ pairs, crack extension is modelled, and the numerical P-v_{LL} as well as Δa-v_{LL} curves are compared with the experimental results. A few of these curves are shown in Fig. 12. It appears from Fig. 12 (a) that the best fit to the experimental behaviour results for $\sigma_{max} = 31$ MPa and Γ values between 1.68 and 1.8kJ/m^2. However, the numerical Δa-v_{LL} curves for these σ_{max}-Γ pairs deviate significantly from the experimental behaviour (see Fig. 12 (b)). Therefore, the pair of $\sigma_{max} = 30.5$ MPa and $\Gamma = 1.55$kJ/m^2 is chosen as the calibrated CZ-parameters for the homogeneous matrix material. The failure of the cohesive elements occurs when the fracture energy of 1.55kJ/m^2 is dissipated, which corresponds to a separation strain of 10%. In the uniaxial stress-strain diagram, the failure strain is 20%. There are two main reasons for the lower value of failure strain in the cohesive elements for same amount of fracture energy: 1) The softening in the stress strain curve is avoided in the modelling. 2) In presence of a crack, failure might occur at a lower strain due to higher constraint in comparison to the uniaxial condition.

From Fig. 12, it is seen that the corresponding P-v_{LL} curve does not fit very well to the experimental curve, especially for higher v_{LL} values. No unique pair of CZ-parameter is able to reflect both experimental curves. The reason is that the CZ-parameters are constraint dependent and in a real specimen, the constraint conditions change, in general, in thickness direction and during crack extension in ligament direction [42]. This behaviour cannot be reflected by two-dimensional CZ modelling with constant pair of CZ parameters.
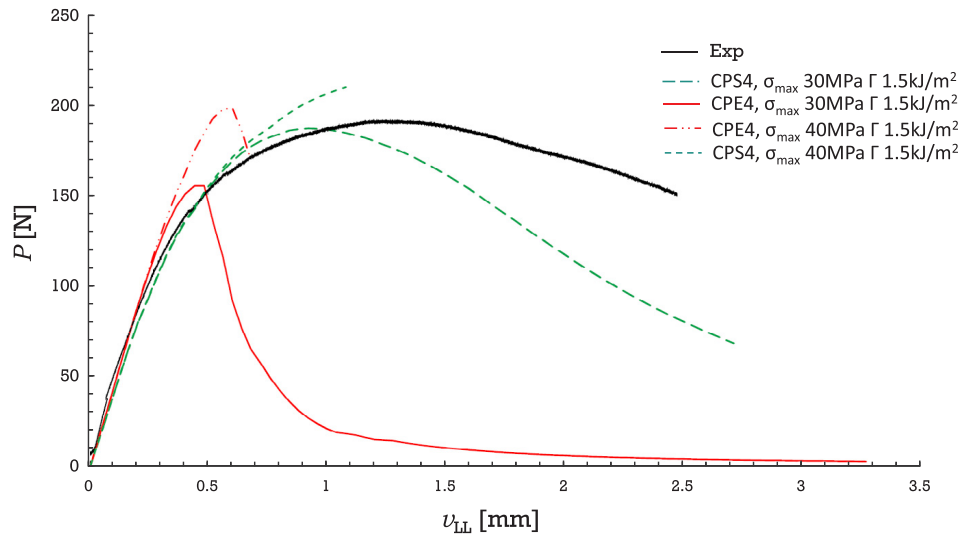
Fig. 11. Comparison of load versus displacement behaviour corresponding to plane stress, plane strain element models with experimental behaviour.

From the numerical P-v_{LL} curve and the corresponding Δa-v_{LL} behaviour, the J-integral values can be evaluated using Eq. (7). These values are denoted as J_{num} values. The J_{num}-Δa curve is compared with the J_{exp}-Δa curve in Fig. 5.

4.2.3. Calibration of cohesive zone parameters for composite specimen

Since no crack growth was observed experimentally in the IL material, the cohesive elements inside the interlayer are not allowed to experience damage. This is performed by assigning only elastic properties for the cohesive elements, so that these elements follow the linear elastic behaviour without any stiffness degradation [25].

For the matrix material the calibrated cohesive zone parameters of the homogeneous model are used. The resulting P-v_{LL} curve is drawn as dashed red line in Fig. 13 (a). It is seen that the result is satisfactory in the pre-IL region, but not in the post-IL region. Especially, when plotting the crack extension beyond the interlayer, Δa_{postIL}, against v_{LL} (Fig. 13 (b)), it is seen that, in the modelling, crack growth initiates too early and the crack extension is too fast.

For accurate modelling of post interlayer crack extension, it is important to realize that the post interlayer matrix does not contain a pre-existing crack. Therefore the constraint level in the post interlayer matrix is significantly different from that in pre-interlayer matrix.

Hence, the CZ parameters will also be different for the post-interlayer matrix. For the calibration of the post-IL CZ parameters for the composite material, an initial trial value of σ_{max} is taken as the true stress corresponding to the maximum engineering stress in the tensile test. The fracture energy is estimated to be significantly higher than for the pre-IL region, as the post interlayer section behaves like an uncracked bending specimen. The P-v_{LL} and Δa_{postIL}-v_{LL} responses for different trial CZ parameters are plotted in Fig. 13.

From the Δa_{postIL}-v_{LL} behaviour, The CZ parameters coming closest to the experimental Δa_{postIL}-v_{LL} response in Fig. 13 (b), are σ_{max} = 27 MPa, and Γ = 15kJ/m^2. The P-v_{LL} curve corresponding to these CZ parameters is shown in Fig. 13 (a). The J_{num}-values are calculated from this P-v_{LL} curve and the corresponding Δa-v_{LL} behaviour, using Eq. (7). The resulting J_{num}-Δa curve is plotted in Fig. 6. It is seen that the numerical modelling predicts re-initiation of crack extension in the post-IL region at a J-integral value of J = 22 kJ/m^2, whereas the experimental value lies at 17.7 kJ/m^2.

When comparing the numerical P-v_{LL} curve to the experimental curve, a significant deviation starts after a v_{LL} of 2.5 mm. The reason for this significant mismatch in the post-IL crack propagation part of the J-Δa curve in Fig. 6 and in the P-v_{LL} curve of Fig. 13 (a), is the change in stress triaxiality: As soon as a new crack is initiated, the stress triaxiality will increase with crack extension and might reach that of a pre-IL crack. The value of σ_{max} will increase and Γ will decrease with increasing triaxiality. It is clear, therefore, that a unique pair of CZ parameters cannot describe both initiation and propagation of a crack in post-IL matrix.

An exact modelling of the post-IL crack propagation does not lie within the scope of the current paper, since the objective of this investigation was to predict numerically the improvement in fracture toughness due to the material inhomogeneity effect. In summary, it can be stated that an accurate CZ modelling of the fracture mechanics experiment on the composite material is difficult, since the constraint conditions significantly change due to the fact that the crack does not extend through the interlayer and a new crack must be initiated beyond the interlayer. In spite of these difficulties, it is possible to achieve a good estimate of the fracture toughness of the composite material with the procedure described in this section.

5. Summary

Possibilities for the improvement of the fracture toughness of a brittle polymer have been explored. The material inhomogeneity effects due to the presence of two soft polymer interlayers, IL1 and IL2, and a stiffer interlayer of an Al-alloy, in the polymer matrix
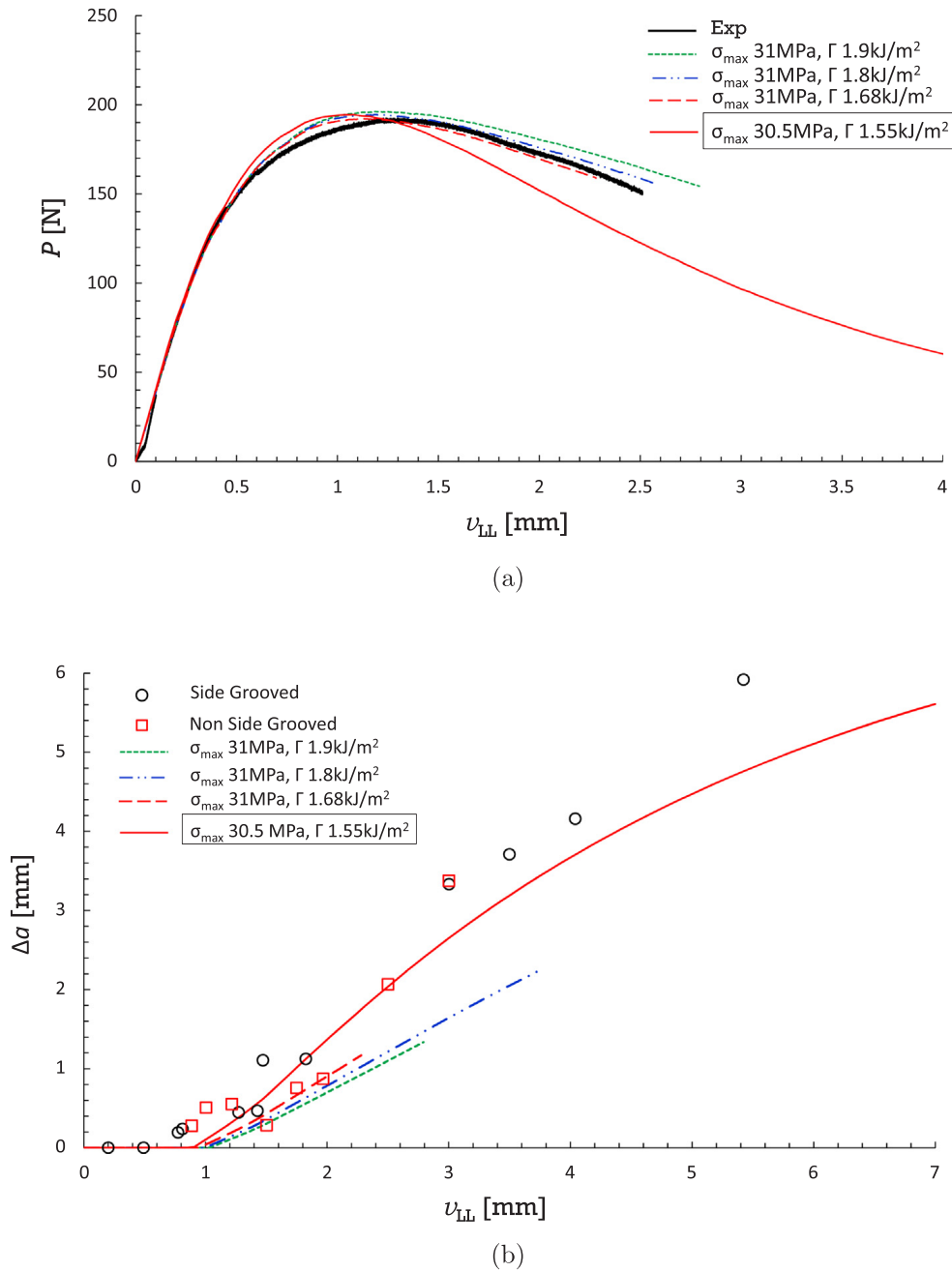
(a)

(b)

Fig. 12. Comparison of (a) load verses displacement and (b) displacement verses crack extension behaviour obtained for various cohesive zone parameters with experimental results of homogeneous matrix material.

have been numerically evaluated with stationary crack model. Analyses based on the configurational force concept have shown that the softest polymer interlayer provides the largest reduction of the crack driving force.

A composite containing a single, soft interlayer has been fabricated, and fracture mechanics experiments for both homogeneous and composite materials have been conducted. The experiments have revealed that the material inhomogeneity effect due to the interlayer results in a 7 times higher fracture toughness of the composite material, in comparison to the homogeneous matrix material.

A procedure has been worked out for the calibration of cohesive zone model to simulate the experimental crack growth behaviour of the homogeneous polymer and the composite material. The numerical analyses show different sets of cohesive zone parameters are required for modelling the crack extension in the pre- and post-interlayer regions of the composite. The modelling procedure is able to predict the improvement in fracture toughness due to the interlayer.
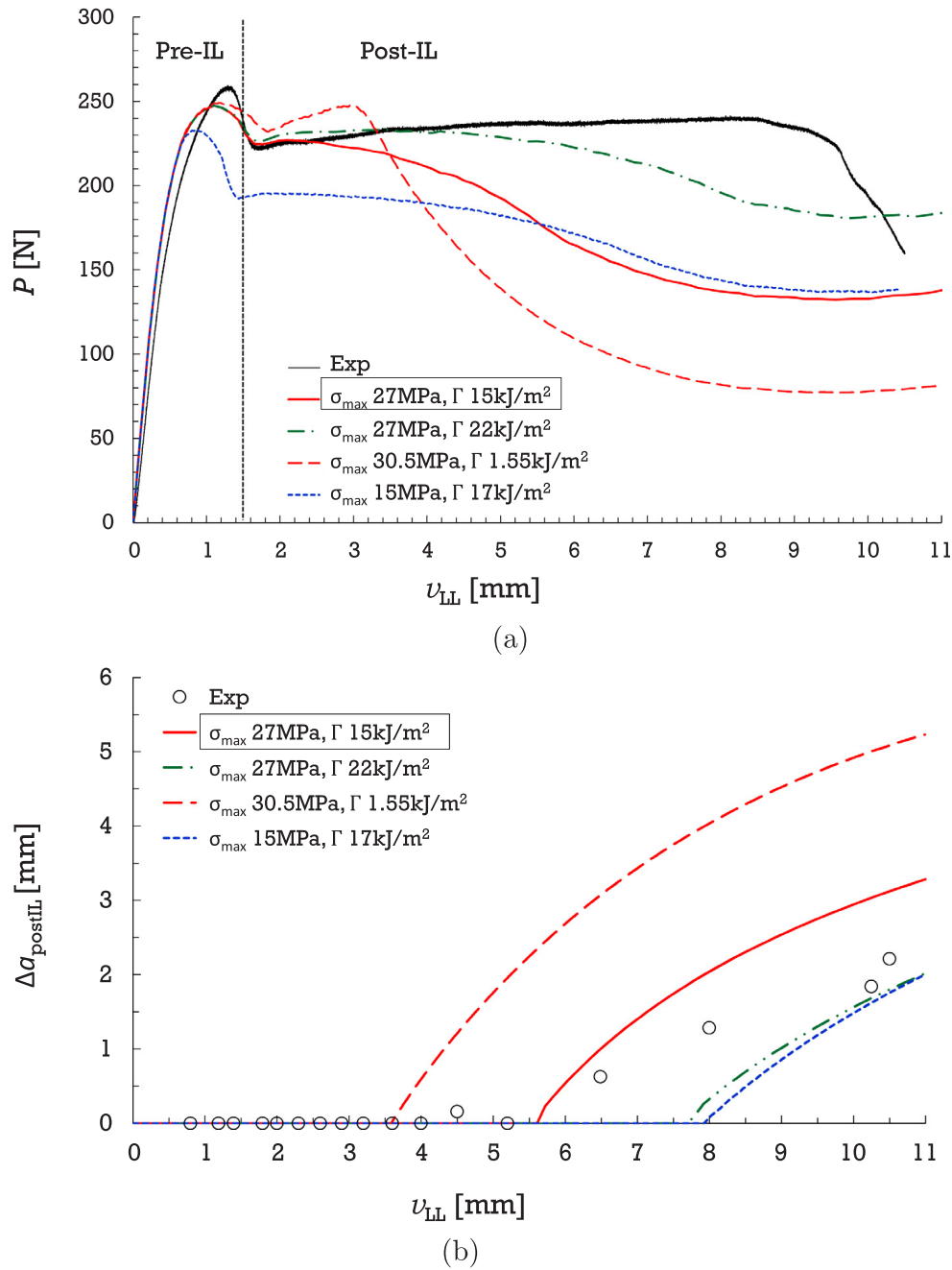
(a)

(b)

Fig. 13. Comparison of (a) load versus displacement and (b) post interlayer crack extension versus displacement behaviour obtained for various cohesive zone parameters with experimental results of composite material.

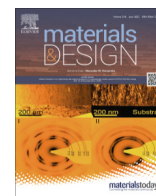## Declaration of Competing Interest

Acknowledgements

References

[1] Monazzah AH, Pouraliakbar H, Bagheri R, Reihani SMS. Al-mg-si/sic laminated composites: fabrication, architectural characteristics, toughness, damage

tolerance, fracture mechanisms. Compos Part B: Eng 2017;125:49–70.

[2] Rohatgi A, Harach DJ, Vecchio KS, Harvey KP. Resistance-curve and fracture behavior of ti–al3ti metallic–intermetallic laminate (mil) composites. Acta Mater 2003;51:2933–57.

[3] Park JG, Keum DH, Lee YH. Strengthening mechanisms in carbon nanotube-reinforced aluminum composites. Carbon 2015;95:690–8.

[4] Gao H. Application of fracture mechanics concepts to hierarchical biomechanics of bone and bone-like materials. Int J Fract 2006;138:101.

[5] Meyers MA, Chen P-Y, Lin AY-M, Seki Y. Biological materials: Structure and mechanical properties. Prog Mater Sci 2008;53:1–206.

[6] Ji B, Gao H. Mechanical principles of biological nanocomposites. Annu Rev Mater Res 2010;40:77–100.

[7] Kolednik O, Predan J, Fischer FD, Fratzl P. Bioinspired design criteria for damage-resistant materials with periodically varying microstructure. Adv Funct Mater 2011;21:3634–41.

[8] Munch E, Launey ME, Alsem DH, Saiz E, Tomsia AP, Ritchie RO. Tough, bio-inspired hybrid materials. Science 2008;322:1516–20.

[9] Ritchie R. Mechanisms of fatigue crack propagation in metals, ceramics and composites: role of crack tip shielding. Mater Sci Eng: A 1988;103:15–28.

[10] Simha N, Fischer F, Kolednik O, Chen C. Inhomogeneity effects on the crack driving force in elastic and elastic–plastic materials. J Mech Phys Solids 2003;51:209–40.

[11] Simha N, Fischer F, Kolednik O, Predan J, Shan G. Crack tip shielding or anti-shielding due to smooth and discontinuous material inhomogeneities. Int J Fract 2005;135:73–93.

[12] Kolednik O, Predan J, Fischer F. Cracks in inhomogeneous materials: comprehensive assessment using the configurational forces concept. Eng Fract Mech 2010;77:2698–711.

[13] Maugin GA. Material inhomogeneities in elasticity vol. 3. CRC Press; 1993.

[14] Gurtin ME. Configurational forces as basic concepts of continuum physics vol. 137. Springer Science & Business Media; 1999.

[15] Kolednik O. The yield stress gradient effect in inhomogeneous materials. Int J Solids Struct 2000;37:781–808.

[16] Sistaninia M, Kolednik O. Effect of a single soft interlayer on the crack driving force. Eng Fract Mech 2014;130:21–41.

[17] Kolednik O, Kasberger R, Sistaninia M, Predan J, Kegl M. Development of damage-tolerant and fracture-resistant materials by utilizing the material in-homogeneity effect. J Appl Mech 2019:1–32.

[18] Zechner J, Kolednik O. Fracture resistance of aluminum multilayer composites. Eng Fract Mech 2013;110:489–500.

[19] Sistaninia M, Kasberger R, Kolednik O. To the design of highly fracture-resistant composites by the application of the yield stress inhomogeneity effect. Compos Struct 2018;185:113–22.

[20] Chen C, Pascual J, Fischer F, Kolednik O, Danzer R. Prediction of the fracture toughness of a ceramic multilayer composite–modeling and experiments. Acta Mater 2007;55:409–21.

[21] Kozic D, Gänser H-P, Brunner R, Kiener D, Antretter T, Kolednik O. Crack arrest in thin metallic film stacks due to material-and residual stress inhomogeneities. Thin Solid Films 2018;668:14–22.

[22] Lee JJ-W, Lloyd IK, Chai H, Jung Y-G, Lawn BR. Arrest, deflection, penetration and reinitiation of cracks in brittle layers across adhesive interlayers. Acta Mater 2007;55:5859–66.

[23] Zhou Y, Rangari V, Mahfuz H, Jeelani S, Mallick P. Experimental study on thermal and mechanical behavior of polypropylene, talc/polypropylene and poly-propylene/clay nanocomposites. Mater Sci Eng: A 2005;402:109–17.

[24] Bouvard J-L, Denton B, Freire L, Horstemeyer MF. Modeling the mechanical behavior and impact properties of polypropylene and copolymer polypropylene. J Polym Res 2016;23:70.

[25] Smith M. ABAQUS/Standard User's Manual, Version 6.9. Simulia 2009.

[26] Parks D. The virtual crack extension method for nonlinear material behavior. Comput Methods Appl Mech Eng 1977;12:353–64.

[27] E. ISO 527, 527–1, (1996)."plastics—determination of tensile properties–part 1: General principles". British Standards Institution; 1996. p. 1–16.

[28] Hale G, Ramsteiner F. J-fracture toughness of polymers at slow speed. European structural integrity society, vol. 28. Elsevier; 2001. p. 123–57.

[29] Schwalbe K-H, Neale B. A procedure for determining the fracture behaviour of materials—the unified fracture mechanics test method efam gtp 94. Fatigue Fract Eng Mater Struct 1995;18:413–24.

[30] Wiener J, Arbeiter F, Tiwari A, Kolednik O, Pinter G. Bioinspired toughness improvement through soft interlayers in mineral reinforced polypropylene. Mech Mater 2019. 103243.

[31] Needleman A. A continuum model for void nucleation by inclusion debonding. J Appl Mech 1987;54:525–31.

[32] Tvergaard V, Hutchinson JW. The relation between crack growth resistance and fracture process parameters in elastic-plastic solids. J Mech Phys Solids 1992;40:1377–97.

[33] Needleman A. An analysis of tensile decohesion along an interface. J Mech Phys Solids 1990;38:289–324.

[34] Pandya K, Williams J. Cohesive zone modelling of crack growth in polymers part 1–experimental measurement of cohesive law. Plastics, Rubber Compos 2000;29:439–46.

[35] Pandya K, Ivankovic A, Williams J. Cohesive zone modelling of crack growth in polymers part 2–numerical simulation of crack growth. Plastics, Rubber Compos 2000;29:447–52.

[36] Yu H, Olsen JS, Olden V, Alvaro A, He J, Zhang Z. Viscous regularization for cohesive zone modeling under constant displacement: an application to hydrogen embrittlement simulation. Eng Fract Mech 2016;166:23–42.

[37] Brocks W. Cohesive strength and separation energy as characteristic parameters of fracture toughness and their relation to micromechanics. Struct Integrity Durab 2005;1:233–43.

[38] Hossain M, Hsueh C-J, Bourdin B, Bhattacharya K. Effective toughness of heterogeneous media. J Mech Phys Solids 2014;71:15–32.

[39] Chen C, Kolednik O, Scheider I, Siegmund T, Tatschl A, Fischer F. On the determination of the cohesive zone parameters for the modeling of micro-ductile crack growth in thick specimens. Int J Fract 2003;120:517–36.

[40] Chen C, Kolednik O. Comparison of cohesive zone parameters and crack tip stress states between two different specimen types. Int J Fract 2005;132:135–52.

[41] Chen C, Kolednik O, Heerens J, Fischer F. Three-dimensional modeling of ductile crack growth: cohesive zone parameters and crack tip triaxiality. Eng Fract Mech 2005;72:2072–94.

[42] Anderson T. Fracture mechanics: fundamentals and applications. 2nd ed. Taylor & Francis; 1994.

7.4. Publication IV

|	
Title:	Influence of Layer Architecture on Fracture Toughness and Specimen Stiffness in Polymer Multilayer Composites
Authors:	Johannes Wiener[a], Florian Arbeiter[a], Otmar Kolednik[b], Gerald Pinter[a]
Affiliation:	[a] Materials Science and Testing of Polymers, Montanuniversitaet Leoben, 8700 Leoben, Austria [b] Erich-Schmid-Institute of Materials Science, Austrian Academy of Science, 8700 Leoben, Austria
DOI:	https://doi.org/10.1016/j.matdes.2022.110828
Conceptualization:	Johannes Wiener (70%), Florian Arbeiter (30%)
Methodology:	Johannes Wiener (70%), Florian Arbeiter (30%)
Validation:	equal contribution by all authors
Investigation:	Johannes Wiener (80%), Florian Arbeiter (20%)
Writing-Original Draft:	Johannes Wiener (80%), Florian Arbeiter (20%)
Writing-Review & Editing	equal contribution by all authors
Supervision	Florian Arbeiter (60%), Gerald Pinter (20%) , Otmar Kolednik (20%)

Influence of layer architecture on fracture toughness and specimen stiffness in polymer multilayer composites

Johannes Wiener [a], Florian Arbeiter [a,*], Otmar Kolednik [b], Gerald Pinter [a]

[a] Materials Science and Testing of Polymers, Montanuniversitaet Leoben, 8700 Leoben, Austria
[b] Erich-Schmid-Institute of Materials Science, Austrian Academy of Science, 8700 Leoben, Austria

HIGHLIGHTS

- Soft interlayers (ILs) led to crack arrest in multilayer composites.
- Very compliant ILs also led to stress decoupling effects and stiffness loss.
- Crack arrest and stress decoupling can occur independently.
- Crack arrest at ILs can be achieved without major stiffness loss.

GRAPHICAL ABSTRACT
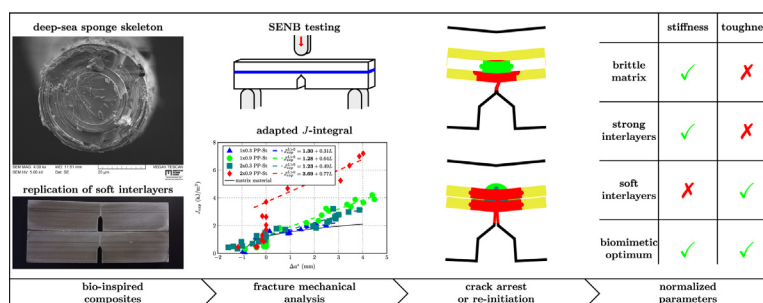
ARTICLE INFO

ABSTRACT

The objective of this contribution was to increase the fracture toughness of talcum reinforced polypropylene (PP) while preserving specimen stiffness. This was accomplished by introducing soft interlayers (ILs) made of standard PP (PP-St) or very compliant PP (PP-Soft) and utilizing the so-called material inhomogeneity effect. Architectures with one or two ILs of either 0.3 or 0.9 mm thickness were tested in single edge notched bending experiments. Layers of PP-Soft always arrested growing cracks due to their low Young's modulus, E, and yield stress, σ_y, which is called an $(E - \sigma_y)$-inhomogeneity. However, the increase in fracture toughness came at the cost of specimen stiffness. For ILs made of PP-St, E was still lower compared to the matrix material, but σ_y was similar (pure E-inhomogeneity). Specimen stiffness remained high for these composites, but crack arrest could not be achieved in most cases, which could be explained by plastic deformation of the soft layers. Plastic deformation could be contained within the ILs in one of the architectures, where two large ILs were used. Crack arrest could be achieved in this adapted IL design, leading to excellent fracture toughness in combination with high stiffness.

1. Introduction

Similar to many other fields of study, inspiration for the design of novel materials can be drawn from nature[1,2]. It is well established, that materials such as bone [3], nacre [4,5] or deep sea sponge skeletons [6–10] have excellent mechanical properties. A combination of high stiffness, strength and outstanding toughness is owed to complex microstructures of "soft" proteins and "hard" matrix materials. In this context, "hard" refers to materials with a large Young's modulus, E, and yield stress, σ_y, while "soft" relates to much smaller E and/or σ_y than the matrix.

Several approaches to replicate biological materials have been explored in literature. First and foremost, the recent advances in the field of 3D-printing have to be mentioned [11]. Threedimensional structures can now be manufactured with high accuracy

using various materials as soft and hard phases [12–14]. Alternative techniques exploit crystallization kinetics to produce patterned coatings [15] or to control the grain structure in metals [16] in an attempt to emulate the natural growth of materials. Layered structures with precise thicknesses can readily be manufactured using physical or chemical vapour deposition [17], although these techniques are typically not applicable to polymers. Estrin et al. even suggest severe plastic deformation as a novel procedure to create gradients of mechanical properties in homogeneous materials [18–20]. Nonetheless, variations of conventional processing techniques, such as microlayer extrusion[21] or microcellular injection moulding[22], are also capable of producing structures on a micrometer scale. Hoffmann et al.[23] used compression moulding to produce bio-inspired sandwich structures from natural fiber reinforced polypropylene, which showed high density specific properties for automotive applications. The consensus is that crack deflection and crack tip blunting combined with a reduction of defect size[24,25] can change the failure behavior in a beneficial way.

An explanation on the basis of fracture mechanics is given by the so-called material inhomogeneity effect [26]. The material inhomogeneity effect describes the change in crack driving force in the vicinity of an interface between two different materials. The crack driving force can be expressed using the J-integral from elastic–plastic fracture mechanics. Note that Rice's J-integral [27] is path dependent in an inhomogeneous material and adaptations are necessary to describe the crack tip accurately. One solution was derived from the concept of configurational forces [28,29], where the crack driving force can be expressed in the form of the near-tip J-integral, J_{tip}. Several sources [26,30] found an increase in J_{tip} when a crack grows from a hard to a soft phase, which is called anti-shielding effect. When a crack grows from the soft to the hard phase, the crack driving force is diminished. This so-called shielding effect can stop crack growth entirely, leading to crack arrest at the interface.

Both effects are combined in a soft IL, so that the fracture toughness of the whole composite may be increased due to the crack arresting properties. An essential requirement for crack arrest is a mismatch in mechanical properties, where two basic categories can be distinguished: In a pure E-inhomogeneity, the matrix material has a higher E than the IL material. In a σ-inhomogeneity the yield stress of the two materials is different. However, the most beneficial form is a combined $(E - \sigma)$-inhomogeneity. Literature promises the best reduction of the crack driving force for the range of $\sigma_{IL}/\sigma_{Matrix} < 0.3$ [31] and $E_{IL}/E_{Matrix} < 0.2$ [32]. Finite element simulations such as those of Tiwari et al. [33] can also be very useful to predict the magnitude of the shielding effect for a specific material configuration.

In addition to the choice of material, layer architecture may have a significant influence in some cases. According to Sistaninia et al. [31], the best IL effectiveness is achieved, when the IL thickness, t, is approximately as thick as the plastic zone radius, r_y^{IL}. These studies have shown that the σ-inhomogeneity retains its crack arresting properties for the most part, even if t is chosen suboptimally. Kolednik et al. [32] state, that the E-inhomogeneity is especially vulnerable to incorrect IL design. The benefits of the E-inhomogeneity are strongly reduced at higher loads due to a larger r_y^{IL}. Fromm et al.[17] also mention that a minimum layer thickness may be required in order to avoid interactions between interfaces due to surface roughness. Thus, layer thickness should be chosen with care, especially when the IL only shows an E-inhomogeneity.

In a previous contribution by the authors [34], the failure of single edge notched bending (SENB) specimens was transformed from crack growth to a bending fracture mechanism due to soft ILs, resulting in a tremendous increase in apparent fracture toughness.

Other studies [35,36] showed similar benefits of a soft phase on the impact behavior of polymeric materials. Tan et al.[37] reported increased fatigue resistance in nacre-like structures as well. In these examples, $(E - \sigma)$-inhomogeneities always showed great success, while in some contributions E-inhomogeneities were unable to improve the properties of the matrix. However, layer architecture was not thoroughly investigated, so that the same pair of materials may perform well, if t is chosen differently.

In this contribution, the effect of layer architecture on fracture toughness was investigated in various multilayer configurations. The same matrix material was augmented using two different soft phases with varying t and number of ILs. One of the IL materials showed an $(E - \sigma)$-inhomogeneity towards the matrix material, the other only an E-inhomogeneity. Using the experimental J-integral, J_{exp}, these multilayer composites were analyzed regarding their fracture toughness. The focus was set on illustrating the effect of layer architecture on the crack arresting properties of the soft layers, while also observing the consequences to specimen stiffness.

2. Experimental

2.1. Characterization of base materials

Two different grades of polypropylene (PP), namely a standard PP (PP-St) and a very compliant PP (PP-Soft), were intended as ILs within a brittle matrix of PP with 60 wt% talcum particles. The tensile properties of matrix and IL materials were investigated according to ISO 527 [38] using a Zwick Z010 testing machine (ZwickRoell GmbH & Co. KG, Germany). Additionally, the Poisson's ratio, v, was determined from surface strains using a high resolution camera (Prosilica GT6600, Allied Vision Technologies GmbH, Germany), a 100-mm Tokina AT-X M100 PRO D macro objective (Kenko Tokina Co., Japan) and the digital image correlation system Mercury 2.8 (Sobriety s.r.o., Czech Republic). An overview of mechanical properties is given in Table 1. J_{exp} as well as the crack extension, Δa, were obtained according to Hale and Ramsteiner (ESIS TC4 recommendation [39]). For the matrix material, the entire crack growth resistance curve (also known as $J - R$ curve) was simplified to a power law fit as shown in Eq. 1, where $A = 1.27$ and $N = 0.32$ (previously determined in[34]). This curve is used in the current contribution as representation of the fracture mechanical properties of the matrix material.

$$J_{exp} = A\Delta a^N \tag{1}$$

2.2. Preliminary layer design

2.2.1. Number of layers

Experiments were performed on specimens with single ILs and with two ILs to investigate the influence of a second IL on the failure behavior of multi-layer composites. The underlying question is, whether the crack arrester effect can be augmented by using multiple ILs in sequence.

2.2.2. Layer placement

Guidelines for SENB testing were given by Hale and Ramsteiner [39], which suggest the specimen dimensions shown in Fig. 1 for homogeneous materials. Adhering to this method requires the initial crack length, a_0, to satisfy the relation $0.55 < a_0/W < 0.65$. Thus, a notch with the length $a_0 \approx 0.6W = 12$ mm was chosen. ILs were introduced accordingly at distances of $D_{IL1} = 13.5$ mm and also at $D_{IL2} = 15$ mm for specimens with two ILs. The spacing between initial notch and the ILs was chosen to be 1.5 mm in order

Table 1
Mechanical properties of base materials.

Material	Function in composite	E [MPa]	σ_y [MPa]	v [-]	E_{IL}/E_{Matrix} [-]	$\sigma_{IL}/\sigma_{Matrix}$ [-]
Talcum reinforced PP	Matrix material	6967 ± 173	25.4 ± 0.4	0.20 ± 0.01	-	-
Standard PP	IL material 1	1444 ± 24	23.9 ± 0.4	0.44 ± 0.03	0.21	0.94
Soft PP	IL material 2	242 ± 13	6.8 ± 0.1	0.28 ± 0.08	0.04	0.27

$W = 20\ mm$
$B = 10\ mm$
$S = 80\ mm$
$R = 3\ mm$
$L = 100\ mm$
$D_{IL1} \approx 13.5\ mm$
$D_{IL2} \approx 15\ mm$
$a_0 \approx 12\ mm$
$0.55 < a_0/W < 0.65$
— soft IL
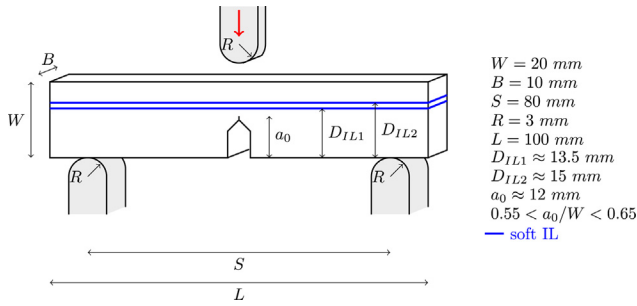
Fig. 1. Dimensions for single edge notched bending (SENB) specimens.

to allow the crack to fully develop between initial notch and first IL as well as between two ILs.

2.2.3. Layer thickness

As mentioned by Sistaninia et al. [31], t should be of similar size as r_y^{IL}. This is a requirement for ILs made of PP-St in particular, which exhibits only an E-inhomogeneity towards the matrix material. An initial estimate for t can be made based on Irwin's model for r_y^{IL} [40], which is given by Eq. 2.

$$r_y^{IL} \approx \beta \frac{JE}{\sigma_y^2(1 - v^2)} \tag{2}$$

Therein, E, σ_y and v are the material parameters of the IL material (PP-St in this case) and $\beta = 1/6\pi$ for plane strain conditions. An estimate for J was obtained using Eq. 1 with a crack extension of Δa = 1.5 mm, representing $J \approx J_{exp}$ when the crack tip reaches the first IL. Plane stress conditions may not be neglected for a matrix of talcum reinforced PP [33], since plastic deformation and crack propagation in regions near the surface of the specimens could also lead to failure. Therefore, larger ILs were also included in the test program to account possible plane stress conditions. Eq. 2 was adapted accordingly with $\beta = 1/2\pi$ and by omitting the term $(1 - v^2)$. These calculations yield $r_y^{IL} = 0.24$ mm for plane strain conditions and $r_y^{IL} = 0.58$ for plane stress conditions, which should be seen as a minimum required t for the following reasons. J varies locally due to the material inhomogeneity and may lead to different plastic zone development at the crack tip. Furthermore, r_y^{IL} is expected to grow after crack arrest due to increased loading during monotonic tests. Therefore, these values were chosen as $t = 0.3$ and $t = 0.9$ mm, respectively, to provide enough space for plastic zone development. Analogous procedures for PP-Soft yield $t = 0.5$ mm and $t = 1.5$ mm. However, this IL material shows a combined $(E - \sigma)$-inhomogeneity, so that the optimization of t is not a necessity. This was shown, e.g. in [34], where crack arresting properties were found despite not optimizing t. Therefore, thicknesses for PP-Soft were also chosen as $t = 0.3$ and $t = 0.9$ mm in order to stay consistent with architectures made of PP-St.

2.3. Specimen preparation

A total of 8 multilayer architectures were manufactured from the base materials using a combined co-extrusion and pressing process. For each IL material, structures with one IL and two ILs with $t = 0.3$ and $t = 0.9$ mm were realized. An overview of all multilayer composites and their respective abbreviations is given in Table 2. The material was supplied as 20 mm thick plates, from which SENB specimens were cut. Notches were machined and then sharpened using a razor broaching tool to obtain sharp initial cracks [41,42]. The initial notch length a_0 was introduced in such a way, that the condition $0.55 < a_0/W < 0.65$ was fulfilled [39]. However, notches could not be introduced as deep in specimens with thick ILs. Otherwise, the initial notches would have already cut into the first IL due to their large thicknesses. As a result, a_0/W was chosen as 0.55 for specimens with thicker ILs, while for specimens with smaller ILs $a_0/W = 0.60$. This has to be kept in mind, since the larger ligament length, $b = W - a_0$, also led to higher forces during testing.

2.4. Testing procedure and evaluation of test data

Three point bending tests were performed on a MTS 831 servo-hydraulic testing machine (MTS-Systems GmbH, USA). The support length was $S = 4W =$ 80 mm and radii of 3 mm were used for the support bearings and the fin, as is shown in Fig. 1. A crosshead speed of 1 mm/min was used in all cases. Final displacements for the individual specimens were increased stepwise between 0.1 and 2 mm to produce different Δa. Images of the fracture surfaces were taken using an OLYMPUS SX12 light microscope (Olympus Life Science Europe GmbH, Germany) and a magnification of 12.5 after the tested specimens were cryofractured. For each specimen, an average Δa was calculated from the total fractured area of the matrix material. A representation of the fracture surface analysis is given in Fig. 2. The ILs themselves did not fracture during any of the experiments and were not included. The same approach was used for b and t, while B and W were measured on the specimens with a caliper. The sections of matrix material were labelled as b_0, b_1 and b_2, although b_2 only occurred in specimens with two ILs. b_0 is the distance between the initial notch and the first IL and is required for a correction of the $J_{exp} - \Delta a$ curve. b_1 and b_2 are not part of any calculation, but are used later on to discuss failure progression.

For the characterization of fracture toughness, J_{exp} was evaluated according to the ESIS TC4 recommendation [39]. This procedure is a multispecimen approach, where between 15 and 25 SENB specimens were tested per material (exact number varied due to the exclusion of invalid specimens). Eq. 3 and Eq. 4 were used to determine J_{exp} from the machine data and Δa. U is the area under the force displacement curve, which was corrected for machine stiffness and plastic deformation due to indentation. The geometry factor is $\eta = 2$ for SENB specimens.

$$J_0 = \frac{\eta U}{B(W - a_0)} \tag{3}$$

Table 2
Overview of layer architectures.

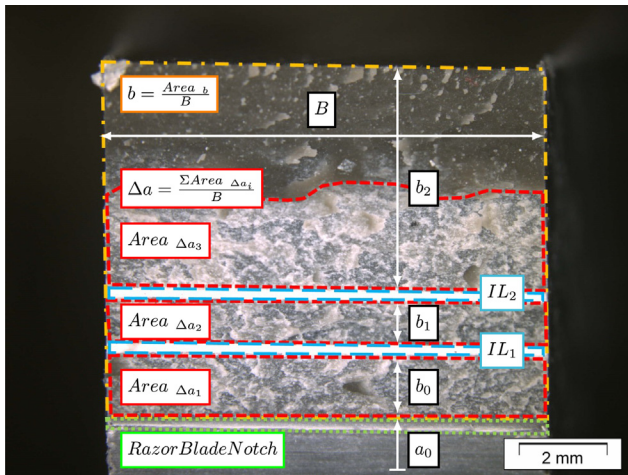| Abbreviation	IL Material	IL thickness t [mm]	Number of ILs [-]	Representation
1×0.3 PP-St	Standard PP	0.3	1	
2×0.3 PP-St	Standard PP	0.3	2	
1×0.9 PP-St	Standard PP	0.9	1	
2×0.9 PP-St	Standard PP	0.9	2	
1×0.3 PP-Soft	Soft PP	0.3	1	
2×0.3 PP-Soft	Soft PP	0.3	2	
1×0.9 PP-Soft	Soft PP	0.9	1	
2×0.9 PP-Soft	Soft PP	0.9	2	

Fig. 2. Analysis of fracture surfaces under the light microscope.

$$J = J_0 \left[1 - \frac{(0.75\eta - 1)\Delta a}{B(W - a_0)} \right] \tag{4}$$

Plotting J_{exp} versus Δa according to [39] led to large data scattering, as can be seen in the left part of Fig. 3. The reasons were the change in fracture behavior at the IL in combination with variances in specimen geometry. Most notably, the distance b_0 had the largest scatter due to the manufacturing and notching processes, so adaptations to the established procedures were necessary. The use of these techniques is illustrated in Fig. 3 and was described in more detail in a previous contribution [34].

Therein, Δa was corrected for variances by an amount equal to b_0, so that a shifted crack extension $\Delta a^* = \Delta a - b_0$ was obtained. The position of the first IL is exactly at $\Delta a^* = 0$ after this shift, so that the influence of ILs can be seen more clearly. The power law function of the matrix material was also shifted by an average value of b_0, that was calculated from the individual b_0 of the mul-

tilayer materials[1]. This was done in order to improve the comparability between the $J - R$ curves of multilayer materials and matrix.

Fracture toughness is usually determined by the onset of crack growth, since this quickly leads to specimen failure in homogeneous materials. Values at certain Δa as well as the intersection of the $J - R$-curve with a so-called blunting line are often used and described in literature [39]. In heterogeneous materials, overcoming the soft ILs is the determining step in specimen failure. More meaningful results can be achieved by looking at the value of J_{exp} when crack growth exceeds the ILs. This value was termed J_c^{ML} and taken as measure for the fracture toughness of the entire multilayer composite. In practice, it was obtained by fitting a regression line through the points of all specimens, that exhibited crack growth past the first IL ($\Delta a^* > 0$). This resulted in a linear equation in the form $J_{exp}^{a^*>0} = J_c^{ML} + k\Delta a^*$, which conveniently yielded J_c^{ML} when it was evaluated at $\Delta a^* = 0$. Regardless of these adaptations, the values for J_{exp} were still obtained according to Eqs. 3 and 4.

Finally, a comprehensive parameter for fracture toughness was needed to compare specific layer architectures to the pure matrix material. For that purpose, J_c^{ML} of the multilayer composites was compared to the value of the shifted matrix curve at $\Delta a^* = 0$, which was labelled $J_{\Delta a^*=0}^{Matrix}$. The two values were put into relation according to Eq. 5 and the new parameter was termed Ω. This parameter describes the relative increase in J_{exp} from the matrix to the multilayer composite, with high values Ω representing a large improvement due to the IL. It is therefore used as normalized measure for the fracture toughness of inhomogeneous materials in this contribution.

$$\Omega = \frac{J_c^{ML}}{J_{\Delta a^*=0}^{Matrix}} \tag{5}$$

---

[1] In diagrams, the average of b_0 was built from all specimens shown in the plot. For calculations, the shift was done separately for each multilayer configuration.
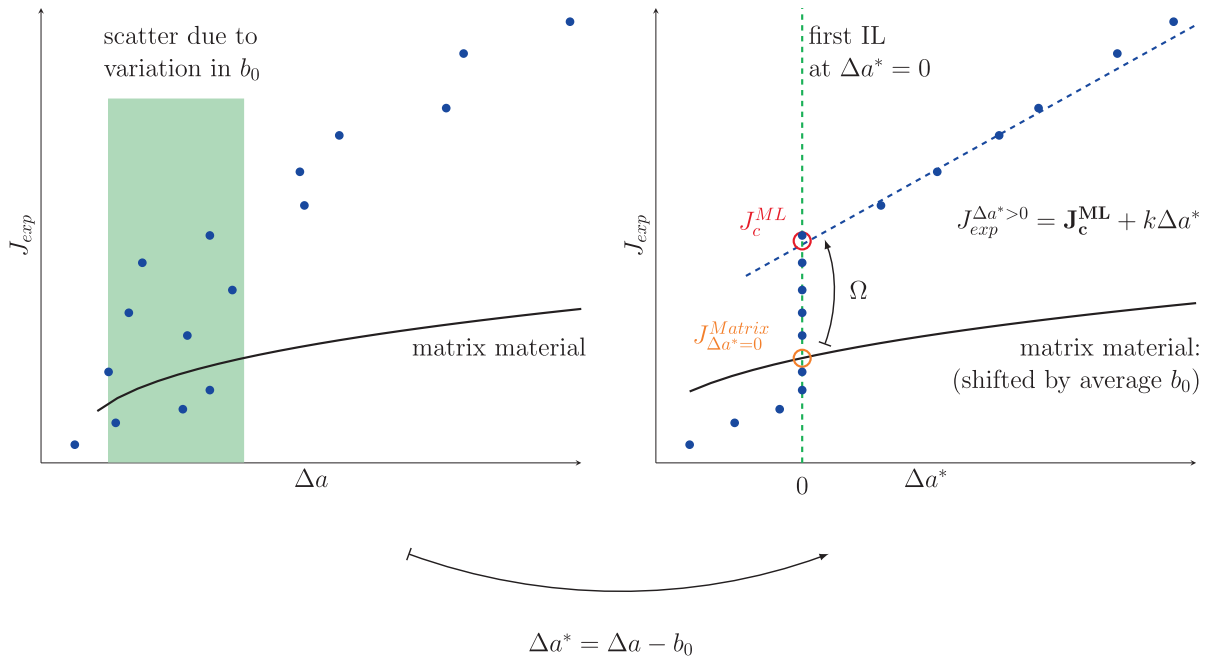
Fig. 3. Coordinate shift by b_0 from a $J_{exp} - \Delta a$ plot to a $J_{exp} - \Delta a^*$ plot.

A measure for the stiffness of the investigated SENB specimens was calculated on the basis of ASTM E1820 [43]. An equation for specimen compliance, C, was reformulated to yield an equivalent modulus, E^{eq} (Eq. 6). C was obtained from the initial slope in the force–displacement curves, which was taken as a secant between 0.1 and 0.2 mm of displacement. E^{eq} should not be directly compared to a conventional Young's modulus (e.g. from ISO 527 [38]) for a number of reasons. For example, the stress triaxiality in a SENB test is vastly different from a uniaxial tensile test due to differences in stress distribution and stress concentration around the notch. Additionally, neither the ASTM E1820 nor the ISO 527 were designed to deal with inhomogeneous materials. Nonetheless, E^{eq} is used to compare and rank the stiffness of the various multilayer composites in this contribution. For reasons of comparability, E^{eq} was also determined for the matrix material in the same way.

$$E^{eq} = \frac{1}{CB}\left(\frac{l}{W - a_0}\right)^2 \left[1.193 - 1.98\left(\frac{a_0}{W}\right) + 4.478\left(\frac{a_0}{W}\right)^2 \right.$$
$$\left. -4.443\left(\frac{a_0}{W}\right)^3 + 1.739\left(\frac{a_0}{W}\right)^4\right] \tag{6}$$

3. Results and Discussion

3.1. Interlayer material PP-Soft with $(E - \sigma)$ inhomogeneity

All $J - R$ curves for architectures with an IL of PP-Soft are shown in Fig. 4a. The values of $J_c^{ML}, J_{L=0}^{Matrix}, \Omega$ and E^{eq} are listed in the upper half of Table 3. The combined $(E - \sigma)$-inhomogeneity led to an increase of fracture toughness ($\Omega > 1$) in all four of the investigated materials. In all cases, the anti-shielding effect can be seen, when J_{exp} is lower than the matrix curve for $\Delta a^* < 0$. This is followed by the shielding effect, elevating J_{exp} above the matrix values for $\Delta a^* > 0$. The shielding effect resulted in crack arrest and specimen failure had to be forced by re-initiating new cracks behind the ILs under increased loading.

3.2. Interlayer material PP-St with E-inhomogeneity

The $J - R$ curves of composites including PP-St IL(s) are shown in Fig. 4b, while the values for $J_c^{ML}, J_{L=0}^{Matrix}, \Omega$ and E^{eq} can be found in the lower half of Table 3. For $t = 0.3$ mm, no improvement over matrix properties could be found. The effects of an increased t are shown in the example of 1x0.9 PP-St: An anti-shielding effect similar to the specimens with a PP-Soft IL (Fig. 4a) can be seen for $\Delta a^* < 0$. However, no distinct shielding effect was developed in the vicinity of $\Delta a^* = 0$. Some improvements to J_{exp} appeared for larger values of Δa^* though. This increase can, for example, be attributed to the large IL, which did not fracture in the experiment. It could act as a stabilizing element to the remaining specimen for large crack lengths, which may have affected J_{exp}. However, a fully developed crack arrest could not be seen. On the other hand, shielding and anti-shielding effect are clearly visible in the case of 2x0.9 PP-St. As a result, fracture toughness was increased significantly, with $J_c^{ML} = 3.69$ kJ/m^2 even surpassing the values of composites with 2 PP-Soft ILs and $t = 0.9$ mm.

3.3. Fracture behavior and force–displacement curves

The force–displacement curves of all investigated layer architectures are compared in Figs. 5a to 6b. It is tempting to compare initial slopes, areas under the curves and the maximum forces and try to rank the composites accordingly. This should be avoided though, since the force–displacement curves are highly sensitive to the individual specimen geometry. The variances in a_0/W, which are mentioned in Section 2.3, make rankings based on the force–displacement curves unreliable. Normalized values such as J_c^{ML}, E^{eq} or Ω (Table 3) are advisable instead. These parameters are discussed thoroughly in the next section. In this section, only the course of the curves is discussed.

The distinguishing features of composites with PP-Soft ILs (Fig. 5a and b) are the sudden decreases in force (pop-ins). These happened when one of the matrix ligaments failed due to unstable crack extension. It occurred the first time when the crack propagated towards the first IL due to the anti-shielding effect. The sec-
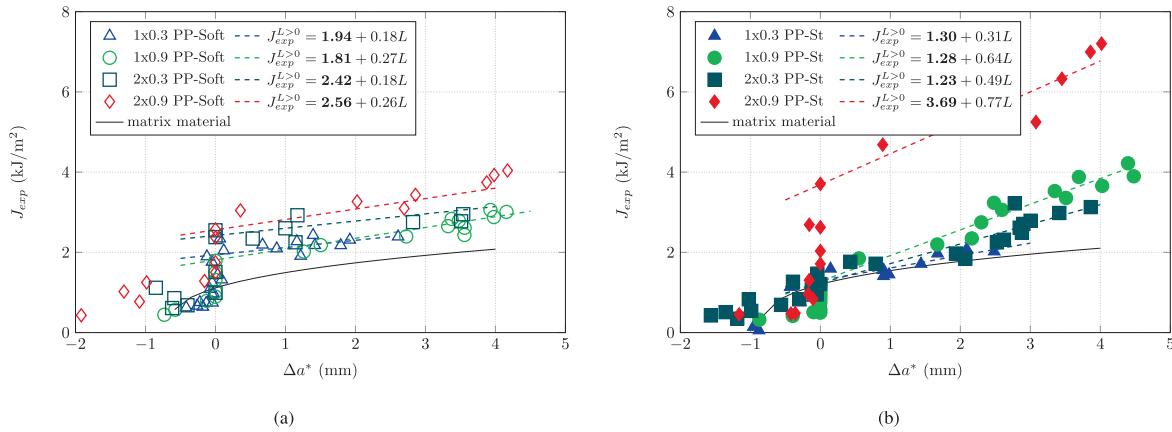
Fig. 4. Adapted crack growth resistance curves for composites with (a) PP-Soft IL(s) and (b) PP-St ILs (matrix material, 1x0.3 PP-St, 1x0.3 PP-Soft and 2x0.3 PP-Soft reprinted with permission of [34]).

Table 3
Overview of results for fracture toughness and specimen stiffness.

Material	J_c^{ML} [kJ/m²]	$J_{\Delta a^*=0}^{Matrix}$ [kJ/m²]	Ω [-]	E^{eq} [MPa]
1×0.3 PP-Soft	1.94	1.12	1.74	4236 ± 400
2×0.3 PP-Soft	2.42	1.18	2.05	3460 ± 233
1×0.9 PP-Soft	1.81	1.27	1.43	3045 ± 251
2×0.9 PP-Soft	2.56	1.44	1.78	2766 ± 438
1×0.3 PP-St	1.3	1.2	1.08	5289 ± 437
2×0.3 PP-St	1.23	1.42	0.86	5555 ± 367
1×0.9 PP-St	1.28	1.13	1.13	5293 ± 340
2×0.9 PP-St	3.69	1.31	2.81	5493 ± 747
Matrix	-	-	1	5849 ± 638

ond pop-in happened after re-initiation of crack growth beyond the first IL. Between these two pop-ins, no crack propagation was observed. The curves of specimens with one and two ILs look

almost the same, since crack arrest and re-initiaion happened in all of those specimens in a similar way and no second crack arrest occurred in specimens with two ILs.

A noteworthy fracture behavior could be observed for 2x0.3 PP-Soft and 2x0.9 PP-Soft and the corresponding fracture behaviors are shown in Fig. 5b. Both exhibited two ILs of PP-Soft, which caused the crack front to skip the matrix section b_1, so that the ligaments failed in the order $b_0 \rightarrow b_2 \rightarrow b_1$. This altered failure sequence was reported in a previous contribution[34] and explained by the inability of the IL material to transfer stresses in a significant way. The decoupling of stresses between the matrix ligaments led to individual stress states in each matrix section. After the sharp crack was neutralized by an IL, the remaining matrix sections were loaded like separate, unnotched bending specimens. The largest of those ligaments failed first due to higher stresses in the outer fiber, so that smaller ligaments were skipped in the failure process. Comparable phenomena were found in met-
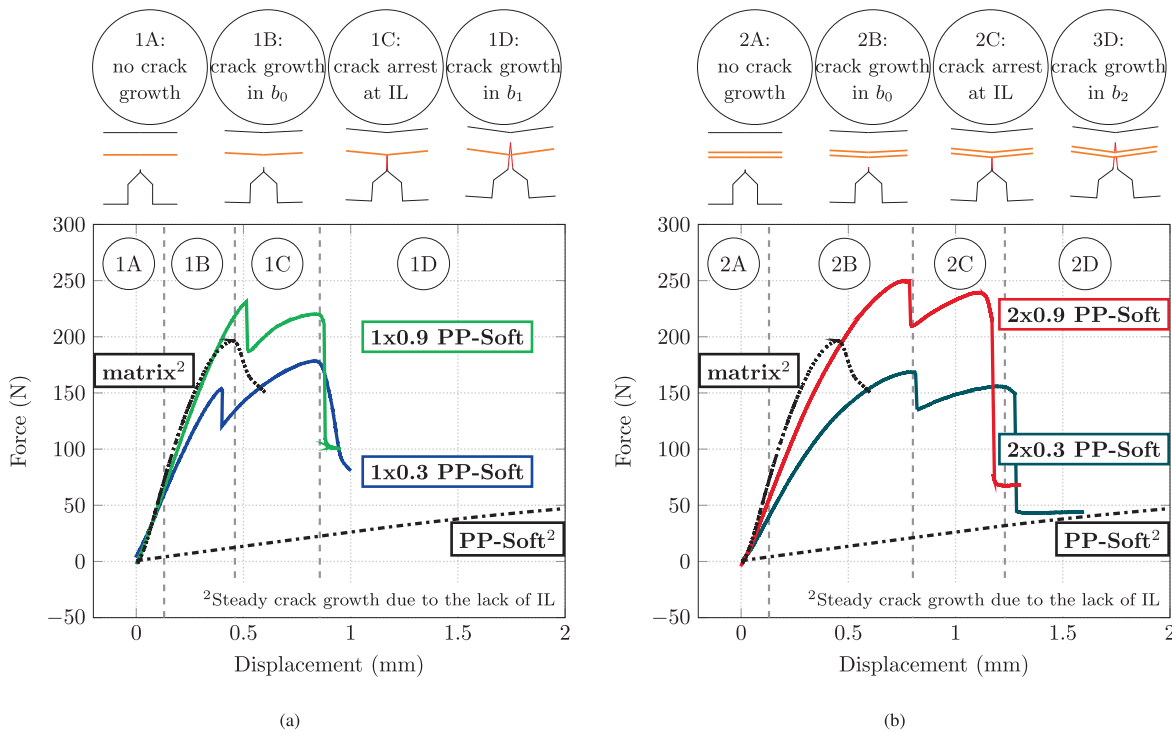

Fig. 5. Force displacement curves during SENB testing of (a) 1x0.3 PP-Soft and 1x0.9 PP-Soft, (b) 2x0.3 PP-Soft and 2x0.9 PP-Soft, PP-Soft and the matrix material.

als, where the stacking sequence of layers affected the progression of fracture [44].

Such extreme cases of stress decoupling were not found in specimens with PP-St ILs (Fig. 6a and b). Crack growth started from the initial notch and did not skip smaller layers in the composites with two ILs. Apparently, the IL of PP-St offered enough stiffness and strength for the transfer of bending stresses, so that all remaining matrix ligaments deformed as one large bending specimen after crack arrest. Therefore, the order failure was $b_0 \rightarrow b_1 \rightarrow b_2$.

In 1x0.3 PP-St, 1x0.9 PP-St and 2x0.3 PP-St the force also decreased after crack initiation, but no pop-ins could be seen. Crack arrest was not achieved in these composites, leading to small areas under the force–displacement curves and low values of J_{exp}. 2x0.9 PP-St, on the other hand, showed the material inhomogeneity effect and growing cracks were stopped. The forces remained relatively high until specimen failure, even if individual ligaments fractured. The constant force suggests sufficient stress transfer by the IL and an even distribution of the load over the whole cross-section.

The stress decoupling effect was linked to a strong decrease in bending stiffness. In investigations of PP microlayer composites under impact, soft ILs were found to increase the impact strength at the cost of stiffness [36]. The decrease was shown to be especially severe under a bending load, since the decoupled matrix ligaments have a reduced area moment of inertia. While this drawback was not as large under tensile loading, it was still noticeable. Wang et al. [44] reported similar findings for titanium-based laminates, where crack tip blunting and crack deflection led to increased ductility at the cost of bending strength.

The stress decoupling, however, appears to be independent from the crack arrester effect, which was present in all composites with PP-Soft ILs as well as in 2x0.9 PP-St. The stress decoupling may have a large influence on the re-initiation process after crack arrest (PP-Soft composites, Fig. 4a), but does not appear to be a requirement for the crack arrester effect (2x0.9 PP-St, Fig. 4b). The independence of stress transfer and crack arrest should be considered beneficial. It means that the material inhomogeneity effect can still be used to increase fracture toughness, while avoiding extreme cases of stress decoupling. Such a combination may be useful for applications, where stiffness and toughness need to be high.

3.4. Comparison of stiffness and fracture toughness

An overview of the normalized parameters for fracture toughness and stiffness, Ω and E^{eq}, is given in Table 3 and Fig. 7. Fig. 7a shows, that all ILs of PP-Soft led to an increase in fracture toughness. For $t = 0.3$ mm, Ω was improved from 1.74 (1x0.3 PP-Soft) to 2.05 (2x0.3 PP-Soft) by adding a second IL. This increase was not caused by a second crack arrest, but can be explained by the smaller bending stress maxima in the two separate matrix sections. Crack re-initiation after arrest was more difficult in 2x0.3 PP-Soft as a result.

The same trend can be seen for 1x0.9 PP-Soft and 2x0.9 PP-Soft, although the improvements overall with $\Omega = 1.43$ and $\Omega = 1.78$ are slightly below their counterparts with $t = 0.3$ mm. This can be attributed to the higher content of soft material, which did not enhance the crack arresting properties, but decreased specimen stiffness. Therefore, less work needed to be spent in order to cause specimen failure. The loss of specimen stiffness is clearly visible in Fig. 7b, where all specimens with PP-Soft IL are below the matrix properties. The reduction in specimen stiffness was more severe for thicker IL and also when adding additional soft layers. Thus, specimen stiffnesses only ranged from 47–72% of the matrix stiffness. It can be concluded, that adding more soft layers improves fracture toughness to some degree at the cost of specimen stiffness. On the other hand, making layers thicker does not improve fracture toughness, once crack arrest has been achieved in the first place.

For PP-St IL with $t = 0.3$ mm, namely 1x0.3 PP-St and 2x0.3 PP-St, no improvement compared to the matrix properties could be found. In fact, 2x0.3 PP-St is even worse than the pure matrix
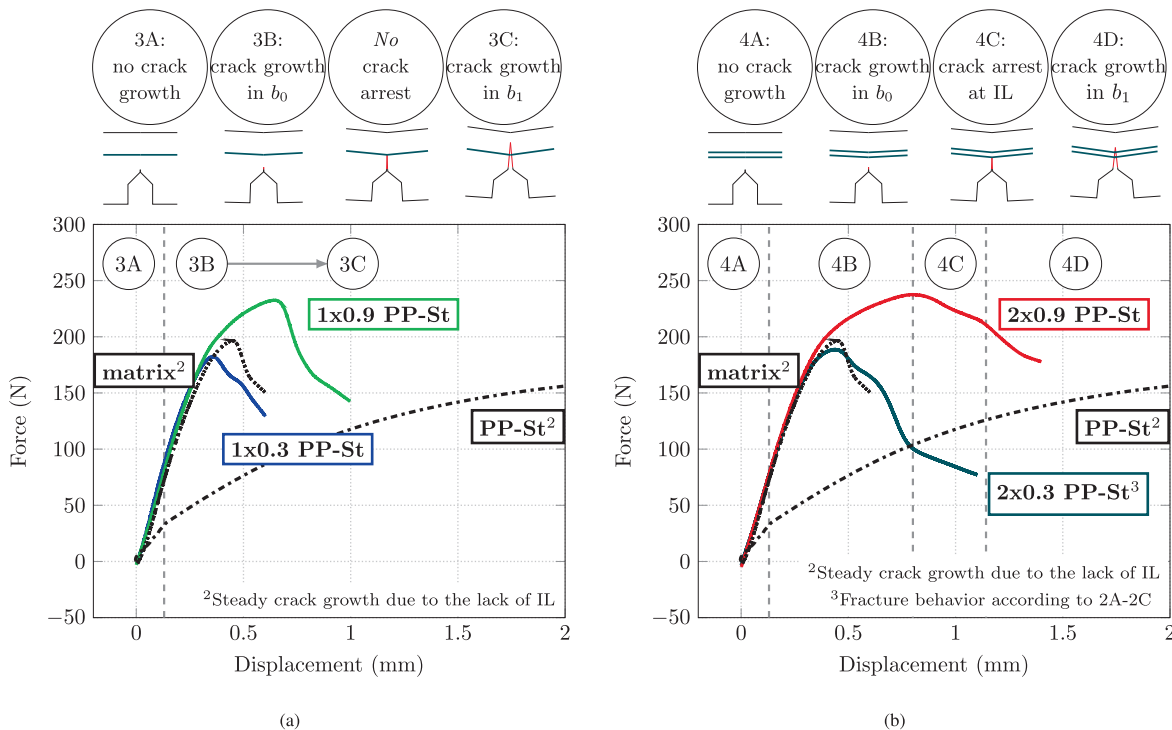

Fig. 6. Force displacement curves during SENB testing of (a) 1x0.3 PP-St and 1x0.9 PP-St, (b) 2x0.3 PP-St and 2x0.9 PP-St, PP-St and the matrix material.
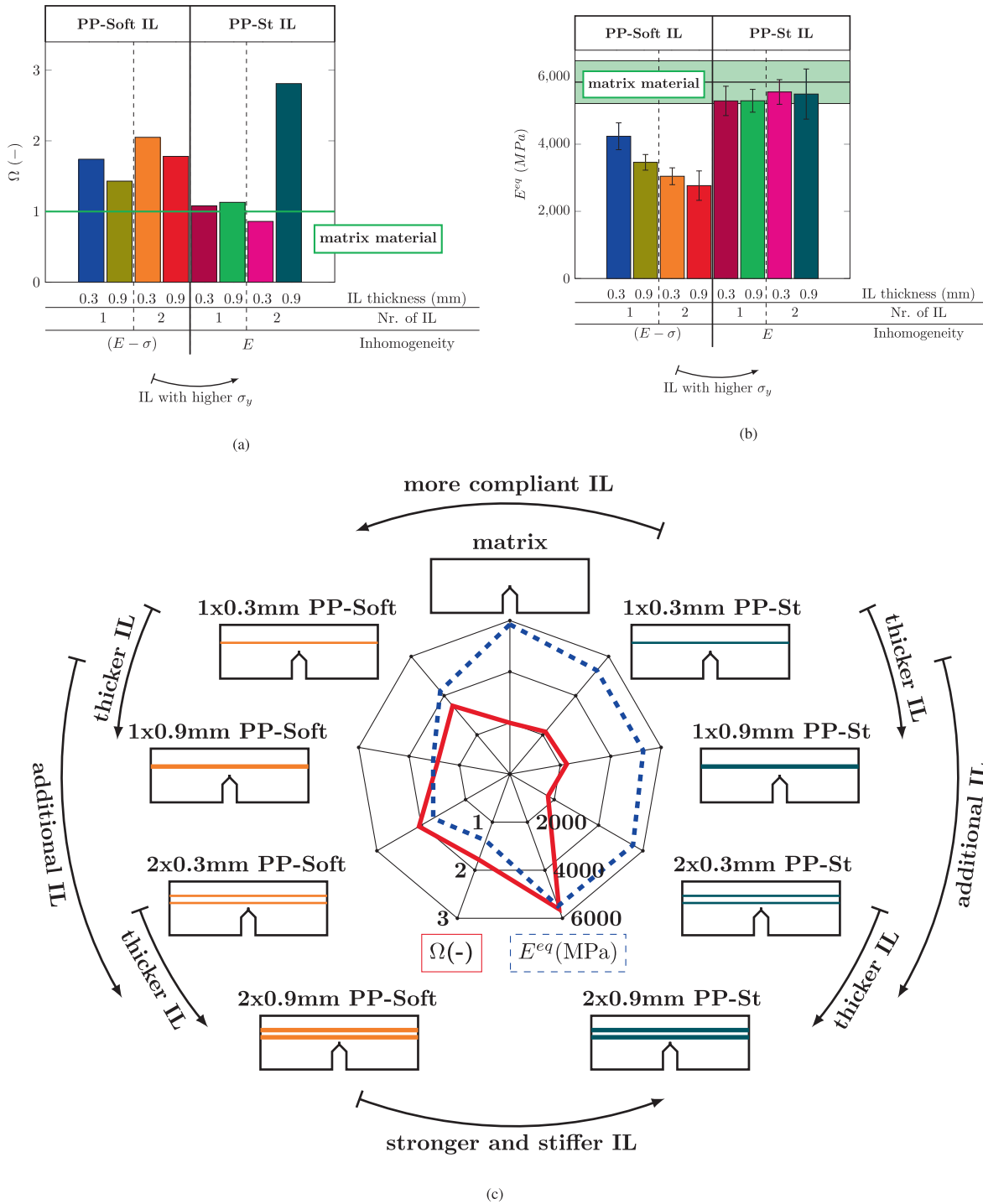
Fig. 7. Comparison of (a) specimen stiffness, (b) fracture toughness and (c) specimen stiffness versus fracture toughness of multilayered composites.

material with $\Omega = 0.86$. Apparently, the E-inhomogeneity on its own was not enough to prevent crack growth. Kolednik et al. [32] offer an explanation in such cases, where the material inhomogeneity effect is strongly reduced due to plastic deformation of the IL. This problem may be avoided by increasing the size or number of IL, so that at least a portion of soft IL avoids plastic deformation.

The 1x0.9 mm PP-St specimens appear to be in a transition region. Although the material inhomogeneity effect is visible in the shape of the $J - R$ curve, the improvement in fracture toughness is rather small with $\Omega = 1.13$. One explanation is, that the

crack arrest worked only for a limited time during the experiment. As the load increased, the plastic zone in the IL grew as well and the benefits of the E-inhomogeneity were lost before major improvements over the matrix material could be accomplished. Such a crack re-initiation due to plastic deformation is illustrated in Fig. 8a.

Adding another IL with 0.9 mm thickness offered sufficient space for plastic deformation within the IL, so that the neighboring matrix ligament is not affected in a negative way (Fig. 8b). At least some portion of the IL in 2x0.9 mm PP-St avoided plastic deformation, thus providing crack arresting properties. This led to the high-
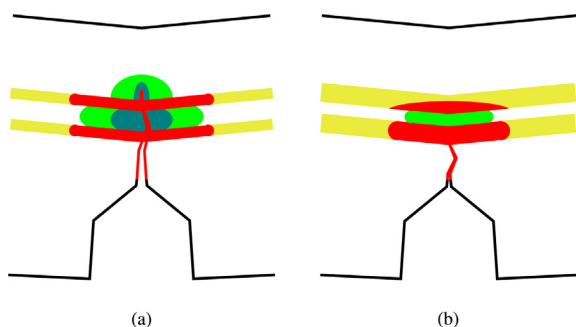
Fig. 8. (a) Crack re-initiation due to plastic deformation and (b) crack arrest with a plastic zone, that is contained within a large IL.

est relative fracture toughness among the investigated materials with $\Omega = 2.81$. While some reduction of E^{eq} occurred due to the introduction of PP-St, the overall specimen stiffness could be kept high. The measured values ranged from 90 to 95% of the matrix stiffness, which is a distinct improvement compared to the IL made of PP-Soft.

As discussed above, using very soft IL materials may have negative effects on specimen stiffness, while using stiffer and stronger materials could compromise the crack arresting properties. Specimen stiffness and fracture toughness should therefore be looked at simultaneously to get a holistic view of material properties. Thus, Ω and E^{eq} are compared for all materials in Fig. 7c. 2x0.9 mm PP-St emerges as the best compromise of properties: An excellent increase in fracture toughness is combined with good stiffness ($\Omega = 2.81$ and $E^{eq} = 5493 \pm 747$ MPa), while all other composites show a shortcoming in one of these parameters. Surprisingly, the best increase of fracture toughness was found using only the E-inhomogeneiy with a favorable layer architecture. This proves once more the importance of microstructure to biomimetic endeavors.

4. Conclusions

Multilayer composites with a highly talcum reinforced polypropylene (PP) matrix and various interlayer (IL) configurations of standard PP (PP-St) and very compliant PP (PP-Soft) were tested in single edge notched bending experiments. PP-St showed lower Young's modulus, E, but similar yield stress, σ_y, compared to the matrix, which is called an E-inhomogeneity. PP-Soft had lower E and σ_y than the matrix, which is an $(E - \sigma)$-inhomogeneity.

PP-Soft IL showed crack arresting properties in all cases, which can be explained by the so-called material inhomogeneity effect between IL and matrix. The resulting increase in fracture toughness ranged from 43–105% compared to the homogeneous matrix material. However, specimen stiffness was reduced as a consequence of the soft IL and, depending on individual layer architecture, only 43–72% of matrix stiffness could be retained.

For PP-St composites, specimen stiffness remained high due to the increased σ_y of the IL material. 90–95% of matrix stiffness were preserved, although ILs with a thickness of 0.3 mm did not show crack arresting properties. This ineffectiveness could be attributed to plastic deformation of the IL, which strongly reduced the effectiveness of the E-inhomogeneity. Two consecutive IL of with 0.9 mm thickness were sufficient to contain plastic deformation and arrest growing cracks. These specimens showed an excellent increase in fracture toughness of 181% and retained 94% of matrix stiffness.

This example shows, that an optimum of fracture toughness and specimen stiffness can be achieved through careful material selection and layer design.

Data availability

The raw/processed data required to reproduce these findings cannot be shared at this time as the data also forms part of an ongoing study.

Declaration of Competing Interest

The authors declare that they have no known competing financial interests or personal relationships that could have appeared to influence the work reported in this paper.

Acknowledgements

References

[1] Y. Estrin, Y. Bréchet, J. Dunlop, P. Fratzl, Architectured Materials in Nature and Engineering, Vol. 282, Springer International Publishing, Cham, 2019. doi:10.1007/978-3-030-11942-3.

[2] Y. Estrin, Y. Beygelzimer, R. Kulagin, P. Gumbsch, P. Fratzl, Y. Zhu, H. Hahn, Architecturing materials at mesoscale: some current trends, Materials Research Letters 9 (10) (2021) 399–421, https://doi.org/10.1080/21663831.2021.1961908.

[3] E.F. Morgan, G.L. Barnes, T.A. Einhorn, The bone organ system, in: Osteoporosis, Elsevier, 2013, pp. 3–20. doi:10.1016/B978-0-12-415853-5.00001-7.

[4] F. Barthelat, H.D. Espinosa, An experimental investigation of deformation and fracture of nacre–mother of pearl, Exp. Mech. 47 (3) (2007) 311–324, https://doi.org/10.1007/s11340-007-9040-1.

[5] J. Song, C. Fan, H. Ma, L. Liang, Y. Wei, Crack deflection occurs by constrained microcracking in nacre, Acta. Mech. Sin. 34 (1) (2018) 143–150, https://doi.org/10.1007/s10409-017-0724-1.

[6] J. Aizenberg, J.C. Weaver, M.S. Thanawala, V.C. Sundar, D.E. Morse, P. Fratzl, Skeleton of euplectella sp. structural hierarchy from the nanoscale to the macroscale, Science (New York, N.Y.) 309 (5732) (2005) 275–278. doi:10.1126/science.1112255.

[7] A. Miserez, J.C. Weaver, P.J. Thurner, J. Aizenberg, Y. Dauphin, P. Fratzl, D.E. Morse, F.W. Zok, Effects of laminate architecture on fracture resistance of sponge biosilica: Lessons from nature, Adv. Funct. Mater. 18 (8) (2008) 1241–1248, https://doi.org/10.1002/adfm.200701135.

[8] A. Woesz, J.C. Weaver, M. Kazanci, Y. Dauphin, J. Aizenberg, D.E. Morse, P. Fratzl, Micromechanical properties of biological silica in skeletons of deep-sea sponges, J. Mater. Res. 21 (08) (2006) 2068–2078, https://doi.org/10.1557/jmr.2006.0251.

[9] C. Levi, J.L. Barton, C. Guillemet, E. Le Bras, P. Lehuede, A remarkably strong natural glassy rod: The anchoring spicule of the monorhaphis sponge, J. Mater. Sci. Lett. 8 (3) (1989) 337–339, https://doi.org/10.1007/BF00725516.

[10] W.E.G. Müller, X. Wang, K. Kropf, H. Ushijima, W. Geurtsen, C. Eckert, M.N. Tahir, W. Tremel, A. Boreiko, U. Schlossmacher, J. Li, H.C. Schröder, Bioorganic/inorganic hybrid composition of sponge spicules: Matrix of the giant spicules and of the comitalia of the deep sea hexactinellid monorhaphis, Journal of structural biology 161 (2) (2008) 188–203, https://doi.org/10.1016/j.jsb.2007.10.009.

[11] M.K. Islam, P.J. Hazell, J.P. Escobedo, H. Wang, Biomimetic armour design strategies for additive manufacturing: A review, Materials & Design 205 (2021) 109730, https://doi.org/10.1016/j.matdes.2021.109730.

[12] L. Wang, J. Lau, E.L. Thomas, M.C. Boyce, Co-continuous composite materials for stiffness, strength, and energy dissipation, Adv. Mater. 23 (13) (2011) 1524–1529, https://doi.org/10.1002/adma.201003956.

[13] L.S. Dimas, G.H. Bratzel, I. Eylon, M.J. Buehler, Tough composites inspired by mineralized natural materials: Computation, 3d printing, and testing, Adv. Funct. Mater. 23 (36) (2013) 4629–4638, https://doi.org/10.1002/adfm.201300215.

[14] J.R. Raney, B.G. Compton, J. Mueller, T.J. Ober, K. Shea, J.A. Lewis, Rotational 3d printing of damage-tolerant composites with programmable mechanics, Proceedings of the National Academy of Sciences of the United States of America 115 (6) (2018) 1198–1203, https://doi.org/10.1073/pnas.1715157115.

[15] Z.-Z. Li, M. Li, Y.-X. Feng, Z. Zhang, Y.-E. Wen, Q.-Q. Huang, Z. Lu, H. Bai, H.-L. Wang, B.-B. Xu, H. Cölfen, P. Fratzl, S. Amini, Y. Jiang, Bioinspired compartmentalization strategy for coating polymers with self-organized

prismatic films, Chem. Mater. 33 (23) (2021) 9240–9251, https://doi.org/10.1021/acs.chemmater.1c02868.

[16] R. Cao, Q. Yu, Y. Li, R.O. Ritchie, Dual-gradient structure leads to optimized combination of high fracture resistance and strength-ductility synergy with minimized final catastrophic failure, Journal of Materials Research and Technology 15 (2021) 901–910, https://doi.org/10.1016/j.jmrt.2021.08.102.

[17] T. Fromm, S. Bruns, M.-C. Müller, A. Fink, R. Borchardt, S.M. Rosiwal, K. Durst, Bioinspired damage tolerant diamond-metal laminates by alternating cvd and pvd processes, Materials & Design 213 (2022) 110315, https://doi.org/10.1016/j.matdes.2021.110315.

[18] Y. Estrin, Y. Beygelzimer, R. Kulagin, Design of architectured materials based on mechanically driven structural and compositional patterning, Adv. Eng. Mater. 21 (9) (2019) 1900487, https://doi.org/10.1002/adem.201900487.

[19] V. Beloshenko, I. Vozniak, Y. Beygelzimer, Y. Estrin, R. Kulagin, Severe plastic deformation of polymers, MATERIALS TRANSACTIONS 60 (7) (2019) 1192–1202, https://doi.org/10.2320/matertrans.MF201912.

[20] R. Kulagin, Y. Beygelzimer, A. Bachmaier, R. Pippan, Y. Estrin, Benefits of pattern formation by severe plastic deformation, Applied Materials Today 15 (2019) 236–241, https://doi.org/10.1016/j.apmt.2019.02.007.

[21] T. Köpplmayr, E. Mayrhofer, C. Unterweger, Thermo-mechanical properties of β-nucleated polypropylene multilayers, Polym. Testing 39 (2014) 79–85, https://doi.org/10.1016/j.polymertesting.2014.08.001.

[22] J. Zhao, Y. Qiao, G. Wang, C. Wang, C.B. Park, Lightweight and tough pp/talc composite foam with bimodal nanoporous structure achieved by microcellular injection molding, Materials & Design 195 (2020) 109051, https://doi.org/10.1016/j.matdes.2020.109051.

[23] K.G. Hoffmann, K. Haag, J. Müssig, Biomimetic approaches towards lightweight composite structures for car interior parts, Materials & Design 212 (2021) 110281, https://doi.org/10.1016/j.matdes.2021.110281.

[24] H. Gao, B. Ji, I.L. Jager, E. Arzt, P. Fratzl, Materials become insensitive to flaws at nanoscale: lessons from nature, Proceedings of the National Academy of Sciences of the United States of America 100 (10) (2003) 5597–5600, https://doi.org/10.1073/pnas.0631609100.

[25] R. Qu, R. Maaß, Z. Liu, D. Tönnies, L. Tian, R.O. Ritchie, Z. Zhang, C.A. Volkert, Flaw-insensitive fracture of a micrometer-sized brittle metallic glass, Acta Mater. 218 (2021) 117219, https://doi.org/10.1016/j.actamat.2021.117219.

[26] O. Kolednik, J. Predan, F.D. Fischer, P. Fratzl, Bioinspired design criteria for damage-resistant materials with periodically varying microstructure, Adv. Funct. Mater. 21 (19) (2011) 3634–3641, https://doi.org/10.1002/adfm.201100443.

[27] J.R. Rice, A path independent integral and the approximate analysis of strain concentration by notches and cracks, J. Appl. Mech. 35 (2) (1968) 379, https://doi.org/10.1115/1.3601206.

[28] G.A. Maugin, Material forces: Concepts and applications, Appl. Mech. Rev. 48 (5) (1995) 213, https://doi.org/10.1115/1.3005101.

[29] M.E. Gurtin, Configurational Forces as Basic Concepts of Continuum Physics, Vol. 137, Springer New York, New York, NY, 2000. doi:10.1007/b97847.

[30] N.K. Simha, F.D. Fischer, O. Kolednik, J. Predan, G.X. Shan, Crack tip shielding or anti-shielding due to smooth and discontinuous material inhomogeneities, Int. J. Fract. 135 (1–4) (2005) 73–93, https://doi.org/10.1007/s10704-005-3944-5.

[31] M. Sistaninia, O. Kolednik, Effect of a single soft interlayer on the crack driving force, Eng. Fract. Mech. 130 (2014) 21–41, https://doi.org/10.1016/j.engfracmech.2014.02.026.

[32] O. Kolednik, R. Kasberger, M. Sistaninia, J. Predan, M. Kegl, Development of damage-tolerant and fracture-resistant materials by utilizing the material inhomogeneity effect, J. Appl. Mech. 86 (11) (2019) 263, https://doi.org/10.1115/1.4043829.

[33] A. Tiwari, J. Wiener, F. Arbeiter, G. Pinter, O. Kolednik, Application of the material inhomogeneity effect for the improvement of fracture toughness of a brittle polymer, Eng. Fract. Mech. 224 (2020) 106776, https://doi.org/10.1016/j.engfracmech.2019.106776.

[34] J. Wiener, F. Arbeiter, A. Tiwari, O. Kolednik, G. Pinter, Bioinspired toughness improvement through soft interlayers in mineral reinforced polypropylene, Mech. Mater. 140 (2020) 103243, https://doi.org/10.1016/j.mechmat.2019.103243.

[35] Z. Jia, Y. Yu, S. Hou, L. Wang, Biomimetic architected materials with improved dynamic performance, J. Mech. Phys. Solids 125 (2019) 178–197, https://doi.org/10.1016/j.jmps.2018.12.015.

[36] J. Wiener, H. Kaineder, O. Kolednik, F. Arbeiter, Optimization of mechanical properties and damage tolerance in polymer-mineral multilayer composites, Materials (Basel, Switzerland) 14 (4). doi:10.3390/ma14040725.

[37] G. Tan, Q. Yu, Z. Liu, X. Wang, M. Zhang, Y. Liu, Z. Zhang, R.O. Ritchie, Compression fatigue properties and damage mechanisms of a bioinspired nacre-like ceramic-polymer composite, Scripta Mater. 203 (2021) 114089, https://doi.org/10.1016/j.scriptamat.2021.114089.

[38] I.O. for Standardization, Din en iso 527–1:2019–12, plastics - determination of tensile properties - part 1: General principles (2019). doi:10.31030/3059426.

[39] G.E. Hale, F. Ramsteiner, J-fracture toughness of polymers at slow speed, in: Fracture Mechanics Testing Methods for Polymers, Adhesives and Composites, Vol. 28 of European Structural Integrity Society, Elsevier, 2001, pp. 123–157. doi:10.1016/S1566-1369(01)80031-5.

[40] G.R. Irwin, Plastic zone near a crack and fracture toughness, Proceeding in Sagamore Ordnance Material Conference (1960) IV63–1V78.

[41] A.B. Martínez, N. León, D. Arencón, J. Rodríguez, A. Salazar, On the effect of the different notching techniques on the fracture toughness of petg, Polym. Testing 32 (7) (2013) 1244–1252, https://doi.org/10.1016/j.polymertesting.2013.07.016.

[42] A.B. Martínez, A. Salazar, N. León, S. Illescas, J. Rodríguez, Influence of the notch-sharpening technique on styrene-acrylonitrile fracture behavior, J. Appl. Polym. Sci. 133 (32) (2016) 11, https://doi.org/10.1002/app.43775.

[43] ASTM International E08 Committee, ASTM E1820, Test method for measurement of fracture toughness (2019). doi:10.1520/E1820-01.

[44] S. Wang, L. Huang, S. Jiang, R. Zhang, F. Sun, Q. An, L. Geng, Multiplied bending ductility and toughness of titanium matrix composites by laminated structure manipulation, Mater. Des. 197 (2021) 109237, https://doi.org/10.1016/j.matdes.2020.109237.

7.5. *Publication V*

Title:	Characterization methods for strain-induced damage in polypropylene
Authors:	Johannes Wiener[a], Florian Preissegger[a], Bernhard Plank[b,c], Florian Arbeiter[a], Otmar Kolednik[d], Gerald Pinter[a]
Affiliation:	[a] Materials Science and Testing of Polymers, Montanuniversitaet Leoben, 8700 Leoben, Austria
	[b] Research Group Computed Tomography, University of Applied Sciences Upper Austria: Campus Wels, Wels, Austria
	[c] Mechanical Engineering, University of Augsburg, Augsburg, Germany
	[d] Erich-Schmid-Institute of Materials Science, Austrian Academy of Science, 8700 Leoben, Austria
DOI:	https://doi.org/10.1002/pen.25979
Conceptualization:	Johannes Wiener (70%), Florian Arbeiter (30%)
Methodology:	Johannes Wiener (60%), Florian Arbeiter (10%), Bernhard Plank (30%)
Validation:	equal contribution by all authors
Investigation:	Johannes Wiener (60%), Florian Preissegger (20%), Bernhard Plank (20%)
Writing- Original Draft:	Johannes Wiener (60%), Florian Arbeiter (20%), Bernhard Plank (20%)
Writing- Review & Editing	equal contribution by all authors
Supervision	Florian Arbeiter (60%), Gerald Pinter (20%), Otmar Kolednik (20%)

RESEARCH ARTICLE

Characterization methods for strain-induced damage in polypropylene

Johannes Wiener[1] | Florian Preissegger[1] | Bernhard Plank[2,3] |
Florian Arbeiter[1] | Otmar Kolednik[4] | Gerald Pinter[1]

[1]Materials Science and Testing of Polymers, Montanuniversitaet Leoben, Leoben, Austria

[2]Research Group Computed Tomography, University of Applied Sciences Upper Austria: Campus Wels, Wels, Austria

[3]Mechanical Engineering, University of Augsburg, Augsburg, Germany

[4]Erich-Schmid-Institute of Materials Science, Austrian Academy of Science, Leoben, Austria

Correspondence
Florian Arbeiter, Materials Science and Testing of Polymers, Montanuniversitaet Leoben, 8700 Leoben, Austria.
Email: florian.arbeiter@unileoben.ac.at

Funding information
State Government of Upper Austria; pore3D, Grant/Award Number: 868735; BeyondInspection, Grant/Award Number: 874540; Austrian Research Promotion Agency (FFG), Grant/Award Number: 858562

Abstract

Various methods are used to characterize the deterioration of mechanical properties in polymers. The focus is set on distinguishing between time-dependent and irreversible damage in two different grades of polypropylene. First, digital image correlation is utilized to capture the stress–strain behavior during monotonic tensile tests. Changes in specimen volume are recorded throughout the experiment and serve as an indicator for crazes and voids. However, the elastic modulus, E, cannot be monitored throughout the entire experiment. Further analysis is performed in the form of cyclic load–unload tests. E and the residual strain, ε_{res}, as a function of the applied strain, $\varepsilon_{\text{appl}}$, are obtained for each cycle. Results show that E primarily suffers from the time-dependent behavior of the tested polymers in this case. Subsequently, an alternative technique is applied, where specimens are prestrained and then allowed to relax. In the following dynamic mechanical analysis, viscoelastic effects can be avoided. Considerations on the onset and evolution of damage are made. Ultimately, these results are confirmed through microcomputed tomography, where the shapes and densities of defects are captured in high resolution.

KEYWORDS

computed tomography, damage, elastic modulus decay, polypropylene

1 | INTRODUCTION

Various mechanisms of microstructural damage are known in literature. Unfortunately, the definitions and descriptions often vary. For the purposes of this contribution, the focus is set on four closely related types of microstructural damage, namely voids, microcracks, polar fans, and crazes (Figure 1A–D). Voids are defects with no characteristic shape or orientation and often act as starting point for material failure. In homogeneous materials, void growth starts from local irregularities in the molecular packing.[1] In heterogeneous materials, voids can initiate from rubber particles[2] or reinforcing particles.[3,4] In these examples, the debonding of particles from the matrix gives rise to void growth. The amorphous boundary layer between large spherulites in semicrystalline polymers may also act as starting point for void growth under certain conditions.[5,6] Under high enough dilatational stresses, voids are able to grow in size and coalesce,[7] usually starting at the yield point.[8] Interestingly, void coalescence
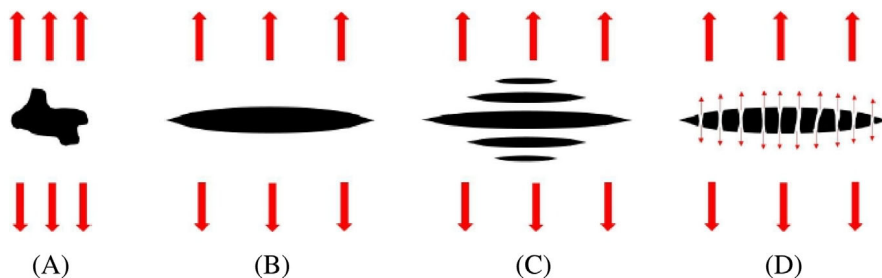
FIGURE 1 Representation of various microdamages and their characteristics, including (A) voids (no aspect ratio and no stress transfer), (B) microcracks (high aspect ratio but no stress transfer), (C) polar fans (column of microcracks), and (D) crazes (high aspect ratio and limited stress transfer)

can lead to larger voids or other classes of damage. While for voids no orientation is assumed, the subsequent mechanisms can be categorized by a characteristic shape and/or aspect ratio. Microcracks, for example, can be seen as an oriented void where two crack flanks join in sharp corners.[9] This gives the defect a high aspect ratio and a slim appearance, which is oriented perpendicular to the main tensile stress. Due to the sharp corners and the lack of stress transfer between the flanks, microcracks have a most detrimental form of notching effect. Thus, cracks grow easily under loading, leading to crack extension and coalescence of microcracks to larger cracks. Over time, the problem enters the domain of fracture mechanics and catastrophic failure may be imminent.[10] Several sources in literature[11–13] report the so-called polar fans specifically in semicrystalline polymers with a well-defined crystal structure. These constructs are localized clusters of microcracks that are aligned parallel to the loading direction. The individual cracks are still separated by thin walls of intact material. Laiarinandrasana et al.[14] found such constructs in polypropylene (PP) as well as polyamide stretching from the poles of spherulites toward the center. The highest density of polar fans was found in the necking area and caused volumetric strains as high as 100%.[15] The final specimen failure happens through coalescence of the individual cracks within one column, followed by catastrophic failure. A craze is a special form of a microcrack and is often described as plane, lens-shaped defect in glassy polymers.[9] It shows mostly the same characteristics as a microcrack, but highly stretched fibrils of polymer are spanned from one edge to the other.[16] Therefore, the craze still has a load bearing capacity to some extent.[17] The fibrils spanning the two crack faces are stretched to their maximum possible elongation. When the craze grows, there are two possibilities for the fibrils to react. When the polymer chains are mobile enough, more material can be drawn in from the surrounding material, so the fibrils become longer and the whole craze wider. This is known as surface drawing or forced reptation.[18] Crazes are able to grow and coalesce through this mechanism.[16] When the material is not mobile enough to perform such a disentanglement process, the fibrils are more likely to fracture. In that case, the craze becomes more similar to a crack the more fibrils are destroyed.[17] While the

preferred orientation for crazes is 90° to the major principal stress, Karger-Kocsis and Barany suggest that slight deviations of orientations are possible to avoid running through spherulites or other obstacles, where surface drawing is hindered.[16]

All of these mechanisms are cavitation-inducing processes that involve a dilatational stress component, which is why they never appear under pure compressive stresses. As a consequence, additional volume is created.[13,15,16,19] Voids and crazes do not close on their own and crack healing is unlikely for most materials, especially if the glass transition temperature is significantly above room temperature. Thus, an irreversible change in volume is expected on the microscale. A macroscopic increase in specimen volume is, therefore, a result of microscopic damage.[10] Additionally, the internal load bearing cross section is reduced, which may lead to a strain softening effect.[20] Voids also promote plastic deformation and can in some cases toughen a brittle material by enhancing plasticity.[21,22] Argon and Cohen even suggest that a brittle material response can be avoided by utilizing this characteristic.[23] In conclusion, increases in volume and residual strains, and a decrease of E can be seen as indicators for microstructural damage.[10] Although shear yielding is a common mechanism in polymers too, the formation of shear bands does not directly contribute to the loss of mechanical properties. Instead, the increased plasticity accelerates the nucleation and growth of voids in regions of high hydrostatic stresses.[24,25] Thus, shear yielding is not discussed in detail in this contribution and the focus is set on the resulting voids and cracks. Distinguishing a damage-induced effects from viscoelastic effects is challenging, since their results on a macroscopic level, such as the deterioration of E, may be the same. Therefore, appropriate testing procedures are needed.

To determine the void volume fraction, X-ray tomography scans or scanning electron microscopy (SEM) on cryofractured specimens are an option.[8,19] These methods have to be employed sometime after testing though, so that the majority of relaxation processes is already completed. Comparable in situ measurements are challenging and suffer from various limitations.[8] One major drawback is the limited temporal resolution of many tomography techniques. Therefore, synchrotron radiation is required even for moderate testing speeds.

Olufsen et al. employed a combination of postprocessing techniques and axisymmetric relations for accelerating X-ray tomography to a point where in situ measurements of tensile tests at moderate testing rates are possible and practical.[26] However, this technique also captures creep effects, which may be reversible. In that case, void size is overestimated by the viscoelastic part of the deformation. Additionally, this approach is limited to round bar specimen types to preserve the axisymmetric relations.

Changes to the microstructure affect optical properties as well. Hamza et al. were able to monitor the refractive index during the cold drawing of PP and nylon fibers using a two-beam polarizing interference microscope. On the one hand, changes to the cross-sectional area,[27] the refractive index profile, and the progression of necking[28] could be detected. On the other hand, the evolution of microcracks at high draw ratios was also visible as disturbances in the microinterferograms.[29]

An indirect, qualitative estimation of microstructure is possible by monitoring E or by capturing surface strains using digital image correlation (DIC). Since no visualization of the actual microstructure is given, these techniques should be verified by other methods, such as computed tomography (CT) or SEM.

In this paper, several characterization techniques are compared regarding their suitability to determine irreversible microstructural damage. Simple modifications to well-known standard testing procedures are offered to distinguish between time-dependent and damage-induced decay of material properties of PP. Stress–strain behavior is determined, starting from monotonic tensile tests. Through cyclic load–unload experiments, the decay of E is recorded. Since these experiments are performed under continuous tensile loading, time-dependent creep effects play a significant role. Therefore, a comparison is made to prestrained specimens after relaxation by dynamic mechanical analyses (DMAs), where time-dependent effects are eliminated. Hereby, assumptions are made on the extent of damage as a function of the applied strain, which is verified by CT.

2 | EXPERIMENT

2.1 | Materials

Two different grades of PP were used for the investigations, an ethylene-propylene block-copolymer (PP-B) and a PP homopolymer (PP-H). Basic microscopy under polarized light with a magnification of 50 was sufficient to give a first impression of the crystalline structures of PP-B and PP-H. As shown in Figure 2A, PP-B exhibited a rather undefined crystalline structure and no clear boundaries of spherulites could be seen. This can be explained by the ethylene

comonomer units, which hindered the crystallization process of the PP segments.[30] PP-H on the other hand did not suffer from such disturbances in the crystallization phase. Thus, a continuous network of large spherulites could be formed. The average size of spherulites was approximately 50 μm (Figure 2B) and the crystalline structure appeared to be more regular compared to PP-B. The amount of amorphous phase between individual spherulites was assumed to be rather small, since sharp corners could be distinguished between large packages of crystalline phase.

2.2 | Methods

For the tensile testing, dumbbell specimens were prepared from both materials. A crosshead speed of 1 mm/min was used for monotonic tests and cyclic load–unload tests, where increasing amplitudes of applied deformation alternated with unloading steps. Strains and volume changes were recorded using two crossed high-resolution cameras and DIC, so that E could be obtained. It should be mentioned that E, the maximum applied strain, ε_{appl}, and the residual strain, ε_{res}, were calculated separately for each load–unload loop of the cyclic tensile tests.

A dumbbell specimen shape was chosen for the DMAas well to avoid failure at the clamping. Specimens were prestrained by 0%, 20%, and 40% before being investigated by DMA with a mean stress level of 0.75 MPa and a stress amplitude of 0.5 MPa. The tests were performed at room temperature (23°C) with a frequency of 1 Hz.

Ultimately, high-resolution X-ray CT scans were used to verify the assumptions on damage onset and evolution.

More detailed descriptions on all the methods mentioned above can be found in Appendix A.

2.3 | Characterization of stress–strain behavior

Only the highest strained sections of the specimens were considered for strain evaluation, since material damage often started and progressed in localized regions. These sections were characterized with virtual extensometers in the DIC measurements. Engineering stress and engineering strain, σ_{eng} and ε_{eng}, were calculated using the well-known relations, Equations (1) and (2). Therein, the force, F, was related to the initial cross section A_0 and effects such as necking or volume change due to void formation could not be captured. The true stress, σ_{true}, which takes a certain amount of necking into account, was calculated by Equation (3). This relation was originally designed for metals and assumes that plastic deformation happens under constant volume. While this may
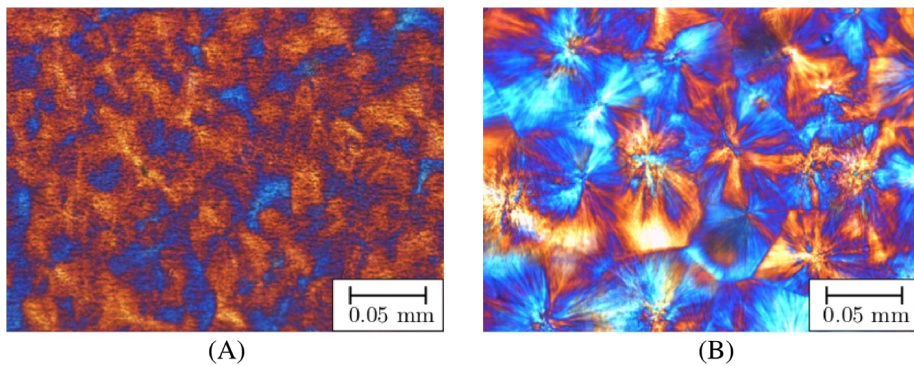
FIGURE 2 Polarized light micrographs with a magnification of 50 for (A) PP-B and (B) PP-H, both in the undeformed state

be true, for example, for shear yielding,[9,17] errors could arise for materials that are prone to void formation or crazing. In these cases, the lateral contraction may be overestimated, since the creation of additional volume inside the material has not been considered. This results in a calculated cross-sectional area that is too small and risks overestimating the stresses. In this contribution, the DIC measurements were used to directly measure the real width and thickness, b_{real} and h_{real}, that occurred at the narrowest specimen section. Using the real cross section, A_{real}, the real stress, σ_{real}, could be calculated (Equations 4 and 5). While this consideration did not consider the loss of internal cross section due to voids, it was still the most accurate estimate that could be made at a macroscopic level. Even more accurate measurements of volume would only be possible by using spectroscopic methods such as in situ tomography. For the sake of simplicity and comparability, all stresses were correlated to the corresponding values of ε_{eng}. In all monotonic tests, E was evaluated according to ISO 527.

$$\sigma_{eng} = \frac{F}{A_0} \tag{1}$$

$$\varepsilon_{eng} = \frac{\Delta l}{l_0} \tag{2}$$

$$\sigma_{true} = \sigma_{eng}\left(1 + \varepsilon_{eng}\right) \tag{3}$$

$$A_{real} = b_{real} h_{real} \tag{4}$$

$$\sigma_{real} = \frac{F}{A_{real}} \tag{5}$$

2.4 | Volume change as sign of damage onset

As mentioned in the introduction and stated by literature, many damage mechanisms are accompanied by an increase in volume.[13,15,16,19] To capture such effects, a normalized volume element, V_{norm}, was calculated from the engineering strains in all three spatial directions (Equation 6 and Figure 3A). These strains were captured in DIC measurements using virtual extensometers (Figure A2B), whereas the load was applied in the y-direction in all experiments. During the monotonic tests, V_{norm} was monitored and served as first indicator of damage onset. However, other effects, such as viscoelastic creep, may also have contributed to the increased volume.

$$V_{norm} = \frac{V_{real}}{V_0} = \frac{b_{real} h_{real} l_{real}}{b_0 h_0 l_0}$$
$$= \left(1 + \varepsilon_{eng,x}\right)\left(1 + \varepsilon_{eng,y}\right)\left(1 + \varepsilon_{eng,z}\right) \tag{6}$$

When plotted against the applied strain, V_{norm} started to increase at a higher rate upon reaching the yield point. This transition point was approximated with two linear regression lines, as shown in Figure 3B, to determine the strain at the intersection point, ε_{vol}. This parameter describes the starting point of accelerated volume increase and may serve as indicator for the onset of material damage with volume change. For stress–strain curves that have a very fluent yield region without a maximum in stress, ε_{vol} could even be used to determine a yield point, if no other options are available.

3 | RESULTS AND DISCUSSION

3.1 | Differences between stress–strain evaluation methods

As a starting point for the investigation, the monotonic tensile tests are chosen. For polymers, the yield point in such experiments is generally determined as the first local maximum in the stress–strain curve, which is often the onset for the necking process. However, time-dependent effects as well as damage to the microstructure cannot be deduced during the experiment, unless the damage is so extensive that it becomes visible, for

FIGURE 3   (A) Volume change due to specimen deformation and (B) determination of ε_{vol}
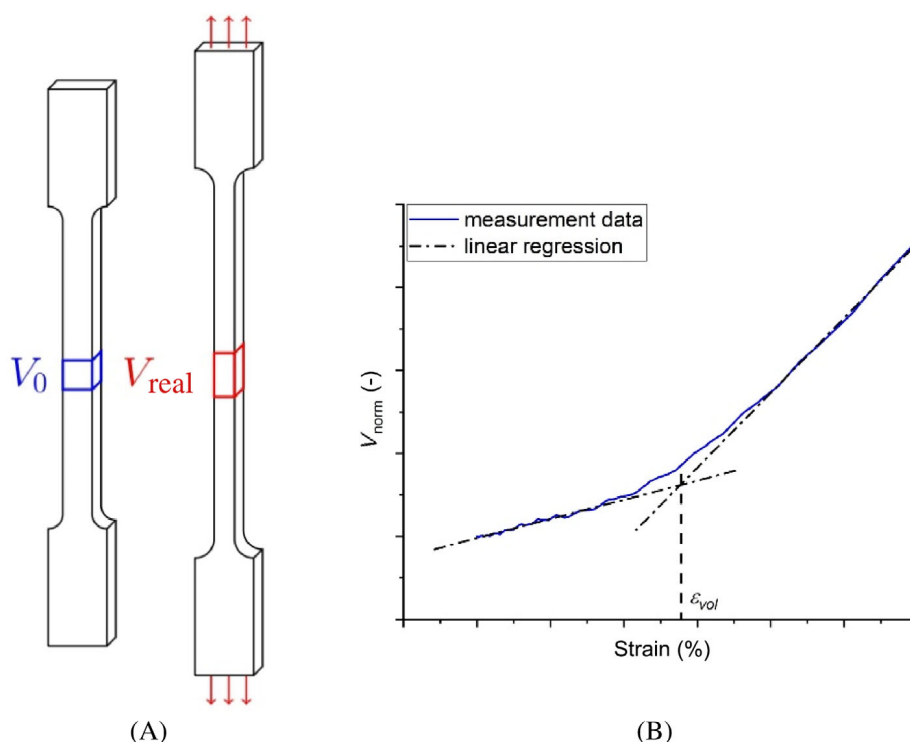
example, as stress whitening or tearing. To gain additional information, V_{norm} was also monitored. Figure 4A, B depicts representative stress–strain curves and the variations of V_{norm} for PP-B and PP-H, whereas the numeric results are listed in Table 1. At first glance, the two materials show a similar stress–strain behavior. Especially the evaluation of E appears unaffected by the method of evaluation (engineering stress–strain, true stress–strain, real stress–strain), although some small differences can be noted in other parts of the curves. PP-H shows approximately 20% higher values of E and σ_{UTS} in comparison with PP-B. The strain at break is high in both cases, but a high data scattering occurred too. When judging only by engineering stress–strain curves, PP-B and PP-H only show strain softening behavior after the yield point. However, this is an error due to extensive necking effects, which are not uncommon for PP. When considering true or real stress–strain curves, both materials show strain hardening after the yield point, presumably caused by cold drawing of the macromolecules. At very high strains, a reduction in stress can be observed as a consequence of extensive material damage. At this advanced stage of damage, the specimens start to slowly tear apart before failing completely. This decrease in stress starts earlier for PP-B than for PP-H. To sum up, engineering stress–strain curves are good approximations for small strains, but for higher deformations other approaches should be considered. As expected, the true stress values overestimate the stresses but give an overall good impression of material behavior. For both materials, the true stress–

strain method seems to underestimate the cross-sectional area, because the changes in volume due to damaging mechanisms are not accounted for. As a result, true stresses at high strains tend to be higher than the real stresses by approximately 15% for PP-B and 20% for PP-H. The real stress–strain method is the most precise due to measuring the actual dimensions of the specimens. Therefore, this method will be used in all further considerations.

The development of V_{norm} over the course of the experiment is also shown in Figure 4. Until to the yield point, V_{norm} remains low for both materials before starting to rise steadily. The point of increased volume gain at ε_{vol} coincides well with the strain at yield point, ε_y, for both PP-B and PP-H. For PP-B, the beginning of specimen failure is accompanied by an increased rate of volume gain, which is not seen in PP-H. In general, PP-B exhibits a higher increase of V_{norm} than PP-H, indicating that the block-copolymer is more susceptible to the formation of voids, cracks, or crazes. Kim et al.[31] suggest, for example, that domains of a second phase or fillers within a matrix play a major role in void formation. Namely, the foreign phases provide initial stress concentrations, which enable the cavitational processes in the first place. Other sources, for example, Kawai et al.[32] claim that the amorphous regions within the material serve as origin of void formation. This may also be a plausible explanation for the increased volume gain of PP-B, which appears to have a less organized crystal structure than PP-H (see Figure 2A vs. Figure 2B). At the end of the experiments, V_{norm} starts dropping for both materials
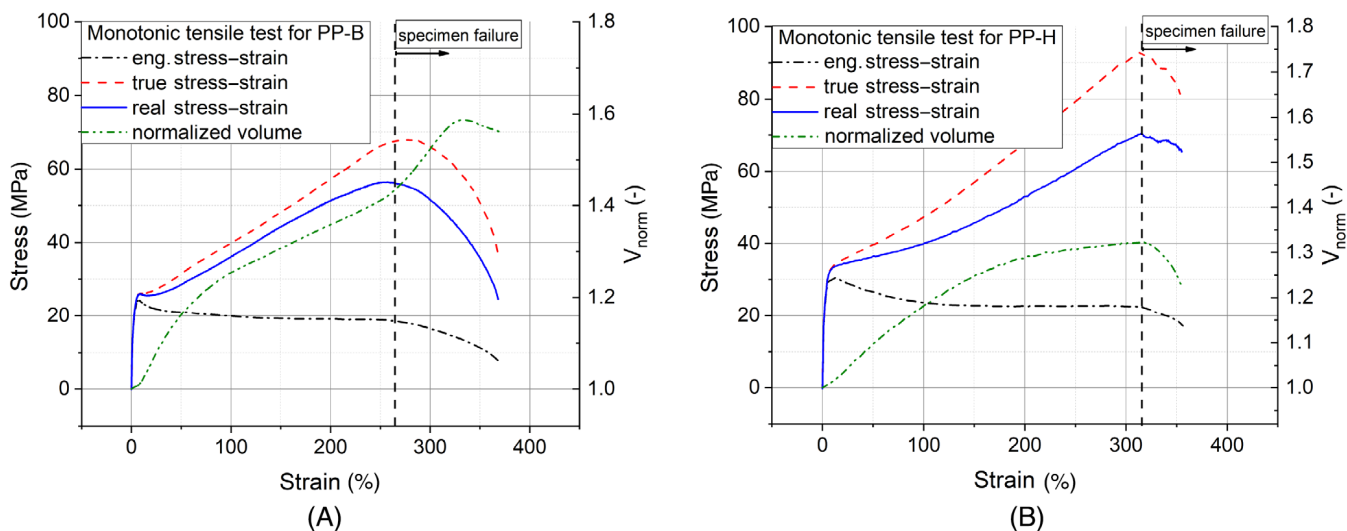
FIGURE 4 Stress–strain curves and normalized volume for (A) PP-B and (B) PP-H, whereas the differences between engineering stress–strain, true stress–strain, and real stress–strain evaluations are visible

TABLE 1 Material parameters obtained from monotonic tensile tests

	PP-B			PP-H		
	Eng.	True	Real	Eng.	True	Real
E (MPa)	1435 ± 44	1450 ± 52	1444 ± 52	1773 ± 56	1801 ± 69	1800 ± 69
σ_y (MPa)	23.9 ± 0.4	26.0 ± 0.3	25.8 ± 0.2	30.8 ± 0.3	33.8 ± 0.3^a	33.3 ± 0.4^a
σ_{UTS} (MPa)	23.9 ± 0.4	64.8 ± 14.1	55.7 ± 12.5	30.8 ± 0.3	108.7 ± 39.8	86.7 ± 37.6
ε_y (%)	9.7 ± 0.4			11.0 ± 3.3		
ε_{vol} (%)	9.5 ± 0.6			9.5 ± 0.5		
ε_{fr} (%)	291 ± 90			428 ± 151		

[a]In some cases, where no distinguished maximum appears in the real stress–strain curves, the stresses at ε_y of the engineering stress–strain curve are taken as σ_y.

as a result of the decreased stresses. However, both materials show noticeable increases of their volume (up to 60% for PP-B and 30% for PP-H), which is a strong indicator for damage in conjunction with volume gain. Thus, a decay of material properties is expected as the applied strain increases.

3.2 | Property deterioration including time-dependent effects

Cyclic load–unload experiments were used to illustrate the deterioration of material properties under tension, which was not possible during the monotonic tests. For each cycle, the values for E and ε_{res} as a function of ε_{appl} of one representative specimen per material are shown in Figure 5A. Figure 5B shows the first 45% of strain in greater detail. Therein it is worth noting that the data points for PP-B and PP-H are not equally spaced. This is

due to differences in the localization of strain between the two materials. PP-B shows moderate strains in the midsection of the specimens throughout the whole experiment. PP-H on the other hand exhibits a very uniform distribution of strain over the whole specimen for the low initial deformations, leading to a dense population of measurement points at the start of the curve. However, the necking process happens very localized, leading to large steps in local strain for higher displacements. Interestingly, ε_{res} as a function of ε_{appl} is nearly identical for PP-H and PP-B. The results suggest increased plastic deformation after 5% of applied strain, since ε_{res} starts rising at higher rates. This is only half of the strain one would expect from the monotonic experiments, where yielding started around 10%. Even at low strains, no reversible regime can be observed, as ε_{res} is always >0. For larger strains, ε_{res} increases linearly with a slope close to 1, which means that ε_{res} increases almost as fast as ε_{appl}. This is an indicator of highly plastic behavior,
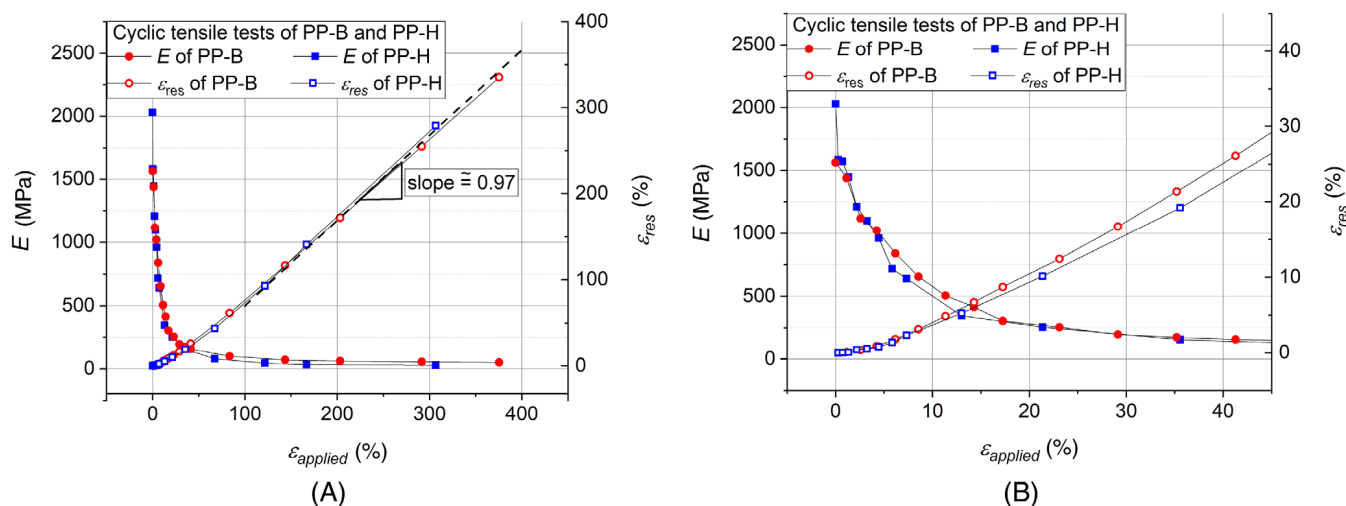
FIGURE 5 Development of modulus and residual strain as a function of the applied strain, evaluated for each cycle in load–unload experiments. Values are depicted (A) throughout the whole experiment and also (B) for the first 45% of strain only

although one cannot distinguish between irreversible plastic behavior and slow components of viscoelastic deformation. Ognedal et al. reported similar findings, stating that the elastic retraction of the material is reduced, the higher the applied strains become.[8] The decay of modulus is striking in both materials, with E dropping to mere fractions of its initial value within 5%–10% of ε_{appl}. The only noticeable difference is that PP-H starts at higher values than PP-B. This is surprising, considering that the microstructures of the homopolymer and the block-copolymer are supposedly different and distinct differences were found in the monotonic tests. Furthermore, the increased stiffness and strength of PP-H should have at least some influence on material properties at higher strains. The testing temperature is above the glass transition temperature for both materials. Thus, it is reasonable to assume that the amorphous PP regions will be the main contributors to long-term deformation, since all crystalline structures are still in their solid state. The materials may therefore also behave similarly under long-term loading, because PP-H and PP-B are both based on a comparable PP backbone. The authors propose that this viscoelastic creep is the dominant factor for the two investigated materials in load–unload experiments. Therefore, initial differences in properties become irrelevant as time progresses. To reach a conclusion on the time-independent effects of loading, two additional questions need to be answered:

1. What are the differences in material behavior when viscoelastic effects are avoided by giving the materials time to relax?
2. What are the differences in microstructure between PP-H and PP-B in the damaged and undamaged state?

3.3 | Property deterioration excluding time-dependent effects

A number of adaptations to the testing procedure have to be made to exclude viscoelastic effects while determining E. On the one hand, high tensile stresses for prolonged periods of time have to be avoided at all costs. On the other hand, sample size and shape play an important role for subsequent imaging techniques. DMA of prestrained specimens is the method of choice in this contribution. Applied forces and displacements are very small compared to tensile testing, while the instrumentation is precise enough to reliably determine E. As another indication of damage, the mechanical loss factor $\tan \delta$ can also be obtained in DMA measurements. Additionally, the specimen size is small enough, so that micro-CT measurements can be employed to analyze the microstructure, even without the need to further dissect the specimens. Since the material is given 7 days to relax, all time-dependent processes are assumed to be completed. The values of E and $\tan \delta$ as a function of ε_{appl} are shown in Figure 6 for PP-H and PP-B. In both cases, the starting modulus tends to be slightly higher than for the tensile tests, which could be caused by the increased loading rate in the DMA procedure. Additionally, E is evaluated at smaller strains in a DMA experiment than in a tensile test, which is also likely to cause increased values. Most interestingly, E of both materials remains high for much higher levels of strain compared to the cyclic tensile tests. More specifically, a noticeable decrease in E for PP-B cannot be seen until 10% of prestrain and PP-H even shows an increase in modulus after 15% of prestrain. In comparison with the load–unload experiments, the prestrained DMA method shows the differences in material behavior much more clearly, since time-dependent effects no longer distort
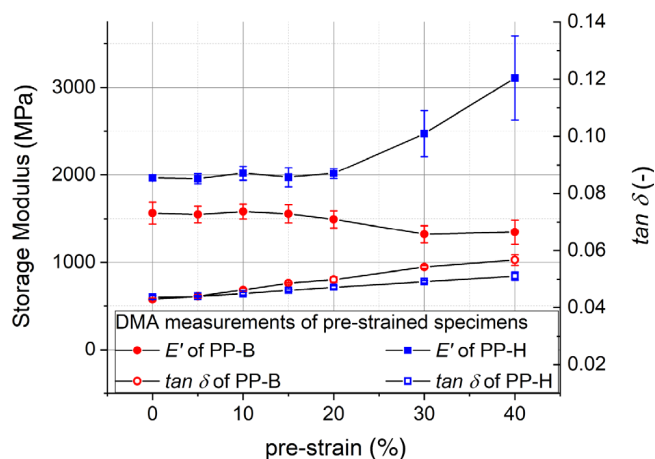
FIGURE 6 Storage modulus and mechanical loss factor versus prestrain for PP-H and PP-B, measured in dynamic mechanical analysis (DMA) experiments of prestrained specimens at room temperature (23°C) with a frequency of 1 Hz

the results. A harsh decrease in stiffness cannot be seen at all, which indicates that the previously observed modulus decay (see Figure 5) is primarily caused by creep effects. The loss factor tan δ shows a slow and steady increase in both materials, suggesting at least some detrimental changes of the microstructures in both materials. To validate these assumptions, the microstructures of the two PP types are investigated using micro-CT.

3.4 | Analysis of microstructure

While a first impression of microstructure could be obtained in polarized light microscopy, some defects may be too small for the resolution of polarized light microscopy. Some defects might also have been destroyed during the preparation of the thin slices. In addition to that, a three-dimensional representation of the microstructure
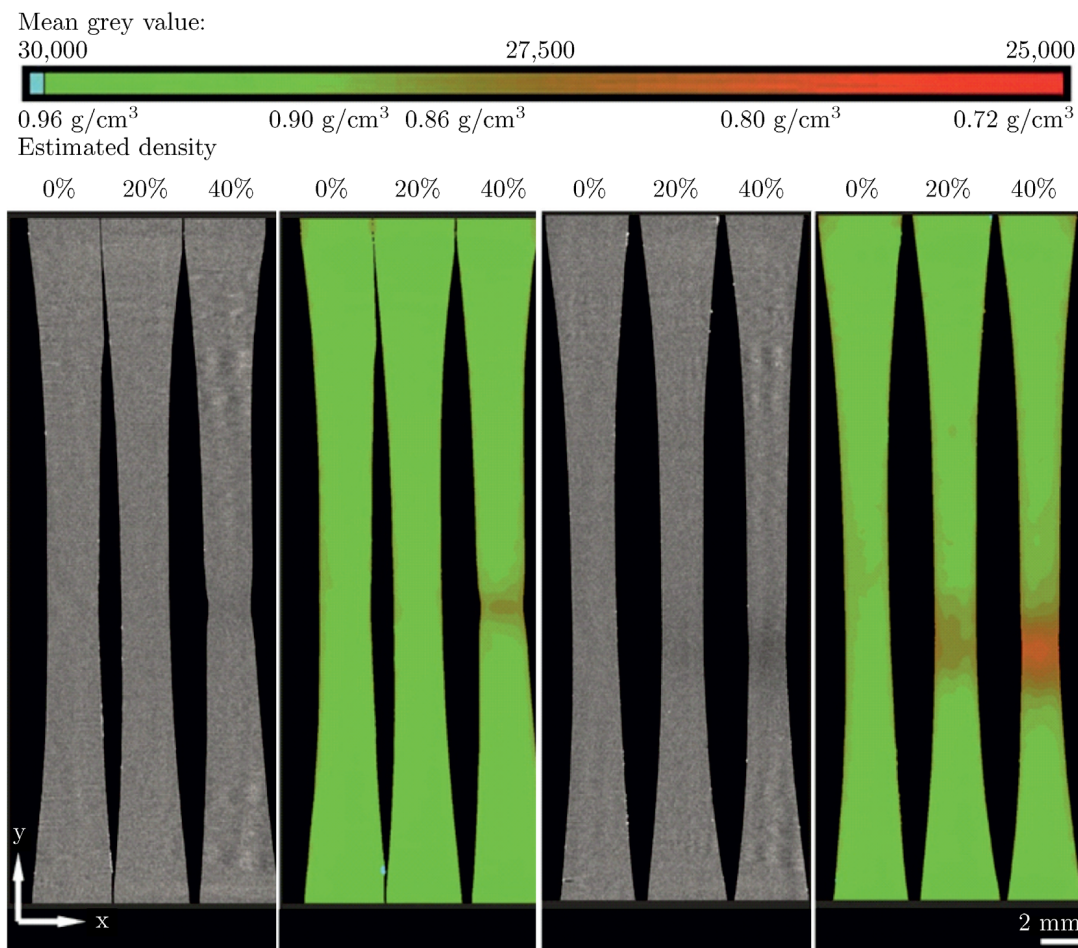

FIGURE 7 Frontal (y–x) slice images from computed tomography (CT) measurements showing (A) PP-H, (B) PP-H estimated density, (C) PP-B, and (D) PP-B estimated density at 0%, 20%, and 40% prestrain scanned at (16.5 μm)³ voxel size. (A) and (C) Gray values corresponding to absorption contrast and (B) and (D) red and green visualizations of these gray values and estimated material densities

TABLE 2   Density and porosity estimated from CT gray values

	PP-B			PP-H			
	0%	**20%**	**40%**	**0%**	**20%**	**40%**	**Air**
Gray value	28,783	27,973	26,684	28,788	28,770	28,043	10,008
ρ (g/cm³)	0.90[a]	0.86	0.80	0.90[a]	0.90	0.86	0.0
Porosity (vol%)	0.0	4.31	11.18	0.0	0.10	3.97	0.0
E (MPa)[b]	1565 ± 124	1493 ± 99	1345 ± 140	1965 ± 32	2017 ± 57	3110 ± 480	0.0

Abbreviations: CT, computed tomography; DMA, dynamic mechanical analysis.
[a]Values from material datasheet.
[b]Values from DMA measurements.
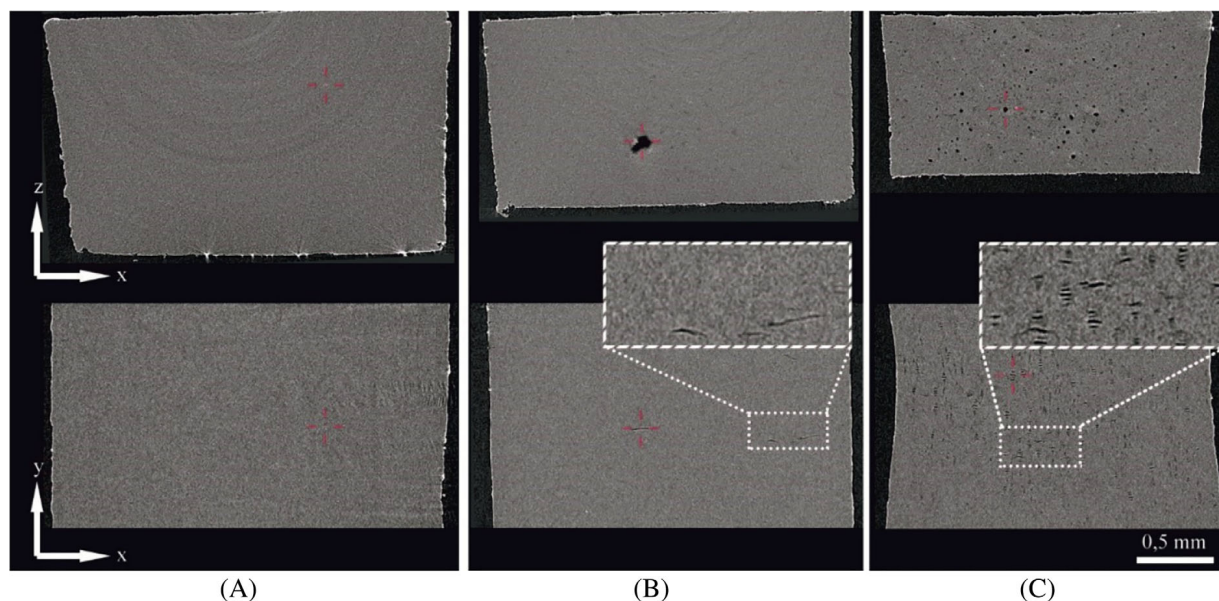
FIGURE 8   Axial (z–x) and frontal (y–x) slice images from computed tomography (CT) measurements showing PP-H at (A) 0% ($E = 1965 \pm 32$ MPa), (B) 20% ($E = 2017 \pm 57$ MPa), and (C) 40% ($E = 3110 \pm 480$ MPa) prestrain scanned at (1.25 μm)³ voxel size

cannot be easily obtained from transmitted light microscopy. Therefore, CT measurements are used to investigate the microstructure more closely at 0%, 20%, and 40% applied strain. In the overview scan in Figure 7 performed at (16.5 μm)³ voxel size, no structural information of damages such as micro cracks or crazes can be seen in any of the investigates samples. Thus, they are expected to be far below the chosen voxel size. But as also shown in the literature,[33] nonvisible defects can lead to a reduction of gray values in the CT images, representing the absorption contrast of X-rays. Therefore, the presence of defects leads to a reduction of X-ray absorption, which is visible in Figure 7A for PP-H 20% and 40% as well in Figure 7C for PP-B 20% and 40%. For better visualization of these small changes in gray values, in Figure 7B,D, the gray values were set to green and red color tones. In addition, a local density in each position of the sample can be estimated by applying the rules of mixture. Table 2 lists the minimal average gray values in the cross section of the different specimens and estimated density and porosity, respectively.

Based on the overview CT scans, the regions for the high-resolution scans were defined in the regions with the highest estimated porosity values and scans at (1.25 μm)³ voxel size are performed (depicted in Figures 8 and 9). In the reference state samples (0% prestrain), no signs of damage can be seen. However, smaller inhomogeneities of higher density, presumably caused during processing, can be distinguished. For the specimens at 20% prestrain, first signs of damage are clearly visible. While the number and size of defects is relatively low for PP-H (Figure 8), PP-B already shows numerous defects present in the microstructure (Figure 9). As a result, the modulus for PP-H remains at its initial value up to this point, while PP-B already displays a decreased E (modulus values taken from prestrained DMA measurements). One explanation for the
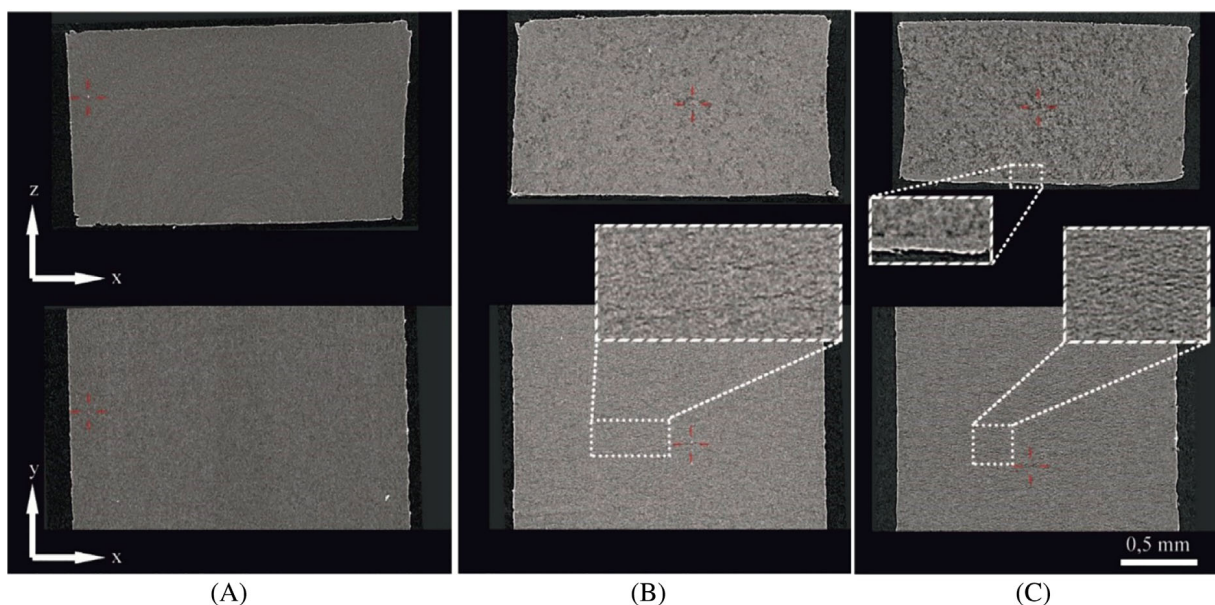
FIGURE 9 Axial (z–x) and frontal (y–x) slice images from computed tomography (CT) measurements showing PP-B at (A) 0% ($E = 1565 \pm 124$ MPa), (B) 20% ($E = 1493 \pm 99$ MPa), and (C) 40% ($E = 1345 \pm 140$ MPa) prestrain scanned at $(1.25\ \mu m)^3$ voxel size
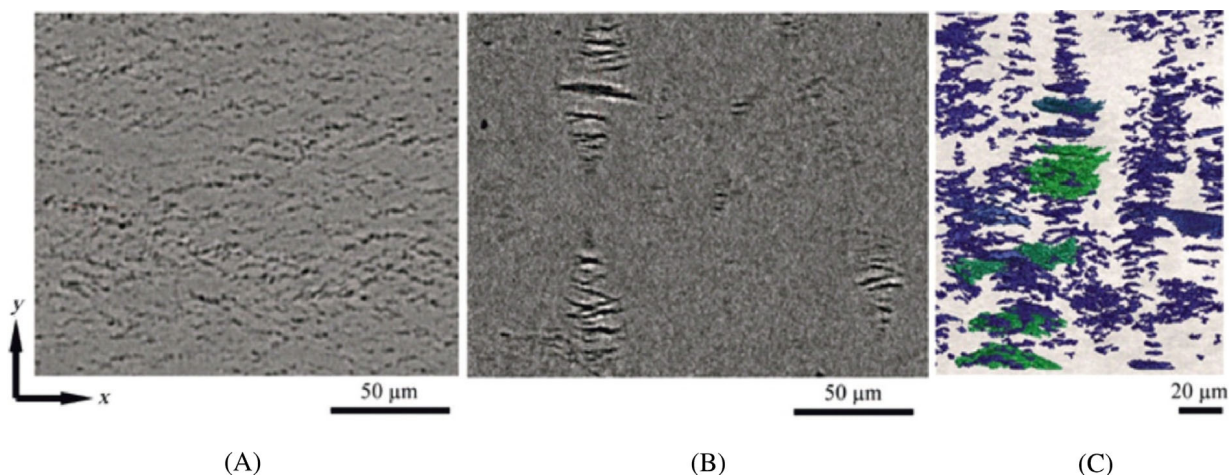

FIGURE 10 Frontal (y–x) slice images from computed tomography (CT) measurements showing (A) PP-B and (B) PP-H at 40% prestrain scanned at $(0.5\ \mu m)^3$ voxel size. (C) Three-dimensional (PP-B at 40%) rendering of segmented defect structures is shown by applying a manual threshold

increased resilience of PP-H against crazing could be its well-defined crystal structure. The reduced amount of amorphous and heterogeneous phases may hinder the formation of voids under strain,[31,32] so that the subsequent progress of damage mechanisms could be impeded as well. Since the number of microcracks increases the more strain is applied, the modulus of PP-B further decreases up to 40% prestrain (see Figure 6). For PP-B, the loss of load bearing cross section is comparably large due to the microcracks being spread randomly throughout the material. Interestingly, PP-H shows an increase in E between 20% and 40% prestrain despite the starting accumulation of

damage (as shown in Figure 8). Although a number of defects can be seen, the mechanical properties are not yet compromised by the loss of load bearing cross section. Fortunately, the damage in PP-H appears very localized, so only small areas of cross section are affected at a time. Instead, it appears that that the load bearing capacity of the macromolecules is maximized due to an increased degree of orientation (similar to a cold drawing effect). The assumption of increased orientations is also supported by Figure 4, where strain hardening can be seen on a macroscopic level. However, the modulus is expected to decrease again for strains exceeding 40%, when extensive

microstructural damage begins to outweigh the orientation effect.

Figure 10 shows the results from the CT scans performed at highest possible resolution for this sample size, reaching a voxel size of $(0.5 \ \mu m)^3$. Compared to Figure 9 now also for the PP-B 40% specimen (Figure 10A), very clear microcrack structures can be resolved and become visible. Crack widths for PP-B are all in the range of a few voxels and even below. In Figure 10B, localized polar fans can be distinguished clearly for the PP-H 40% sample, but nearly no smaller microcracks appear in the remaining polymer. As mentioned in the introduction, such structures have been reported before in semicrystalline polymers with well-defined spherulites.[13–15] On the other hand, crazes can be ruled out as damaging mechanism, since no fibrils stretching across the crack flanks are visible. A segmentation by a manually defined threshold results in a defect content of ∼10 vol% for PP-B at 40% strain and 2 vol% for PP-H at 40% strain. These values are in the order of magnitude of the estimated porosity from Table 2. In Figure 10C, such a segmentation is visualized as three-dimensional rendering of a small region from the PP-H 40% specimen. It is worth noting that these porosity values are recorded in the relaxed and unloaded state of the specimen, so that a comparison to the volume increase in the monotonic tensile tests (Figure 4) is not advisable. All of the trends discovered in the CT measurements are in good agreement with the previously conducted prestrained DMA experiments. Thus, the prestrained DMA may serve as complementary method for CT measurements. It could be used as convenient, low-cost tool for the preselection of the most relevant specimens, before conducting high-resolution CT as a more thorough investigation. The CT measurements also confirm the prestrained DMA as the most reliable of the methods discussed to estimate damage, without creep interactions in a material.

4 | CONCLUSION

Different measurement techniques are investigated to capture the damage-induced and time-dependent deterioration in mechanical properties of the semicrystalline polymer PP. Two different grades are tested, namely an ethylene-propylene block-copolymer and a PP homopolymer.

In monotonic tensile tests, the true stress–strain behavior, which includes necking as well as three-dimensional volume change during testing, is captured using DIC of two crossed cameras. The elastic modulus, E, is only available at the start of the measurement, making the change in volume the only parameter to monitor the state of the material. This volume is found to increase

the more strain is applied, especially after the yield point has been reached.

In cyclic load–unload experiments, the decrease of E with each cycle of increased loading can be studied over a wide range of applied strains. E starts plummeting in the same fashion for both investigated polymers after small amounts of strain are applied. Simultaneously, the residual strain after each cycle is found to drastically increase over the course of the experiment. It is shown that the decrease in E is mainly caused by viscoelastic effects due to the extended duration of tensile loading, making this method ill-suited to characterize damage to the microstructure. However, the values of E under the combined influence of damage and viscoelasticity can be monitored throughout the whole experiment.

In contrast to that, prestrained specimens are analyzed using DMA. Due to a relaxation period between the prestraining and the DMA measurements, time-dependent effects are eliminated. E retains higher values in these experiments until a certain amount applied strain (10%–15% in the investigated materials). Afterward, the modulus starts either to decrease as a result of damage or increase as a result of increased molecule orientation. All in all, this method yields a better representation of the integrity of the investigated materials by excluding viscoelastic effects.

Finally, the damages to microstructure are illustrated in high-resolution computer tomography of specimens that were strained by 0%, 20%, and 40%. Therein, the investigated PP block-copolymer is prone to extensive microcracking throughout the whole specimen. The PP homopolymer on the other hand shows localized damage in the form of polar fans, which are clusters of microcracks, along the polar axis of spherulites. The increasing amount of internal damage is made visible and is found to be in good agreement with the prestrained DMA measurements. Therefore, prestrained DMA experiments may be considered as a tool to preselect specimens. Subsequent CT investigations would then only need to be performed on specimens of the most interest, thus saving time and effort.

DATA AVAILABILITY STATEMENT

The data that support the findings of this study are available from the corresponding author upon reasonable request.

ORCID

Johannes Wiener https://orcid.org/0000-0002-0956-7420

Florian Arbeiter https://orcid.org/0000-0003-4638-0849

REFERENCES

[1] A. Galeski, *Prog. Polym. Sci.* **2003**, *28*(12), 1643.
[2] V. Delhaye, A. H. Clausen, F. Moussy, R. Othman, O. S. Hopperstad, *Int. J. Impact Eng.* **2011**, *38*(4), 208.
[3] V. Delhaye, A. H. Clausen, F. Moussy, O. S. Hopperstad, R. Othman, *Polym. Test.* **2010**, *29*(7), 793.
[4] H. S. Katz, J. V. Milewski, *Handbook of Fillers for Plastics*, Van Nostr and Reinhold, New York **1987**. ISBN: 978-0-442-26024-8.
[5] J. L. Way, J. R. Atkinson, J. Nutting, *J. Mater. Sci.* **1974**, *9*(2), 293.
[6] J. M. Schultz, *Polym. Eng. Sci.* **1984**, *24*(10), 770.
[7] T. F. Guo, J. Faleskog, C. F. Shih, *J. Mech. Phys. Solids* **2008**, *56*(6), 2188.
[8] A. S. Ognedal, A. H. Clausen, T. Berstad, T. Seelig, O. S. Hopperstad, *Int. J. Solids Struct.* **2014**, *51*(7–8), 1494.
[9] W. Retting, *Mechanik der Kunststoffe: Die mechanischen Eigenschaften von Polymer-Werkstoffen*, Hanser, Munich **1992**. ISBN: 3446161015.
[10] A. S. Ognedal, A. H. Clausen, A. Dahlen, O. S. Hopperstad, *Mech. Mater.* **2014**, *72*, 94.
[11] G. Boisot, L. Laiarinandrasana, J. Besson, C. Fond, G. Hochstetter, *Int. J. Solids Struct.* **2011**, *48*(19), 2642.
[12] A. Pawlak, A. Galeski, *Macromolecules* **2008**, *41*(8), 2839.
[13] H.-A. Cayzac, K. Sai, L. Laiarinandrasana, *Int. J. Plast.* **2013**, *51*, 47.
[14] L. Laiarinandrasana, N. Selles, O. Klinkova, T. F. Morgeneyer, H. Proudhon, L. Helfen, *Polym. Test.* **2016**, *55*, 297.
[15] L. Laiarinandrasana, T. F. Morgeneyer, H. Proudhon, F. N'guyen, E. Maire, *Macromolecules* **2012**, *45*(11), 4658.
[16] J. Karger-Kocsis, T. Barany, *Polypropylene Handbook*, Springer International Publishing, Cham **2019**. https://doi.org/10.1007/978-3-030-12903-3
[17] W. Grellmann, B. Langer, *Deformation and Fracture Behaviour of Polymer Materials*, Springer International Publishing, Cham **2017**. https://doi.org/10.1007/978-3-319-41879-7
[18] T. C. B. McLeish, C. J. G. Plummer, A. M. Donald, *Polymer* **1989**, *30*(9), 1651.
[19] S. N. Olufsen, K. R. Tekseth, D. W. Breiby, A. H. Clausen, O. S. Hopperstad, *Polym. Test.* **2020**, *91*, 106834. https://doi.org/10.1016/j.polymertesting.2020.106834
[20] J. Mohanraj, D. C. Barton, I. M. Ward, A. Dahoun, J. M. Hiver, C. G'Sell, *Polymer* **2006**, *47*(16), 5852.
[21] Z. Bartczak, A. S. Argon, R. E. Cohen, M. Weinberg, *Polymer* **1999**, *40*(9), 2347.
[22] I. Kemal, A. Whittle, R. Burford, T. Vodenitcharova, M. Hoffman, *Polymer* **2009**, *50*(16), 4066.
[23] A. S. Argon, R. E. Cohen, *Polymer* **2003**, *44*(19), 6013.
[24] A. L. Gurson, *J. Eng. Mater. Technol.* **1977**, *99*(1), 2.
[25] V. Tvergaard, A. Needleman, *Acta Metall.* **1984**, *32*(1), 157.

[26] S. N. Olufsen, A. H. Clausen, D. W. Breiby, O. S. Hopperstad, *Mech. Mater.* **2020**, *142*, 103296. https://doi.org/10.1016/j.mechmat.2019.103296
[27] A. A. Hamza, T. Z. N. Sokkar, M. A. El-Bakary, *Meas. Sci. Technol.* **2004**, *15*, 831.
[28] A. A. Hamza, T. Z. N. Sokkar, M. A. El-Bakary, A. M. Ali, *Opt. Laser Technol.* **2010**, *42*, 703.
[29] A. A. Hamza, A. E. Belal, T. Z. N. Sokkar, M. A. El-Bakary, K. M. Yassien, *J. Opt. A: Pure Appl. Opt* **2007**, *9*, 820.
[30] Z. Bartczak, A. Galeski, E. Martuscelli, *Polym. Eng. Sci.* **1984**, *24*(15), 1155.
[31] G. M. Kim, G. H. Michler, M. Gahleitner, J. Fiebig, *J. Appl. Polym. Sci.* **1996**, *60*(9), 1391.
[32] T. Kawai, S. Soeno, S. Kuroda, S. Koido, T. Nemoto, M. Tamada, *Polymer* **2019**, *178*, 121523.
[33] J. Kastner, C. Gusenbauer, S. Senck & G. Rao in: Proceedings of 15th Asia Pac. Conf. Non-Destr. Test. (APCNDT 2017), Singapore, November 2017, pp. 7. https://www.ndt.net/search/docs.php3?id=22081
[34] B. Plank, M. Schiwarth, S. Senck, J. Herr, S. Ayalur-Karunakaran & J. Kastner in: Proceedings of Int. Symp. Digit. Ind. Radiol. Comput. Tomogr. (DIR 2019), Germany, July 2019, pp. 11. https://www.ndt.net/search/docs.php3?id=24749
[35] L. A. Feldkamp, L. C. Davis, J. W. Kress, *J. Opt. Soc. Am. A* **1984**, *1*(6), 612. https://doi.org/10.1364/JOSAA.1.000612.
[36] A. Khudiakova, M. Berer, S. Niedermair, B. Plank, E. Truszkiewicz, G. Meier, H. Stepanovsky, M. Wolfahrt, G. Pinter, J. Lackner, *Addit. Manuf.* **2020**, *36*, 101671. https://doi.org/10.1016/j.addma.2020.101671
[37] J. Kastner, B. Plank, D. Salaberger & J. Sekelja in: Proceedings of 2nd Int. Symp. NDT Aerosp., November 2010, pp. 12. https://www.ndt.net/search/docs.php3?id=10410
[38] P. S. Stelzer, B. Plank, Z. Major, *Nondestruct. Test. Eval.* **2020**, *35*(3), 342.
[39] P. Weissenbacher MSc Thesis, University of Applied Sciences Upper Austria, 2019.
[40] A. Y. Raja, M. Moghiseh, C. J. Bateman, N. De Ruiter, B. Schon, N. Schleich, T. B. F. Woodfield, A. P. H. Butler, N. G. Anderson, *Appl. Sci.* **2018**, *8*, 467.

APPENDIX A

A.1 | EXPERIMENTAL DETAILS
A.1.1. | Specimen preparation

Dumbbell specimens for monotonic and cyclic tensile tests were machined from 4-mm-thick extruded sheets of PP-H and PP-B. In all cases, the length axis of the specimens was parallel to the direction of extrusion. The exact dimensions are shown in Figure A1. To accommodate the small dimension of the dynamic mechanical analysis (DMA) apparatus,
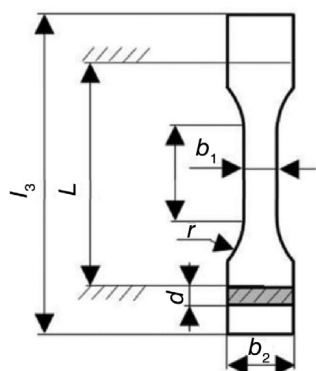
	Specimen feature	Tensile specimens	DMA specimens
l_3	Total length (mm)	80	50
l_1	Parallel length (mm)	15	10
L_1	Clamping length (mm)	42	35
b_1	Minimum width (mm)	10	2.3
b_2	Shoulder width (mm)	23	4
d	Thickness (mm)	4	1.3

FIGURE A1 Specimen dimensions for tensile tests and dynamic mechanical analysis (DMA)

miniature specimens had to be sanded from thin slices of the same 4-mm-thick plates. The dimensions are also given in Figure A1. The dumbbell form was used instead of prismatic specimens to ensure that damage would occur localized in the center of the specimen. This was necessary, since preliminary tests showed a tendency of the material to yield and fail at the clamping. This has to be kept in mind, when comparing exact modulus values, as the introduction of force and the resulting stress state in prismatic specimens are different from dumbbell specimens.

A.1.2. | Test setup for tensile tests

Monotonic and cyclic tensile tests were performed on a Zwick Z010 (Zwick/Roell, Ulm, Germany) at a crosshead speed of 1 mm/min and ambient conditions. In the monotonic tests, specimens were continuously loaded until fracture. A total of four specimens was tested per material. For the cyclic tests, a load–unload procedure was employed. The specimens were deformed with a rate of 1 mm/min until a predetermined displacement was reached. Then, the specimen was unloaded using a crosshead speed of 1 mm/min. After unloading to zero force, the next loading step was started immediately without time for relaxation. By increasing the maximum displacement from step to step, the specimens were tested until fracture. The increments of displacement were 0.5 mm for displacements between 0 and 5 mm, 1 mm between 5 and 10 mm, 5 mm between 10 and 25 mm, and 15 mm until fracture. Due to the extensive testing time of this procedure, only three specimens were tested per material. The deformations of the test specimens were monitored using cameras in a 90° angle as shown in Figure A2A so that a front view as well as a side view of the specimen could be obtained. Two Prosilica GT6600 (Allied Vision Technologies GmbH, Stadtroda, Germany) equipped with

100-mm Tokina AT-X M100 PRO D macro objectives (Kenko Tokina Co., Nakano, Japan) were used for that purpose. Digital image correlation of the surface strains was performed using the software package Mercury 2.8 (Sobriety s.r.o., Kurim, Czech Republic), see Figure A2B.

A.1.3. | Determination of modulus in cyclic tests

A decay of E can be caused by damage or by viscoelastic creep effects. In a monotonic tensile experiment, this decay cannot be observed. For that purpose, cyclic load–unload experiments can be used. The modulus can be evaluated for each loading cycle, so that the evolution of E throughout the experiment becomes visible. Due to the viscoelastic material response at the start of each cycle, an evaluation of E according to ISO 527 is unreliable, but the curves have a more linear behavior at intermediate stress levels. Therefore, the part of the curve between the data points at 5 and 10 MPa was chosen for evaluation of E, as is shown in Figure A3. For each cycle, the maximum applied strain and the minimum residual strain, ε_{appl} and ε_{res}, were evaluated as well. Correlating ε_{res} with ε_{appl} of the previous cycle offered additional information on the deformation behavior. Increasing values of ε_{res} indicated the presence of plastic deformation, which was a result of exceeding the flow stress and may have been accompanied by the creation of additional volume. However, the applied forces were greater than zero for the majority of time, so creep behavior was expected too. Additionally, viscoelastic effects and irreversible deformation could not be easily distinguished as source of ε_{res}. Some sources[19] suggest to prestrain the samples and continue characterization after a thorough relaxation period. In this paper, we opt to show the continuous load–unload procedure as well as DMA measurements with prestrain as a discontinuous approach, since both loading profiles could be relevant for specific applications.
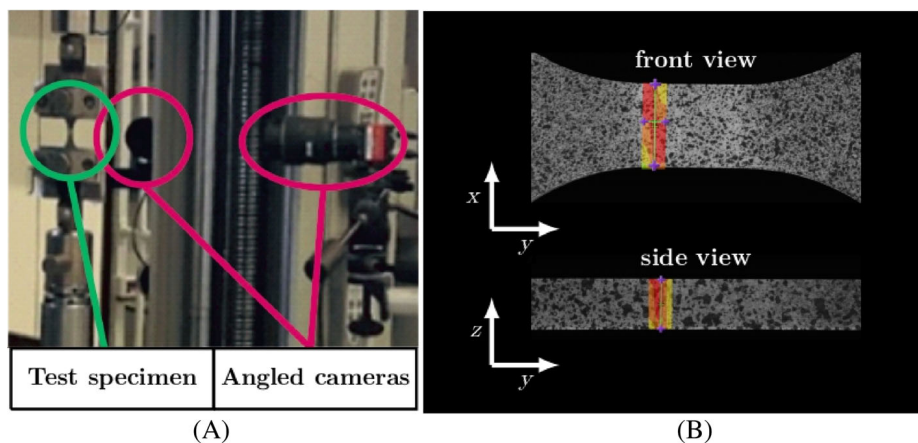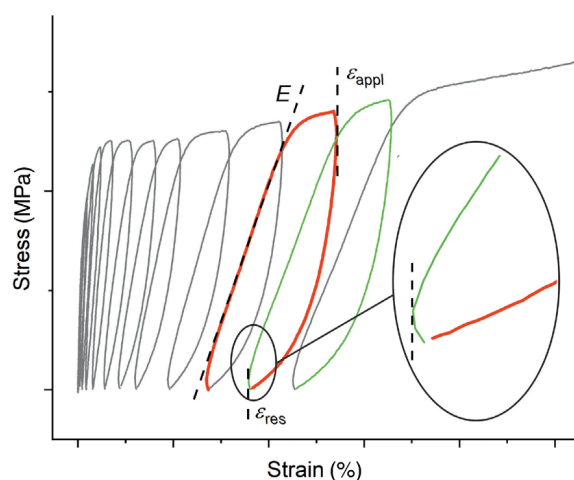
FIGURE A3   Representative stress–strain curve of a cyclic load–unload experiment. The applied strain ε_{appl} and the Young's modulus E are recorded for each cycle as well as the residual strain ε_{res}, which stems from previous loading cycles

A.1.4. | DMA measurements with prestrain

The DMA specimens were loaded on a Zwick Z001 (Zwicke/Roell) with a 1-kN load cell, up to a certain prestrain to gradually induce damage. These prestrains were measured locally on the specimen surface via digital image correlation, as described above. Pneumatic grips were used for the clamping of the specimens. The prestraining was performed at 1 mm/min crosshead speed and room temperature. Although some literature sources suggest complete relaxation as early as 10 min after prestraining,[8] specimens were carefully removed and left to relax for 7 days. Subsequent DMA measurements were performed at room temperature (23°C) at a frequency of 1 Hz using a Modular Compact Rheometer MultiDrive by Anton Paar (Anton Paar, Graz, Austria). The stress amplitude was set to 0.5 MPa in tension, while the mean stress level was 0.75 MPa. This ensured tensile loading throughout the whole experiment. The clamping length for the prestraining and the DMA measurements was 35 mm. The measured storage moduli were interpreted as the material's Young's modulus, E, at different stages of damage, depending on the prestrain. As additional parameter to judge the integrity of the materials, the mechanical loss factor, tan δ, was evaluated as well. This way, prestrains of 0%, 5%, 10%, 15%, 20%, 30%, and 40% were investigated using three specimens per material and level of prestrain. Here, it should be noted again that the values for E and tan δ should primarily be used to compare the two materials in question. A comparison of exact values to other sources in the literature is problematic due to the adapted specimen geometry used in these experiments.

A.1.5. | X-ray computed tomography

A.1.5.1. | Equipment for X-ray computed tomography

Several X-ray computed tomography (CT) scans were performed using a Nanotom 180 NF (GE Phoenix/X-ray, Wunstorf, Germany), equipped with a 180-kV nano-focus X-ray tube and a molybdenum target on a beryllium window. Because the structural resolution by CT is highly dependent on the investigated sample size and the amount of available detector pixels, a multiscale approach according to Plank et al.[34] was followed. To get an overview of a large region of interest, six specimens (PP-B 0%, 20%, 40% and PP-H 0%, 20%, 40%) were scanned at once with an edge length of a volumetric pixel (voxel size) of 16.5 μm^3. With this voxel size, a field of view of approximately 39^3 mm^3 could be investigated at once and structures larger approximately three times the

voxel size can be resolved. These overview scans were carried out at 60-kV tube voltage, 500-ms integration time, and 600 projections within a total measurement time of 30 min. To investigate the three-dimensional material behavior in the micrometer range, high-resolution CT scans with a voxel size of 1.25 μm^3 were performed. These scans were limited to regions with the highest degrees of damage, which were determined in the overview scans. The horizontal amount of detector pixels was extended from 2304 to ~4600 pixels and the virtual detector mode "VSensor 2" was used. This was done to capture the entire cross sections of two specimens (~2.5 × 1.5 mm^2 each) in the field of view of one scan. Applying 50 kV as tube voltage and an integration time of 500 ms for all 1900 projection images resulted in a total measurement time of ~340 min. To verify the recorded microstructures in strained samples, additional high-resolution CT scans in the submicron range were performed on an Easytom 160 (RX Solutions, Chavanod, France). This device was equipped with a 160-kV nano-focus X-ray tube and a LaB6 Filament reaching an X-ray focal spot diameter in the range of 400 nm. As target material, tungsten on a diamond window was used, as well as a 4032 × 2688 Pixel 14-bit CCD camera as imager system. A voxel size of 0.5 μm^3 could be reached without cutting the sample cross section. The field of view within the region of interest spanned 1 × 1 × 1 mm^3 and a tube voltage of 50 kV was used. About 1568 projection images were recorded at 3500 ms integration time, resulting in a total measurement time of 548 min for each scan.

To reconstruct a 3D volume from the recorded 2D projection images, a filtered back projection algorithm (e.g., Feldcamp et al.[35]) implemented in the reconstruction software tools of the abovementioned CT manufacturer was applied.

A.1.5.2. | X-ray tomography data analysis

The CT data analysis was performed using the commercially available software tool, VG Studio MAX 3.4 (Volume Graphics, Germany). This software package includes a porosity/inclusion analysis tool, as well as tools to determine mean gray values of certain defined regions of interest. Segmentation and three-dimensional visualization of the defect structures were done by applying a simple threshold method often used for porosity[36,37] or matrix evaluations[38] in composites. To determine a proper threshold value, a multiscale approach as shown in the study by Kastner et al.[37] is usually used. Most of the times, this leads to sufficient quantitative values, as long as all available microstructures can be resolved by the used voxel resolution. However, the maximum used resolution of 0.5 μm^3 voxel size showed that there are much smaller defects within the investigated specimens. Thus, a reliable quantification of defect volume was not possible using this multiscale approach. To overcome this problem, a rule of mixture was applied on the gray levels of the CT images recorded at 16.5 μm^3 voxel size. The mean gray values of the undamaged specimens are set as a reference density of 0.9 g/cm^3 (data sheet value for both materials) and a density of 0 g/cm^3 is assumed for the surrounding air. By correlating these reference values to the gray levels of the damaged specimens, an estimation of the porosity can be made, assuming that nonvisible cracks and voids lead to a reduction of material density and therefore a linear change in gray level. Weissenbacher[39] demonstrates that a density contrast of 0.1 g/cm^3 can be resolved clearly at 120 kV. By using 60 kV as tube voltage for the investigations, the density contrast between different samples in terms of change in gray values is significantly higher.[40]